

*Editorial corner – a personal view*

## Becoming the symbol of recycling instead of consumption – 50 years of PET bottles

Ferenc Ronkay\* 

Department of Innovative Vehicles and Materials, GAMF Faculty of Engineering and Computer Science, John von Neumann University, H-6000 Kecskemét, Hungary

Around 30 years after the discovery of poly(ethylene terephthalate) (PET), in 1973, DuPont designer Nathaniel Wyeth developed the first transparent plastic bottle made from this material, which can withstand the pressure of carbonated liquids (<https://doi.org/10.1016/j.wasman.2007.11.003>). Over the past 50 years, this product has spread worldwide, with about 30 million tons of PET bottles now being produced yearly (<https://doi.org/10.1016/j.resconrec.2020.105014>), representing about 7% of total plastic consumption. Presumably, this is why the PET bottle has become a symbol of plastics for ordinary people.

The fact is that plastic packaging can increase sales: for example, in Hungary, where good quality drinking water is available in almost every household, in the 1980s, the average person bought 3 liters of bottled mineral water a year, while today it is 130 liters. This is partly thanks to PET bottles: they are stylish and aesthetic, encourage us to buy, and we feel safer drinking packaged water instead of tap water. However, there are many places in the world where PET bottles are the only means of providing people with good quality drinking water (<https://doi.org/10.34172/hpp.2021.09>); in these areas, they can mean not only comfort but also survival. Like other packaging, the use of bottles is often justified on functional grounds (shelf life, transportability, *etc.*), but in many cases, they are used purely for marketing purposes. In terms of sustainable development, we should strive not to waste the good qualities of plastics: the low weight of the product, its cost-effectiveness, or its aesthetic

optical properties, so not to use them unnecessarily. This is not only the responsibility of manufacturers, who primarily satisfy the demand generated by consumers. It is up to each individual to decide what products or packaging they buy, as their purchases can have a knock-on effect on the development directions of manufacturers. Therefore, it is important that, in addition to institutional education and research, polymer experts should also disseminate up-to-date knowledge on plastics to a wide range of society. This would help to raise people's awareness of their personal responsibility for the management of packaging and to emphasize that plastics are not just packaging materials.

PET bottles that end up in nature because of improper waste management are not only unsightly but could also pose a threat to wildlife when they decompose in the natural environment. It has been shown that inorganic and organic substances associated with PET degradation can promote the adsorption of inorganic compounds onto weathered plastic surfaces, with implications for the transfer of hazardous chemicals to marine life (<https://doi.org/10.1038/s41529-023-00377-y>). Recognizing this, plastic waste recovery from rivers, seas and oceans has started in recent years (<https://doi.org/10.1088/1748-9326/abbb4f>).

The large amount of PET bottle waste generated has led some to predict an ecological disaster, even though the solution is relatively simple from a technological point of view, and many countries have already achieved good results in terms of professional

\*Corresponding author, e-mail: [ronkay.ferenc@nje.hu](mailto:ronkay.ferenc@nje.hu)

© BME-PT

waste management. Once separated from other materials, PET waste can be recycled by physical-mechanical and chemical methods. However, this requires collection and appropriate sorting. Decision-makers and the public in the countries have a role in building the necessary infrastructure and ensuring its efficient operation. The regulation of plastic waste management is becoming more and more stringent to promote the transition to a circular economy. This has led to legislation such as the European Single-Use Plastics Directive, which aims, among other things, to increase the collection rate and implement closed-loop recycling of PET bottles (<https://doi.org/10.1016/j.cogsc.2021.100462>).

Recycling initially involved the production of low-value textiles and nonwovens from collected PET waste, but in recent decades, a number of technologies have been developed to purify bottle waste to food-grade quality and compensate for molecular weight loss by solid-state polycondensation (<https://doi.org/10.1038/s41586-020-2149-4>). In addition to the bottle-to-bottle process, it is now possible to develop technical products from waste with a longer

lifetime, for example, by improving mechanical properties or flame resistance (<https://doi.org/10.1007/s10973-022-11423-3>). Increasingly large capacity plants for chemical recycling of more contaminated waste are being built worldwide, mainly based on methanolysis, ammonolysis and glycolysis. New opportunities for biological recycling through enzymatic degradation of PET are also opening up, and PET has been successfully synthesized from the resulting monomers (<https://doi.org/10.1038/s41586-020-2149-4>).


The rational use and proper post-consumer management of PET bottles minimize the risk of environmental harm. In 50 years, humankind has learned a lot about the benefits and drawbacks of plastic packaging, and hopefully, after an initial, sometimes irrational consumption, their use will be balanced in more and more countries as the best available recycling technologies become more widespread. The aim in the upcoming decades is to continue along this path so PET bottles will become a symbol of renewal and the recycling of materials rather than a symbol of disposable, worthless things.



Prof. Dr. Ferenc Ronkay  
Topic editor

Research article

# Construction of a thermally conductive network to improve the thermal and mechanical performance of silicone rubber foam

Hongjie Xie<sup>1</sup>, Lijuan Zhao<sup>1</sup>, Yanli Chen<sup>1</sup>, Bing Han<sup>2</sup>, Yu Hua<sup>2</sup>, Dongliang Zhang<sup>2</sup>, Zhaoqiang Li<sup>2</sup>, Qibo Deng<sup>3,4</sup>, Yunfeng Zhao<sup>1\*</sup> 

<sup>1</sup>School of Materials Science and Engineering, Tianjin University of Technology, 300384 Tianjin, China

<sup>2</sup>Suzhou Techinno New Materials Technologies Co., Ltd., 215500 Changshu, Jiangsu, China

<sup>3</sup>Key Laboratory of Hebei Province on Scale-span Intelligent Equipment Technology, Tianjin Key Laboratory of Power Transmission and Safety Technology for New Energy Vehicles, and School of Mechanical Engineering, Hebei University of Technology, 300401 Tianjin, China

<sup>4</sup>Advanced Equipment Research Institute Co., Ltd. of HEBUT, 300401 Tianjin, China

Received 17 May 2023; accepted in revised form 20 August 2023

**Abstract.** Silicone foam (SF) is a porous silicone rubber with a lower density, higher elasticity, and good thermal stability. In this work, we selected aluminum spheres and carbon fiber (CF) as thermally conductive fillers to prepare hybrid SF. After optimization, we found that Al and CF hybrid SF (Al-CF-SF) has a higher thermal conductivity ( $1.37 \text{ W} \cdot \text{m}^{-1} \cdot \text{K}^{-1}$ ) than the single-filler filled SF (CF-SF,  $1.2 \text{ W} \cdot \text{m}^{-1} \cdot \text{K}^{-1}$  or Al-SF,  $0.52 \text{ W} \cdot \text{m}^{-1} \cdot \text{K}^{-1}$ ) under the same filling amount of 60 wt%. The finite element simulation was used further to explore the thermal conductive mechanism of the hybrid SF. Meanwhile, the compressive and tensile modulus of the material (CF-SF) was increased to 10.8 and 3.3 MPa compared with pure SF, respectively, and the mechanical properties were improved. In addition, infrared thermography further demonstrated that Al-CF-SF has a faster heat transfer rate under relaxation and applied pressure.

**Keywords:** polymer composites, mechanical properties, thermal properties, silicone foam, hybrid filler

## 1. Introduction

Polymer foam is a kind of functional polymer with many pores inside [1]. Due to their unique cellular structure properties, lower weight and mechanical damping make the foams attractive in many applications [2, 3]. Specially, silicone rubber foam (SF) possesses the advantages of flexibility, electrical insulation and excellent chemical and thermal stability [4, 5] and many applications in energy absorption and insulation [6–8]. However, the presence of a large number of cellular structures causes the foam to turn into thermal insulation and destroy its mechanical strength which limits the use of foam in situations

where both mechanical damping and thermal conductivity requirements [9, 10], such as the battery and the sensors of vehicles.

Adding high thermal conductivity ( $K$ ) fillers to the polymer matrix is an effective way to improve thermal conductivity [11, 12]. Li *et al.* [13] proposed a simple foaming method to immobilize the thermal conductive pathway using the gelation of cured polysaccharides under heating conditions, and a high  $K$  of  $1.253 \text{ W} \cdot \text{m}^{-1} \cdot \text{K}^{-1}$  was recorded from a 3D- $\text{Al}_2\text{O}_3$ -PDMS composite with high alumina loading (69.6 wt%) prepared by vacuum-assisted impregnation. Zhang *et al.* [14] synthesized a carbon nanotube

\*Corresponding author, e-mail: [yfzhao@tjut.edu.cn](mailto:yfzhao@tjut.edu.cn)

© BME-PT

and graphene oxide composite 3D network by a simple self-assembly process to prepare foam composites, and the results showed that the electrical, thermal, and mechanical properties of the composites could be effectively improved [15, 16]. The type and proportion of fillers affect the constructive effect of thermal conductive networks, and the synergistic effect of mixed fillers is closely related to the magnitude of thermal conductivity [17–19].

The purpose of this paper is to utilize the shock-absorbing properties of silicon foam to reduce the damage to electronic components in the collision process, and the heat can be quickly transferred out simultaneously. It has been reported that the combination of one-dimensional carbon fiber and particles with high  $K$  makes it easier to obtain a continuous structure with high thermal conductivity [20]. Therefore we designed a series of hybrid SF filled with high  $K$  fillers of Al powder ( $230 \text{ W}\cdot\text{m}^{-1}\cdot\text{K}^{-1}$ ) [21, 22] and the carbon fiber (CF,  $900 \text{ W}\cdot\text{m}^{-1}\cdot\text{K}^{-1}$ ) [23, 24] to investigate the relationship between fillers and thermal conductivity of SF composites. It was found that the thermal and mechanical properties of SF filled with different sizes of Al (5, 10 and 30  $\mu\text{m}$ ) and CF were improved. In addition, we constructed a more efficient thermal conductive pathway using the filler synergy between Al powder and CF, and the optimized Al-CF-SF composite obtained the highest  $K$  ( $1.37 \text{ W}\cdot\text{m}^{-1}\cdot\text{K}^{-1}$ ). Infrared thermography also showed that the increase in the filler amount and external pressure favored the heat transfer rate of SF composites.

## 2. Experimental section

### 2.1. Materials

Liquid silicone rubber (F663A and F663B) was supplied by Hongyejie Technology Co., Ltd. (Guangdong, China). Mix component A and component B

in a 1:1 ratio, with a foaming coefficient of three times. Short-cut carbon fibers (CF, >99%) with a diameter of 45  $\mu\text{m}$  and a length of 7–10  $\mu\text{m}$  were procured from Cangzhou Zhongli New Material Technology Co., Ltd. (Hebei, China). Aluminum powders with purity of 99.9% were supplied by Ansteel Group Aluminum Powder Co., Ltd. (Liaoning, China). In this article, three different particle sizes of Al powders of 5, 10, and 30  $\mu\text{m}$  were used as fillers. All chemical reagents used in this paper were analytically pure and did not require further purification at the time of use.

### 2.2. Composite preparation

First, component A was prepared by mixing hydroxyl-containing silicone oil and Karstedt catalyst for two minutes. Similarly, component B consists of hydrogen-containing silicone oil and an inhibitor. Component A was mixed with component B in a weight ratio of 1:1, and the H-containing silicone oil and the OH-silicone oil reacted in the presence of the catalyst to produce hydrogen ( $\text{H}_2$ ), and  $\text{H}_2$  also acts as a foaming agent. And then, the mixture is put in the middle of two glass plates, and pressed down by four weights (1 kg) on the top plate. Finally, the glass plate was transferred to an oven for heat treatment at 30  $^\circ\text{C}$  for 24 h for foaming. We named the silicone rubber foam prepared without any fillers SF. For the hybrid SF, the thermally conductive filler (CF/Al) is uniformly mixed with component A/B through mechanical stirring. The other steps are the same as the preparation of SF. According to the type and content of fillers, the naming of hybrid SF is detailed in Table 1.

### 2.3. Characterization

Scanning electron microscopy (SEM) images were obtained by using a field emission electron microscope (FEI-Quanta FEG 250, USA). Before shooting

**Table 1.** The formulation of the SF, Al-SF, CF-SF, and Al-CF-SF.

Sample name	Component A [wt%]	Component B [wt%]	Al [wt%]	CF [wt%]
SF	50	50	0	0
Al-SF(20 wt%)	40	40	20	0
Al-SF(40 wt%)	30	30	40	0
Al-SF(60 wt%)	20	20	60	0
CF-SF(20 wt%)	40	40	0	20
CF-SF(40 wt%)	30	30	0	40
CF-SF(60 wt%)	20	20	0	60
Al-CF-SF(60 wt%)	20	20	2	58

the SEM, the sample was cut into a small flat surface and fixing to the sample stage with a conductive adhesive, and sputtering gold was performed on the surface of the samples to increase the conductivity; the test voltage is 3 or 5 kV. X-ray diffraction (XRD) patterns were taken from a Rigaku diffractometer (D/Max 2500, Japan) with Cu  $K_{\alpha}$  radiation ( $\lambda = 0.154598$  nm) and scanned from  $20^{\circ}$  to  $70^{\circ}$  at a rate of  $5^{\circ} \cdot \text{min}^{-1}$ . Tensile and compression tests were obtained by an electronic universal testing machine (XJ830, Shanghai Xiangjie Testing Instruments Co., Ltd.). The elongation at break and tensile strength of silicone foam was characterized according to ASTM D412-98a. Dumbbell-shaped specimens with a narrow width of 1.3 mm were tested at room temperature at a tensile speed of  $5 \text{ mm} \cdot \text{min}^{-1}$ , and three parallel tests were performed for each group of specimens, and the average values were taken. Because the specimen is too thin, the compression test did not use the national standard, instead the sample was a small 30 mm diameter disc, and the loading rate was  $1 \text{ mm} \cdot \text{min}^{-1}$ . The thermal conductivity was tested by a heat flow method thermal conductivity instrument (DRL-V, Xiangtan Xiangyi Instruments Co. Ltd., Hunan, China). The infrared (IR) thermal images were captured by an IR camera (HIKMICRO, H11, China). Thermogravimetric analysis (TGA) was performed with a TGA 209F3A (NETZSCH, Germany) in the range of 40 to  $800^{\circ}\text{C}$  at a  $10^{\circ}\text{C} \cdot \text{min}^{-1}$  heating rate under an air atmosphere. Fourier transform infrared spectrometer (Perkin Elmer, America) can obtain spectra with a resolution of  $0.5 \text{ cm}^{-1}$  in the wave number range of 4000 to  $400 \text{ cm}^{-1}$ . We use a

$100 \times 100 \times 1$  mm sheet for the voltage breakdown test (Jilin Feng Yuan Precision Electronic Equipment Co., Ltd., China).

## 2.4. Finite element simulation experiment

The simulations were modeled in two dimensions using SEM images as a reference in a  $200 \times 150 \mu\text{m}$  area of the matrix. Silicone is the matrix, and circles of different diameters represent similarly sized aluminum spheres that are randomly distributed in the matrix. Rectangles of different sizes represent CF, which is anisotropically distributed within the matrix, and ellipses represent vesicles produced by foaming. For transient heat transfer analysis, a constant temperature of 353.15 K was set at the lower boundary, and an ambient temperature of 298.15 K was set at the upper boundary, the left and right boundaries were designated as insulating boundaries, and the vesicles were set to radiate from the surface to the ambient.

## 3. Results and discussion

### 3.1. Microstructure of the composite materials

The specific preparation scheme is shown in Figure 1. Component A containing Si–OH bond with component B containing Si–H bond can crosslink together and produce hydrogen gas ( $\text{H}_2$ ) in the presence of catalysts. The reaction occurs at  $30^{\circ}\text{C}$  for foaming, the generated  $\text{H}_2$  acts as foaming agent, and therefore the production process is simple and clean. CF and Al powder are both high thermally conductive fillers; they can be evenly dispersed within the silicone oil matrix. After mixing, they are evenly spread

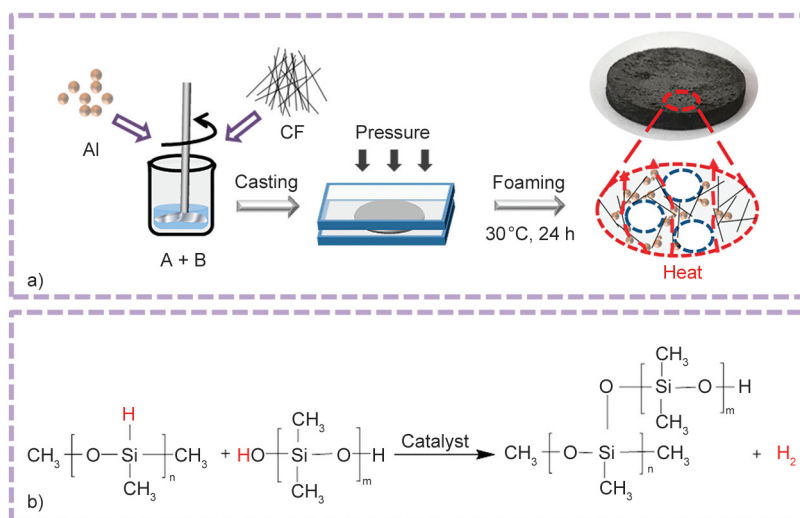


**Figure 1.** a) Preparation scheme of silicone foam with heat transfer network, b) foam generation mechanism.

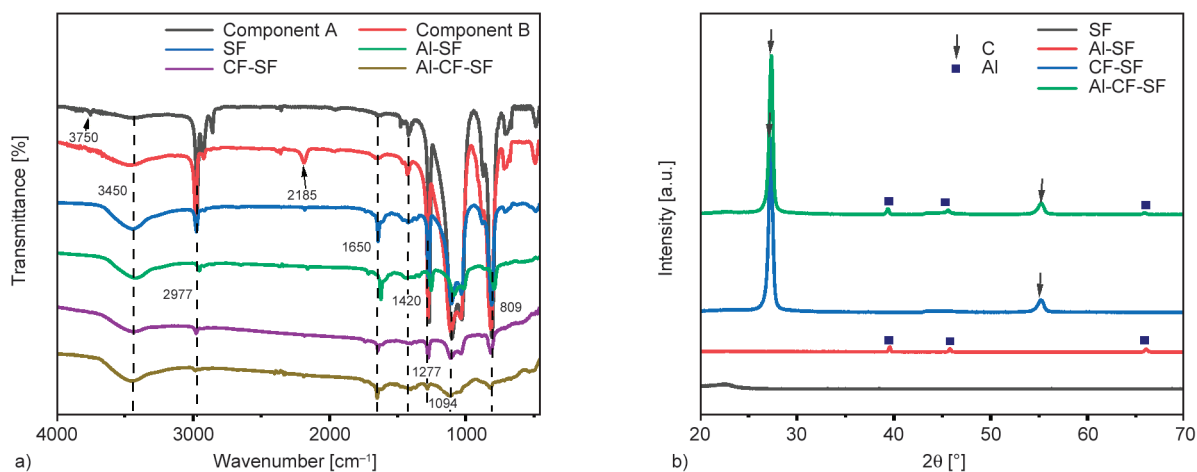


**Figure 2.** a) Fourier transform infrared spectrum of matrix and SF. b) The XRD patterns of SF, Al-SF, CF-SF and Al-CF-SF.

on the glass plate and a certain pressure is applied, which can control the foam thickness. The  $K$  of SF composites can be improved by forming thermal conductive paths inside the composites so that the excess heat can be dissipated.

Figure 2a shows the IR spectra of silicone oil A/B and SF. The peak at  $3450\text{ cm}^{-1}$  is the absorption of the O–H group, which comes from  $\text{H}_2\text{O}$  in KBr. The peaks at  $2977$  and  $1277\text{ cm}^{-1}$  are the absorption of Si–CH<sub>3</sub> stretching and bending vibrations, respectively. The peak at  $1650$  and  $1420\text{ cm}^{-1}$  corresponds to the expansion vibration of CH<sub>2</sub>=CH<sub>2</sub>. The peaks at  $1094\text{ cm}^{-1}$  are the Si–O–Si group of the coupling agent. The peak at  $809\text{ cm}^{-1}$  is the stretching vibrations of the –CH=CH<sub>2</sub> and Si–CH<sub>3</sub> groups [25]. The peak at  $3750\text{ cm}^{-1}$  in component A is the absorption of Si–OH deformation vibrations. The peak at  $2185\text{ cm}^{-1}$  in component B is the absorption of the Si–H group. As can be seen from the figure, the peaks at  $3750$  and  $2185\text{ cm}^{-1}$  disappear after the synthesis of SF, indicating that components A and B were successfully crosslinked. In addition, after adding the filler Al spheres and CF, the infrared spectrum of SF did not produce new peaks, indicating that there is only physical mixing between the filler and the SF without chemical reaction.

The crystal structure analysis of the composites was performed and the XRD spectra is shown in Figure 2b. The peaks observed at  $26.3^\circ$  and  $54.1^\circ$  are the diffraction peaks corresponding to carbon with the corresponding crystal planes (002) and (004). The peaks observed at  $38.4^\circ$ ,  $44.7^\circ$ , and  $65.1^\circ$  are the diffraction peaks corresponding to Al spheres with corresponding crystal planes (111), (200), and (220). With the

increase of CF content, the higher the intensity of the diffraction peak of carbon peak, the amount of Al spheres in the Al-CF-SF is very little, so the intensity of the diffraction peak is weak.

Without any fillers, pristine SF dispersed a soft and transparent appearance (Figure 3). A large number of closed cells with an average diameter of  $500\text{--}1500\text{ }\mu\text{m}$  were formed in SEM images, and the wall thickness is around  $150\text{ }\mu\text{m}$  between the vesicles.

Al spheres with the size of  $5$ ,  $10$ , and  $30\text{ }\mu\text{m}$  were used as fillers to investigate the effect of particle size on the cellular size, and thermal and mechanical properties. After being filled with Al particles, the hybrid Al-SF appears gray (Figure 4). From the SEM images of  $5\text{ }\mu\text{m}$  Al particles filled SF (Al-SF) in Figure 4, it can be seen that the Al spheres are uniformly dispersed in the matrix. When the filling amount of Al sphere is  $20\text{ wt}\%$ , the size of the bubble pore is about  $650\text{ }\mu\text{m}$ ; as the filling amount of Al spheres increases, the bubble pores are destroyed, and the size decreases. With the filling amount of  $40\text{ wt}\%$ , the pore size is about  $350\text{ }\mu\text{m}$ , and with the filling amount of  $60\text{ wt}\%$ , the pore size is about  $230\text{ }\mu\text{m}$ . It can be seen that the increase in the number of Al spheres makes the bubble holes get destroyed, and the bad conductor of heat is reduced, which is conducive to the formation of thermal conductivity paths.

When filled with  $10\text{ }\mu\text{m}$  Al spheres, the foam size of Al-SF was  $400\text{ }\mu\text{m}$  at  $20\text{ wt}\%$  filling, which was  $200\text{ }\mu\text{m}$  smaller than  $5\text{ }\mu\text{m}$  filled Al-SF, and the cell sizes were reduced by  $70$  and  $20\text{ }\mu\text{m}$  at  $40$  and  $60\text{ wt}\%$  filling, respectively (Figure 5).

The SEM images of  $30\text{ }\mu\text{m}$  Al particles filled Al-SF composite are shown in Figure 6. When the filling

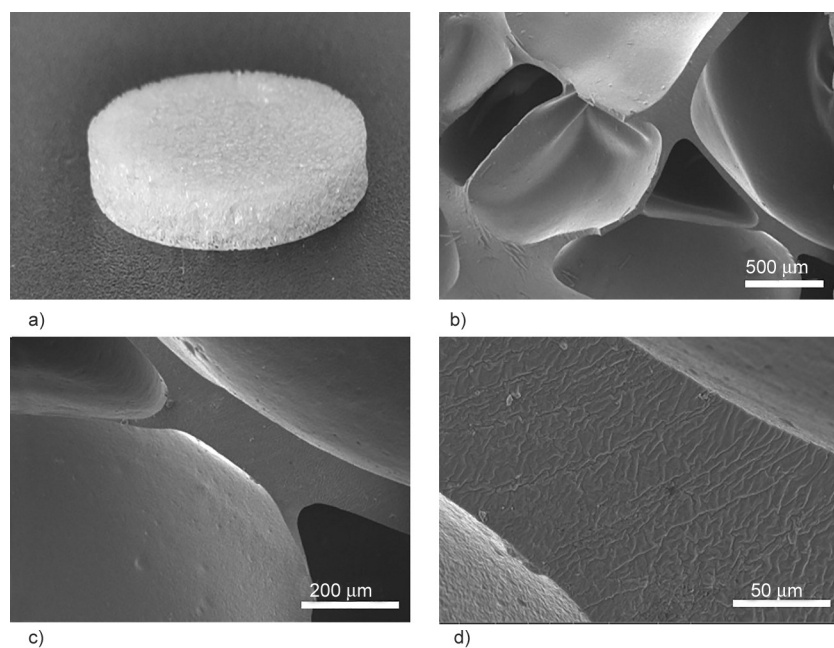


**Figure 3.** a) The appearance ( $d = 30$  mm) and SEM images at b) 150 $\times$ , c) 500 $\times$ , d) 2000 $\times$  of pristine SF.

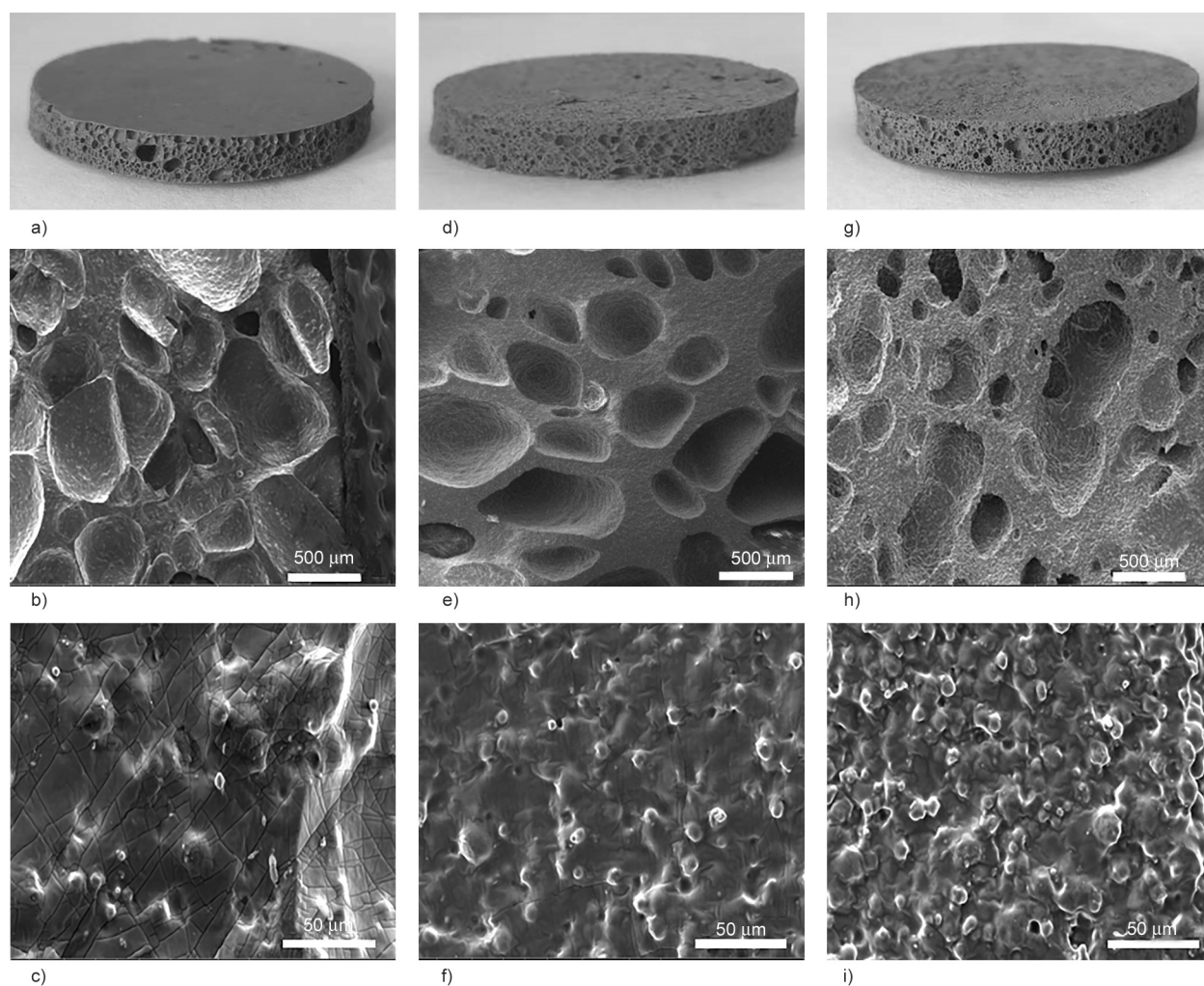


**Figure 4.** Morphology of 5  $\mu\text{m}$  Al particles filled sample (Al-SF), Al with 20 wt% filling: a) appearance ( $d = 30$  mm), SEM at b) 150 $\times$  and c) 2000 $\times$ . Al with 40 wt% filling: d) appearance ( $d = 30$  mm), SEM at e) 150 $\times$  and f) 2000 $\times$ . Al with 60 wt% filling: g) appearance ( $d = 30$  mm), SEM at h) 150 $\times$  and i) 2000 $\times$ .

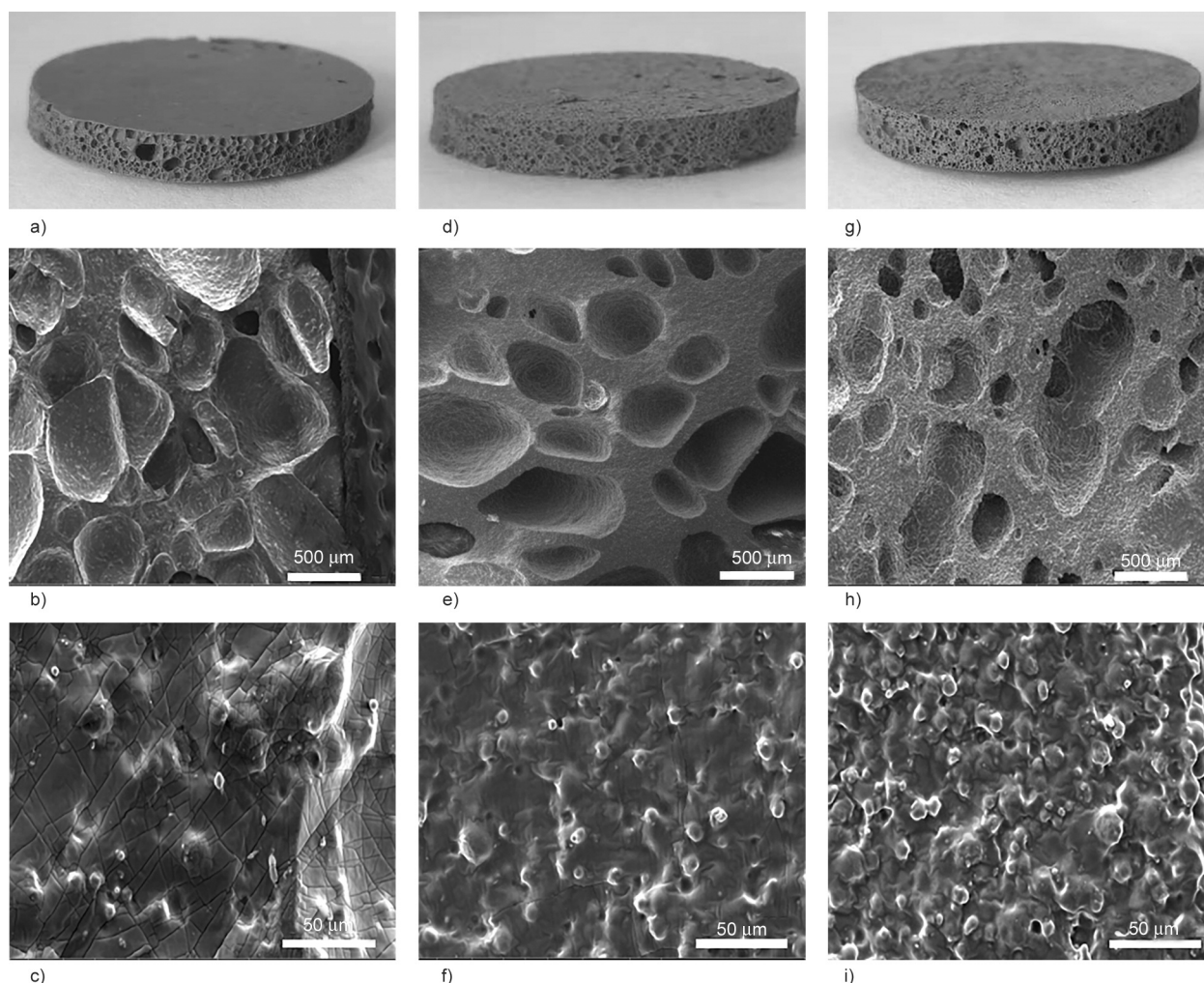


**Figure 5.** Morphology of 10  $\mu\text{m}$  filled sample Al with 20 wt% filling: a) appearance ( $d = 30$  mm), SEM at b) 150 $\times$  and c) 2000 $\times$ . Al with 40 wt%: filling d) appearance ( $d = 30$  mm), SEM at e) 150 $\times$  and f) 2000 $\times$ . Al with 60 wt%: filling g) appearance ( $d = 30$  mm), SEM at h) 150 $\times$  and i) 2000 $\times$ .

amount was 20 wt%, the size of vesicles was 350  $\mu\text{m}$  and open pores with a size of 100  $\mu\text{m}$  started to appear. Under the same filling amount, 30  $\mu\text{m}$  Al spheres can occupy more voids between the bubble pores, which can preferentially form a thermally conductive network with low interfacial thermal resistance, and can effectively improve the thermal conductivity of the composite [26].

CF with higher  $K$  along its fiber direction is further used as fillers to prepare the hybrid SF. Figure 7 is the SEM photograph of CF-SF, from which it can be seen that CF is randomly distributed in the matrix at different angles, and some CF are connected with each other. CF-SF is almost always open-pore; with the increase of the filling amount, the size of the opening gets bigger and bigger; when the filling amount is 60 wt%, the filling amount inside the material tends to be saturated, and there is almost no

extra void, so it is difficult to continue to increase the thermal conductivity filler.

In order to construct a more effective heat transfer network, we adopt a combination of point and line methods to hybridize Al spheres and CF to obtain more excellent thermal conductivity. Figure 8 shows the microstructure of the Al-CF-SF at 60 wt% filling; SEM images show the uniform dispersion of CF and Al spheres in the silicone rubber matrix with good compatibility, which can effectively improve thermal conductivity. As can be seen from the energy dispersive spectroscopy (EDS) image, CF occupies a large number of voids; Al spheres can fill small voids to form a more compact heat transport network. The morphology of CF is a one-dimensional rod, represented as a long rectangle in Figure 8e, so we can determine the position of CF by comparing the morphology of the C element. The PDMS is mainly



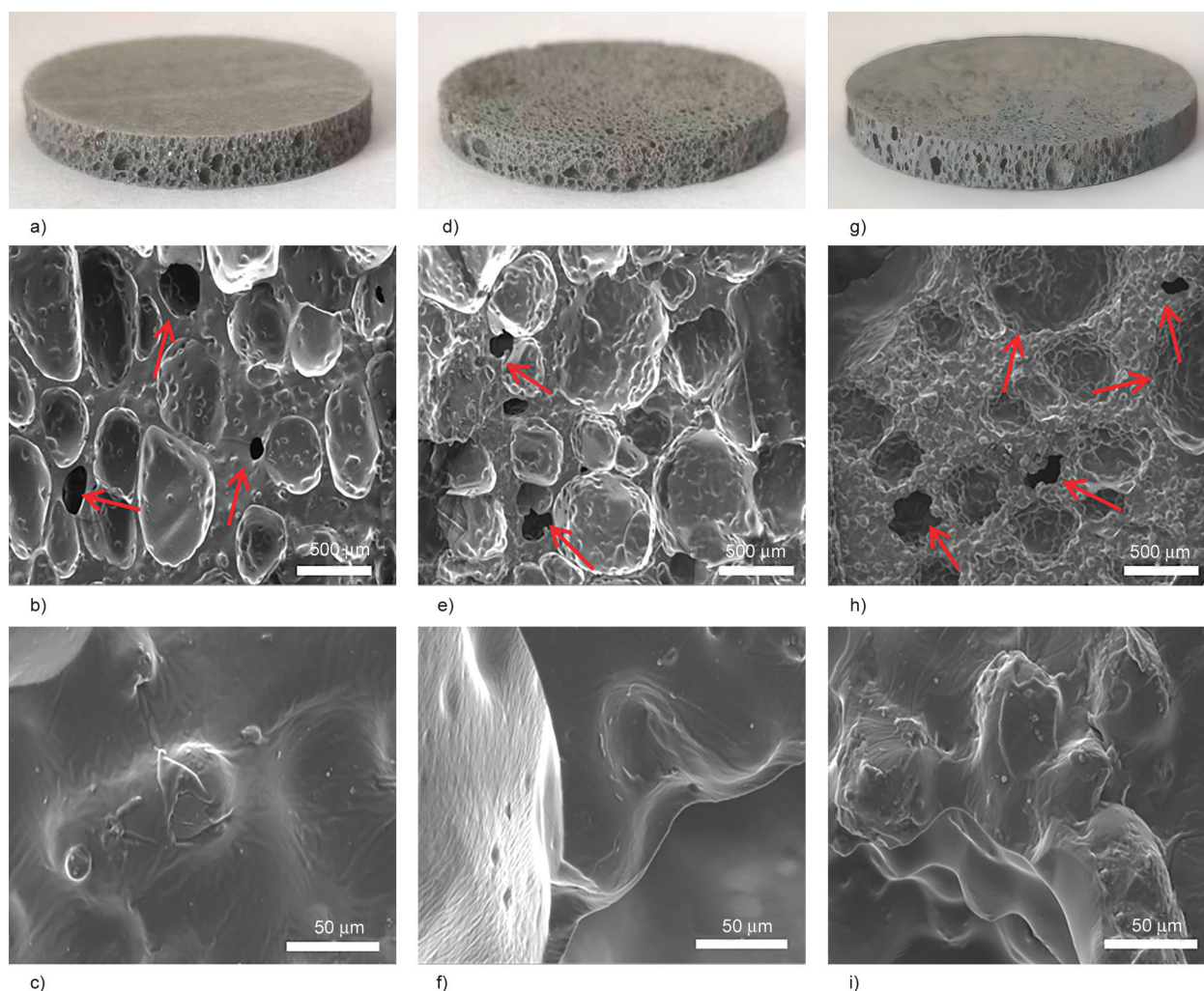


**Figure 6.** Morphology of 30  $\mu\text{m}$  filled sample, Al with 20 wt% filling: a) appearance ( $d = 30\text{ mm}$ ), SEM at b) 150 $\times$  and c) 2000 $\times$ . Al with 40 wt% filling: d) appearance ( $d = 30\text{ mm}$ ), SEM at e) 150 $\times$  and f) 2000 $\times$ . Al with 60 wt% filling: g) appearance ( $d = 30\text{ mm}$ ), SEM at h) 150 $\times$  and i) 2000 $\times$ .

composed of Si, O and C for rubber. The Si element has a large relative atomic mass and a strong signal, which makes it easy to determine the distribution of the PDMS, so the position of C in the matrix can also be determined from the position of Si. There is almost no air inside the composite material, the volume of the formed vesicles is extremely small, almost open pores, forming a filler synergistic heat transfer network mechanism which has a great improvement on the thermal conductivity.

### 3.2. Breakdown voltage of composites

The variation curves of the breakdown strength of Al-SF, CF-SF and Al-CF-SF with different filler levels are shown in Figure 9. It can be seen that the breakdown voltage strength of SF decreases with the increase of filling amount, and the dielectric strength decreases from 2.23 to 0.25  $\text{kV}\cdot\text{mm}^{-1}$  when

adding CF of 60 wt%. The 5  $\mu\text{m}$  Al, 10  $\mu\text{m}$  Al, and 30  $\mu\text{m}$  Al filled silicon foams also decrease by 2, 3.6, and 2.8  $\text{kV}\cdot\text{mm}^{-1}$ , respectively. This is due to the more filler content, the poorer the dispersion in the matrix agglomeration phenomenon is more obvious, the defects of the silicon foam increase, the charge aggregation occurs the more prone to breakdown. In addition to this, the addition of filler introduces more starting electrons, which is easier to move, and as the electrons collide with each other more electrons are produced, and the breakdown voltage strength is therefore reduced.

### 3.3. Mechanical properties of composites

#### 3.3.1. Compressive properties of composites

Silicone rubber foams are highly elastic materials with compression capability, so the study of compression properties is an important indicator of the

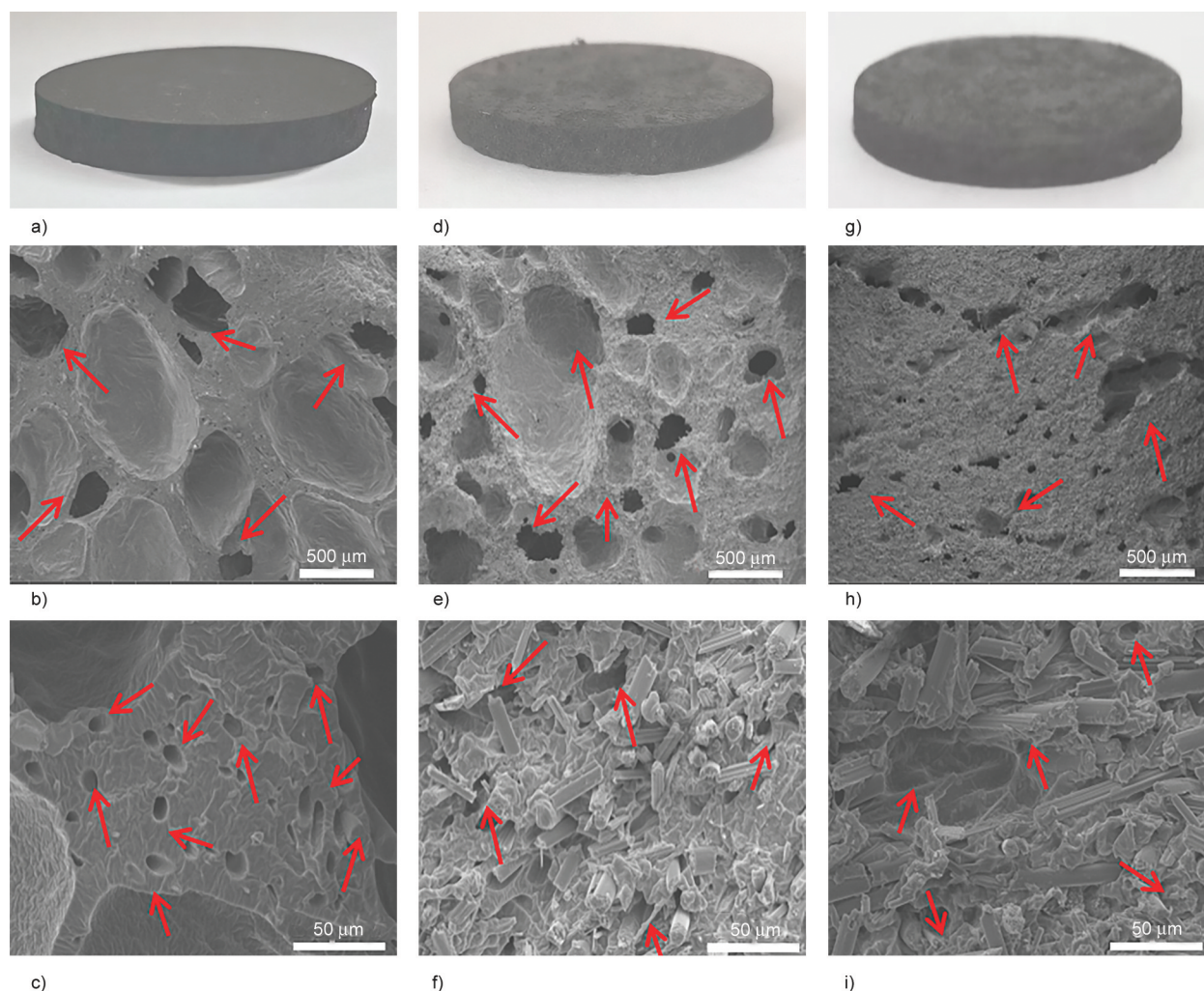


**Figure 7.** Morphology of CF-SF, CF with 20 wt% filling: a) appearance ( $d = 30$  mm), SEM at b) 150 $\times$  and c) 2000 $\times$ . CF with 40 wt% filling: d) appearance ( $d = 30$  mm), SEM at e) 150 $\times$  and f) 2000 $\times$ . CF with 60 wt% filling: g) appearance ( $d = 30$  mm), SEM at h) 150 $\times$  and i) 2000 $\times$ .

response of foams to strain rates [27]. Figure 10 shows the stress-strain graphs and compression modulus of silicone rubber foam composites with different fillers. It can be seen that the incorporation of Al spheres and CF significantly increased the stress and modulus of the composites, where the 60 wt% CF-SF had the highest compressive stress of 1.34 MPa and compressive modulus of 3.36 MPa at a compressive strain of 40%, which were higher than those of the pure SF by 1.3 and 3.26 MPa, respectively. At low filling levels the foam is soft, and the particles are individually distributed in the composite matrix, making it difficult to form a continuous network. At this time, most of the pores in the foam material are closed and contain a large amount of gas inside. When the pore wall and the internal gas are subjected to part of the pressure, the pore collapses, then the gas quickly overflows outward, and

a very small pressure value can make the foam material produce a large deformation. However, when the foam material with 60 wt% filler is deformed by external force, the interaction between particles will hinder molecular movement, and the hardness of the composite material will become large and difficult to deform. It is noted that Al-CF-SF is hard to compress with a high compress ratio. Under the same testing condition, the compress stress is 0.5 MPa (a strain of 10%) and 2.0 MPa (a strain of 20%), respectively. A larger compression ratio would be beyond the test range of the instrument (2 MPa).

### 3.3.2. Tensile properties of composites

Tensile properties are an important indicator that characterizes the resistance of the foam to elastic deformation under the action of external forces. Figure 11 shows the tensile stress-strain curves of CF and Al

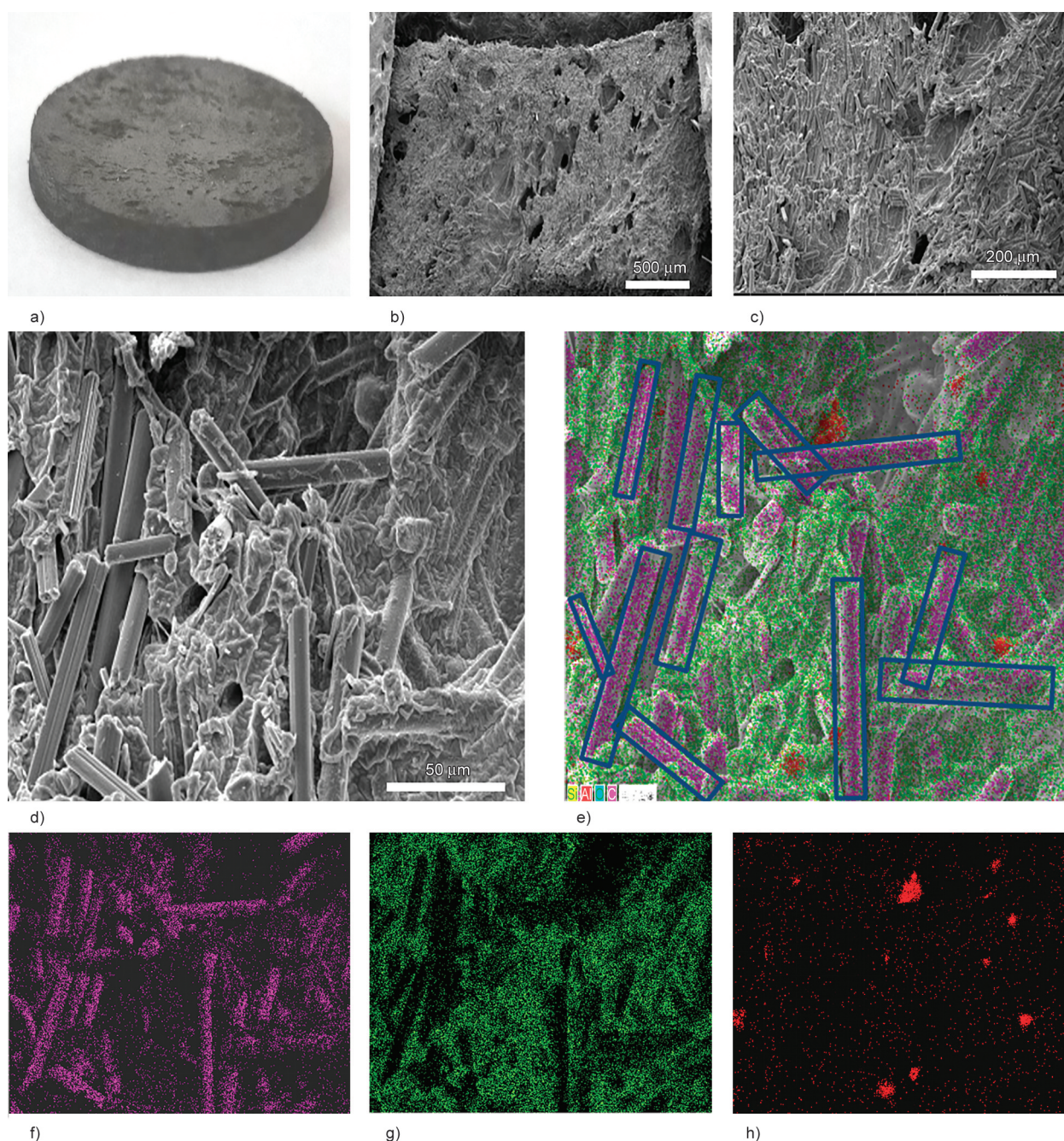


**Figure 8.** Morphology of Al-CF-SF: a) appearance ( $d = 30$  mm). SEM at b) 150 $\times$ , c) 500 $\times$ , d) 2000 $\times$ . e) EDS at 2000 $\times$ , elements mapping of f) C, g) Si, and h) Al.

spheres filled alone and mix filling of Al-CF-SF. It can be seen that pure SF requires only 0.1 MPa of stress to achieve 105% strain and has good elasticity. With the increase of the filling amount the stress gradually becomes larger, and the strain becomes smaller, indicating that the addition of filler makes the SF harder and more difficult to deform. 60 wt% CF-SF has the highest stress of 0.72 MPa, but only 6% deformation.

Tensile strength is the maximum stress that a material can withstand during the stretching process and

it can be seen that the tensile strength and tensile modulus of the composite increases with the increase of the filler amount. The increase in the amount of filler facilitates the formation of a tight crosslinked network of SF, which increases the hardness and requires more force in tension and increases the tensile strength. For the tensile strength of Al-SF with different particle sizes, 5  $\mu\text{m}$  Al > 10  $\mu\text{m}$  Al > 30  $\mu\text{m}$  Al. It is possible that this is due to the greater number of small particle size fillers at a given weight of filling and the greater contact area with the matrix. When

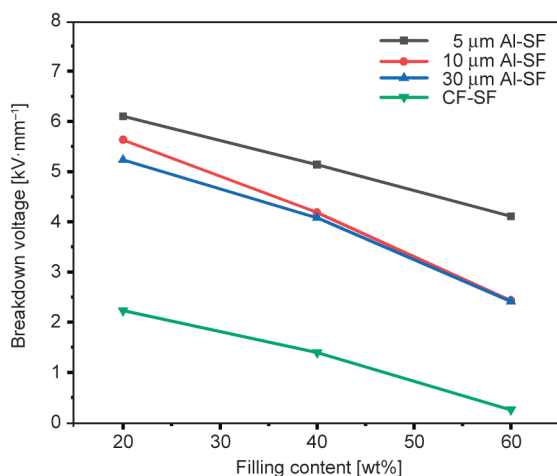


**Figure 9.** Variation of breakdown strength of prepared silicone rubber foam composites with different filling content.

the filling amount is 60 wt%, the tensile strength and tensile modulus of 30 μm Al-SF is the minimum of 0.24 and 0.86 MPa, respectively, and the maximum of CF-SF is 0.72 and 10.86 MPa, respectively.

Fracture strain is the maximum strain to which the material is subjected before fracture. The trend of the fracture strain of SF is the opposite of the tensile strength, which gradually decreases with the increase of the filling amount. It may be due to the formation of stress concentration points by restricting the movement of molecular chains when filling Al spheres and CF in the matrix. These stress concentration points increase when the filler content increases, making the composites susceptible to fracture when subjected to external forces, which decreases the fracture strain. The material does not yield at fracture and is brittle with poor fracture toughness.

### 3.4. Thermal properties of composite materials

#### 3.4.1. Effect of filler on thermal conductivity

To explore the relationship between  $K$  and filler distribution, the  $K$  of the composites was measured by the heat flow method. The  $K$  of the composite was measured at 70 °C using different pressures (50 N/100 N/150 N/200 N/250 N/300 N). The thermal conductivity of the filler itself and its filling amount and distribution in the silicon matrix affect the overall thermal conductivity of the composite. Different particle sizes of fillers have different distributions in silicone rubber, and at a certain amount

of filling, it can be seen from Figure 12a that the  $K$  sizes corresponding to different particle sizes of fillers are: 30 μm Al > 10 μm Al > 5 μm Al. Since the Al spheres are small, the particles cannot contact each other and do not form a complete thermal conductivity network chain within the matrix; the thermal conductivity of the composites formed by different particle size Al spheres is not significantly enhanced. CF has a high thermal conductivity and aspect ratio compared to Al spheres, making it easier to form a thermal conductivity network. Therefore, the highest thermal conductivity of 1.2 W·m<sup>-1</sup>·K<sup>-1</sup> was achieved for CF with 60 wt% filling at 300 N, which is more than five times higher than the thermal conductivity of Al-SF composite.

The change of filling amount also affects the thermal conductivity of the composite. Taking 5 μm Al spheres as an example, when the filling amount is small, the particles are uniformly dispersed in the silica matrix without contacting with each other, which may lead to a larger thermal resistance and low thermal conductivity. But with the increase of thermally conductive filler, Al spheres began to have contact, the thermal conductivity network chain gradually improved, the thermal conductivity increased rapidly. But when the Al spheres increased to a certain extent, the formation of the overall thermal conductivity network structure, reached the maximum filling volume, continue to increase the amount of filler, the filler will disperse the matrix outside can not be completely surrounded. In this experiment, the composite reached the critical filling amount when the filling amount was 60 wt%, and it was more difficult to mix. In addition, carbon fibers are one-dimensional columnar structures, the effective connection between carbon fibers is limited, and the ability to participate in phonon transport directly is poor, resulting in high interface thermal resistance.

In order to optimize the thermal conductivity of the composite material, we fix the maximum filling amount of the composite material to 60 wt%, based on which the CF and Al spheres are compounded because the CF can improve the thermal conductivity of the composite material more effectively, we use a small percentage adjustment to replace the CF with Al spheres. Al spheres can fill the gaps between CF and increase site contact. The thermal conductivity of CF compounded with different particle sizes of Al spheres is shown in Figure 12b, from which it

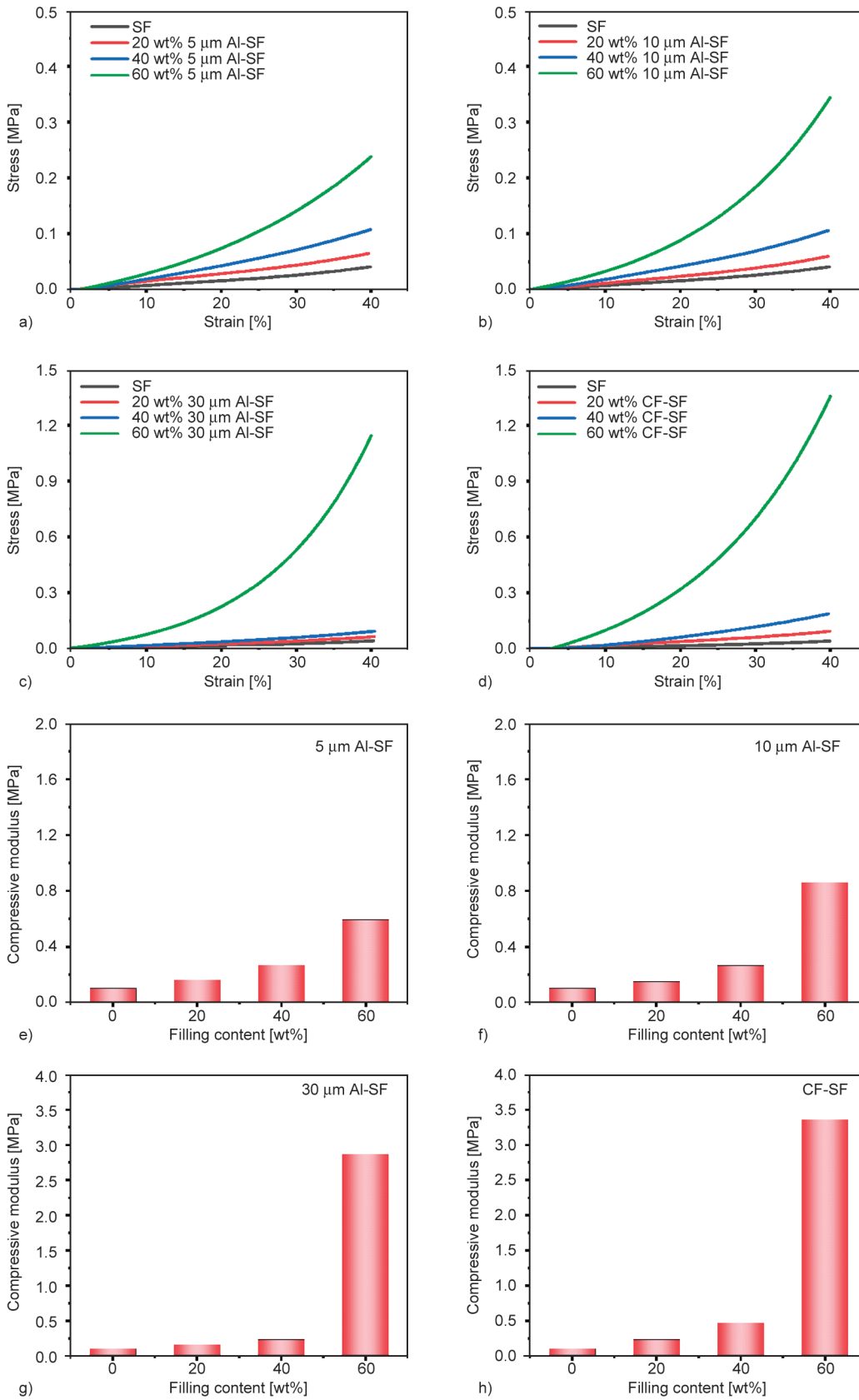


**Figure 10.** Compressive stress-strain curves for composites filled with different fillers a) 5 μm Al, b) 10 μm Al, c) 30 μm Al, d) CF. Compressive modulus curves for composites filled with different fillers e) 5 μm Al, f) 10 μm Al, g) 30 μm Al, h) CF.

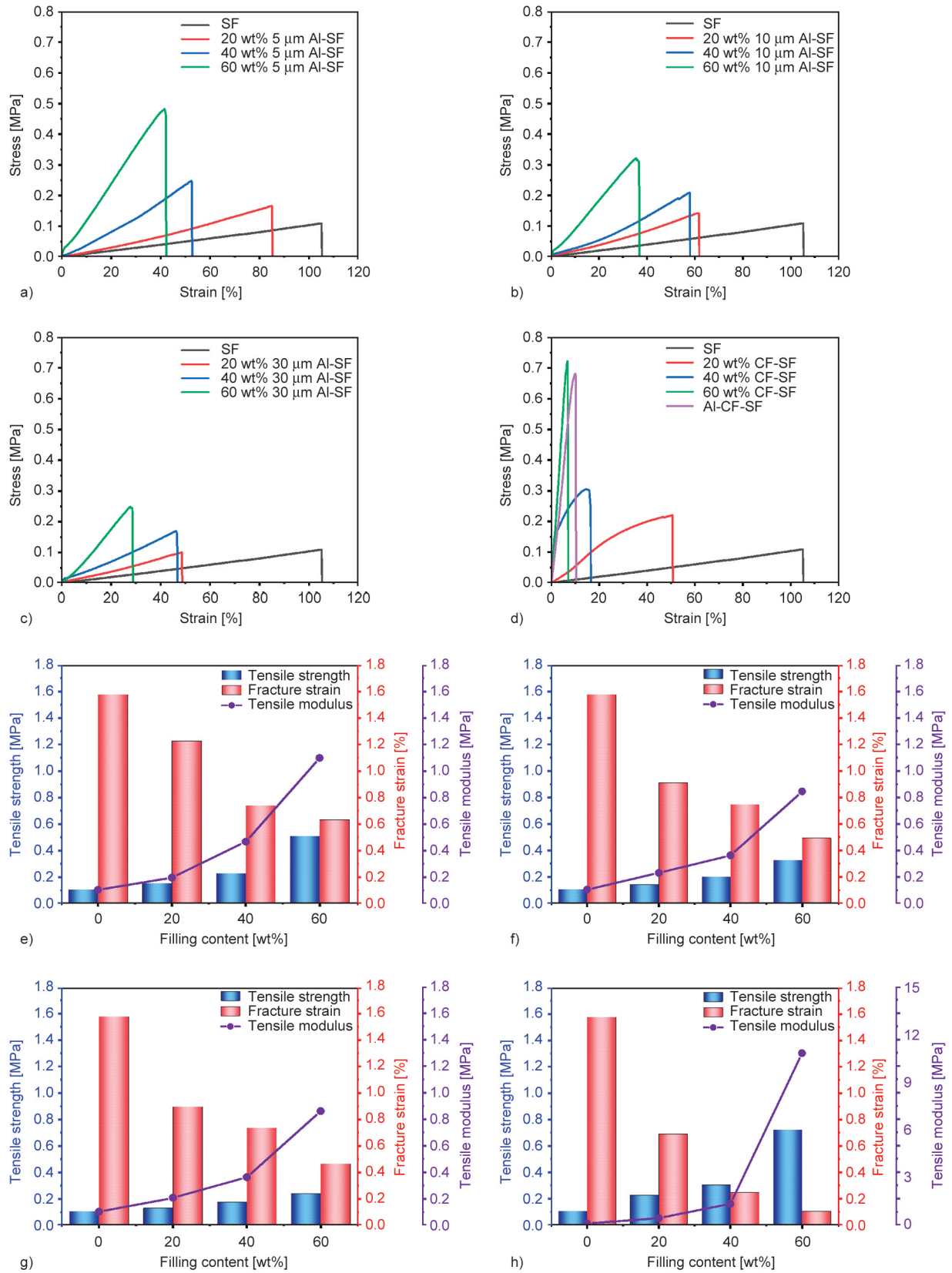


**Figure 11.** Tensile stress-strain curves for composites filled with different fillers a) 5 μm Al, b) 10 μm Al, c) 30 μm Al, d) CF. Variation of tensile strength, modulus and fractures strain with filler content e) 5 μm Al, f) 10 μm Al, g) 30 μm Al, h) CF.

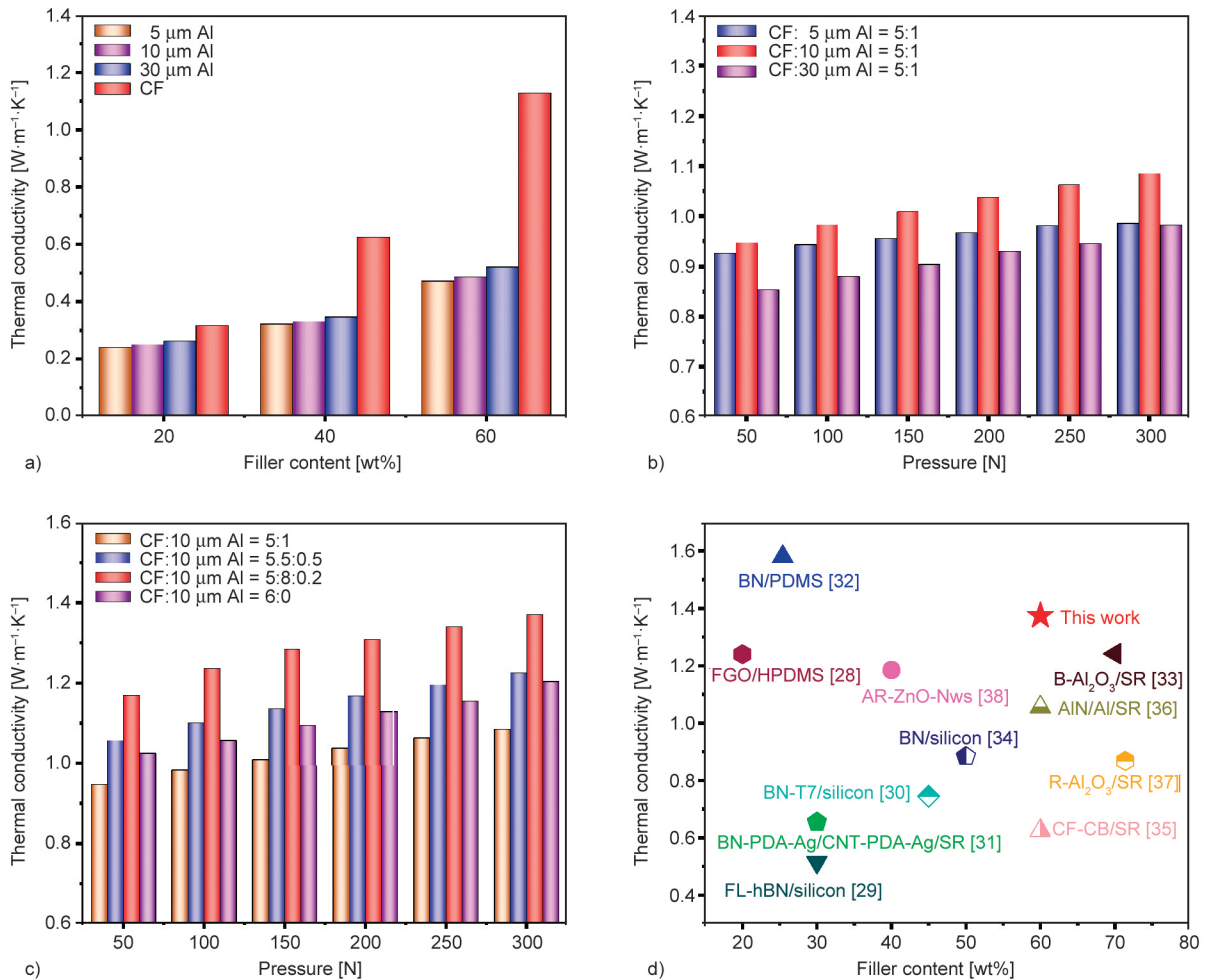


**Figure 12.** Thermal conductivity of a) SF composites formed by different fillers, b) compounding of CF and Al of different particle sizes, c) compounding of CF and 10 μm Al at different filler ratios, d) comparison of this work with previous studies.

can be seen that the thermal conductivity of carbon fiber compounded with 10 μm Al spheres is higher than that with the other two particle sizes, and the thermal conductivity is  $1.08 \text{ W}\cdot\text{m}^{-1}\cdot\text{K}^{-1}$  at 300 N pressure. Therefore, we investigated the effect of the compounding ratio on the thermal conductivity of the composites by changing the compounding ratio of carbon fiber to 10 μm Al spheres. As shown in Figure 12c, the thermal conductivity of the composites reached a maximum value of  $1.37 \text{ W}\cdot\text{m}^{-1}\cdot\text{K}^{-1}$ , when the filler ratio CF:10 μm Al = 5.8:0.2, which is 9.7 times higher than that of the pure silica matrix. Figure 12d shows the effect of thermally conductive fillers on the thermal properties of silicone composites, and by comparing it with the results of previous studies, it shows that this experiment effectively constructs a dense and efficient thermal conductivity network [28–38].

### 3.4.2. Finite element model of SF composites

In order to explain the thermal conductivity mechanism of the composites in more depth we performed simulations using finite element analysis. We have created three simulations for single filler (Al-SF, CF-SF) and mixed filler (Al-CF-SF) as shown in Figure 13. The simulation results proved that the hybrid filler had a faster heat transfer rate than the single filler. Al powder exists in the matrix in point form and it is difficult to contact between particles, which mainly depends on the heat transfer of the matrix. CF is arranged in the matrix in a linear form, which increases the possibility of contact with each other, but it also hampers the improvement of the thermal conductivity because of the limited space inside the matrix. When CF and Al powder are added to the matrix in a certain ratio, the internal space of the matrix can be fully utilized, and the carbon fiber can

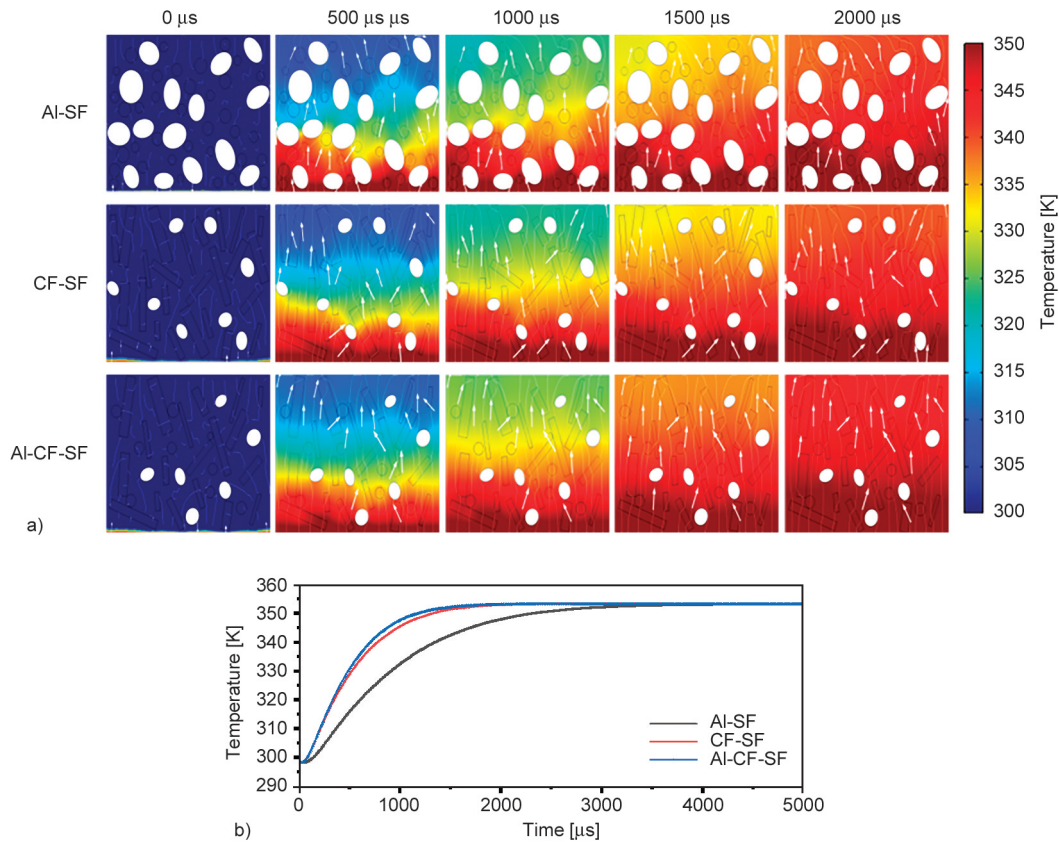


**Figure 13.** The finite element analysis results of Al-SF, CF-SF, and Al-CF-SF a) temperature distribution and heat flux direction modeling, white flow lines, and arrows indicate the heat flux and the direction of heat flux, respectively, b) time-temperature profile.

form a long-distance thermal conductivity pathway, while the Al powder plays the role of a bridge connecting the pathways, forming a ‘point and line synergistic’ thermal conductivity network conductivity mode inside the matrix.

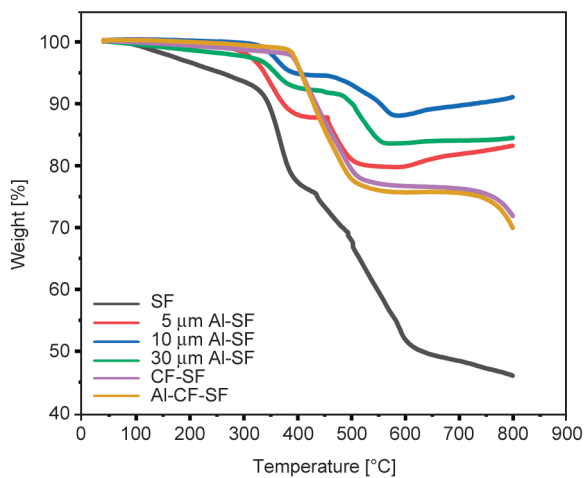


**Figure 14.** The weight loss curves of silicone foam composite.

### 3.4.3. Stability of the composites

The thermal stability is a measure of the ease of thermal decomposition of the sample, the thermal weight loss behavior of the silica foam composite filled with 60 wt% under an O<sub>2</sub> atmosphere is shown in Figure 14. The results showed that the temperature of 5% weight loss of these composites occurred at 246 °C (SF), 338 °C (5 μm Al-SF), 358 °C (10 μm Al-SF), 391 °C (30 μm Al-SF) and 405 °C (CF-SF, Al-CF-SF). At 600 °C, the weight loss of SF, 5 μm Al-SF, 10 μm Al-SF, 30 μm Al-SF, CF-SF, and Al-CF-SF were 49, 21, 12, 17, 24 and 25%, respectively. It can be seen that the weight loss of the composites after the addition of fillers is significantly lower than that of the pure SF, and the thermal stability is better.

In the actual work condition, the performance of foam has kept stability undergoing multiple compresses. To calculate the mechanical dissipation loss of stress-strain, we did the compression-release cycle test and measured the thermal conductivity every



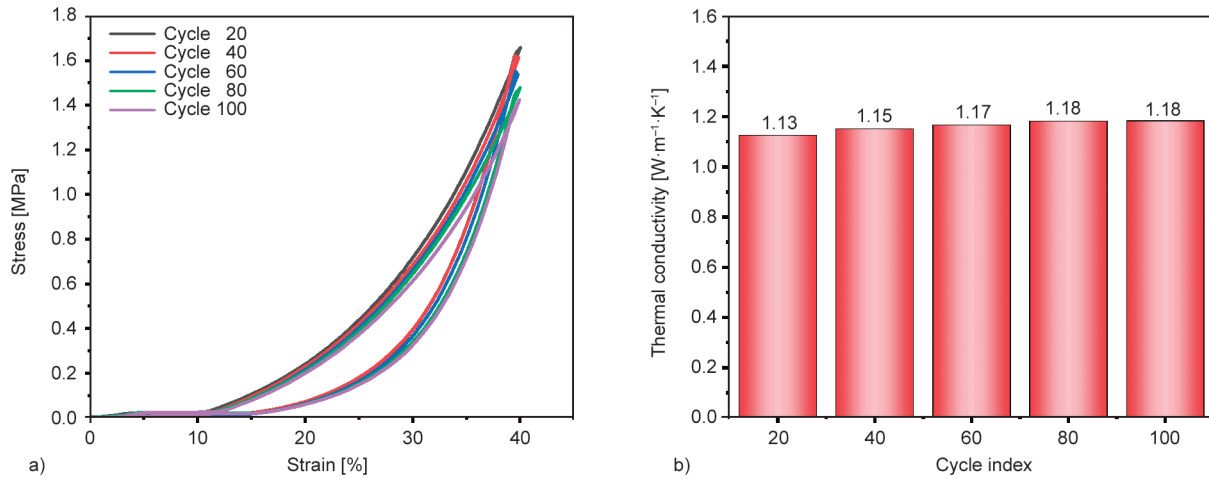


**Figure 15.** a) Stress-strain curve of CF-SF during compression-release cycle process. b) The thermal conductivity of CF-SF was measured every 20 cycles.

twenty cycles from CF-SF (60 wt%) [39]. The cycle test curve of CF-SF with 60 wt% filler compression of 40% is shown in Figure 15a, and it can be found that the hysteresis returns a line of the foam material in the shape of a crescent and partially overlapped, which indicates that the CF-SF has undergone a relatively small energy loss in the cycling process. The dissipated energy was obtained from the area of the closed graph of the stress-strain curve, and it was found that the energy dissipation was 4.77 J at 100 cycles, which is a small amount of 2 J compared with the loss at the first cycle. At the same time, it can be

seen that the thermal conductivity corresponding to Figure 15b is slightly increased. The thermal conductivity of the sample before the start of the cycle is  $1.05 \text{ W}\cdot\text{m}^{-1}\cdot\text{K}^{-1}$ . After 100 cycles, the thermal conductivity is  $1.18 \text{ W}\cdot\text{m}^{-1}\cdot\text{K}^{-1}$ , which is an increase of  $0.13 \text{ W}\cdot\text{m}^{-1}\cdot\text{K}^{-1}$ . Therefore the mechanical loss of SF can improve its thermal conductivity.

### 3.4.4. Thermal management application of SF composites

To study the thermal management ability of silicone rubber foam materials, we record the surface

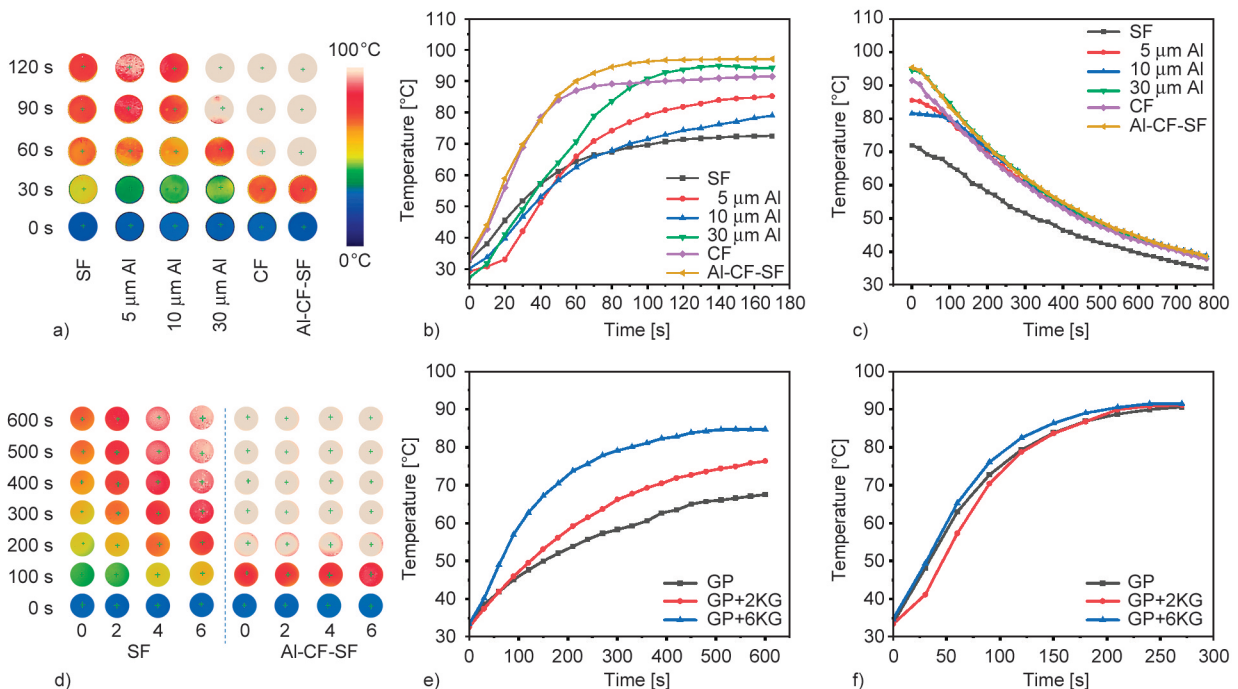


**Figure 16.** Surface temperature change of composites a) infrared thermal images, b) heating process and c) cooling process. After applying pressure d) infrared thermal images, heating up process of e) pure SF and f) Al-CF-SF.

temperature change of the sample with the help of the infrared camera. We placed the SF in the middle of a ceramic heating plate with a heating temperature range of 30–100 °C. The temperature change in the center of the sample was extracted every 30 s using an infrared thermographic camera, and the image of the sample surface temperature is shown in Figure 16a. Blue represents the lowest surface temperature of the sample; from the bottom to the top, the sample temperature gets higher and higher, and white represents the surface temperature of the sample that reaches above 90 °C. During the heating process, the color of the sample changes from dark to light, and the heat transfer rate becomes faster as time goes on. The images in Figures 16b and 16c represent the sample warming and cooling processes. The pure SF reached the heat transfer limit of 72 °C after heating for 170 s, while Al-CF-SF reached the sample surface temperature of 96 °C at 100 s, showing better thermal conductivity and heat dissipation during the heating and cooling processes.

In addition, to study the effect of pressure on the thermal conductivity of the foam, we placed a glass plate (GP) on the pure SF and Al-CF-SF and placed 0, 2, and 6 weights (one weight is 1 kg) on the glass plate to observe their thermal conductivity, respectively. The infrared thermography and heat transfer rates of the samples are shown in Figure 16d. We find from Figure 16e that the pressure has a greater effect on the thermal conductivity of pure SF, the heat transfer rate reaches equilibrium after heating 600 s. The highest heat transfer temperature of SF material with only glass plates placed is 68.3 °C, and the highest heat transfer temperature increases with the increase of the number of weights, and the highest heat transfer temperature of SF material with 6 weights placed can reach 84.5 °C which is 16.2 °C higher than that of pure SF. This is because the bubble pores are destroyed after applying pressure, which improves the heat transfer path inside the sample, and the heat transfer efficiency is greatly improved. However, as shown in Figure 16f, the effect of pressure on the Al-CF-SF is not obvious, and the temperature change tends to stabilize to 90 °C after 280 s, which is due to the that there are no voids inside the Al-CF-SF. The fillers are interconnected to form a complete crosslinked network.

#### 4. Conclusions

In summary, we successfully synthesized silicone foam and hybrids by a simple process. A series of SF composites with highly efficient thermal conductive networks were designed and prepared by optimizing fillers' particle size and dimension. Observing the size of the vesicles inside the matrix by SEM demonstrated that incorporating fillers could exclude the excess air inside the matrix and thus improve thermal conductivity. The hybridized fillers made of Al particles and CF composite can occupy more voids to improve the thermal conductivity of the composites further. Infrared thermography and finite element modeling also further proved the accuracy of the experiments. Tensile and compressive characterization also demonstrated that the mechanical properties of the composites were improved compared to pure SF and that the loss of mechanical properties also contributed to the improvement of the material's thermal conductivity. Using a small amount of Al powder instead of CF in this study can reduce the cost and has great potential in the preparation of reinforced thermally conductive composites.

#### Acknowledgements

This work was supported by the Chinese National Natural Science Fund (12172118), the Research Program of Local Science and Technology Development under the Guidance of Central (216Z4402G) and the Foundation of State Key Laboratory of Coal Conversion of Shanxi Institute of Coal Chemistry, CAS (J22-23-610). Dr. Qibo Deng acknowledges support from the 'Yuanguang' Scholar Program of the Hebei University of Technology.

#### References




- [1] Rostami-Tapeh-Esmaeil E., Vahidifar A., Esmizadeh E., Rodrigue D.: Chemistry, processing, properties, and applications of rubber foams. *Polymers*, **13**, 1565 (2021). <https://doi.org/10.3390/polym13101565>
- [2] Duan Y., Chen X., Yin B., Zhao X., Zhao Z., Hou B., Li Y.: Understanding the effect of defects on compressive behaviors of closed-cell foams: Experiment and statistical model. *Composites Part B: Engineering*, **244**, 110179 (2022). <https://doi.org/10.1016/j.compositesb.2022.110179>
- [3] Peixinho N., Carvalho O., Areias C., Pinto P., Silva F.: Compressive properties and energy absorption of metal-polymer hybrid cellular structures. *Materials Science and Engineering: A*, **794**, 139921 (2020). <https://doi.org/10.1016/j.msea.2020.139921>

- [4] Yang J., Li P.: Characterization of short glass fiber reinforced polypropylene foam composites with the effect of compatibilizers: A comparison. *Journal of Reinforced Plastics and Composites*, **34**, 534–546 (2015).  
<https://doi.org/10.1177/0731684415574142>
- [5] Yan H., Wang K., Zhao Y.: Fabrication of silicone rubber foam with tailored porous structures by supercritical CO<sub>2</sub>. *Macromolecular Materials and Engineering*, **302**, 1600377 (2017).  
<https://doi.org/10.1002/mame.201600377>
- [6] Abbad A., Jaboviste K., Ouisse M., Dauchez N.: Acoustic performances of silicone foams for sound absorption. *Journal of Cellular Plastics*, **54**, 651–670 (2017).  
<https://doi.org/10.1177/0021955x17732305>
- [7] Grande J. B., Fawcett A. S., McLaughlin A. J., Gonzaga F., Bender T. P., Brook M. A.: Anhydrous formation of foamed silicone elastomers using the Piers-Rubinsztajn reaction. *Polymer*, **53**, 3135–3142 (2012).  
<https://doi.org/10.1016/j.polymer.2012.05.033>
- [8] Yu Z., Ma L., Zhu B., Phule A. D., Wen S., Zhao Y., Zhang Z.: Development of EVA/POE/SEBS microcellular foam: Network structure, mechanics performance and midsole application. *Express Polymer Letters*, **16**, 1322–1330 (2022).  
<https://doi.org/10.3144/expresspolymlett.2022.95>
- [9] Zhang C., Qu L., Wang Y., Xu T., Zhang C.: Thermal insulation and stability of polysiloxane foams containing hydroxyl-terminated polydimethylsiloxanes. *RSC Advances*, **8**, 9901–9909 (2018).  
<https://doi.org/10.1039/c8ra00222c>
- [10] Wang X. J., Niu X. H., Wang X. X., Qiu X. W., Istikomah N., Wang L. B.: Thermal conductivity of porous polymer materials considering pore special-shape and anisotropy. *Express Polymer Letters*, **15**, 319–328 (2021).  
<https://doi.org/10.3144/expresspolymlett.2021.28>
- [11] Lin X., Zhang X., Ji J., Liu L., Yang M., Zou L.: Experimental investigation of form-stable phase change material with enhanced thermal conductivity and thermal-induced flexibility for thermal management. *Applied Thermal Engineering*, **201**, 117762 (2022).  
<https://doi.org/10.1016/j.applthermaleng.2021.117762>
- [12] Li P., Lan B., Zhang Q., Yang Q., Gong P., Park C. B., Li G.: Microcellular foams simultaneous reinforcing and toughening strategy of combining nano-fibrillation network and supercritical solid-state foaming. *Polymer*, **252**, 124928 (2022).  
<https://doi.org/10.1016/j.polymer.2022.124928>
- [13] Li S. J., Li J. C., Ji P. Z., Zhang W. F., Lu Y. L., Zhang L. Q.: Bubble-templated construction of three-dimensional ceramic network for enhanced thermal conductivity of silicone rubber composites. *Chinese Journal of Polymer Science*, **39**, 789–795 (2021).  
<https://doi.org/10.1007/s10118-021-2581-4>
- [14] Zhang Y.-L., Zang C.-G., Jiao Q.-J.: Electrical, thermal, and mechanical properties of silicone foam composites filled with carbon-based nanofillers. *Journal of Applied Polymer Science*, **137**, 49191 (2020).  
<https://doi.org/10.1002/app.49191>
- [15] Shi S., Wang Y., Jiang T., Wu X., Tang B., Gao Y., Zhong N., Sun K., Zhao Y., Li W., Yu J.: Carbon fiber/phenolic composites with high thermal conductivity reinforced by a three-dimensional carbon fiber felt network structure. *ACS Omega*, **7**, 29433–29442 (2022).  
<https://doi.org/10.1021/acsomega.2c03848>
- [16] Li H., Chen W., Xu J., Li J., Gan L., Chu X., Yao Y., He Y., Li B., Kang F., Du H.: Enhanced thermal conductivity by combined fillers in polymer composites. *Thermochimica Acta*, **676**, 198–204 (2019).  
<https://doi.org/10.1016/j.tca.2019.04.008>
- [17] Zhang Y. L., Zang C. G., Jiao Q. J.: Electrical and thermal properties of silicone rubber composites filled with Cu-coated carbon fibres and functional carbon nanotubes. *Plastics Rubber and Composites*, **48**, 327–337 (2019).  
<https://doi.org/10.1080/14658011.2019.1625249>
- [18] Wu Z., Xu C., Ma C., Liu Z., Cheng H.-M., Ren W.: Synergistic effect of aligned graphene nanosheets in graphene foam for high-performance thermally conductive composites. *Advanced Materials*, **31**, 1900199 (2019).  
<https://doi.org/10.1002/adma.201900199>
- [19] Wang X., Liu H., Qiu X., Wang L., Wang L.: Thermal conductivity of filled composite materials considering interactions between fillers. *Applied Thermal Engineering*, **141**, 835–843 (2018).  
<https://doi.org/10.1016/j.applthermaleng.2018.06.022>
- [20] Jiao T., Han B., Zhao L., Zhang Z., Zeng Y., Li D., Zhang K., Deng Q., Zhao Y., Li Z.: Pie-rolling-inspired construction of vertical carbon fiber high thermal conductivity hybrid networks. *Applied Surface Science*, **618**, 156711 (2023).  
<https://doi.org/10.1016/j.apsusc.2023.156711>
- [21] Zhang P., Zeng J. H., Zhai S. P., Xian Y. Q., Yang D. G., Li Q.: Thermal properties of graphene filled polymer composite thermal interface materials. *Macromolecular Materials and Engineering*, **302**, 1700068 (2017).  
<https://doi.org/10.1002/mame.201700068>
- [22] Smorygo O., Mikutski V., Marukovich A., Sadykov V., Bepalko Y., Stefan A., Pelin C.-E.: Preparation and characterization of open-cell epoxy foams modified with carbon fibers and aluminum powder. *Composite Structures*, **202**, 917–923 (2018).  
<https://doi.org/10.1016/j.compstruct.2018.04.063>
- [23] Meng Z., Dai Z., Chen K., Wang S.: Investigation on preparation, thermal, and mechanical properties of carbon fiber decorated with hexagonal boron nitride/silicone rubber composites for battery thermal management. *International Journal of Energy Research*, **45**, 4396–4409 (2021).  
<https://doi.org/10.1002/er.6110>

- [24] Wei J., Liao M., Ma A., Chen Y., Duan Z., Hou X., Li M., Jiang N., Yu J.: Enhanced thermal conductivity of polydimethylsiloxane composites with carbon fiber. *Composites Communications*, **17**, 141–146 (2020).  
<https://doi.org/10.1016/j.coco.2019.12.004>
- [25] Zhang C., Zhang C., Huang R., Gu X.: Effects of hollow microspheres on the thermal insulation of polysiloxane foam. *Journal of Applied Polymer Science*, **134**, 44778 (2017).  
<https://doi.org/10.1002/app.44778>
- [26] Woldesenbet E.: Low velocity impact properties of nanoparticulate syntactic foams. *Materials Science and Engineering: A*, **496**, 217–222 (2008).  
<https://doi.org/10.1016/j.msea.2008.05.024>
- [27] Shi Z., Zhao G., Zhang L., Wang G.: Lightweight, strong, flame-retardant PVDF/PMMA microcellular foams for thermal insulation fabricated by supercritical CO<sub>2</sub> foaming. *Composites Part B: Engineering*, **230**, 109554 (2022).  
<https://doi.org/10.1016/j.compositesb.2021.109554>
- [28] Ge T., Zhang M., Tang K., Tang H.: Diisocyanate-modified graphene oxide/hydroxyl-terminated silicone rubber composites for improved thermal conductivity. *Materials Chemistry and Physics*, **252**, 123250 (2020).  
<https://doi.org/10.1016/j.matchemphys.2020.123250>
- [29] Cheng W-C., Hsieh Y-T., Liu W-R.: Enhanced thermal conductivity of silicone composites filled with few-layered hexagonal boron nitride. *Polymers*, **12**, 2072 (2020).  
<https://doi.org/10.3390/polym12092072>
- [30] Kuo C-F. J., Dewangga G. R. S., Chen J-B.: Fabrication of a thermally conductive silicone composite by incorporating surface-modified boron nitride. *Textile Research Journal*, **89**, 2637–2647 (2018).  
<https://doi.org/10.1177/0040517518798654>
- [31] Wei Q., Yang D.: Formation of thermally conductive network accompanied by reduction of interface resistance for thermal conductivity enhancement of silicone rubber. *ACS Applied Electronic Materials*, **4**, 3503–3511 (2022).  
<https://doi.org/10.1021/acsaelm.2c00475>
- [32] Li J., Li F., Zhao X., Zhang W., Li S., Lu Y., Zhang L.: Jelly-inspired construction of the three-dimensional interconnected BN network for lightweight, thermally conductive, and electrically insulating rubber composites. *ACS Applied Electronic Materials*, **2**, 1661–1669 (2020).  
<https://doi.org/10.1021/acsaelm.0c00227>
- [33] Ouyang Y., Li X., Tian H., Bai L., Yuan F.: A novel branched Al<sub>2</sub>O<sub>3</sub>/silicon rubber composite with improved thermal conductivity and excellent electrical insulation performance. *Nanomaterials*, **11**, 2654 (2021).  
<https://doi.org/10.3390/nano11102654>
- [34] Zhao L., Shi X., Yin Y., Jiang B., Huang Y.: A self-healing silicone/BN composite with efficient healing property and improved thermal conductivities. *Composites Science and Technology*, **186**, 107919 (2020).  
<https://doi.org/10.1016/j.compscitech.2019.107919>
- [35] Wang J., Ni L., Li Q., Wu C.: The synergistic effects of carbon black and carbon fibre on the thermal conductivity of silicone rubber. *Polymers and Polymer Composites*, **23**, 271–275 (2014).  
<https://doi.org/10.1177/096739111502300408>
- [36] Chiu H-T., Liu Y-L., Lin C-W., Shong Z-J., Tsai P-A.: Thermal conductivity and electrical conductivity of silicone rubber filled with aluminum nitride and aluminum powder. *Journal of Polymer Engineering*, **33**, 545–549 (2013).  
<https://doi.org/10.1515/polyeng-2013-0025>
- [37] Song J., Wu L., Zhang Y.: Thermal conductivity enhancement of alumina/silicone rubber composites through constructing a thermally conductive 3D framework. *Polymer Bulletin*, **77**, 2139–2153 (2020).  
<https://doi.org/10.1007/s00289-019-02839-3>
- [38] Liu C., Wu W., Drummer D., Shen W., Wang Y., Schneider K., Tomiak F.: ZnO nanowire-decorated Al<sub>2</sub>O<sub>3</sub> hybrids for improving the thermal conductivity of polymer composites. *Journal of Materials Chemistry C*, **8**, 5380–5388 (2020).  
<https://doi.org/10.1039/c9tc06805h>
- [39] Huang C., Wang Y., Cheng Y., Qi Z., Liu A., Deng Q., Hu N.: Naturally dried superelastic bioinspired graphene aerogel for pressure/stretch sensing and separation. *Composites Science and Technology*, **226**, 109549 (2022).  
<https://doi.org/10.1016/j.compscitech.2022.109549>

Research article

# Low-temperature supramolecular adhesives based on hyperbranched polyester

Yiting Jing<sup>1,2</sup>, Sufang Chen<sup>2\*</sup>, Zejun Xu<sup>1</sup>, Tingcheng Li<sup>1</sup>, Daohong Zhang<sup>1</sup>

<sup>1</sup>Key Laboratory of Catalysis and Energy Materials Chemistry of Ministry of Education & Hubei Key Laboratory of Catalysis and Materials Science, Hubei R&D Center of Hyperbranched Polymer Synthesis and Applications, South-Central Minzu University, 430074 Wuhan, China

<sup>2</sup>Key Laboratory for Green Chemical Process of Ministry of Education, Hubei Key Laboratory of Novel Reactor and Green Chemical Technology, School of Chemical Engineering and Pharmacy, Wuhan Institute of Technology, 430205 Wuhan, Hubei, PR China

Received 13 June 2023; accepted in revised form 26 August 2023

**Abstract.** Adhesives have been widely applied in various fields. However, most industrial adhesives contain organic solvents, which are toxic and difficult to clean after use. Importantly, most adhesives are used in a relatively small temperature range (0–50 °C), which is due to the fragmentation of the morphology and properties of supramolecular polymer gels at low temperatures. Most of the supramolecular adhesives need to be heated during the bonding process, which cannot meet the requirements of low-temperature adhesion in daily life and industry. In this study, based on the concept of using deep eutectic solvents (DESS) as a platform, cyclodextrin ( $\beta$ -CD) and carboxyl terminated hyperbranched polyester (DCHP) were used to prepare solvent-free supramolecular polymer gel (CD-DCHP), which was non-toxic and easy to clean. Due to the joint action of deep eutectic solvent and supramolecular polymer structure, CD-DCHP showed excellent mechanical properties, super strong adhesion (up to 4.55 MPa on glass surface), and excellent low-temperature performance (up to 1.64 MPa at –60 °C). This supramolecular polymer gel also showed excellent tolerance to acids, alkalis, and various organic solvents. It greatly expanded the application of DES and provided a new approach to the development of supramolecular adhesives.

**Keywords:** supramolecular adhesives, deep eutectic solvents, supramolecular polymerization, self-assembly

## 1. Introduction

Adhesives are indispensable to industry, agriculture, transportation, medical treatment, national defense, and people's daily lives [1]. At present, industrial adhesives have completely replaced natural adhesives, but most of them are solvent-based, which is toxic and difficult to clean. With the development of supramolecular self-assembly, supramolecular polymer adhesives have received increasing attention [2]. The supramolecular polymer can be formed by the self-assembly of the molecular structural units through non-covalent interactions [3]. The rich supramolecular structures endow the materials with reversibility,

adaptability, self-healing, and bonding functions, all of which may be attributed to non-covalent interactions [4], including hydrogen bond interaction [5, 6], metal coordination [7, 8], hydrophobic interaction [9], van der Waals force [10, 11], electrostatic interaction [12, 13] and  $\pi$ - $\pi$  interaction [14, 15]. Supramolecular polymers have the advantage of easily changing the topological structure by introducing dynamic non-covalent interactions [16]. Traditional adhesives can only stick to wooden boards, glass, and other common substrates but are difficult to adhere to plastics (polyethylene, polytetrafluoroethylene, *etc.*) and cannot be bonded for a long time [17].

\*Corresponding author, e-mail: [csfzdh@126.com](mailto:csfzdh@126.com)

© BME-PT

The polymer structure in modern adhesives was crucial for achieving the adhesion effect [18], and compared with traditional adhesives, supramolecular polymer adhesives have particularly outstanding reversibility and low-temperature bonding ability.

Cyclodextrin (CD) is a naturally occurring macromolecule containing cyclic glucosyl repeating units [19]. The most studied  $\alpha$ -,  $\beta$ -, and  $\gamma$ -CDs contain 6, 7, and 8 glucose molecules [20] respectively. The cavity of CD is hydrophobic, which can form supramolecular polymer gel through non-covalent hydrogen bonding or electrostatic interactions without affecting the biological, chemical, and physical properties [21, 22]. CDs have been widely studied in recent years. Fiorica *et al.* [23] reported the synthesis and application of CD-coated metal complexes, revealing the reversible hydrogen bonding interaction. Wu *et al.* [24] reported  $\beta$ -CD as a mixed carrier of smart drugs. Supramolecular polymer gel based on the CD-acid group is a kind of multifunctional material, and with the application of deep co-solvents as platforms, it has attracted extensive attention.

In this study,  $\beta$ -CD as hydrogen bond donor and carboxyl-ended hyperbranched polyester (DCHP) as hydrogen bond acceptor were mixed in proportion to prepare the supramolecular polymer gel (CD-DCHP) through the intermolecular and intramolecular hydrogen bonding [19]. Specifically, CD-DCHP is a supramolecular polymer gel formed by cross-linking various physical interactions, and its main driving force is the hydrogen bond interaction between CD and DCHP [25–27]. The supramolecular polymer gel based on the CD-hyperbranched polyester is a multifunctional material, so CD-DCHP is a kind of supramolecular adhesive with great development space [28].

## 2. Experimental sections

### 2.1. Materials

$\beta$ -cyclodextrin ( $\beta$ -CD) was purchased from Meryer Chemical Technology Co., Ltd (Shanghai, China) and used as received. Carboxyl-ended hyperbranched polyester (DCHP-18) was prepared according to the procedure in the literature [29]. The chemical structures of  $\beta$ -CD and DCHP-18 are shown in Figures 1a and 1b, respectively.

### 2.2. Instruments and characterization

Fourier transform infrared spectra (FT-IR) were collected by a Vertex 470 infrared spectrometer (Bruker

Company, Germany). Thermogravimetric analysis (TGA) was carried out on a NETZSCH TG 209 F3 thermogravimetric analyzer (NETCHI Instrument Manufacturing Company, Germany) at a heating rate of 10 °C/min from 30 to 790 °C. The nitrogen flow rate was 20 ml/min, and the amount of sample was 10 mg. Differential scanning calorimetry (DSC) measurements were carried out using NETZSCH TG 209 F3 thermogravimetric analyzer (NETCHI Instrument Manufacturing Company, Germany), with a nitrogen flow of 20 ml/min, and a heating rate of 10 °C/min from –80 to 80 °C. X-ray diffraction (XRD) spectra were collected on a Bruker-D8 X-ray diffractometer (Bruker company, Germany). Rheology measurements were performed on a DHR-1 rotary rheometer (TA Instrument Company, USA) using a 40 mm parallel laminator model 110626 Peltier steel plate at a gap of 1 mm. Scanning electron microscopy (SEM) images were collected on a SU8010 electron microscope (Hitachi Company, Japan). The adhesion strength was tested on a 5966 universal testing machine (INSTRON Company, USA). Nuclear magnetic resonance (NMR) spectra were collected on an AVANCE III 400 MHz NMR instrument (Bruker Company, Germany).

### 2.3. Preparation of supramolecular polymer gel

Preparation of CD-DCHP- $x$  ( $x$ : Molar ratio of  $\beta$ -CD to DCHP-18): In a typical procedure,  $\beta$ -CD (1.5 mmol, 1.7017 g) and DCHP-18 (1.5 mmol, 1.8150 g) were added into a 100 ml beaker, then 80 ml ultrapure water was added. The mixture was stirred at 25 °C for 30 min and then dried at 80 °C for 10 h. During heating, a transition from solid mixture to viscous liquid was observed, and the supramolecular polymer gel could be obtained by cold sweat at room temperature. A series of supramolecular polymer gels with different molar ratios of  $\beta$ -CD to DCHP-18 was prepared using a similar method, as summarized in Table 1. No reprocessing or further

**Table 1.** The proportion of each component of CD-DCHP- $x$ .

Supramolecular polymer gel	Moles [mmol]		Molar ratio of DCHP-18/ $\beta$ -CD ( $x$ )
	$\beta$ -CD	DCHP-18	
CD-DCHP-0.5	3.0	1.5	0.5
CD-DCHP-1	1.5	1.5	1.0
CD-DCHP-1.5	2.0	3.0	1.5
CD-DCHP-2	2.0	4.0	2.0
CD-DCHP-3	2.0	6.0	3.0

treatments are needed before applying these polymer gels for adhesion tests.

#### 2.4. Preparation of bonded sample bars

Take glass substrate as an example. The supramolecular polymer gel was evenly coated on a piece of glass and then covered with another glass plate and pressed for 10 min, with an adhesion area of 6.25 cm<sup>2</sup>. The pair of adhered glass sheets were heated at 80 °C for 60 min and then cooled to room temperature for tensile tests.

### 3. Results and discussion

The mixtures of CD and DCHP-18 were used to synthesize deep eutectic supramolecular polymers (DESPs) by simple heating [30]. An irreversible transformation from the solid mixture (CD and DCHP-18) to high viscosity supramolecular polymer gel was observed in the process (Figure 1), which was a good indication that supramolecular polymerization had taken place between  $\beta$ -CD and DCHP-18.

Flexible and viscous fibers can be easily extracted from the viscous gel (Figure 1d) [31]. The hydrogen bonding formed in supramolecular polymers not only affects the aggregation but also affects the morphology of supramolecular polymers. Moreover, the infrared spectra of the supramolecular polymer gel fully match the standard of deep eutectic solvent [18, 25]. The FT-IR spectra of CD, DCHP, and CD-DCHP are shown in Figure 2a. In Figure 2a, the characteristic peaks of  $\beta$ -CD appeared at 3321, 2932, and 1030 cm<sup>-1</sup>, corresponding to –OH, C–H, and C–O stretching vibrations, respectively [21]. The characteristic peaks of DCHP appeared at 1172, 1699, 1750, and 3292 cm<sup>-1</sup>, which corresponded to the stretching vibrations of C–O–C, C=C, C=O and –OH groups, respectively [32]. In the spectrum of CD-DCHP-1, the vibration of C=O shifted to 1716 cm<sup>-1</sup>, the intensity of the characteristic C–O–C peak decreased somewhat, and new peaks due to the formation of CD-DCHP-1 appeared at 2947 and 1032 cm<sup>-1</sup>. Compared with  $\beta$ -CD, the absorption of the –OH group

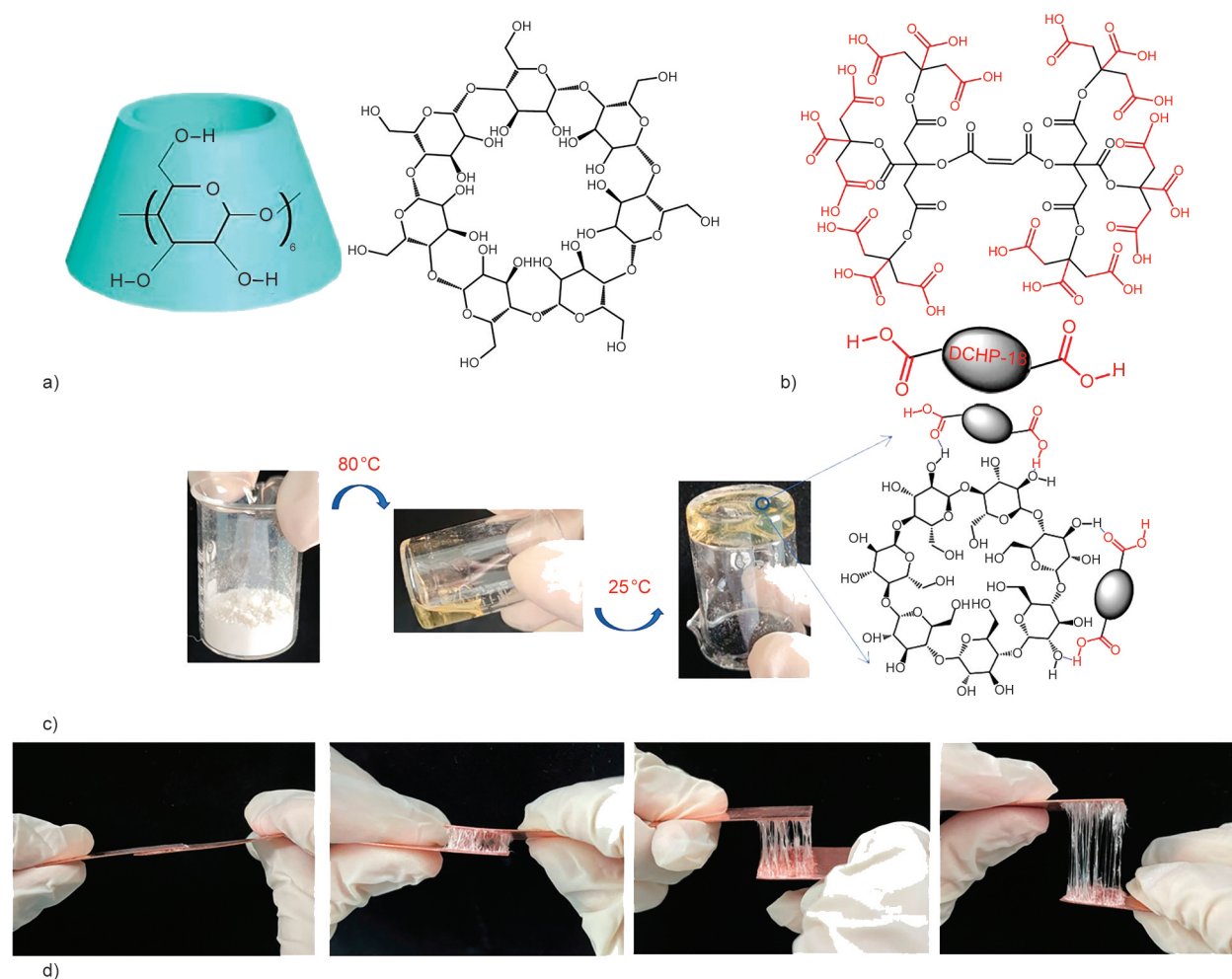


**Figure 1.** Chemical structures of a) CDs and b) DCHP-18, c) preparation of supramolecular polymer gel, d) the fibers drawn from CD-DCHP.

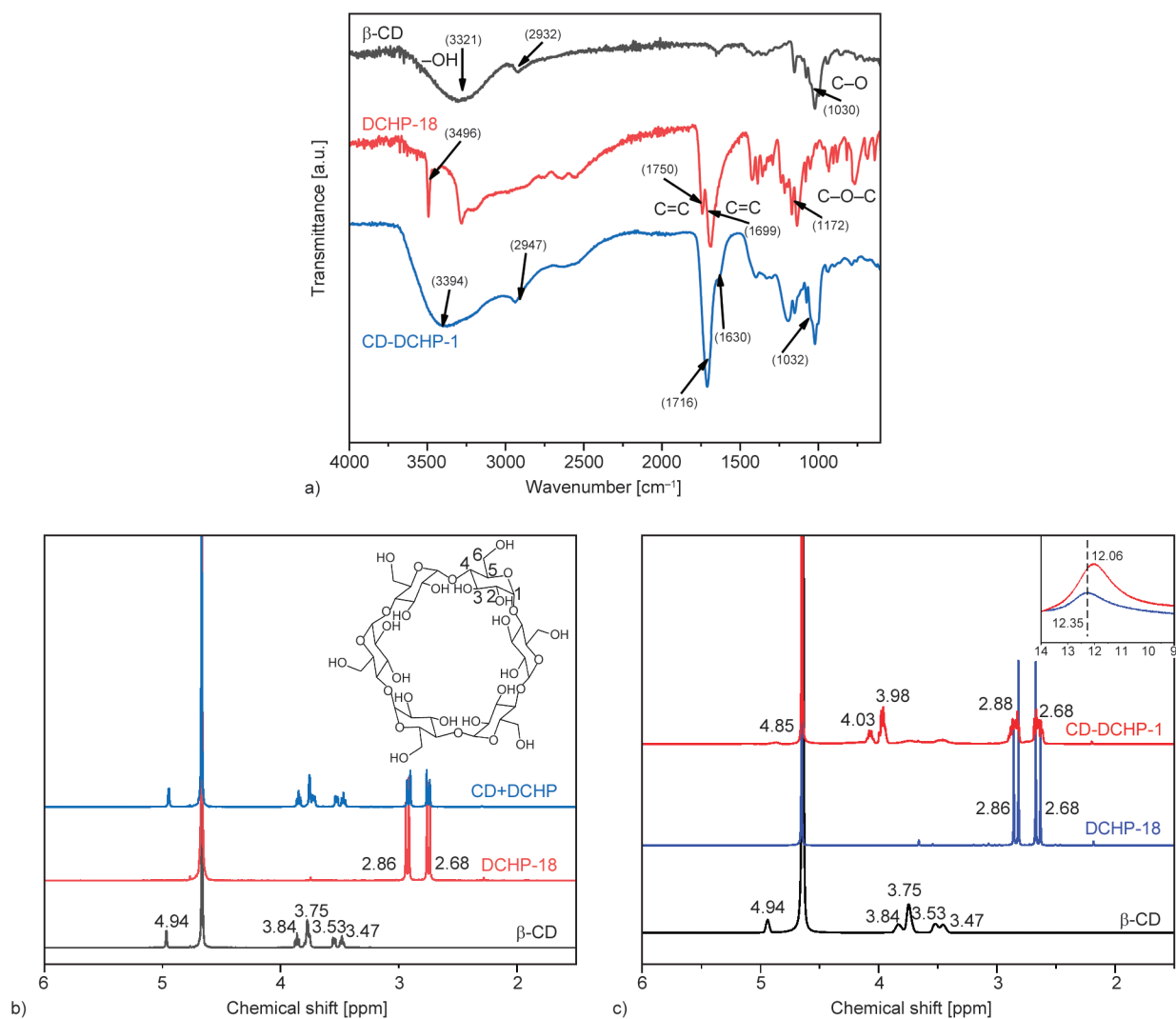


**Figure 2.** a) FT-IR spectra of CD, DCHP-18, and CD-DCHP-1, b)  $^1\text{H-NMR}$  comparison of CD, DCHP-18, and CD+DCHP, and c)  $^1\text{H-NMR}$  spectra of CD, DCHP-18, and CD-DCHP-1, insert: chemical shift at 14–9 ppm.

of CD-DCHP-1 ( $3394\text{ cm}^{-1}$ ) was shifted and intensified as a result of the formation of hydrogen bonding between the C=O of DCHP-18 and the –OH of  $\beta$ -CD. [33–36]. The IR spectra of CD-DCHP-1 were consistent with the formation of typical deep eutectic solvents [25].

CD-DCHP-1,  $\beta$ -CD, DCHP-18, and the heated mixture of  $\beta$ -CD and DCHP-18 (named CD+DCHP) were tested by  $^1\text{H-NMR}$  (Figures 2b, 2c). As can be seen from Figure 2b, the chemical shifts of –OH at positions 2, 3, 4, and 6 in  $\beta$ -CD were 3.53, 3.84, 3.47, and 3.75 ppm, respectively [37]. The chemical shift of –COOH in DCHP-18 was 12.35 [32], and compared with the  $^1\text{H-NMR}$  spectra of  $\beta$ -CD and DCHP-18, the characteristic peaks of simple mixture CD+DCHP showed no change, suggesting that there was no hydrogen bonding interaction. On the other hand, the chemical shifts of –OH at positions 3 and

6 of  $\beta$ -CD in CD-DCHP-1 shifted downfield from 3.84 and 3.75 ppm to 4.03 and 3.98 ppm (Figure 2c), respectively, and the hydroxyl peaks at positions 2 and 4 gradually disappeared. Meanwhile, the chemical shift of –COOH in DCHP-18 shifted from 12.23 to 12.31 ppm (insert in Figure 2c). All these proved that –OH in  $\beta$ -CD and –COOH in DCHP-18 have formed hydrogen bonding. The  $^1\text{H-NMR}$  results also provided evidence that CD-DCHP-1 was a hydrogen-bonded supramolecular complex [38].

The solid-state structure of CD-DCHP-1 was investigated by XRD and shown in Figure 3a. There was a wide diffraction peak centered around  $20^\circ$ , which was typical of an amorphous structure. This was because CD-DCHP-1 formed hydrogen bonds during the synthesis, which inhibited the crystallization of the chain segments [39]. Combining the results of the  $^1\text{H-NMR}$  spectrum of CD-DCHP-1, it is concluded



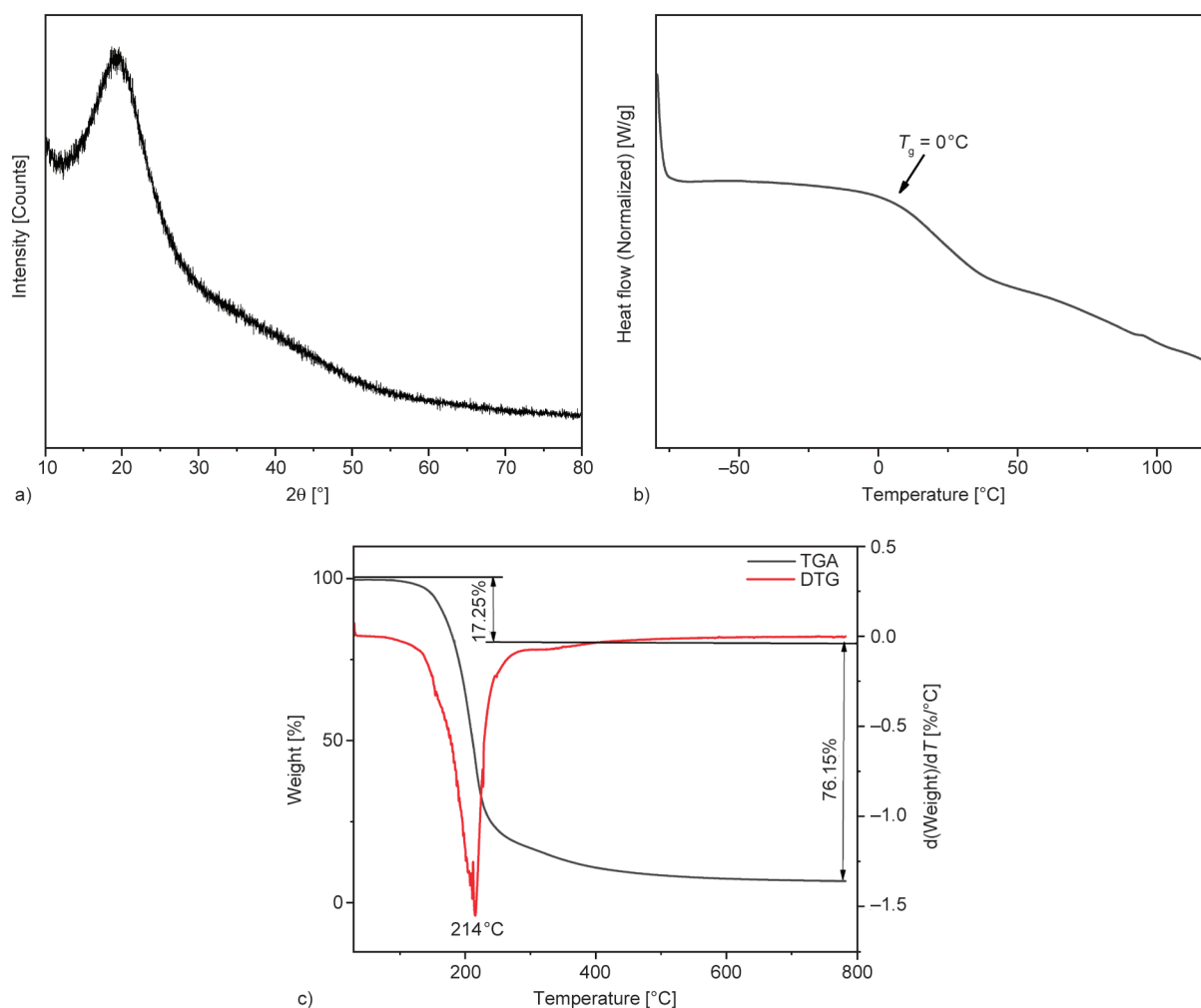


**Figure 3.** a) XRD pattern of CD-DCHP-1, b) DSC, and c) TGA characterization of CD-DCHP-1.

that there is a hydrogen bond interaction between  $-\text{OH}$  in  $\beta\text{-CD}$  and  $-\text{COOH}$  in DCHP-18.

The thermal stability of CD-DCHP-1 was tested by DSC and TGA. As shown in Figure 3b, the glass transition temperature of CD-DCHP-1 was about  $0^\circ\text{C}$ , which was lower than room temperature [40]. The TGA curve showed that the gel began to lose weight at about  $100^\circ\text{C}$  (Figure 3c), owing to the loss of hydrophilic binding water. The initial and maximum degradation temperatures were  $135$  and  $214^\circ\text{C}$ , respectively, and the physical and chemical properties of the gel remained the same below  $135^\circ\text{C}$ , indicating high thermal stability [40, 41]. It showed that the CD-DCHP-1 was not only suitable for general bonding applications but also suitable for application at low temperatures.

The rheology of CD-DCHP- $x$  was also studied, and the mechanical properties of supramolecular adhesive were quantitatively evaluated by a dynamic frequency scanning test. Under the condition of a fixed strain of  $0.1\%$ , an angular frequency increment of

$5 \text{ rad}\cdot\text{s}^{-1}$  between  $1$  and  $100 \text{ rad}\cdot\text{s}^{-1}$ , the storage modulus ( $G'$ ) of different supramolecular adhesives CD-DCHP-0.5, CD-DCHP-1, CD-DCHP-2, and CD-DCHP-3 were measured and shown in Figure 4b. When the molar ratio of  $\beta\text{-CD}$  to DCHP-18 is  $1:1$ , the modulus was at a maximum due to the fact that the molar ratio of  $-\text{OH}$  to  $-\text{COOH}$  was also  $1:1$ , thus forming a dense hydrogen bonding network. As shown in Figure 4a, there was no intersection point between  $G'$  and ( $G''$ ) with the increase of frequency, and the storage modulus ( $G'$ ) was always smaller than the loss modulus ( $G''$ ), suggesting that CD-DCHP- $x$  had always been a viscoelastic gel, and had no tendency to change into solid fluid [40, 42].

Dynamic temperature scanning on different CD-DCHP- $x$  samples was performed, with the results presented in Figure 4b. The viscosity gradually decreased with the increase in temperature due to the breaking of hydrogen bonds, and the fluidity of CD-DCHP- $x$  increased. However, when the temperature decreased, hydrogen bonds would be formed

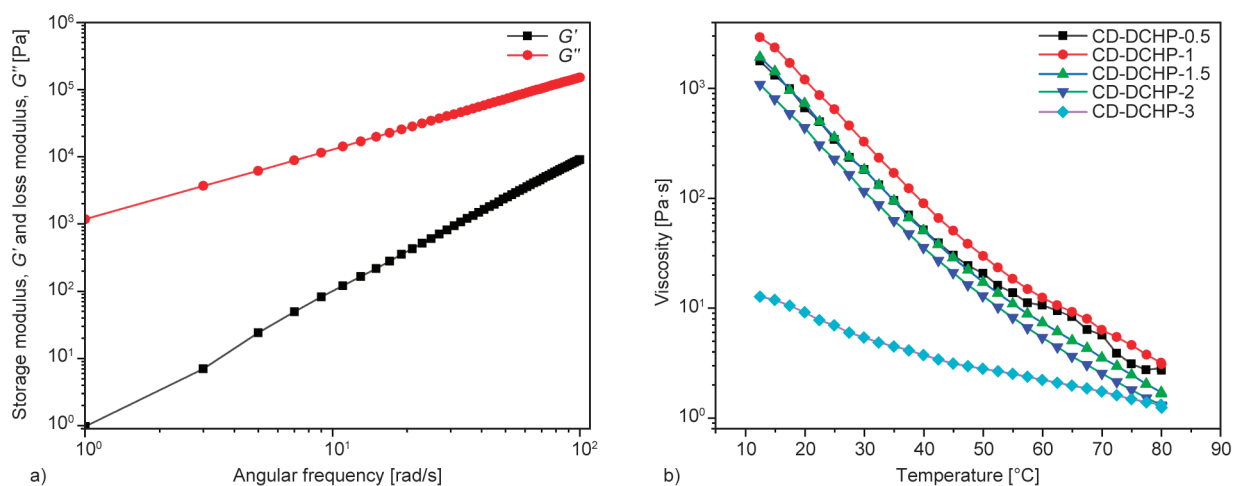


**Figure 4.** a) Storage modulus ( $G'$ ) and loss modulus ( $G''$ ) values of CD-DCHP-1 on frequency sweep at 25 °C, b) effects of temperature on viscosity of CD-DCHP- $x$ .

again, giving the supramolecular gels adhesive force, as proved in the subsequent reuse experiments. This showed that supramolecular adhesive was a kind of physical gel constructed by intermolecular hydrogen bonding interaction, so when the external environment changed or external forces acted on, it would affect the adhesive strength.

The XPS spectra of  $\beta$ -CD, DCHP-18, and CD-DCHP-1 were shown in Figure 5a, all of which displayed carbon and oxygen peaks. Narrow scans for C 1s and O 1s were performed at 285–298 eV and 520–545 eV and shown in Figures 5b, 5c, respectively. Compared with  $\beta$ -CD and DCHP-18, the binding energy of C 1s increased, and that of O 1s decreased in the spectrum of CD-DCHP-1, also an indication of the formation of hydrogen bonds between  $\beta$ -CD and DCHP-1.

The C 1s spectrum of  $\beta$ -CD was deconvoluted into three peaks (Figure 5d): 283.69 eV belonged to C–H, 285.36 eV belonged to C–C, and 286.76 eV belonged to C–OH and C–O–C. The C 1s spectrum of DCHP-18 was divided into five peaks (Figure 5e): 284.09 eV belonged to C–C and C–H, 285.92 eV belonged to C=C, and 288.32 eV belonged to C–OH and O–C=O [41]. The deconvolution of C 1s subpeak of CD-DCHP-1 was also performed (Figure 5f), and five peaks of 283.85, 285.78, 287.80, 288.4, and 289.1 eV were obtained. The binding energy of C–H and C–C increased and overlapped at 283.85 eV. The peak at 285.78 eV was attributed to C=C, 288.4 eV to C=O, 289.1 eV to O–C=O, and the new peak at 287.80 eV was attributed to C=O $\cdots$ O–H after hydrogen bonding interaction.

O 1s spectra of  $\beta$ -CD, DCHP-18, and CD-DCHP-1 were deconvoluted and shown in Figure 5g–5i. The 531.49 and 532.12 eV peaks of O 1s were attributed to C–O–C and C–OH of  $\beta$ -CD, respectively. The 531.39, 532.40, and 533.22 eV peaks were attributed to C–O–C, C=O, and O–C=O of DCHP-18, respectively. The O 1s of CD-DCHP-1 have been divided into five peaks, 530.59, 531.19, 532.65, and 533.37 eV, which were attributed to C–OH, C–O–C, C=O, and O–C=O respectively, while the new peak at 531.83 eV was attributed to C=O $\cdots$ O–H, also proving that there existed hydrogen bonding interaction between  $\beta$ -CD and DCHP-18.

The CD-DCHP- $x$  showed superior adhesion strength on the surface of various materials. As can be seen from Figure 6, it can easily adhere to wood, polytetrafluoroethylene (PTFE), paper copper, carnelian, rubber, aluminum, copper, iron, glass, and silicone [30]. The adhesion properties were carefully studied from the aspects of polymerization behavior and macroscopic properties. As can be seen from Figure 7a, it can be easily bonded on different substrates. CD-DCHP- $x$  was firstly coated on the surface of the substrate at 80 °C for 1 hour; then, a new substrate was covered. After pressing for 30 min, the two pieces of substrates were adhered together, followed by cooling to room temperature (Figure 7a) [42].

The bound glass and steel sheets did break apart or misalign when attached with a weight of 10 kg (the adhesion area is 6.25 cm<sup>2</sup>, Figures 7a, 7b), clearly demonstrating strong and stable adhesion. The CD-DCHP-1 bonded copper sheet was less strong but could also hold up to 6 kg of weight (Figure 7c) [17].

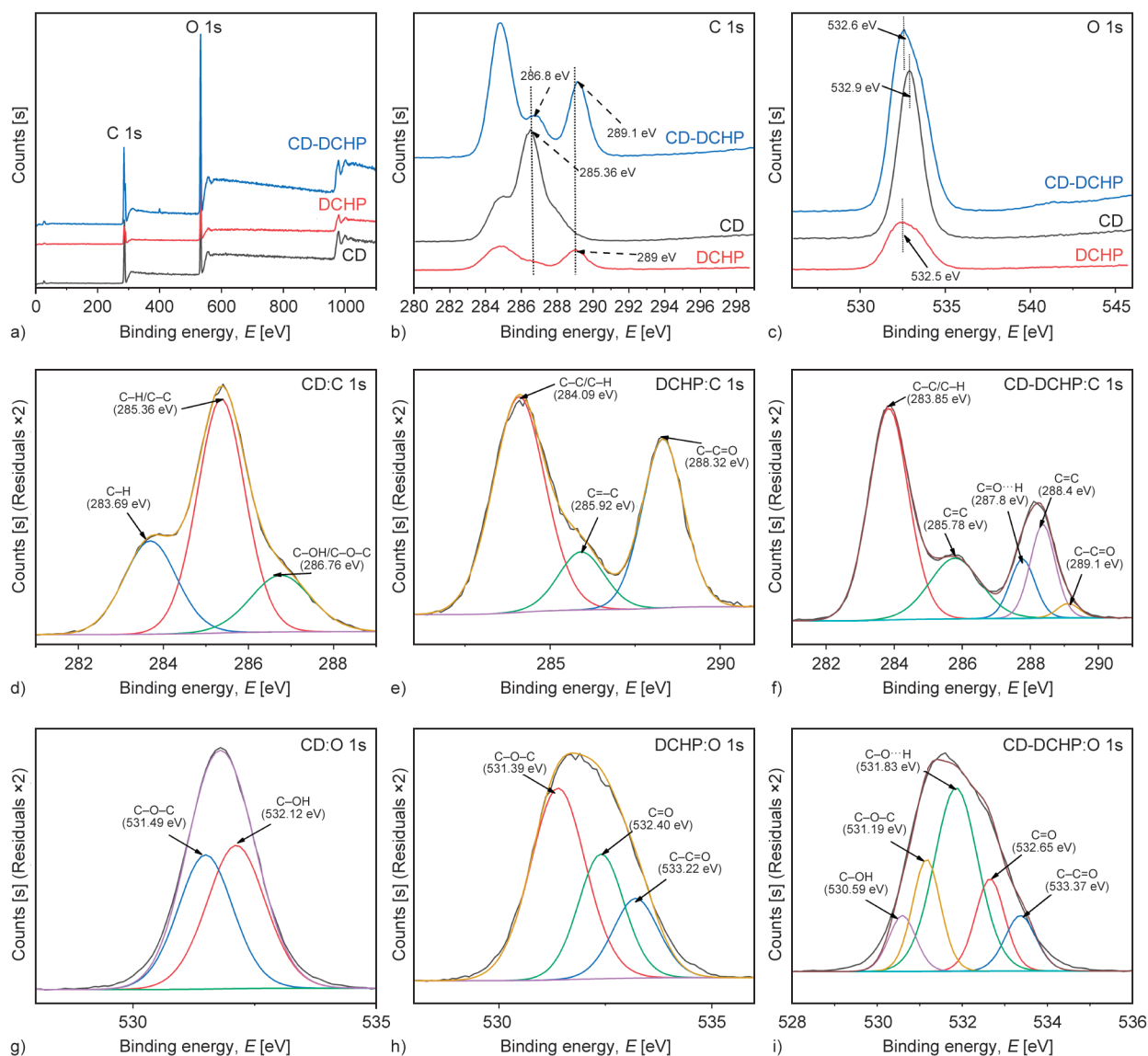


**Figure 5.** XPS full spectrum (a), C 1s (b, d–f) and O 1s (c, g–i) XPS spectrum of  $\beta$ -CD, DCHP-18, and CD-DCHP-1.

The CD-DCHP- $x$  adhesives with various CD to DCHP-18 ratios were applied for the adhesion tests at 25 °C. The adhesive strength of CD-DCHP- $x$  (Figure 8a) on glass increased first and decreased afterward as the molar ratio of  $\beta$ -CD to DCHP-18 increased [17]. The adhesive strengths of CD-DCHP-0.5, CD-DCHP-1, CD-DCHP-1.5, CD-DCHP-2, and CD-DCHP-3 were  $2.52\pm 0.23$ ,  $4.02\pm 0.08$ ,  $2.78\pm 0.24$ ,  $1.98\pm 0.43$ , and  $1.47\pm 0.12$  MPa, respectively, with the maximum found at a 1:1 ratio. When the molar ratio of  $\beta$ -CD to DCHP-18 was 1:1, the ratio of –OH to –COOH was also 1:1, which was conducive to forming a dense hydrogen bond network. The shear adhesion strength of CD-DCHP-1 to different types of substrates was measured, as can be seen in Figure 8b. The shear adhesion strengths of the CD-DCHP-1 for iron, steel, wood, aluminum, and glass

substrates were  $1.21\pm 0.18$ ,  $1.73\pm 0.11$ ,  $2.41\pm 0.24$ ,  $2.48\pm 0.21$ , and  $4.02\pm 0.08$  MPa, respectively, demonstrating excellent adhesion property for various substrates.

Supramolecular assembly is usually sensitive to temperature. The shear tests at different temperatures showed that high temperature was not conducive to the bonding of CD-DCHP-1 on the substrate, as depicted in Figure 8c. Too low a temperature was also shown to reduce the adhesion strengths. The adhesive strength of CD-DCHP-1 (Figure 8c) on a glass plate increased first and decreased afterward as the temperature increased from –60 to 25 °C, which were  $1.64\pm 0.04$  MPa at –60 °C,  $1.85\pm 0.24$  MPa at –30 °C,  $1.94\pm 0.20$  MPa at –20 °C,  $3.13\pm 0.22$  MPa at –10 °C,  $4.08\pm 0.18$  MPa at 0 °C,  $4.55\pm 0.21$  MPa at 10 °C, and  $4.02\pm 0.08$  MPa at 25 °C, respectively.

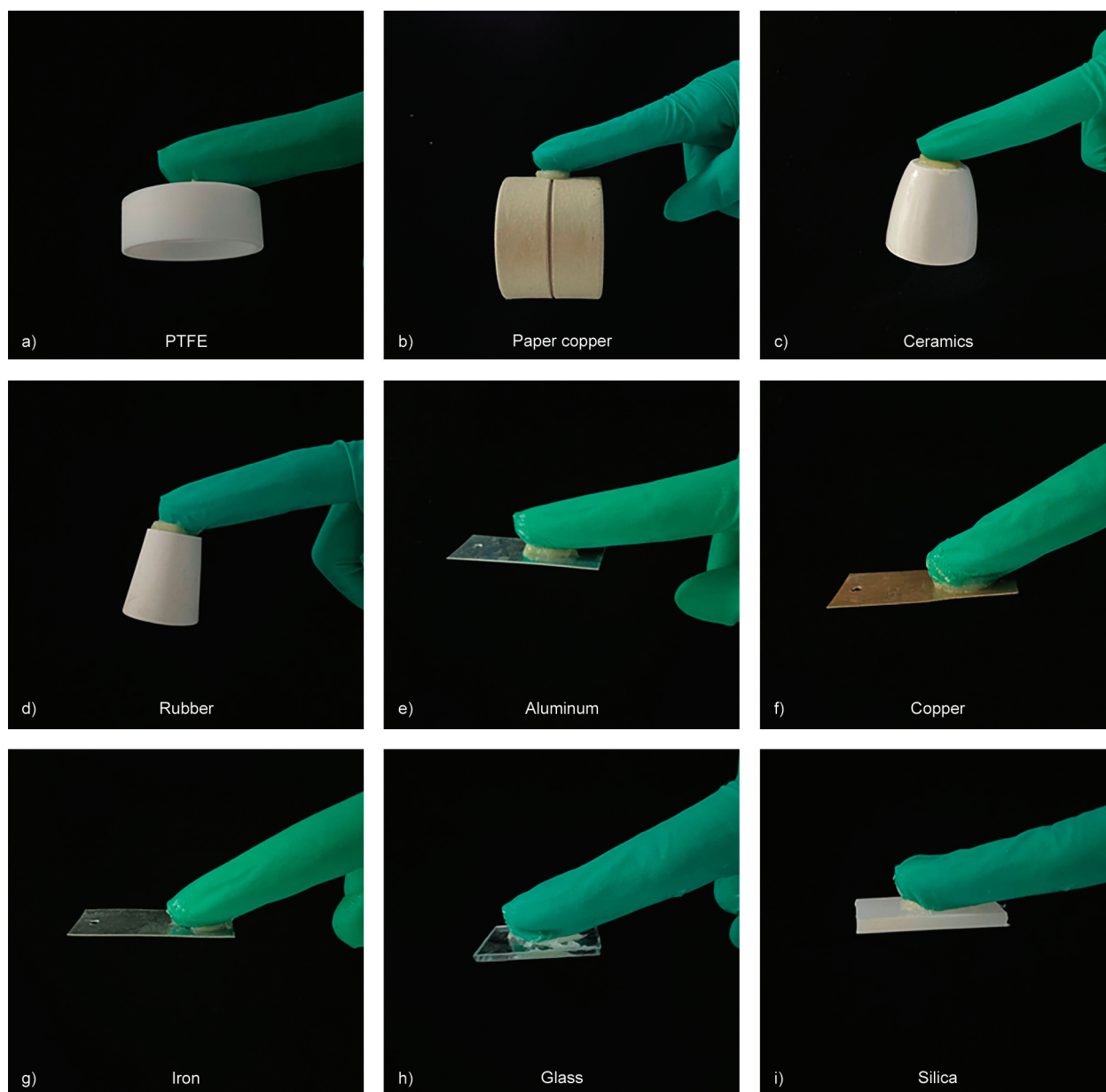


**Figure 6.** Schematic diagram of adhesion of CD-DCHP-1 to a) PTFE, b) paper copper, c) ceramics, d) rubber, e) aluminum, f) copper, g) iron, h) glass, and i) silica.

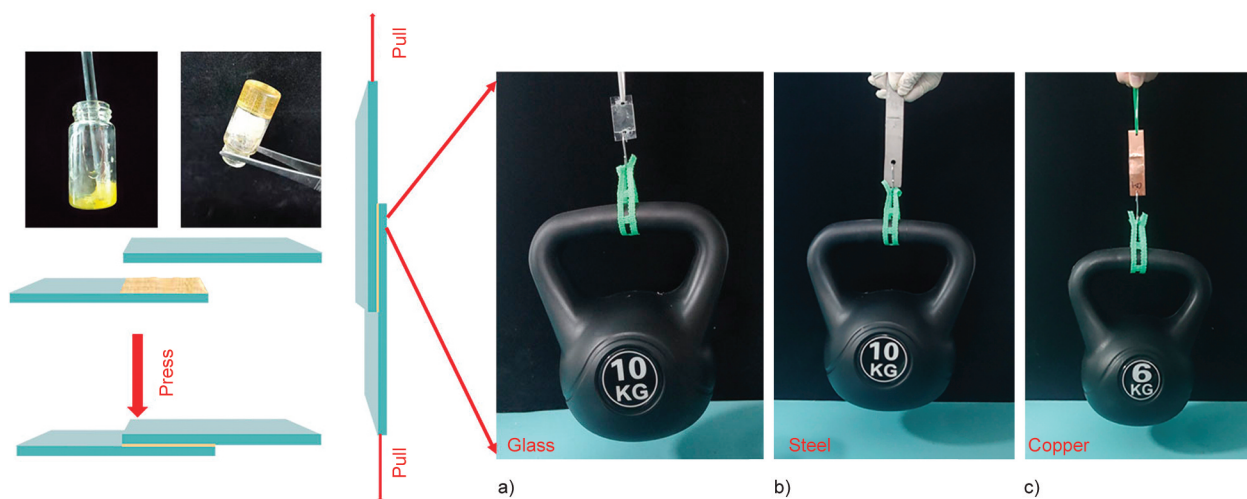


**Figure 7.** Adhesion experiment and adhesion properties of CD-DCHP gel to a) glass, b) steel, c) copper.

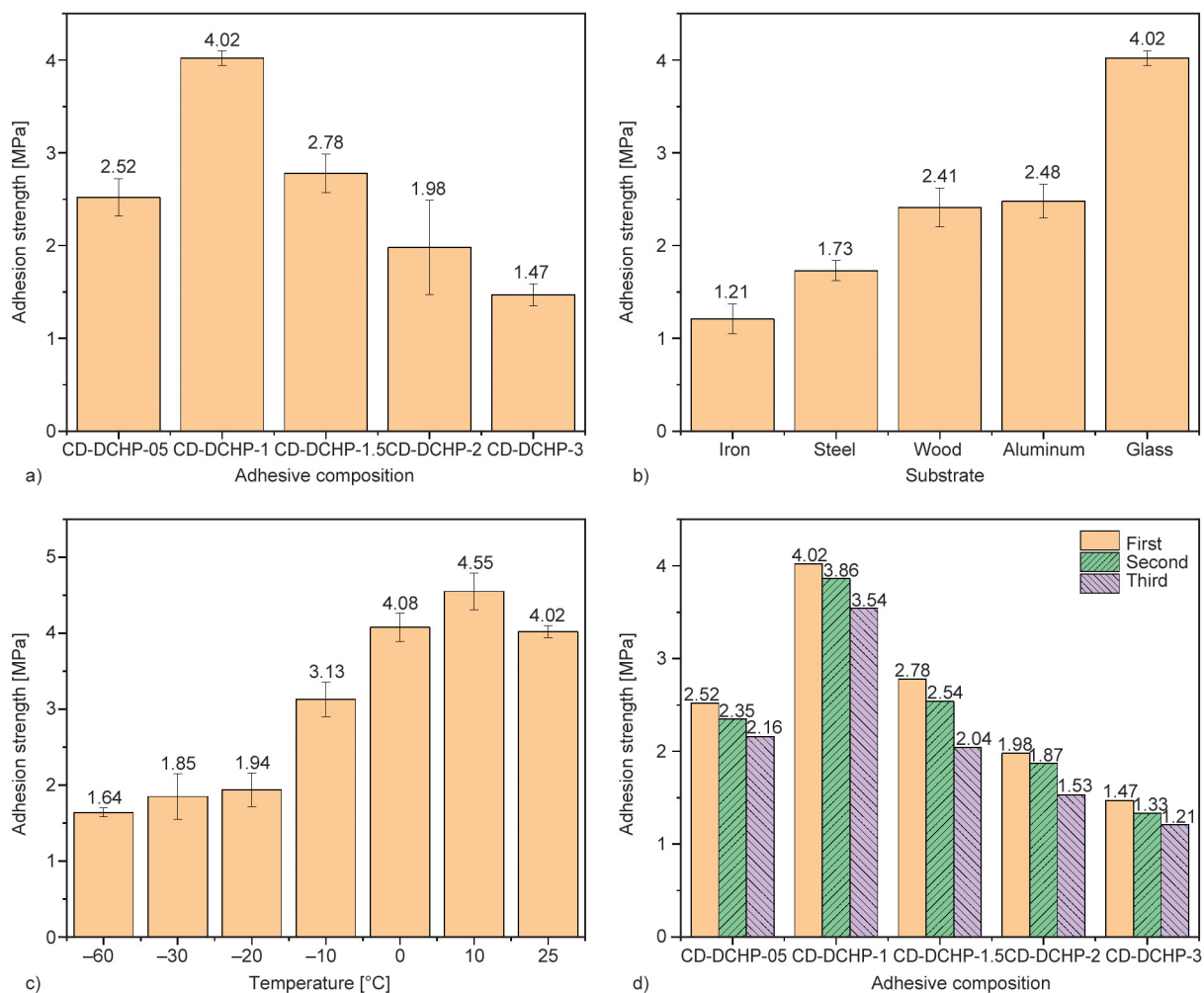


**Figure 8.** a) Tensile test of CD-DCHP with different proportions, b) tensile test of CD-DCHP-1 gel on different substrates, c) tensile test of CD-DCHP-1 gel on the glass surface at different temperatures, d) cyclic tensile test of different proportions of CD-DCHP on the glass plate.

The adhesion results varied with temperature in accordance with rheological measurements and macroscopic adhesion tests (Figure 4).

After three heating and cooling cycles on the steel substrate, the bonding strength of CD-DCHP-1 remained around 3.54 MPa (Figure 8d), indicating excellent reusability [40]. Although the tensile external force destroyed the hydrogen bonding, it tended to form again after cooling down and made the glass plates stick together again. However, due to the increase of plasticity after repeated heating, the bonding

strength of CD-DCHP-1 decreased slightly [42], as shown in Table 2.

Figure 9 presents the adhesion tests after soaking the plates in various solvents. As can be seen from Figure 9a, the adhesive force was still maintained after soaking in liquid nitrogen (−196 °C). To test the resistance of CD-DCHP-1 to organic solvents, CD-DCHP-1 was immersed in transformer oil and *N*-octane, and a 1 kg object could be hung on the adhered glass sheet without breaking up or displacement (Figures 9b, 9c). All these indicated that CD-DCHP

**Table 2.** Cyclic tensile test of different proportions of CD-DCHP on the glass plate.

Number of cycles	Adhesion strength [MPa]				
	CD-DCHP-0.5	CD-DCHP-1	CD-DCHP-1.5	CD-DCHP-2	CD-DCHP-3
1	2.52	4.02	2.78	1.98	1.47
2	2.35	3.86	2.54	1.87	1.33
3	2.16	3.54	2.04	1.53	1.21

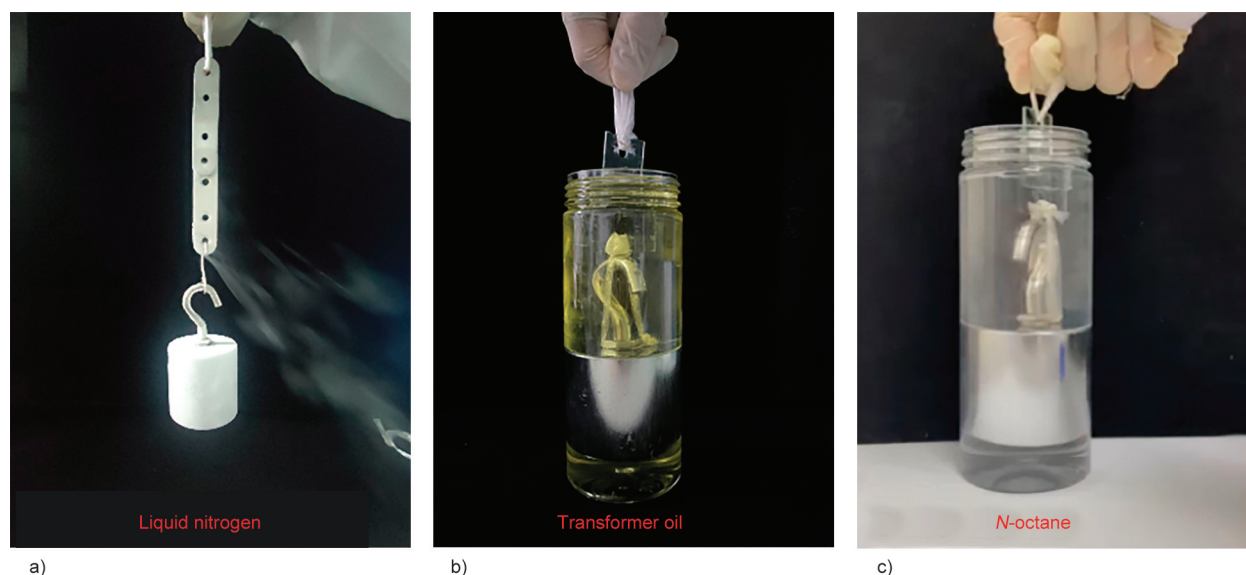


**Figure 9.** a) Macro bonding test of CD-DCHP-1 on steel sheet (soak in liquid nitrogen for 10 min after bonding), b) transformer oil, and c) *N*-octane of CD-DCHP-1 on the glass sheet.

could be used in some harsh environments and had good tolerance to various solvents.

#### 4. Conclusions

In conclusion, supramolecular adhesives based on hyperbranched polyester and cyclodextrin (CD-DCHP-*x*) were constructed by hydrogen bonding interaction between  $\beta$ -CD and DCHP-18. A dense hydrogen bonding network was formed to provide excellent adhesions by utilizing the rich hydroxyl groups in  $\beta$ -CD and the carboxyl groups in DCHP-18. The successful synthesis of supramolecular adhesives was confirmed by FT-IR,  $^1\text{H-NMR}$ , XRD, and XPS. Tensile tests show that the binding effect of  $\beta$ -CD and DCHP-18 is the best when the molar ratio of  $\beta$ -CD to DCHP-18 is 1:1 (CD-DCHP-1). CD-DCHP-1 also showed excellent adhesion on various substrates (iron sheet, wood sheet, aluminum sheet, glass, *etc.*), with adhesive strengths found between 1.21 and 4.55 MPa. Tensile tests of CD-DCHP-1 at different temperatures showed that the supramolecular adhesives were not only suitable for room-temperature application but also worked well at low-temperature. The adhesive strengths of CD-DCHP-1 were  $1.64 \pm 0.04$  MPa at  $-60^\circ\text{C}$ ,  $1.85 \pm 0.24$  MPa at  $-30^\circ\text{C}$ ,  $1.94 \pm 0.20$  MPa at  $-20^\circ\text{C}$ ,  $3.13 \pm 0.22$  MPa at  $-10^\circ\text{C}$ ,  $4.08 \pm 0.18$  MPa at  $-0^\circ\text{C}$ ,  $4.55 \pm 0.21$  MPa at  $10^\circ\text{C}$ , and  $4.02 \pm 0.08$  MPa at  $25^\circ\text{C}$ , respectively. The adhesives also demonstrated excellent reusability and resistance to various organic solvents. The cyclic tensile test of CD-DCHP-1

showed that the supramolecular bond between different substrates was reversible and could be reused multiple times.

#### Acknowledgements

We gratefully acknowledge financial support from the National Natural Science Foundation of China (51703250 and 51873233), Natural Science Foundation of Hubei Province (2021CFB514), Innovation Group of National Ethnic Affairs Commission of China (MZR20006), the Fundamental Research Funds for the Central Universities in South-Central Minzu University (CZQ23038), South-Central Minzu University (YZZ19019) and Graduate Education Innovation Foundation of Wuhan Institute of Technology (CX2022004).

#### References

- [1] Wu S., Cai C., Li F., Tan Z., Dong S.: Supramolecular adhesive materials from natural acids and sugars with tough and organic solvent-resistant adhesion. *CCS Chemistry*, **3**, 1690–1700 (2021). <https://doi.org/10.31635/ccschem.020.202000318>
- [2] Chen J., Guo D., Liang S., Liu Z.: A supramolecular copolymer based on small molecules, used for a multifunctional adhesive and rapid hemostasis. *Polymer Chemistry*, **11**, 6670–6680 (2020). <https://doi.org/10.1039/D0PY00926A>
- [3] Qin B., Yin Z., Tang X., Zhang S., Wu Y., Xu J-F., Zhang X.: Supramolecular polymer chemistry: From structural control to functional assembly. *Progress in Polymer Science*, **1**, 101167 (2020). <https://doi.org/10.1016/j.progpolymsci.2019.101167>
- [4] Chen S., Xu Z., Zhang D.: Synthesis and application of epoxy-ended hyperbranched polymers. *Chemical Engineering Journal*, **343**, 283–302 (2018). <https://doi.org/10.1016/j.cej.2018.03.014>

- [5] Grabowski S. J.: Intramolecular hydrogen bond energy and its decomposition –O–H···O interactions. *Crystals*, **11**, 5 (2021).  
<https://doi.org/10.3390/cryst11010005>
- [6] Grabowski S. J.: Molecular hydrogen as a Lewis base in hydrogen bonds and other interactions. *Molecules*, **25**, 3294 (2020).  
<https://doi.org/10.3390/molecules25143294>
- [7] Zhu Z-Z., Tian C-B., Sun Q-F.: Coordination-assembled molecular cages with metal cluster nodes. *The Chemical Record*, **21**, 498–522 (2021).  
<https://doi.org/10.1002/ctr.202000130>
- [8] Zheng S., Xue H., Pang H.: Supercapacitors based on metal coordination materials. *Coordination Chemistry Reviews*, **373**, 2–21 (2018).  
<https://doi.org/10.1016/j.ccr.2017.07.002>
- [9] Mozo-Villarias A., Cedano J., Querol E.: The importance of hydrophobic interactions in the structure of transcription systems. *European Biophysics Journal*, **50**, 951–961 (2021).  
<https://doi.org/10.1007/s00249-021-01557-x>
- [10] Shang X-Y., Zhao K., Qian W-X., Zhu Q-Y., Zhou G-Q.: On the calculation of van der Waals force between clay particles. *Minerals*, **10**, 993 (2020).  
<https://doi.org/10.3390/min10110993>
- [11] Xu L., Fu Z.: Effects of van der Waals force on nonlinear vibration of electromechanical integrated electrostatic harmonic actuator. *Mechanics Based Design of Structures and Machines*, **47**, 136–153 (2019).  
<https://doi.org/10.1080/15397734.2018.1490651>
- [12] Qiu G., Wong G., Ting Y-P.: Electrostatic interaction governed solute transport in forward osmosis. *Water Research*, **173**, 115590 (2020).  
<https://doi.org/10.1016/j.watres.2020.115590>
- [13] Jing Z., Dai X., Xian X., Du X., Liao M., Hong P., Li Y.: Tough, stretchable and compressive alginate-based hydrogels achieved by non-covalent interactions. *RSC Advances*, **10**, 23592–23606 (2020).  
<https://doi.org/10.1039/D0RA03733H>
- [14] Faltova L., Kuffner A., Hondele M., Weis K., Arosio P.: Multifunctional protein materials and microreactors using low complexity domains as molecular adhesives. *ACS Nano*, **12**, 9991–9999 (2018).  
<https://doi.org/10.1021/acsnano.8b04304>
- [15] Wang K., Shao Y-G., Yan F-Z., Zhang Z., Li S.: Construction of supramolecular polymers with different topologies by orthogonal self-assembly of cryptand-paraquat recognition and metal coordination. *Molecules*, **26**, 952 (2021).  
<https://doi.org/10.3390/molecules26040952>
- [16] Lei K., Zhu Q., Wang X., Xiao H., Zheng Z.: *In vitro* and *in vivo* characterization of a foam-like polyurethane bone adhesive for promoting bone tissue growth. *ACS Biomaterials Science and Engineering*, **5**, 5489–5497 (2019).  
<https://doi.org/10.1021/acsbomaterials.9b00918>
- [17] Li X., Deng Y., Lai J., Zhao G., Dong S.: Tough, long-term, water-resistant, and underwater adhesion of low-molecular-weight supramolecular adhesives. *Journal of the American Chemical Society*, **142**, 5371–5379 (2020).  
<https://doi.org/10.1021/jacs.0c00520>
- [18] Dossmann H., Fontaine L., Weisgerber T., Bonnet V., Monflier E., Ponchel A., Przybylski C.: First steps to rationalize host–guest interaction between  $\alpha$ -,  $\beta$ -, and  $\gamma$ -cyclodextrin and divalent first-row transition and post-transition metals (subgroups VIII, VIII, and IIB). *Inorganic Chemistry*, **60**, 930–943 (2021).  
<https://doi.org/10.1021/acs.inorgchem.0c03052>
- [19] Zhu F-D., Zhang Z-H., Chi S-M., Chen S-L., Wang Y-F., Zhu H-Y., Lei Z., Zhao Y.: Experimental and molecular docking investigation of the inclusion complexes between 20(S)-protopanaxatriol and four modified  $\beta$ -cyclodextrins. *Carbohydrate Research*, **500**, 108256 (2021).  
<https://doi.org/10.1016/j.carres.2021.108256>
- [20] Gieroba B., Kalisz G., Sroka-Bartnicka A., Płazińska A., Płaziński W., Starek M., Dąbrowska M.: Molecular structure of cefuroxime axetil complexes with  $\alpha$ -,  $\beta$ -,  $\gamma$ -, and 2-hydroxypropyl- $\beta$ -cyclodextrins: Molecular simulations and Raman spectroscopic and imaging studies. *International Journal of Molecular Sciences*, **22**, 5238 (2021).  
<https://doi.org/10.3390/ijms22105238>
- [21] Shaffer C., Smith B.: Macrocyclic and acyclic supramolecular elements for *co*-precipitation of square-planar gold(III) tetrahalide complexes. *Organic Chemistry Frontiers*, **8**, 1294–1301 (2021).  
<https://doi.org/10.1039/D0QO01562H>
- [22] dos Passos Gomes G., Xu G., Zhu X., Chamoreau L-M., Zhang Y., Bistri-Aslanoff O., Roland S., Alabugin I., Sollogoub M.: Mapping C–H···M interactions in confined spaces: ( $\alpha$ -ICyDMe)Au, Ag, Cu complexes reveal ‘contra-electrostatic H bonds’ masquerading as anagostic interactions. *Chemistry, A European Journal*, **27**, 8127–8142 (2021).  
<https://doi.org/10.1002/chem.202100263>
- [23] Fiorica C., Palumbo F., Pitarresi G., Puleio R., Condorelli L., Collura G., Giammona G.: A hyaluronic acid/cyclodextrin based injectable hydrogel for local doxorubicin delivery to solid tumors. *International Journal of Pharmaceutics*, **589**, 119879 (2020).  
<https://doi.org/10.1016/j.ijpharm.2020.119879>
- [24] Wu S., Cai C., Li F., Tan Z., Dong S.: Deep eutectic supramolecular polymers: Bulk supramolecular materials. *Angewandte Chemie International Edition*, **59**, 11871–11875 (2020).  
<https://doi.org/10.1002/anie.202004104>
- [25] Wei X., Chen D., Zhao X., Luo J., Wang H., Jia P.: Underwater adhesive HPMC/SiW-PDMAEMA/Fe<sup>3+</sup> hydrogel with self-healing, conductive, and reversible adhesive properties. *ACS Applied Materials and Interfaces*, **3**, 837–846 (2021).  
<https://doi.org/10.1021/acsapm.0c01177>

- [26] Smith E., Abbott A., Ryder K.: Deep eutectic solvents (DESs) and their applications. *Chemical Reviews*, **114**, 11060–11082 (2014).  
<https://doi.org/10.1021/cr300162p>
- [27] Soares B., da Costa Lopes A. M., Silvestre A. D. J., Rodrigues Pinto P. C., Freire C. S. R., Coutinho J. A. P.: Wood delignification with aqueous solutions of deep eutectic solvents. *Industrial Crops and Products*, **160**, 113128 (2021).  
<https://doi.org/10.1016/j.indcrop.2020.113128>
- [28] Yu Q., Liang Y., Cheng J., Chen S., Zhang A., Miao M., Zhang D.: Synthesis of a degradable high-performance epoxy-ended hyperbranched polyester. *ACS Omega*, **2**, 1350–1359 (2017).  
<https://doi.org/10.1021/acsomega.7b00132>
- [29] Xie X., Xu X., Jiang Y.: Hydrogen-bonding interaction-driven catechin assembly into solvent-free supramolecular adhesive with antidrying and antifreezing properties. *ACS Applied Polymer Materials*, **4**, 4319–4328 (2022).  
<https://doi.org/10.1021/acsapm.2c00280>
- [30] Zhang Q., Li T., Duan A., Dong S., Zhao W., Stang P.: Formation of a supramolecular polymeric adhesive *via* water-participant hydrogen bond formation. *Journal of the American Chemical Society*, **141**, 8058–8063 (2019).  
<https://doi.org/10.1021/jacs.9b02677>
- [31] Gu C., Peng Y., Li J., Wang H., Xie X-Q., Cao X., Liu C-S.: Supramolecular G4 eutectogels of guanosine with solvent-induced chiral inversion and excellent electrochromic activity. *Angewandte Chemie International Edition*, **59**, 18768–18773 (2020).  
<https://doi.org/10.1002/anie.202009332>
- [32] Zheng J., Fan R., Wu H., Yao H., Yan Y., Liu J., Ran L., Sun Z., Yi L., Dang L., Gan P., Zheng P., Yang T., Zhang Y., Tang T., Wang Y.: Directed self-assembly of herbal small molecules into sustained release hydrogels for treating neural inflammation. *Nature communications*, **10**, 1604 (2019).  
<https://doi.org/10.1038/s41467-019-09601-3>
- [33] Liu M., Liu P., Lu G., Xu Z., Yao X.: Multiphase-assembly of siloxane oligomers with improved mechanical strength and water-enhanced healing. *Angewandte Chemie International Edition*, **57**, 11242–11246 (2018).  
<https://doi.org/10.1002/anie.201805206>
- [34] Liu M., Wang Z., Liu P., Wang Z., Yao H., Yao X.: Supramolecular silicone coating capable of strong substrate bonding, readily damage healing, and easy oil sliding. *Science Advances*, **5**, eaaw5643 (2019).  
<https://doi.org/10.1126/sciadv.aaw5643>
- [35] Floare C., Bogdan M., Tomoia-Coti M., Mocanu A.: <sup>1</sup>H NMR spectroscopic characterization of inclusion complex of desferrioxamine B chelator and β-cyclodextrin. *Journal of Molecular Structure*, **1248**, 131477 (2022).  
<https://doi.org/10.1016/j.molstruc.2021.131477>
- [36] Wang H., Liu H., Cao Z., Li W., Huang X., Zhu Y., Ling F., Xu H., Wu Q., Peng Y., Yang B., Zhang R., Kessler O., Huang G., Wu J.: Room-temperature autonomous self-healing glassy polymers with hyperbranched structure. *Proceedings of the National Academy of Sciences of the United States of America*, **117**, 11299–11305 (2020).  
<https://doi.org/10.1073/pnas.2000001117>
- [37] Zhang M-H., Li C-H., Zuo J-L.: A variable stiffness adhesive enabled by joule heating effect. *Chemical Engineering Journal*, **433**, 133840 (2022).  
<https://doi.org/10.1016/j.cej.2021.133840>
- [38] Liu H., Feng Y., Cao X., Luo B., Liu M.: Chitin nanocrystals as an eco-friendly and strong anisotropic adhesive. *ACS Applied Materials and Interfaces*, **13**, 11356–11368 (2021).  
<https://doi.org/10.1021/acscami.1c02000>
- [39] Dong S., Leng J., Feng Y., Liu M., Stackhouse C. J., Schönhals A., Chiappisi L., Gao L., Chen W., Shang J., Jin L., Qi Z., Schalley C. A.: Structural water as an essential comonomer in supramolecular polymerization. *Science Advances*, **3**, eaao0900 (2017).  
<https://doi.org/10.1126/sciadv.aao0900>
- [40] Zhao Y., Song S., Ren X., Zhang J., Lin Q., Zhao Y.: Supramolecular adhesive hydrogels for tissue engineering applications. *Chemical Reviews*, **122**, 5604–5640 (2022).  
<https://doi.org/10.1021/acs.chemrev.1c00815>
- [41] Liu T., Peng X., Chen Y., Zhang J., Jiao C., Wang H.: Solid-phase esterification between poly(vinyl alcohol) and malonic acid and its function in toughening hydrogels. *Polymer Chemistry*, **11**, 4787–4797 (2020).  
<https://doi.org/10.1039/D0PY00023J>
- [42] Liu H., Geng H., Zhang X., Wang X., Hao J., Cui J.: Hot melt super glue: Multi-recyclable polyphenol-based supramolecular adhesives. *Macromolecular Rapid Communications*, **43**, 2100830 (2022).  
<https://doi.org/10.1002/marc.202100830>



Research article

# Shrinkage restraint forces in oriented PET, PMMA and PET/PMMA blend: Contrasting effects on cooling

John Sweeney\*<sup></sup>, Davide Nocita<sup></sup>, Paul Edward Spencer<sup></sup>, Glen Peter Thompson<sup></sup>,  
Maxims Babenko<sup></sup>, Phillip David Coates<sup></sup>

IRC in Polymer Science and Technology, School of Engineering, Faculty of Engineering and Digital Technologies,  
University of Bradford, BD7 1DP Bradford, UK

Received 13 June 2023; accepted in revised form 31 August 2023

**Abstract.** We have performed shrinkage restraint force measurements on three shape memory polymers of polyethylene terephthalate (PET), polymethyl methacrylate (PMMA) and a blend of the two at a range of temperatures. Observations are made of the change in stress during temperature rise, hold and cooling. All materials show an increase in stress during rise and hold, but on cooling, the three materials behave differently; the PET shows a drop in stress, the PMMA a rise and the blend a much smaller rise. This behaviour correlates with the reversible thermal dimensional change below the shrinkage threshold temperature; the expansion coefficients are negative for PET, positive for PMMA and positive at a lower order of magnitude for the blend. We model the behaviour by supposing that the shrinkage forces are created by prestressed strains effective at long range within a matrix of shorter chains effective at short range. The total stress is the sum of the shrinkage stress and the thermal stress in the matrix. The drops in stress on cooling are modelled using an elastic analysis based on measured elastic moduli and thermal expansion coefficients. For the blend, downward jumps in temperature produce small transient increases in the total stress, leaving it effectively unchanged. This phenomenon and the results of the elastic model for the stress drops imply that the shrinkage stress from the long-range chain network is largely unaffected by the temperature change and so is not entropic.

**Keywords:** shape memory polymer, fiber orientation, static testing, blends, thermomechanical analysis

## 1. Introduction

Shape memory polymers (SMPs) are of continuing interest as their levels of sophistication increase and their field of applications develops [1, 2]. The range of materials now includes polymer nanocomposites [3–5]. Programmable materials that can memorize multiple shapes have been demonstrated [6] that could, in principle, form the basis of devices with complex responses. However, most practical applications use simple ‘one-way’ SMPs. Such a rudimentary SMP is typically amorphous, becoming an SMP by being stretched around its glass transition to induce molecular orientation and then cooled while maintained in its temporary stretched state;

the original or permanent shape can then be recovered by reheating. The shape memory effect is most commonly observed in this way, in the form of changes in shape. Alternatively, the shape on reheating can be physically restrained so that measurable restraint forces are produced instead of shape recovery. Such a force, referred to as ‘shrinkage force’ [7] or as causing ‘recovery stress’ [8], is the basis of operation of some SMP devices, such as shrink-fit tubing for electrical insulation, shrink wrap packaging, and crack closing devices in structural applications [9]. Shrinkage force and its evolution with heating and cooling is the subject of this paper.

\*Corresponding author, e-mail: [j.sweeney@bradford.ac.uk](mailto:j.sweeney@bradford.ac.uk)  
© BME-PT

We report the results of experiments in which specimens of oriented SMPs are held at constant length and heated to temperatures at which the shape memory effect is triggered. The shrinkage forces are monitored as they evolve with time at constant temperature. Specimens are then cooled while held at a constant length, and the shrinkage force evolves further. Since there is no shape recovery, some molecular orientation is retained. As the specimens cool to room temperature, tensile forces develop to levels that can be maintained over long periods of time. These forces may be either lower or higher than those observed before cooling. Here, we quantify them and analyze their physical origin.

## **2. Experimental method**

### **2.1. Materials**

Two commercial grades of polymers were used. A polyethylene terephthalate (PET) material, Dow LIGHTER C93 (Dow Chemical Company, Midland, Michigan, USA), and a polymethyl methacrylate (PMMA), Diakon CMG302 (Lucite International, Mitsubishi Chemical Corporation, Tokyo, Japan), were obtained in granular form. These materials were melt-blended in equal proportions by mass to give a third material, also produced in granular form. According to manufacturers' data, the densities for PET and PMMA are respectively 880 and 1,180 kg/m<sup>3</sup>, to give volume proportions for the blend as PET:PMMA of 57.3:42.7. All three materials were made into SMPs. Before processing, the granules were dried in a vacuum oven overnight.

### **2.2. SMP preparation**

The manufacture of the PET SMP has been described previously [10] and is summarised here. The polymer was formed into circular section fibres. First, it was extruded using a single-screw Killion S1748 25 mm extruder (Arlington Machinery, USA) operating at a screw speed of 15 rpm and a screw pressure of 30 bar. The maximum melt temperature in the extruder was 280 °C, and the die head was at 270 °C. The material was extruded through a circular die of 4 mm internal diameter and hauled off at 5 m/min. On exit from the die, it was cooled in a glycerol bath at room temperature. The final diameter of the cooled product was 1.8 mm. The next stage of the process was to introduce molecular orientation. The technique of die-drawing was used, as described for polymers by Coates and Ward [11]. Fibre

at room temperature was pulled through a 1.5 m length fan-assisted oven. On exit from the oven, it entered a converging conical die with a cone angle of 30° and final diameter of 1 mm, held at a constant temperature. After the die, the fibre was gripped by a caterpillar-type haul-off device operating at a constant linear speed corresponding to a mean strain rate of 17 s<sup>-1</sup>. To maximize the level of orientation, both the oven and die temperatures were lowered from 80 °C to as low a level consistent with an undamaged oriented product; temperatures of 70 and 80 °C were identified in this way for the oven and die, respectively. After exiting the die, further drawing took place during cooling between the die and the caterpillar, resulting in a final diameter of 0.9 mm, corresponding to a draw ratio of 4.0. The circular section was chosen on the basis of its robustness for the planned end use as bundles of fibres in crack-closing devices [10].

A similar two-stage process was used to produce SMP from PMMA. A Thermo 16 mm extruder was used, operating at a screw speed of 50 rpm and pressure of 70 bar. The maximum melt temperature and the die head temperature were both 210 °C. The material was extruded through a rectangular section die with dimensions 8×0.5 mm and hauled off at 0.5 m/min. The extruded tape was collected directly onto speed-controlled rollers at room temperature. In a second process, the tape passed through the 1.5 m oven at 115 °C and was then die-drawn through a rectangular section converging die held at the same temperature to give a drawn material of section 5.1×0.31 mm, corresponding to a draw ratio of 2.4. As with the PET, the draw speed and temperatures of the oven and die were chosen to produce the highest level of orientation, with the draw speed corresponding to a strain rate of 9 s<sup>-1</sup>. The rectangular section was chosen as a convenient form for tensile testing. The PET and PMMA materials were blended using a twin-screw Prism TSE 25/LD co-rotating twin-screw extruder (Thermo Fisher Scientific Inc., USA). Equal masses of granules of the two polymers were mixed together and fed into the extruder's nitrogen-filled hopper. The extruder operated at a screw speed of 50 rpm and screw pressure 35 bar. The maximum melt temperature was 250 °C, and the die head was 260 °C. The blended material was extruded through an 8.0×0.5 mm rectangular die at a haul-off speed of 2 m/min. The extruded tape was collected directly onto speed-controlled rollers at room temperature.

The rectangular section was chosen as a convenient form for tensile testing.

Molecular orientation was applied to 75 mm lengths of the blended material by tensile stretching within a fan oven at 90 °C using an Instron 5568 testing machine. The constant stretching speed was set to give an initial strain rate of  $0.011 \text{ s}^{-1}$ , and the final extension corresponded to an extension ratio of 3.1. The temperature and rate were arrived at on the basis of achieving the highest possible extension ratio.

### 2.3. Dynamic mechanical thermal analysis measurements

Dynamic mechanical thermal analyses (DMTA) measurements were carried out with a TA Instruments Q800 DMA device using tensile grips. For the elimination of errors in strain measurement resulting from thermal expansion of the loading system, the instrument was calibrated with a stainless steel standard before each test, as recommended by the manufacturer.

To study the thermal expansion (or contraction) behaviour, we used the DMTA in controlled force mode, with a pre-load and constant static force of 0.05 N and applied a temperature ramp of 5 °C/min from 28 to 100 °C. The samples were free to move along the orientation axis, as opposed to the restraint applied during shrinkage tests (see Section 2.5.).

For the determination of the visco-elastic response to oscillatory stress and strain and to correlate them with the observed blend morphologies, we used the DMTA in multi-frequency-strain mode, applying a temperature ramp of 3 °C/min from 28 to 170 °C, constant frequency of 10 Hz and a tensile displacement amplitude of 15  $\mu\text{m}$ . These were found to be the optimal test conditions for a fair comparison between undrawn and drawn samples, considering the geometry and the thickness of the specimens and their difference in elastic modulus.

### 2.4. Stress-strain measurements

We performed uniaxial tensile tests to measure elastic modulus using an Instron 5568 testing machine (Instron, High Wycombe, Bucks, UK). Specimens of oriented polymer fibre or strip of 250 mm gauge length were stretched at room temperature at low speeds corresponding to thermally induced rates of strain at 5 °C/min; these were  $2.1 \cdot 10^{-6} \text{ s}^{-1}$  for PET and  $1.5 \cdot 10^{-6} \text{ s}^{-1}$  for PMMA. For modulus measurement at higher rates, 100 mm specimens were tested

at  $8.33 \cdot 10^{-3} \text{ s}^{-1}$  at a range of temperatures from room (21–23 °C) to 90 °C.

### 2.5. Shrinkage force measurements

We have measured the shrinkage restraint forces using an apparatus consisting of a small  $90 \times 90 \times 40 \text{ mm}$  oven containing a single fibre or tape specimen that is held in grips that are situated outside the oven, one of which is connected to a load cell (see Figure 1). Since the grips are outside the oven, they remain at room temperature and do not contribute any thermal strain to the system. The chamber was heated by compressed air at a controlled temperature, and both the force and temperature were monitored. Temperatures were measured using K-type thermocouples with beads within 1 mm of the centre of the specimen gauge length. One of these thermocouples provided the control for a Eurotherm 3200 series controller (Eurotherm Limited, UK), by means of which temperature was raised at a constant rate of 5 °C/min and held at a constant level for a prescribed time. The specimen was then cooled at a set rate of 5 °C/min, though since there was no active cooling, the actual rate lessened progressively once the temperature had fallen to around 50 °C. Forces were monitored throughout the experiment using a 1 kN capacity load cell and transducer indicator (Omega Engineering Ltd. UK) with output to a PC via a Pico TC-08 data logger (Pico Technology, UK) with data capture at 1 Hz. Thermocouple measurements were input into the same data logger. The uniformity of the air temperature close to the specimen was investigated by placing thermocouples within 1 mm of the specimen at either end of its

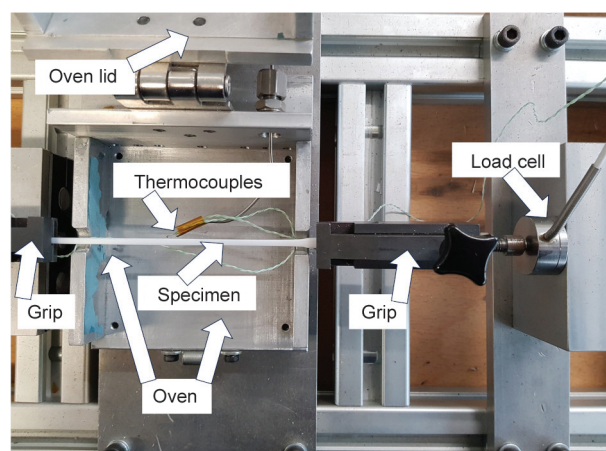


**Figure 1.** Shrinkage force measurement apparatus showing open oven with blend tape specimen in situ and load cell on the right.

gauge length within 5 mm of the oven exit holes; the specimen centre and end positions were found to differ by 0.5 °C or less.

## 2.6. Differential scanning calorimetry measurements

Differential scanning calorimetry (DSC) tests were performed using a TA Instruments Discovery DSC, using standard Al pans and N<sub>2</sub> gas purge. Samples of approximately 10 mg weight were subject to subsequent heating, cooling and second heating cycles at a rate of 10 °C/min: we applied temperature ramps from 40 to 300 °C, from 300 to –80 °C and then from –80 to 300 °C. For the oriented PET and blend materials, the crystallinity was calculated from the normalized melt enthalpy peak, using the value for crystalline PET of 140 J/g [12].

## 2.7. Scanning electron microscopy

Scanning electron microscopy (SEM) images were obtained with a FEI Quanta 400 (FEI Company, USA), operating in low vacuum mode and at 10 or 15 kV. Samples were cryo-fractured using liquid N<sub>2</sub> to observe brittle fracture surfaces. Secondary electrons with large field detector (LFD) and backscattered electrons with solid state detector (SSD) modes were both used to investigate the morphology of PET-PMMA blends before and after the drawing process.

## 3. Results and discussion

### 3.1. Thermal expansion and contraction

In Figure 2, we show the thermal strains that arise for unrestrained specimens of oriented polymer measured in Section 2.3. In all cases, we see the highly negative slopes associated with shape memory that develop after a threshold temperature has been reached. At lower temperatures below this threshold, the slopes are lower in absolute value and may be associated with a coefficient of linear expansion. For oriented polymers, the coefficients differ depending on the direction with respect to the axis of orientation, and can be either positive or negative [13]. The thermal expansion along the draw axis is of interest here.

In the case of oriented PET, the pre-shrinkage expansion coefficient along the draw axis can have negative values [14, 15] when there is a significant level of crystallinity. These values become more negative as the extension ratio and crystallinity increase. This is consistent with our observation for PET in Figure 2. In the temperature range of 28–40 °C, the result for

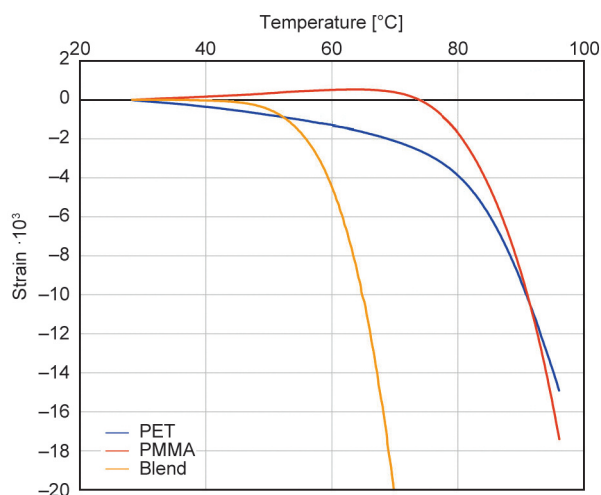


Figure 2. Free thermal expansion and contraction of the three materials.

PET in Figure 2 corresponds to a coefficient of  $-2.54 \cdot 10^{-5} \text{ °C}^{-1}$ . This can be compared with that of Choy *et al.* [15] for a PET at the extension ratio of 4.8 and 26% crystallinity of around  $-6 \cdot 10^{-6} \text{ °C}^{-1}$  at room temperature. We would expect our material to have a more negative expansion coefficient as it has a similar extension ratio of 4.0 and, according to DSC testing, a higher crystallinity of 41%, though the materials are not strictly comparable because of their different grades and orientation processes.

For PMMA, the pre-shrinkage expansion coefficient in the temperature range 28–55 °C obtained from the data of Figure 2 is  $1.76 \cdot 10^{-5} \text{ °C}^{-1}$ ; the positive value is consistent with there being no crystallinity detected by DSC. It can be compared with a published value for PMMA oriented to an extension ratio of 3.0 of approximately  $4 \cdot 10^{-5} \text{ °C}^{-1}$  [16]. This is reasonably comparable to our finding given its different grade, orientation process and extension ratio of 2.4.

With the blend, shrinkage begins at a much lower temperature threshold. For the pre-threshold temperature range of 28–35 °C, the thermal expansion coefficient is much lower in magnitude than either of the constituent polymers, with a value of  $4.4 \cdot 10^{-6} \text{ °C}^{-1}$ . DSC testing of the blend has given a crystallinity for the PET component of 26%, considerably lower than for the pure oriented PET material. This suggests that the thermomechanical properties of the blend cannot be simply deduced from the properties measured for its components.

### 3.2. Blend morphology

In Figure 3a we show a fracture surface of undrawn blend material. This clearly shows phase separation

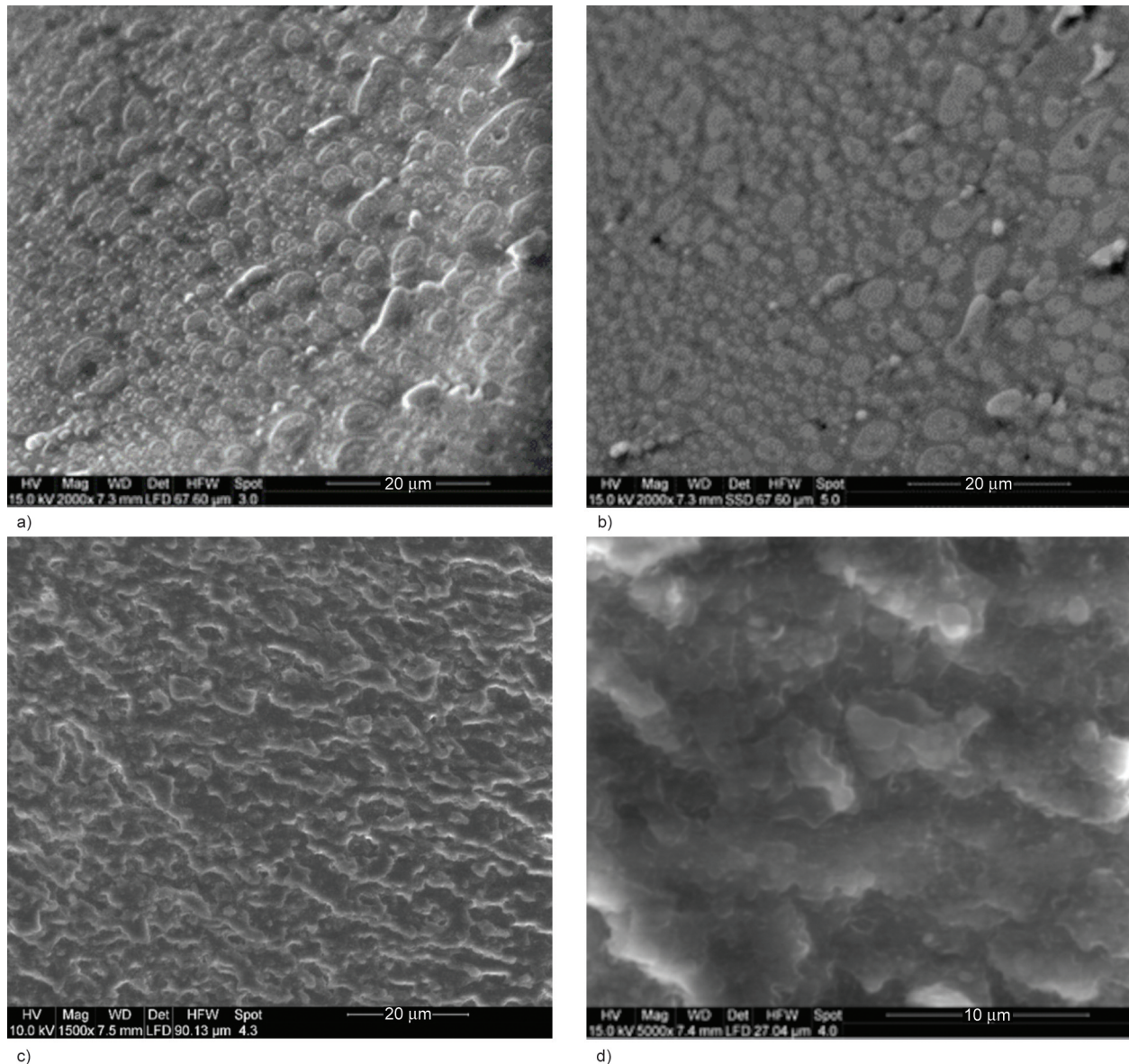


**Figure 3.** SEM images. a) Undrawn blend surface, showing roughly circular domains of PET within a PMMA matrix. b) The same region of interest as Figure 3a, image produced with backscattered electrons (both 2000× magnifications), c) drawn blend with rough, brittle fracture surface (500× magnification), d) drawn blend at 5000× magnification.

evidence, with large PET domains of greater density (as demonstrated by the backscattered electron image in Figure 3b), as would be expected for an immiscible blend with a large difference in melt viscosity between the components. A similar morphology is reported for PET/PMMA blends by Mallette *et al.* [17].

For the oriented material, shown in Figure 3c, we observed a much different fracture surface, driven by the presence of smaller polyester domains (Figure 3d): the drawing process appears to be forcing some break-up of the PET domains and consequent morphological rearrangement. Similar morphologies have been reported by Dewangan and Jagtap [18] for a

PET/PMMA blend of the same weight ratio (50/50) compatibilized with a poly(*tert*-butyl acrylate)-*b*-poly(methyl methacrylate) (PtBA-*b*-PMMA) amphiphilic block copolymer.

In Figure 4, we compare DMTA scans of loss modulus for undrawn and drawn blend and drawn blend that has also been subjected to shrinkage force testing (17.5 h at 70 °C – see Figure 9). For the undrawn case, there are maxima at 81 and 112 °C. Previously, DSC studies on the oriented PET product used in this study have yielded a glass transition temperature in the range of 70–78 °C [10]. DSC testing using the method described above in Section 2.6. for the pure oriented PMMA material gave a glass transition temperature

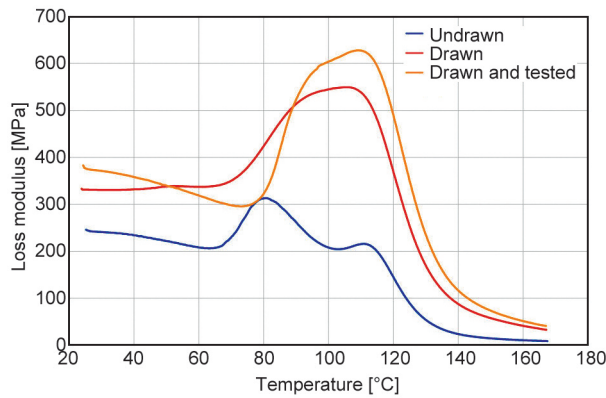


**Figure 4.** DMTA temperature sweeps of loss modulus for the blend, showing distinct minima for the undrawn material.

of 113 °C. Thus, for the undrawn blend, we see a consistency between the loss modulus maxima and the glass transitions of the separate phases. For the drawn materials, only a single maximum is exhibited, providing further evidence of a morphological rearrangement, leading to finer dispersion of the PET phase with reduced domain size.

### 3.3. Shrinkage force

#### 3.3.1. PET

Shrinkage stresses for the oriented PET material were measured for the range of temperature histories shown in Figure 5a, with each one featuring an interval at constant hold temperature (60, 65, 70, 75, 80, 85 and 90 °C) for 17.5 h followed by cooling. The stresses are shown in Figure 5b. They continue to increase gradually after the hold temperature has been reached, apparently approaching an asymptotic value, and decrease to a steady level on cooling. The maximum stress increases with hold temperature up to 85 °C and then drops at 90 °C as stress viscoelastic effects appear to become significant. We have thus established the temperature at which the recovery

stress is a maximum and the SMP most effective. The lowering of stress at 90 °C may reflect the beginning of disentanglement in the long-range chain network. The development of shrinkage stress with time has been observed previously for oriented PET by Lim and Kim [19] and for oriented polyethylene terephthalate glycol (PETG) by Shih [20].

Some level of stress is detectable immediately on heating, as we would expect from the negative thermal expansion coefficient reported in the previous section, but remains small below 60 °C. Stress at the early stages of heating is shown in Figure 6. We associate the low initial gradient below 50 °C in this figure with a negative thermal expansion (see Section 3.1.). At around 60 °C, there is a change to a higher slope, which we associate with the shape memory effect. Previously, DSC studies on this oriented product have yielded a glass transition temperature in the range 70–78 °C [10]. Further DSC testing using the method described above in Section 2.6. gives a result consistent with the higher end of this range. We cannot make a precise distinction in these observations between force generated by reversible

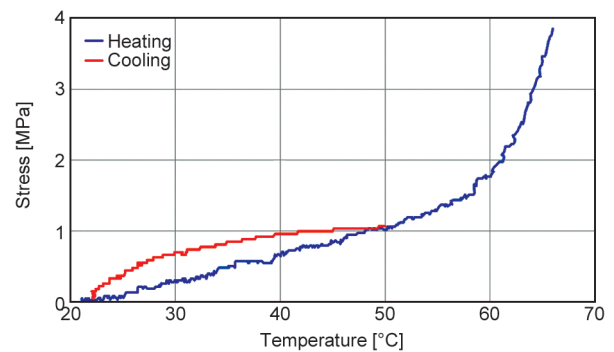


**Figure 6.** Initial development of stress in PET as the temperature is raised at 5 °C/min (heating curve). The cooling curve shows the temperature on cooling from 50 °C.

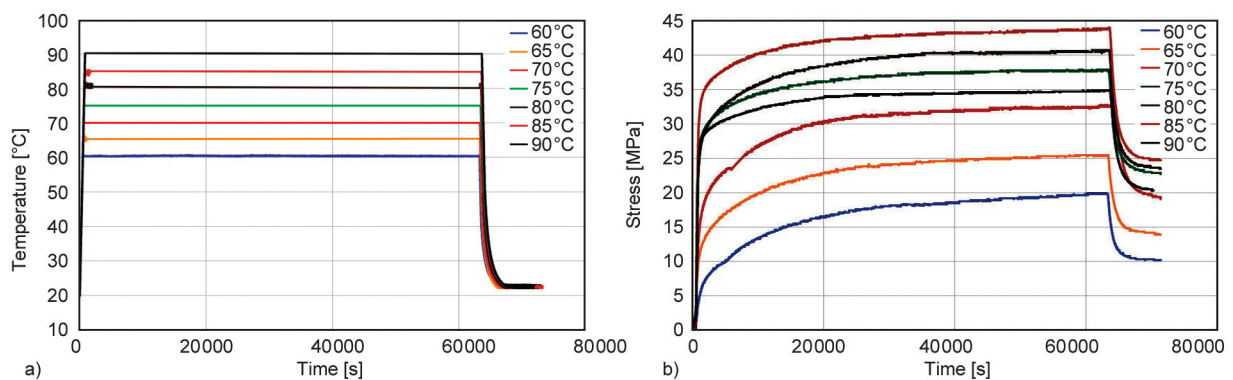


**Figure 5.** a) Temperature histories in PET shrinkage tests. Legend denotes hold temperatures. b) Evolution of PET shrinkage stress with time. Legend denotes hold temperatures in Figure 5a.

thermal contraction and that from shape memory associated with irreversible changes. Examples of retractive forces of oriented glassy polymers at below glass transition temperature have been reported by Cheng and Wang [21].

Also, in Figure 6, we show the effect of heating to 50 °C followed by cooling. The stress falls on cooling, showing that the thermal contraction effect is reversible, at least under these conditions of fixed specimen length.

### 3.3.2. PMMA

The same method was used as with PET, but shape memory forces were observable over a narrower temperature range. Temperature histories are shown in Figure 7a, and the related shrinkage forces are shown in Figure 7b. Stresses are generally lower than with PET and are at similar levels as those reported for oriented PET by Wright *et al.* [22]. Except at the highest temperature, stresses increase gradually after the hold temperature is reached, as with PET. At 85 °C, the stress reaches an early peak and then begins to relax, indicating a significant degree of viscoelasticity and possible chain disentanglement. The maximum stress is at 82.5 °C. On cooling, this material shows a stress increase in contrast to the decrease seen in PET.

DSC measurement yielded a glass transition temperature of 114 °C, significantly higher than the lowest temperature – 75 °C – at which shrinkage force was detected. This is an effect similar to that seen in PET. There is no significant shrinkage stress below 75 °C. In Figure 8, we show the initial development of stress with temperature averaged over the experiments of Figure 7 together with the results for the other two materials. At first, the PMMA stress is

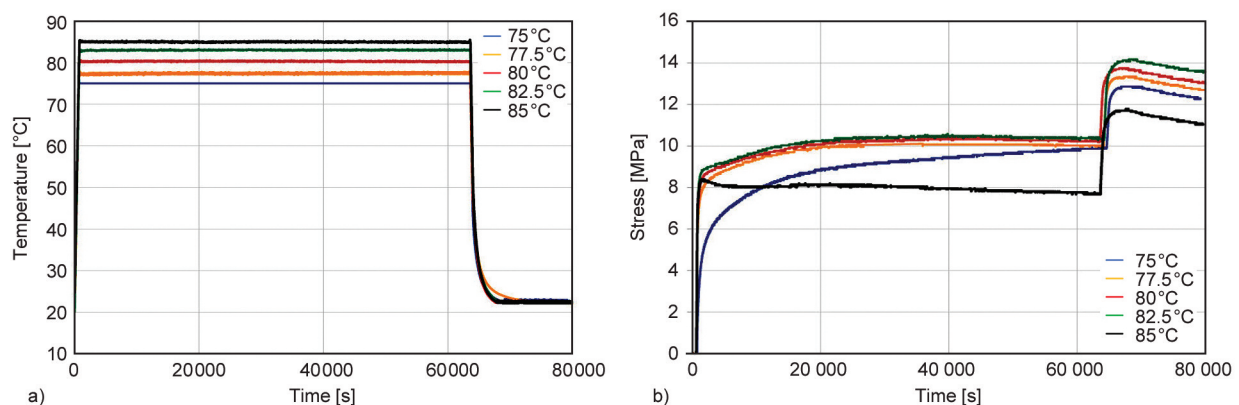


Figure 7. a) Temperature histories in PMMA shrinkage tests. Legend denotes hold temperatures. b) Evolution of PMMA shrinkage stress with time. Legend denotes hold temperatures in Figure 7a.

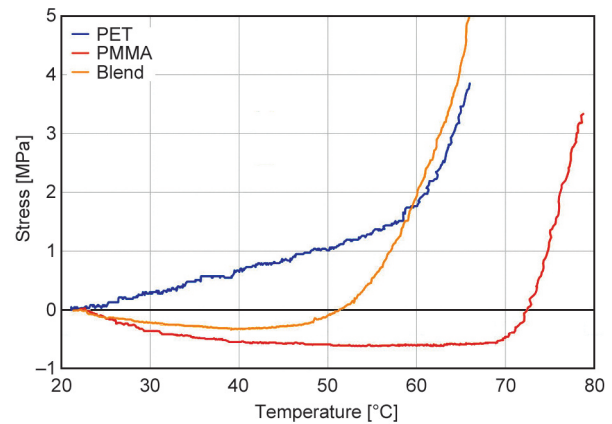


Figure 8. Initial development of stress in PMMA and in the PET/PMMA blend as the temperature is raised at 5 °C/min, with the PET curve shown for comparison.

negative, corresponding to a positive coefficient of thermal expansion (see Section 3.1.). This stress is consistent with the Euler buckling load. Stress begins to grow at around 70 °C, but the beginning of shape memory cannot be located accurately as there is a constant negative stress, corresponding to a buckled specimen, between 50 and 70 °C.

The difference between PET and PMMA behaviour on initial heating – positive stress for PET and negative for PMMA, as shown in Figure 8 – is consistent with their thermal expansion behaviour and compares directly to the difference in cooling behaviour – a stress drop for PET and an increase for PMMA.

### 3.3.3. PET/PMMA blend

Shrinkage stress measurements were made on the blend material using the same method. The temperature histories and stresses are shown in Figure 9, respectively. Broadly, the stress levels at the hold temperatures lie intermediately between those of PET

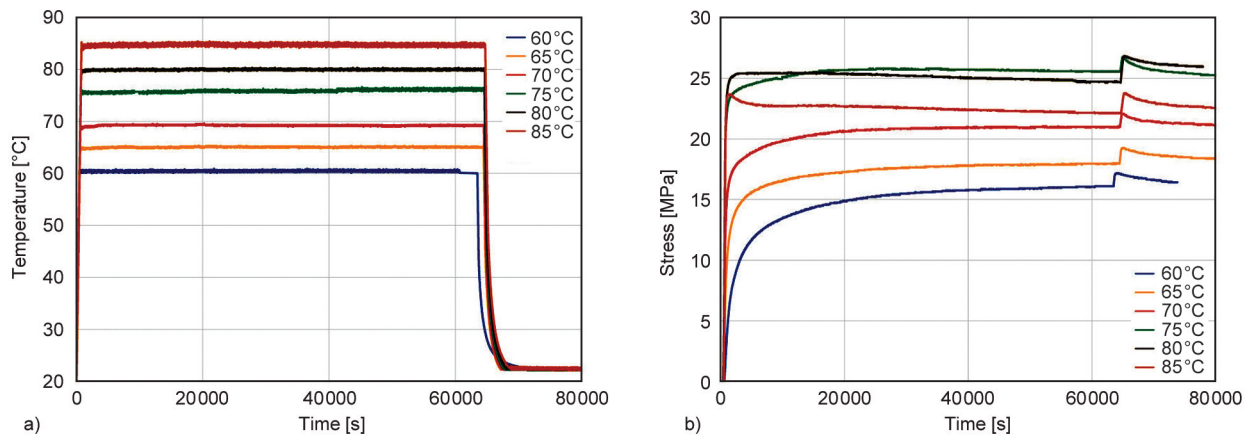


**Figure 9.** a) Temperature history for PET/PMMA blend. Legend denotes hold temperatures. b) Shrinkage stresses for PET/PMMA blend. Legend denotes hold temperatures in Figure 9a.

and PMMA. Stress changes on cooling are relatively small and positive; this correlates with the small and positive thermal expansion coefficient reported in Section 3.1. The shape of the recovery stress curve at 85 °C resembles that of PMMA at the same temperature, suggesting a similar mechanism of disentanglement in the long-range chain network.

The initial stages of stress development are shown in Figure 8. The initial negative stress corresponds to the initial positive thermal expansion in Figure 2. The increase in shrinkage stress between 40 and 50 °C corresponds to the beginning of shrinkage in Figure 2.

### 3.4. Interpretation

In all cases, shrinkage force increases with time as the specimen temperature is held constant. We can interpret this behaviour in similar terms to those outlined by Cheng and Wang [21], in which a long-range network of polymer chains supplies the shrinkage force while acting within a matrix of polymer chains with only short-range effects. In the case of the semicrystalline oriented polymer, some or all of the long-range chains may be identified with taught tie molecules [23]. The matrix of short chains applies localized shear forces to the prestressed network chains and inhibits the transmission of tension through the network; the network tension is partially equilibrated locally by compression of the matrix. The matrix chains act viscoelastically so that the restraint forces on the long-range chains relax with time. This corresponds to the gradual increase of the observed shrinkage stress with time when the temperature is held constant. We may visualize the long-range chains steadily evolving tubes of free volume around them. The

viscoelastic properties of the short-range chain matrix ensure that the evolution of shrinkage stress is faster at higher temperatures, as observed.

The magnitudes of the recovery stress for the blend lie between those for PMMA and those for PET. The circular zones of PET material in the undrawn blend become elongated on drawing (see Figure 3). As a result, their surface area to volume ratio increases, leading to stronger coupling between the two phases and to mechanical behaviour that more closely resembles that of a single material. This is reflected in the DMTA results of Figure 4, where the double peaks of loss modulus in the undrawn blend are replaced by a single peak. The long-range chain networks within the PET domains give rise to tensile forces when heated, and the coupling to the PMMA phase is sufficient to produce shrinkage stresses that are around twice those observed in the PMMA results (see Figures 7b and 9b).

Changes in stress on cooling correlate in sign and magnitude with the thermal expansion coefficients, corresponding to reversible thermal strains at pre-shrinkage temperatures. We associate these changes with the short-range chain matrix, which we envisage acts in parallel with the shape memory forces arising in the long-range chain network. A rigorous model of stress on cooling would include the viscoelastic behaviour of the short-chain matrix. However, a realistic estimate of the stress change on cooling may be obtained using a pseudo-elastic analysis, provided the modulus is measured at a strain rate comparable with that during cooling. This method approximately accounts for the loss in stress arising from stress relaxation during cooling. During cooling, thermal strains will be induced at all temperatures;



the effectiveness of the elastic model we propose depends on the rate at which associated stresses relax. When cooling from higher test temperatures, viscoelastic effects will become more important, and we would expect the model to become less effective. For stress change  $\sigma$ , modulus  $E$ , expansion coefficient  $\alpha$  and temperature change  $T$ , with zero strain, Hooke's law gives (Equation (1)):

$$0 = \frac{\sigma}{E} + \alpha T \quad (1)$$

During cooling,  $E$  varies with  $T$  while  $\alpha$  remains constant, and the stress change is governed by Equation (2):

$$d\sigma = -E(T)\alpha dT \quad (2)$$

For a temperature drop from  $T_H$  to  $T_L$ , the stress change  $\Delta\sigma$  is given by Equation (3):

$$\Delta\sigma = -\alpha \int_{T_H}^{T_L} E(T) dT = \alpha \bar{E}(T_L, T_H)(T_H - T_L) \quad (3)$$

where the mean value of  $E$  between the temperatures  $T_H$  and  $T_L$  is given by Equation (4):

$$\bar{E}(T_L, T_H) = \frac{\int_{T_L}^{T_H} E(T) dT}{(T_H - T_L)} \quad (4)$$

With this model, we assume that the matrix of short-range chains behaves as a solid with constant expansivity throughout the cooling process. For both PET and PMMA, small strain (up to 0.5%) linear stress-strain behaviour was measurable over the range of test temperatures to give modulus values varying with temperature in an essentially linear manner as shown in Figure 10. Values of  $E$  were obtained by tensile testing using the method of Section 2.4. Applied strain rates were equivalent to cooling at 5 °C/min, which is the set rate; this gives strain rates of  $2.1 \cdot 10^{-6}$ ,  $1.5 \cdot 10^{-6}$  and  $3.7 \cdot 10^{-7} \text{ s}^{-1}$  for the PET, PMMA and blend, respectively. This approximates to the experimental conditions under which there is no active cooling, causing the rate to slow below the set rate at low temperatures. For reasons of practicality, the blend modulus was obtained at  $2.1 \cdot 10^{-6} \text{ s}^{-1}$ . Strain rate sensitivity was explored by testing at room temperature at the higher rate of  $8.3 \cdot 10^{-3} \text{ s}^{-1}$ . This showed no significant effect on the modulus value for PET or the blend, and values for PMMA increased by 16% at the higher rate.

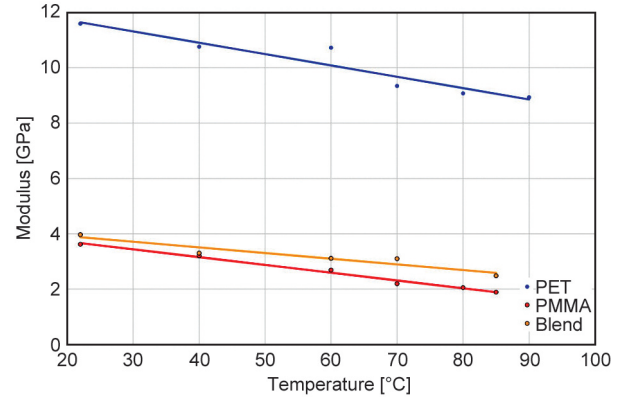


**Figure 10.** Temperature dependence of mean values of modulus for the three materials.

Values of  $\alpha$  are those given in Section 3.1. for the three materials, and values of  $\Delta T$  correspond to the temperature drops in Figures 5a, 7a and 9a. Values of  $\bar{E}$  were obtained using Equations (4), integrating using the fitted linear temperature dependence. The effect of experimental error on the values of  $\bar{E}$  was evaluated via the statistics associated with the linear fits shown as averaged points in Figure 10. For each material, temperature dependence was assumed to be in the form (Equation (5)):

$$E(T) = E_0 + mT \quad (5)$$

The raw data was fitted to give optimum values of the intercept  $E_0$  and the gradient  $m$ , which we label  $E_c$  and  $m_c$ , respectively. The LINEST function in Excel [24] also provides their respective standard errors  $\sigma_E$  and  $\sigma_m$ . This data enabled the calculation of 95% confidence intervals for both these quantities using Student's  $t$ -distribution [25]. The confidence interval for  $E_0$  is given by Equation (6):

$$[E_c - \sigma_E t(0.05), E_c + \sigma_E t(0.05)] = [E_c - \Delta E, E_c + \Delta E] \quad (6)$$

and for  $m$  (Equation (7)):

$$[m_c - \sigma_m t(0.05), m_c + \sigma_m t(0.05)] = [m_c - \Delta m, m_c + \Delta m] \quad (7)$$

where  $t(0.05)$  is the value of the two-tailed  $t$  variable for the appropriate number of degrees of freedom. Values of intercept and gradient corresponding to the limits of the confidence intervals were used to calculate  $\bar{E}$  from Equation (4), and thus the upper and lower limits for  $\Delta\sigma$  are from Equation (3). For all materials, the error associated with the thermal

expansion  $\alpha$  is negligible compared with that associated with  $\bar{E}$ , and so the constant values of Section 3.1. are used in Equation (3). Parameter values are shown in Table 1.

The observed and modelled stress changes are shown in Figure 11; central values are for  $E_0 - E_c$  and  $m - m_c$ , and the upper and lower estimates are as explained above. In the case of PET, the experimental points lie between the upper and lower estimates, suggesting that uncertainties in the modulus data are responsible for much of the discrepancy in the model prediction. However, the low-stress drop at the highest temperature appears to have a physical origin, such as disentanglement of the long-range chain network at the post-glass transition test temperature of 90 °C. The blend results are generally realistic. The gradients of the estimates for the PMMA stress drop are low compared with the experimental result. The overall impression is that, while this pseudo-elastic approach neglects details of time-dependent effects, its performance demonstrates that the stress drops are directly driven by reversible thermal expansion or contraction.

The results of the pseudo-elastic model suggest that the shrinkage stress arising from the shape memory effect stays constant as the temperature drops and that the stress we observe on cooling is the sum of this stress and the change arising from the cooling of the

Table 1. Parameters for statistical analysis.

Material	$E_c$ [GPa]	$\Delta E$ [GPa]	$m_c$ [GPa/°C]	$\Delta m$ [GPa/°C]	$\alpha$ [°C <sup>-1</sup> ]
PET	12.64	1.10	-42.33	16.59	-2.54·10 <sup>-5</sup>
PMMA	4.28	0.17	-28.11	2.92	1.76·10 <sup>-5</sup>
Blend	4.32	0.43	-20.62	7.91	4.40·10 <sup>-6</sup>

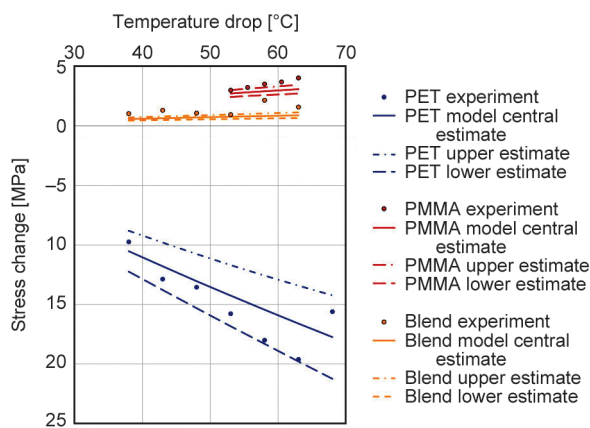


Figure 11. Observed stress changes on cooling to room temperature at the end of shrinkage tests compared with results of a pseudo-elastic model.

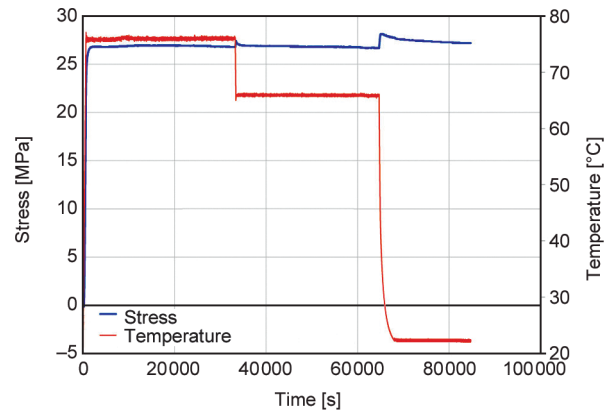


Figure 12. Shrinkage stress for PET/PMMA blend with accompanying temperature drops.

short-range chain network. With the PET/PMMA blend, the low coefficient of thermal expansion allows for some clear observations. In Figure 12, we show shrinkage stress for the blend as the temperature drops rapidly from 80 to 65 °C and then from 65 °C to room temperature. There is little change in shrinkage stress at these points and the small changes that we see decay quite rapidly. In contrast, there would be a substantial change in response to an increase in temperature of a similar size (see Figure 9b). Similarly, in Figure 13, we show the effects of repeated cooling and heating of the blend, which leaves the shrinkage stress relatively unperturbed. The general finding is that once a shrinkage force has been established by heating, it is largely unaffected by cooling. Reverting to our interpretation of long-range chains within tubes of free volume, this corresponds to the permanency of the viscoelastic dimensional changes in the matrix of short-range chains so that the tubes of free volume do not shrink as the temperature drops.

The small changes in shrinkage stress that accompany significant changes in absolute temperature (up

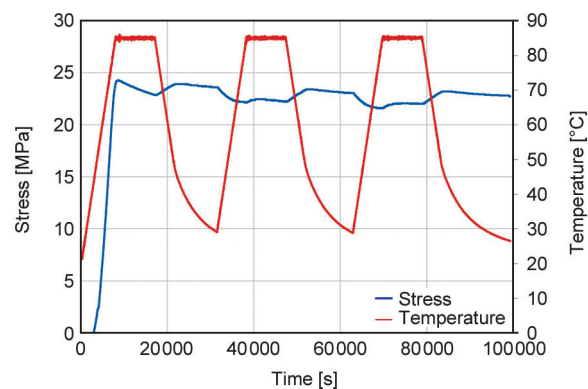


Figure 13. Shrinkage stress for PET/PMMA blend with repeated cooling and heating.

to 20% in [Figures 12 and 13](#)) show that the shrinkage stress is not proportional to absolute temperature and, therefore, not entropic. This is consistent with the work of Cheng and Wang [21] on stress recovery in polymer glasses, in which they specifically rule out rubber elasticity as the source of stress recovery. Non-entropic recovery stress has also been observed by Kim *et al.* [26] while working with an epoxy system.

#### 4. Conclusions

Oriented PET, PMMA and an oriented PET/PMMA blend have been subjected to measurements of shrinkage restraint forces while heated to a constant hold temperature and held at constant length. Stresses develop similarly with time for all materials while heating is maintained, but on cooling, the behaviour contrasts. PET shows a drop in stress on cooling, PMMA rises in stress, and the blend rises in stress to a much smaller extent than the PMMA. This behaviour correlates with the thermal expansion at temperatures below the onset of shrinkage, for which the expansion coefficients are negative for PET, positive for PMMA and positive but around two orders of magnitude lower for the blend. The relationship between stress drop and thermal expansion is established quantitatively using a pseudo-elastic model. The effectiveness of the pseudo-elastic model is consistent with the stress being the sum of two components: the major tensile stress associated with shape memory and a network of polymer molecules with long-range effects; and a matrix of chains with effects at relatively short range. This is an arrangement similar to that suggested by Cheng and Wang [21]. The latter matrix is a viscoelastic medium that inhibits the transmission of stress through the long-range network, with the degree of inhibition fading with time, accompanying the gradual rises in shrinkage stress. The stress on cooling can be interpreted as the thermoelastic behaviour of the short-range chain matrix.

The blend has a low coefficient of thermal expansion and, in line with the pseudo-elastic model, the stress changes with cooling are small. Once a shrinkage stress has been established by heating, cooling while maintaining restraint produces negligible change in it. This shows clearly that the shrinkage force is not proportional to the absolute temperature and implies that it is not entropic in origin.

#### Acknowledgements

Funding: This research was funded in part by the UKRI-EPSC Resilient Materials 4 Life (RM4L), grant number EP/P02081X/1.

The authors acknowledge use of the facilities and the assistance of Stuart Fox in the Analytical Centre at the University of Bradford for the SEM imaging.

#### References

- [1] Zende R., Ghase V., Jamdar V.: A review on shape memory polymers. *Polymer-Plastics Technology and Materials*, **62**, 467–485 (2023).  
<https://doi.org/10.1080/25740881.2022.2121216>
- [2] Hager M. D., Bode S., Weber C., Schubert U. S.: Shape memory polymers: Past, present and future developments. *Progress in Polymer Science*, **49–50**, 3–33 (2015).  
<https://doi.org/10.1016/j.progpolymsci.2015.04.002>
- [3] Gao H., Li J., Kong F., Wang Z., Xu F.: Interpenetrating shape memory polyimide-polyaniline composites with electrical conductivity. *Polymer Composites*, **44**, 4134–4141 (2023).  
<https://doi.org/10.1002/pc.27385>
- [4] Yao J., Ma S., Zhang J., Wang Y., Wang C., Zhou H., Chen C., Liu G.: Multiple shape memory effects of polyimide nanocomposites based on octa(aminophenyl)silsequioxanes. *Express Polymer Letters*, **15**, 433–444 (2021).  
<https://doi.org/10.3144/expresspolymlett.2021.37>
- [5] Kamyab A., Ghasemi-Ghalebahman A., Fereidoon A., Khonakdar H. A.: Shape memory and mechanical properties of polycaprolactone/polypropylene carbonate nanocomposite blends in the presence of G-POSS nanoparticles. *Express Polymer Letters*, **15**, 473–489 (2021).  
<https://doi.org/10.3144/expresspolymlett.2021.40>
- [6] Pilate F., Toncheva A., Dubois P., Raquez J-M.: Shape-memory polymers for multiple applications in the materials world. *European Polymer Journal*, **80**, 268–294 (2016).  
<https://doi.org/10.1016/j.eurpolymj.2016.05.004>
- [7] Long S. D., Ward I. M.: Shrinkage forces studied of oriented polyethylene terephthalate. *Journal of Applied Polymer Science*, **42**, 1921–1929 (1991).  
<https://doi.org/10.1002/app.1991.070420715>
- [8] Maksimkin A. V., Kaloshkin S. D., Zadorozhnyy M. V., Senatov F. S., Salimon A. I., Dayyoub T.: Artificial muscles based on coiled UHMWPE fibers with shape memory effect. *Express Polymer Letters*, **12**, 1072–1080 (2018).  
<https://doi.org/10.3144/expresspolymlett.2018.94>
- [9] Maddalena R., Sweeney J., Winkles J., Tuinea-Bobe C., Balzano B., Thompson G., Arena N., Jefferson A.: Applications and LCA of shape memory PET in concrete for crack closure. *Polymers*, **14**, 933 (2022).  
<https://doi.org/10.3390/polym14050933>

- [10] Teall O., Pilegis M., Sweeney J., Gough T. D., Thompson G. P., Jefferson A., Lark R., Gardner D.: Development of high shrinkage polyethylene terephthalate (PET) shape memory polymer tendons for concrete crack closure. *Smart Materials and Structures*, **26**, 045006 (2017). <https://doi.org/10.1088/1361-665X/aa5d66>
- [11] Coates P. D., Ward I. M.: Die drawing: Solid phase drawing of polymers through a converging die. *Polymer Engineering and Science*, **21**, 612–618 (1981). <https://doi.org/10.1002/pen.760211007>
- [12] Li L., Huang R., Lu A., Nie F., Hong S., Wang C., Zhong Y., Wang D.: High pressure crystallized poly(ethylene terephthalate): High crystallinity and large extended-chain crystals. *Polymer*, **41**, 6943–6947 (2000). [https://doi.org/10.1016/S0032-3861\(00\)00024-0](https://doi.org/10.1016/S0032-3861(00)00024-0)
- [13] Smith K. J.: Thermal expansion of oriented glassy polymers. *Polymer Engineering and Science*, **24**, 205–210 (1984). <https://doi.org/10.1002/pen.760240307>
- [14] Pereira J. R. C., Porter R. S.: Extrusion drawn amorphous and semicrystalline poly(ethylene terephthalate): 3. Linear thermal expansion analysis. *Polymer*, **25**, 869–876 (1984). [https://doi.org/10.1016/0032-3861\(84\)90020-X](https://doi.org/10.1016/0032-3861(84)90020-X)
- [15] Choy C. L., Ito M., Porter R. S.: Thermal expansivity of oriented poly(ethylene terephthalate). *Journal of Polymer Science Polymer Physics Edition*, **21**, 1427–1438 (1983). <https://doi.org/10.1002/pol.1983.180210813>
- [16] Wang L-H., Choy C. L., Porter R. S.: Thermal expansion of oriented poly(methyl methacrylate). *Journal of Polymer Science Polymer Physics Edition*, **21**, 657–665 (1983). <https://doi.org/10.1002/pol.1983.180210414>
- [17] Mallette J. G., Márquez A., Manero O., Castro-Rodríguez R.: Carbon black filled PET/PMMA blends: Electrical and morphological studies. *Polymer Engineering and Science*, **40**, 2272–2278 (2000). <https://doi.org/10.1002/pen.11359>
- [18] Dewangan B., Jagtap R. N.: Amphiphilic block copolymers of PtBA-*b*-PMMA as compatibilizers for blends of PET and PMMA. *Polymer Engineering and Science*, **46**, 1147–1152 (2006). <https://doi.org/10.1002/pen.20577>
- [19] Lim J. Y., Kim S. Y.: Thermal shrinkage stress in high-speed-spun, high molecular weight poly(ethylene terephthalate) filaments. *Journal of Polymer Science Part B: Polymer Physics*, **39**, 964–972 (2001). <https://doi.org/10.1002/polb.1072>
- [20] Shih W. K.: Shrinkage modelling of polyester shrink film. *Polymer Engineering and Science*, **34**, 1121–1128 (1994). <https://doi.org/10.1002/pen.760341405>
- [21] Cheng S., Wang S-Q.: Elastic yielding after cold drawing of ductile polymer glasses. *Macromolecules*, **47**, 3661–3671 (2014). <https://doi.org/10.1021/ma500570w>
- [22] Wright D. D., Lautenschlager E. P., Gilbert J. L.: Constrained shrinkage of highly oriented poly(methyl methacrylate) fibers. *Journal of Applied Polymer Science*, **91**, 4047–4056 (2004). <https://doi.org/10.1002/app.13621>
- [23] Choy C. L., Chen F. C., Young K.: Negative thermal expansion in oriented crystalline polymers. *Journal of Polymer Science Polymer Physics Edition*, **19**, 335–352 (1981). <https://doi.org/10.1002/pol.1981.180190213>
- [24] McFedries P.: *Microsoft Excel formulas and functions (Office 2021 and Microsoft 365)*. Pearson, London (2022).
- [25] Devore J. D.: *Probability and statistics for engineering and the sciences*. Brooks/Cole, Belmont (2012).
- [26] Kim Y., Kim H., Choi J.: Mechanical origin of shape memory performance for crosslinked epoxy networks. *European Polymer Journal*, **194**, 112162 (2023). <https://doi.org/10.1016/j.eurpolymj.2023.112162>

Research article

# Assessing novel thermoset materials from Brazil nut oil: Curing, thermal and mechanical properties

Aina Perez-Nakai<sup>1</sup>, Alejandro Lerma-Canto<sup>1</sup>, Acerina Trejo-Machín<sup>2</sup>, Iván Dominguez-Candela<sup>3</sup>, Jose Miguel Ferri<sup>1\*</sup>, Vicent Fombuena<sup>1</sup>

<sup>1</sup>Technological Institute of Materials (ITM), Universitat Politècnica de València (UPV), Plaza Ferrándiz y Carbonell 1, 03801 Alcoy, Spain

<sup>2</sup>Resortecs (Regeneration BV), Quai Fernand Demets 23, 1070 Anderlecht, Belgium

<sup>3</sup>Institute of Industrial, Radiophysical and Environmental Safety (ISIRYM), Universitat Politècnica de València (UPV), Plaza Ferrándiz y Carbonell s/n, 03801 Alcoy, Spain

Received 4 August 2023; accepted in revised form 7 September 2023

**Abstract.** The present work describes, for the first time, the chemical modification and characterization of epoxy resins derived from Brazil nut oil (BNO). The development of a bio-based resin has been carried out by chemically modifying BNO, resulting in epoxidized Brazil nut oil (EBNO). Moreover, through a maleinization process, a crosslinker based on maleinized Brazil nut oil (MBNO) has been employed. Analysis using techniques like iodine value (IV) and oxirane oxygen content (Oo) indicate successful chemical modification. FTIR analysis confirms the presence of reactive functional groups in both EBNO and MBNO, which are responsible for resin crosslinking. Mechanical testing of the different bio-resins developed shows that, in the cured resins, flexural strength and modulus decrease with increasing MBNO content, indicating improved flexibility due to the introduction of MBNO as a crosslinker. Thermal analysis using differential scanning calorimetry (DSC) reveals exothermic peaks corresponding to resin curing appearing at progressively lower temperatures. Therefore, this study successfully modifies BNO and demonstrates its effectiveness as a precursor to develop bio-based epoxy resins. The resulting resins exhibit improved ductile and thermal properties, making them suitable for various applications requiring low mechanical stresses.

**Keywords:** bio-based thermoset, epoxidized Brazil nut oil, maleinized Brazil nut oil, mechanical properties, ductility, thermal properties

## 1. Introduction

Thermosetting polymers or thermosets are widely used in different engineering sectors, such as automobiles, navigation, communication, or construction, as coatings, adhesives, and polymeric matrices for composite materials [1, 2]. They account for approximately 18–20% of the total polymeric material manufactured worldwide, with an annual production of about 65 million tons [3, 4]. Thermosets are characterized by a permanently crosslinked network, which gives the material excellent chemical resistance, thermal and mechanical properties, and dimensional

stability. However, this is also a major drawback for recycling due to the difficult degradation, reprocessing, and dissolution of the polymer [5]. In addition to this disadvantage, the vast majority of thermosets are derived from petroleum-based chemicals such as bisphenol A, which results in this material having a significant carbon footprint, besides possible negative health impacts [6].

In particular, epoxy resins are one of the most important commercial thermosetting polymers due to their outstanding properties for their use in the production of composite materials [7, 8]. These properties,

\*Corresponding author, e-mail: [joferraz@upvnet.upv.es](mailto:joferraz@upvnet.upv.es)

© BME-PT

which include mechanical strength, chemical resistance, adhesion, low shrinkage, electrical insulation, dimensional stability, and processability, lead to a high demand for this material, with an estimated production volume of more than 3 million tons [5, 9]. This value makes it very significant to develop eco-efficient epoxy resins. Even though compared to thermoplastics, much less research has been done on sustainable thermosets, there is a growing interest in more environmentally friendly solutions, especially focusing on their chemical perspective. Numerous studies have been conducted using precursors from renewable resources to develop bio-based thermosetting resins [10]. Examples include vegetable oils (VOs), cardanol, lignin, itaconic acid, or tannins, among others [11–17].

VOs, especially polyunsaturated oils, are among the most widely used natural raw materials in polymer synthesis, not only because of their physicochemical properties but also due to their abundance in nature, low cost, and easy extraction [18, 19]. In addition, the wide variety of VOs with different monomers, functionalities, and reactivities provide different results in the properties of the polymer obtained [1]. In this context, VOs have proven to be attractive as substitutes for petrochemical epoxy resins for specific low-load-bearing applications. They also ameliorate the brittleness issues that these materials present due to their highly crosslinked structure and sensitivity to moisture [20].

VOs mainly comprise triglycerides formed by the esterification of three fatty acids and glycerol. These fatty acids are classified according to the number of unsaturation (C=C, double bonds) they contain, and they can be saturated fatty acids (SFAs), monounsaturated fatty acids (MUFAs), and polyunsaturated fatty acids (PUFAs). These double bonds are reactive sites that can be easily modified for functionalisation with active molecules such as oxirane oxygen, maleic anhydride, hydroxyl, or acrylate [21, 22]. This functionalisation of triglycerides allows these VOs to be employed in polymer engineering in different ways: plasticisers, compatibilisers, stabilisers, and also to develop bio-based thermosetting resins [23, 24]. A standardized way of expressing the average unsaturation value is the iodine value (IV), expressed in  $\text{I g I}_2 \cdot (100 \text{ g})^{-1} \text{ oil}$ , meaning that the higher the amount of double bonds, the higher the IV value. Those oils that possess a high IV have more potential to be modified and, therefore, used in industrial

**Table 1.** IV content of different VOs.

VOs	IV [I g I <sub>2</sub> · (100 g) <sup>-1</sup> oil]	References
Linseed	155–205	[25]
Soybean	124–139	[26]
Cottonseed	99–113	[25]
Rapeseed	91–108	[27]
Sunflower	110–143	[27]
Brazil nut	94–106	Current study

applications. For this reason, some of the most commonly used VOs are those shown in Table 1, where their iodine content is indicated.

Brazil nut (*Bertholletia Excelsa*) oil (BNO) has an IV of 94–106  $\text{I g I}_2 \cdot (100 \text{ g})^{-1} \text{ oil}$  [28], indicating a great potential for developing thermosets. This nut has an oil content of between 60–70% [29], with around 75.6% unsaturated fatty acids (UFAs) [30], including MUFAs such as palmitic, stearic, and oleic, and PUFAs such as linoleic, this one accounting for 36% [30] of the total. Despite the interesting lipid profile of BNO, there is hardly any literature related to its functionalisation for use in industrial applications.

As aforementioned, unsaturation (C=C) are reactive sites to functionalise the triglycerides for using these modified VOs (MVOs) to synthesise polymers. Especially the epoxidation process has received special attention. In this process, epoxy groups (oxirane rings) are introduced into the carbon-carbon double bonds of unsaturated fatty acids with peracids, resulting in epoxidized vegetable oils (EVOs) [31]. The reactive points, *i.e.* the oxirane rings as an end group of the triglycerides, will act as crosslinking points of the three-dimensional chain to form these thermosets. Some of the commercially available EVOs are epoxidized soybean oil (ESBO) and epoxidized linseed oil (ELO) and have been demonstrated for use in developing bio-based thermosetting epoxy resins as coating and polymer matrices [32, 33].

On the other hand, to convert the uncured epoxy resin into a hard, infusible thermosetting network with the desired properties, it is necessary to have the presence of a hardener acting as a curing agent [34]. Some of the most commonly used hardeners for epoxy-type resins are petrochemical-based, such as amines or anhydrides [35]. They are not only environmentally unfriendly but also toxic to humans. Aliphatic amines, cycloaliphatic amines, and anhydride-curing agents can be responsible for skin, eyes,

and lung problems [36]. In literature, many works have been carried out to develop bio-based thermosets from EVOs such as ESBO, ELO, or epoxidized canola oil (ECO) using these types of hardeners [37–39]. Nevertheless, fewer studies have combined both EVOs and bio-based hardeners, obtaining promising results. For instance, Stemmelen *et al.* [40] have demonstrated the feasibility of synthesising a fully bio-based epoxy resin by amination of VO's, in this case using an aminated grapeseed oil (AGSO) as a hardener of ELO. Chen *et al.* [41] synthesized a high bio-content epoxy resin by developing a maleopimaric acid by grafting anhydride maleic groups onto the molecular structure of rosin to act as a curing agent for ESO. Samper *et al.* [42] also developed an epoxy resin using ELO and a mixture of a petroleum-derived crosslinking agent, methyl nadic anhydride (MNA), and a VO-based maleinized linseed oil (MLO). Following this line, Fombuena *et al.* [43] developed a composite with over 98% bio-based content, using solely derivatives from linen.

Therefore, the novelty of the present work lies in the study of a novel source of VO, which is highly abundant and can aspire to replace part of the petrochemical resins used to manufacture composite materials or coatings, among many other applications. This study aims to develop and optimise a novel epoxy resin obtained from the use of BNO. On the one hand, EBNO is used as a thermosetting matrix and, on the other hand, a petroleum-derived hardener methylhexanhydrophthalic anhydride (MHHPA) is combined with maleinized Brazil nut oil (MBNO) to achieve a high bio-based content comprised between 56.3 and 75.2 as will be seen in Table 2. The ratio of MBNO and MHHPA is systematically varied to analyse the variability of the mechanical and thermal properties that can be obtained. Finally, it should be noted that the results of this work allow the study of future works of composite materials with a high content of bio-based material and low impact on the environment if compared to those obtained from petrochemical resins.

## 2. Materials and methods

### 2.1. Materials

Brazil nuts were provided by FrutoSeco S. L. for this project (Alicante, Spain). The mechanical extraction method at room temperature was used to obtain BNO with a pressing machine model DL-ZYJ05 purchased

from Nanchang Dulong Industrial Corporation (Zucheng, China).

Afterwards, the BNO is chemically modified by the epoxidation process to obtain EBNO, used as an epoxy matrix. It was performed in situ using hydrogen peroxide (30% v/v) (CAS: 7722-84-1), acetic acid (99.7%) (CAS: 64-19-7), and sulfuric acid (97%) (CAS: 7664-93-9) supplied by Sigma Aldrich (Madrid, Spain).

Two different hardeners were used to crosslink EBNO. On the one hand, MBNO was used as a hardener of biological origin to increase the bio-based content of thermosets. The maleinization of BNO was performed by adding maleic anhydride (MA) of >98% purity (CAS: 33225-51-3), supplied by Sigma Aldrich (Madrid, Spain). On the other hand, MHHPA (CAS: 25550-51-0), which has an anhydride equivalent weight (AEW) of 168.19 g·eq<sup>-1</sup> and was provided by Sigma Aldrich (Madrid, Spain), was used as a petrochemical crosslinker.

Besides, glycerol (CAS: 56-81-5) was used as an initiator and 1-methylimidazole (CAS: 616-47-7) as an accelerator, both supplied by Sigma Aldrich (Madrid, Spain).

All chemical structures of all the components used (epoxy resin (EBNO), crosslinkers (MBNO and MHHPA), initiator (glycerol), and accelerator (1-methylimidazole)) are shown in Figure 1.

### 2.2. Chemical modifications of BNO

To conduct the epoxidation reaction of BNO to obtain the bio-based epoxy matrix, the method described by Dominguez-Candela *et al.* [44] was followed. The BNO was introduced into a three-neck round-bottomed flask immersed in a thermostatic water bath at a constant internal flask temperature of 60 °C. After the oil reached this temperature, glacial acetic acid was introduced at a stirring speed of 220 rpm. After 10 min, sulfuric acid and hydrogen peroxide were mixed and added dropwise for approximately 30 min. Then, the reaction was carried out for 8 h, cooled at room temperature, and cleaned by decantation and centrifugation.

On the other hand, to carry out the maleinization of BNO to obtain a bio-hardener, the process described in previous works [45] was used. The maleinization was conducted with a molar ratio of 2.4:1 of maleic anhydride to virgin oil, also in a three-neck round-bottomed flask stirred at a constant speed of 300 rpm.

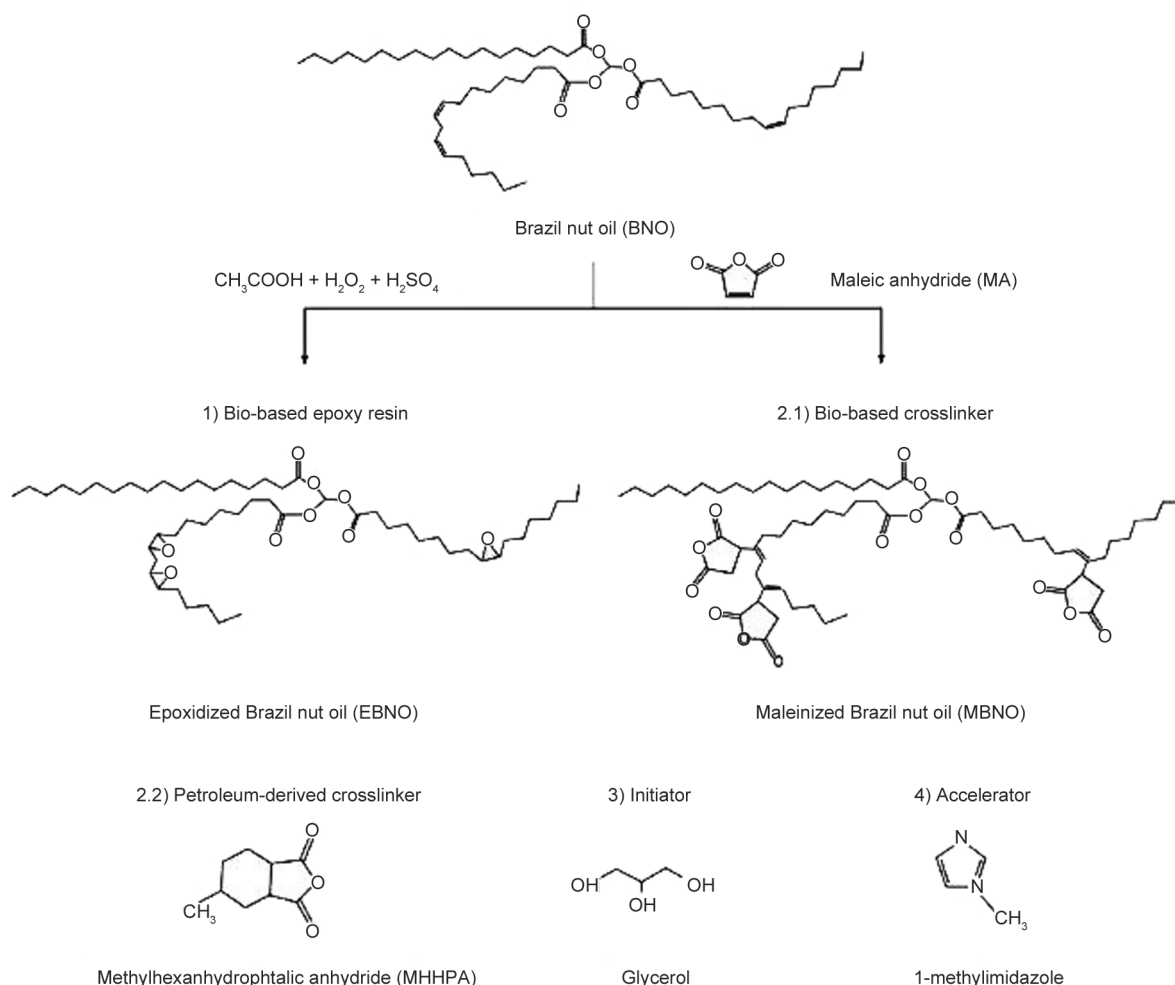


**Figure 1.** Chemical structures of the components used to obtain the bio-based epoxy resin.

Three temperature steps, 180, 200, and 220 °C, were used, split over the 3 h of reaction.

### 2.3. Characterization of chemically modified EBNO and MBNO

The Oo of EBNO was determined. This value allows for assessing the number of oxirane oxygen groups in the fatty acids due to their substitution by the double bonds through the epoxidation of the oil. For this purpose, the process described in ASTM D1652 was followed. According to this standard, a sample must be dissolved in chlorobenzene, followed by the addition of crystal violet drops and titration with a solution of hydrobromic acid (HBr) in glacial acetic acid. By using the Equation (1), the Oo content is calculated:

$$\text{Oo [wt\%]} = 1.6 \cdot N \cdot \frac{V - B}{W} \quad (1)$$

where  $V$  is the volume of HBr solution used for titration sample [ml],  $B$  is the volume of HBr solution

used for blank titration [ml], and  $W$  refers to the sample mass of oil used [g].

The epoxy equivalent weight (EEW) expressed in grams of epoxy resin containing one equivalent of the epoxy group [ $\text{g} \cdot \text{eq}^{-1}$ ] is one of the most relevant parameters to characterize epoxy resins. It is related to the crosslinking density and allows the calculation of the required amount of crosslinking agent for the curing process. It was also determined following ASTM D 1652 by titration using the Equation (2):

$$\text{EEW [g} \cdot \text{eq}^{-1}] = \frac{1000 \cdot W}{(V - B) \cdot N} \quad (2)$$

where  $N$  is the equivalent concentration of HBr to glacial acetic acid. At least five measurements are made for each sample, and the average value is given.

On the other hand, IV refers to the mass of iodine absorbed by 100 g of oil. It is an index used to assess the amount of double bonds available in fatty acid chains. Therefore, when epoxidation occurs, this value decreases. The IV was determined with a Wijs



solution that reacted with the double bonds and by titration process using sodium thiosulfate solution following the guidelines of ISO 3961. The value was calculated using the Equation (3):

$$IV = \frac{12.69 \cdot c \cdot (V_1 - V_2)}{m} \quad (3)$$

where IV refers to the iodine value in  $\text{g I}_2 \cdot (100 \text{ g})^{-1}$  oil,  $c$  is the normality of sodium thiosulfate solution,  $V_1$  is the volume of thiosulphate sodium needed for titration of the blank [ml],  $V_2$  is the volume of sodium thiosulphate used for titration [ml], and  $m$  is the mass of the oil sample [g].

The acid value (AV) is a parameter that allows to assess the degree of maleinization of the MBNO. As the maleinization takes place, the value of AV increases since the molecules of anhydride maleic are added to the double bonds. It was obtained according to ISO 660 by titration of a sample of the oil dissolved in ethanol using a potassium hydroxide solution. Then, the AV is calculated with Equation (4):

$$AV = \frac{56.1 \cdot V \cdot C}{m} \quad (4)$$

where  $C$  refers to the concentration of the potassium hydroxide solution [ $\text{mol} \cdot \text{l}^{-1}$ ],  $V$  to the potassium hydroxide volume used for the sample titration [ml], and  $m$  to the mass of oil used for the titration [g].

## 2.4. Samples preparation

Several epoxy resin formulations were developed to evaluate the highest percentage of bio-based resins that can be obtained with good performance. For this purpose, the amounts of EBNO, glycerol, and 1-methyl imidazole have been kept constant in the way that glycerol was incorporated at 0.8 wt% and 1-methylimidazole at 2.0 wt% concerning the mass of the epoxy component, as recommended in the literature [46]. The molar ratio of the hardeners, MBNO and MHHPA, has been modified to replace MHHPA with the bio-based hardener as much as

possible. All the formulations are prepared using a ratio EEW:AEW of 1:1.5 since this relationship seems appropriate to achieve a good curing degree of EBNO. This ratio depends on the epoxy groups contained in the EVO that will allow its crosslinking with the hardener [47]. The different formulations are gathered in Table 2.

The formulations were carried out manually, stirring all the components vigorously at room temperature in aluminum containers, ensuring a homogeneous mix. After, the mixtures are poured into a silicone mold with dimensions of  $80 \times 10 \times 4$  mm to obtain samples for standard tests, according to ISO 178 and ISO 179. The mold is placed into an air oven model Conterm 80L from J. P Selecta (Barcelona, Spain) to perform the curing. The curing cycle was carried out at  $90^\circ\text{C}$  for 3 h and post-curing at  $120^\circ\text{C}$  for 2 extra hours. The appearance of the cured samples is shown in Figure 2.

Figure 3 shows a schematic approach to the process of proposed polymerisation through the interaction of EBNO and MHHPA (Figure 3a) and EBNO, MBNO and MHHPA (Figure 3b). In it, the black dots refer to the reactive oxirane groups in EBNO, red dots represent the maleic groups anchorage in the structure of MBNO, and green dots represent the chemical structure of the MHHPA. Figure 3a shows the reaction using only MHHPA as the crosslinker for the EBNO epoxy resin. It shows how the structure

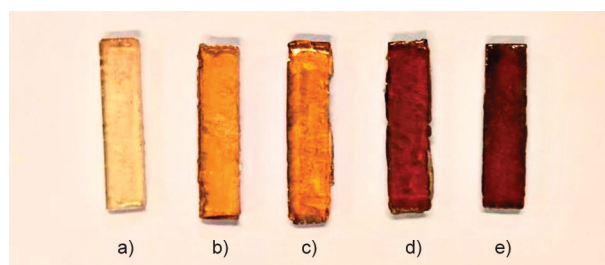


**Figure 2.** Cured samples a) MHHPA100, b) MHHPA90:MBNO10, c) MHHPA80:MBNO20, d) MHHPA70:MBNO30, e) MHHPA60:MBNO40.

**Table 2.** Composition of different samples of epoxy resin based on EBNO.

Sample	MHHPA [%]	MBNO [%]	Glycerol [wt%]	1-methylimidazol [wt%]	Bio-based content [%]
MHHPA100	100	0	0.8	2	56.3
MHHPA90:MBNO10	90	10	0.8	2	61.4
MHHPA80:MBNO20	80	20	0.8	2	66.2
MHHPA70:MBNO30	70	30	0.8	2	70.8
MHHPA60:MBNO40	60	40	0.8	2	75.2

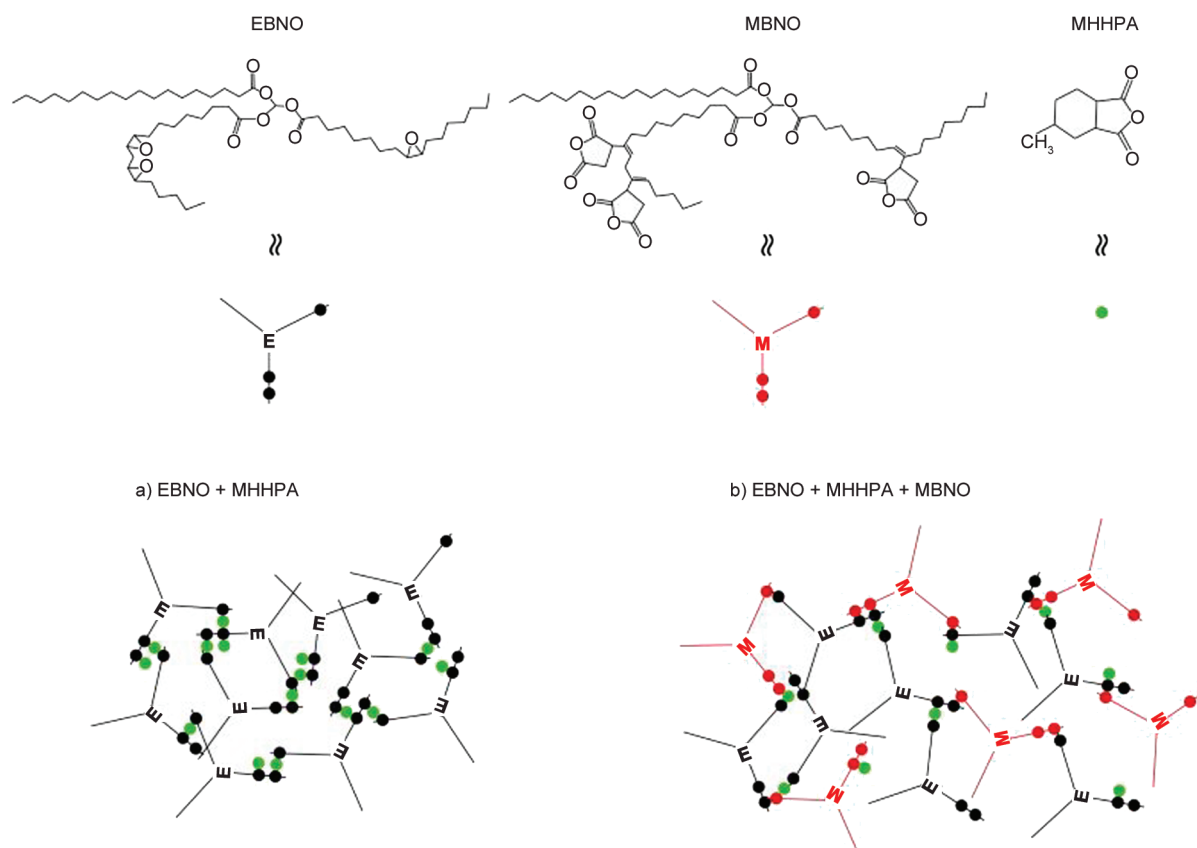


**Figure 3.** Schematic representation of polymerization effect of EBNO with MHPHA (a) and MHPHA:MBNO mixture (b).

resulting from this reaction is more compact and clustered due to the lower length, viscosity, and molecular weight of the petrochemical hardener, MHPHA. However, as shown in [Figure 3b](#), when MBNO is added, the free volume between molecular chains increases, contributing to better mobility and, thus, flexibility of the final thermoset resin [48].

## 2.5. Fourier transform infrared spectroscopy (FTIR)

FTIR was performed using a Bruker Vector 22 spectrometer from Bruker Española, S. A. (Madrid, Spain) to analyse the chemical structure of BNO, EBNO, and MBNO, as well as that of the cured samples. The wavelength range employed was  $4000\text{--}400\text{ cm}^{-1}$ , with a spectral resolution of  $4\text{ cm}^{-1}$  and performing an average of 20 scans. All the FTIR spectra obtained were normalized with a limit ordinate of 1 absorbance unit by using the Perkin-Elmer Software Spectrum.

## 2.6. Mechanical characterization

Flexure, impact, and hardness tests of the different solid samples were conducted to analyse their mechanical properties. The flexural test was carried out using an Ibertest ELIB 30 universal testing machine

from S.A.E. Ibertest (Madrid, Spain) at room temperature and a crosshead speed of  $5\text{ mm}\cdot\text{min}^{-1}$  using a load cell of 5 kN, according to ISO 178. The impact test was conducted using a 6 J Charpy pendulum from Metrotec S.A (San Sebastian, Spain), following the guidelines of ISO 179. For both tests, flexural and impact, the samples tested had the mentioned dimensions,  $80\times 10\times 4\text{ mm}$ , according to their respective standards. Lastly, the hardness test was performed (15 tests per sample) using a Shore D durometer 673-D from J. Bot S.A. (Barcelona, Spain), according to ISO 868. The reported results are obtained by averaging the test over a minimum of 5 samples. The Dixon Q test was applied to the mechanical characterization values in order to provide more reliable values.

## 2.7. Thermal characterization

Differential scanning calorimetry (DSC) was carried out to analyse the curing process and the post-cured samples of the different combinations of novel epoxy bio-resins. The DSC test was performed on a Mettler Toledo DSC 821 (Schwerzenbach, Switzerland). The test conditions were under a nitrogen atmosphere with a flow rate of  $66\text{ ml}\cdot\text{min}^{-1}$ , with a thermal program consisting of a temperature ramp of  $30\text{--}340\text{ }^{\circ}\text{C}$  at a

heating rate of  $10^{\circ}\text{C}\cdot\text{min}^{-1}$ . From the calorimetric curves resulting from the test, the values of the initial temperature, the maximum crosslinking temperature (peak), and the final temperature of the process are obtained. Likewise, from the integration of the area of the exothermic peak of each sample, the normalized enthalpy values are determined in  $\text{J}\cdot\text{g}^{-1}$ . The normalized enthalpy of the exothermic peak was obtained using Mettler Toledo's STARe Evaluation software, explicitly using the 'integration' function and selecting an equal temperature range for all samples. In addition, to determine the  $T_g$  of the cured samples, three analyses (temperature ramp of  $30\text{--}340^{\circ}\text{C}$  at a heating rate of  $10^{\circ}\text{C}\cdot\text{min}^{-1}$ ) per sample were performed, and the mean value was chosen.

Thermogravimetric analysis (TGA) was carried out to analyse the thermal stability with model TGA PT1000 from Linseis Inc. (Selb, Germany). The analysed samples have a weight between  $20\text{--}25\text{ mg}$ , with the temperature program from  $30$  to  $700^{\circ}\text{C}$  with a speed of  $10^{\circ}\text{C}\cdot\text{min}^{-1}$  and with a constant nitrogen flow of  $30\text{ ml}\cdot\text{min}^{-1}$ . Three analyses were performed for each sample to try to provide average values.

### 2.8. Morphological characterization

The morphologies of the cross-sectional areas of the fractured samples collected from the impact test were evaluated. For this, a field emission scanning electron microscopy (FESEM) model Zeiss Ultra 55 from Oxford Instruments (Oxfordshire, UK), was used. The samples were previously coated with a thin layer of gold-palladium alloy under vacuum conditions employing an EM MED020 sputter coater from Leica Microsystems (Wetzlar, Germany). The surfaces were observed applying an acceleration voltage to an electron beam of  $2\text{ kV}$ .

## 3. Results

### 3.1. Chemical characteristics of the oils

Concerning the values obtained with the characterization of BNO, EBNO, and MBNO by the different titration methods, all of them have demonstrated that the chemical modifications of the oil have occurred. Starting with IV, BNO was found to have a value of  $102.4\text{ g I}_2\cdot(100\text{ g})^{-1}$ . This high unsaturation value is related to the fatty acid composition of BNO, which is rich in MUFA and PUFA. The most representative fatty acids determined by gas chromatography were briefly: MUFA, consisting mainly of oleic acid ( $34.56\%$ ) and PUFA, highlighting linoleic acid

( $37\%$ ), which has the highest number of double bonds with two double bonds for each fatty acid [30]. These results show the high availability of double bonds that can react during the epoxidation or maleinization of the oil and be replaced by oxirane oxygen or maleic anhydride molecules. This value of IV decreases in the case of EBNO to  $11.6\text{ g I}_2\cdot(100\text{ g})^{-1}$ , which indicates that the epoxidation process took place. This success in the modification of the oil is also corroborated by the values of EEW and Oo, which indicates that this decrease in the amount of the double bonds is due to their substitution with the epoxy groups. The value of EEW is  $365\text{ g}\cdot\text{eq}^{-1}$ , and the Oo value was  $4.22\%$ , representing a conversion of  $69\%$ , determined from the theoretical Oo value of  $6.11\%$ , calculated from the average of its fatty acids. These values are similar to the ones reported by Kim and Sharma [49], who obtained the IV and the Oo of several EVOs such as linseed (IV  $31.02\text{ g I}_2\cdot(100\text{ g})^{-1}$  and Oo  $8.91\%$ ), soybean (IV  $17.11\text{ g I}_2\cdot(100\text{ g})^{-1}$  and Oo  $6.65\%$ ) or radish (IV  $20.30\text{ g I}_2\cdot(100\text{ g})^{-1}$  and Oo  $4.89\%$ ). Regarding the maleinization, MBNO also shows a decrease in the availability of the double bonds. The IV was found to be  $49.3\text{ g I}_2\cdot(100\text{ g})^{-1}$ . Moreover, the AV increased from  $0.20\text{ mg KOH g}^{-1}$  of BNO to  $130\text{ mg KOH g}^{-1}$  with the MBNO, indicating that the maleinization process occurred. This value is in line with the one reported by Ferri *et al.* [50] who indicates a value from  $105$  to  $130\text{ mg KOH g}^{-1}$  for a commercial MLO.

### 3.2. Functional group analysis of raw materials and cured samples

To verify the chemical modification performed on the BNO, Figure 4 presents FTIR spectra of the BNO, the EBNO, and the MBNO. On the one hand, the spectrum of BNO was characterized by the appearance of the band at  $3006\text{ cm}^{-1}$  assigned to the C–H stretching vibration of the cis-double bond (=CH). Also, in the fingerprint region, two peaks appear at  $1170$  and  $1236\text{ cm}^{-1}$  related to the stretching vibration of the C–O ester groups. At  $1748\text{ cm}^{-1}$ , in the double bond's stretching region, appears an ester carbonyl functional group of the triglycerides [51]. On the other hand, the spectrum of EBNO was characterized by the epoxy group's appearance at the band  $824\text{ cm}^{-1}$  and the disappearance of the carbon-carbon double bond absorption band at  $3006\text{ cm}^{-1}$ , indicating that the epoxidation reaction took place. In addition, a broad band was observed at  $3300\text{--}3600\text{ cm}^{-1}$  that

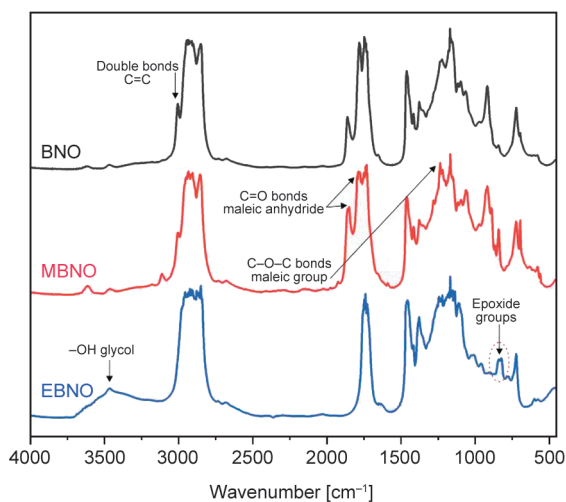


**Figure 4.** FTIR spectra of BNO, EBNO, and MBNO.

could be associated with the glycol's production in the epoxidation process, as shown in other studies [52]. This is because other reactions, such as hydrolysis, can occur, leading to the opening of the oxirane ring and, therefore, to the formation of other sub-products. Epoxides can be attacked by water (acid-catalysed), acetic acid, and peracetic acid [53].

About the FTIR spectrum of the bio-based crosslinker MBNO, the characteristic bands of the maleic group of MBNO can be observed, especially highlighting the increase in the intensity of the peaks at 1850 and 1788  $\text{cm}^{-1}$  corresponding to the symmetric and asymmetric stretching of the C=O bond of the maleic anhydride. Additionally, at 1250 and 1170  $\text{cm}^{-1}$ , the symmetric and asymmetric stretching of the C–O–C bonds of the maleic groups are observed [54]. Therefore, from the FTIR spectrum of MBNO, it can be confirmed that the maleic anhydride has been anchored to the triglyceride structure of the BNO and, as a consequence, it was modified, providing a more reactive oil to be used as a crosslinker.

After analysing the starting materials, the crosslinking reaction was monitored by FTIR to verify the formation of chemical bonds between EBNO and the different crosslinker mixtures (MHHPA:MBNO) in the cured samples. Figure 5 shows the FTIR spectra of all resins developed, highlighting the main characteristic peaks. As previously discussed in the FTIR of raw materials, the characteristic peaks of the functional groups are located mainly at 1850 and 1788  $\text{cm}^{-1}$ , corresponding to the anhydride groups in the MHHPA or MBNO structure, and at 824  $\text{cm}^{-1}$  for the epoxy group in the EBNO structure. These peaks, highlighted with vertical black dashed lines,

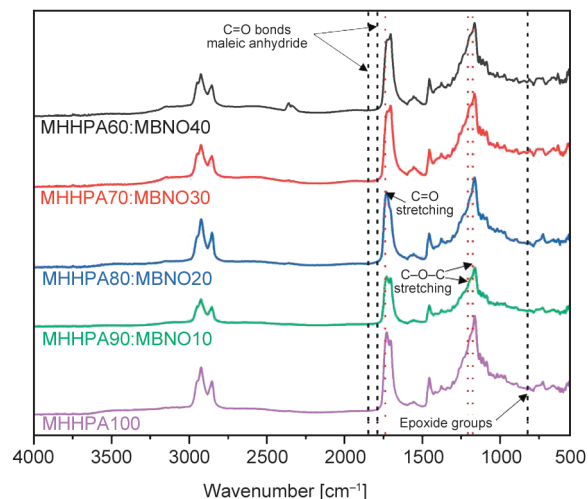


**Figure 5.** FTIR of cured samples based on EBNO cross-linked with different MHHPA:MBNO mixtures.

disappeared in all samples due to the opening of the epoxy ring and anhydride groups as a consequence of the crosslinking reaction. In the FTIR spectra of the different resins cured, the main groups evidencing the chemical bonds formed. It is important to highlight the group related to the carbonyl C=O stretching at 1730  $\text{cm}^{-1}$  and the C–O–C stretching at 1184 and 1162  $\text{cm}^{-1}$ , which were highlighted with vertical red dotted lines in the FTIR spectra. Therefore, the disappearance or decrease of the main reactive groups in epoxidized and maleinized oils and the change in the intensity of new groups related to the chemical interaction of the compounds provide evidence of the observed crosslinking at the macroscopic level through the hardening of the new bio-resins.

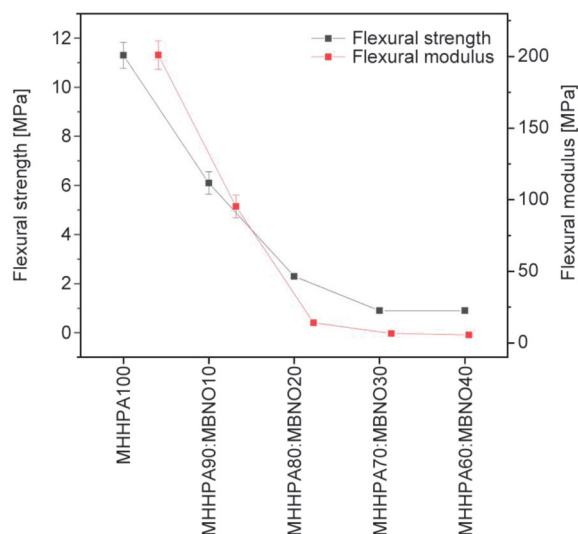
### 3.3. Mechanical properties

After characterizing the crosslinking of the resins using FTIR, Table 3 and Figure 6 show a summary of the macroscopic behavior through the flexural properties. As it can be clearly seen, as the MBNO content increases, both the flexural strength and modulus decrease, thus indicating the flexibilisation effect provided by the introduction of the MBNO. The EBNO system cured with a petrochemical anhydride shows a flexural strength of 11.3 MPa and a flexural modulus of about 210 MPa. As can be seen, when 10 wt% MHHPA is replaced by MBNO, MHHPA90:MBNO10, the flexural strength decreases to 6.1 MPa while the flexural modulus goes down to 95.4 MPa. At first, the decrease in both flexural strength and modulus follows a linear tendency, although, from the MHHPA70:MBNO30 mixture

**Table 3.** Influence of cured samples based on EBNO cross-linked with different MHHPA:MBNO mixtures in terms of flexural strength and flexural modulus.

Samples	Flexural strength [MPa]	Flexural modulus [MPa]
MHHPA100	11.3±0.5	210.1±10.2
MHHPA90:MBNO10	6.1±0.5	95.4±7.9
MHHPA80:MBNO20	2.3±0.1	14.1±0.1
MHHPA70:MBNO30	0.9±0.1	6.7±0.7
MHHPA60:MBNO40	0.9±0.1	5.6±0.6

onwards, flexibility is high that both flexural strength and modulus strength show values close to zero, as can be seen in Figure 6. Dominguez-Candela *et al.* [55] showed values of 57.0 and 765.0 MPa for flexural strength and modulus, respectively, using an epoxidized chia oil (ECO) cured with methyl nadic norbornene anhydride (MNA). These differences with the present study can be ascribed to different amounts of linkage points of epoxy resins used. While EBNO has an EEW of  $365 \text{ g}\cdot\text{eq}^{-1}$ , ECO has an EEW of  $219 \text{ g}\cdot\text{eq}^{-1}$ , which justifies that some mechanical parameters, such as flexural modulus, are practically three times higher. MBNO, therefore, serves as an efficient crosslinker to replace current petrochemical hardeners. However, due to its high molecular weight formed by the long chains of triglycerides, it imparts excellent ductile properties to the resulting resins, making it suitable for applications subjected to low mechanical stress. It should be noted that the mechanical properties of the samples are strictly related to the chemical structure of the crosslinker, as observed. While MNA or MHHPA provides a very compact and semi-rigid crosslinking unit, functionalized long fatty acid chains lead to an increase in free volume and, thus, to an increase in chain mobility, which contributes to improved flexibility of the thermosetting resins. Other studies showed similar properties to the present work. Lerma-Canto *et al.* [56] showed similar results in their work employing an epoxidized hemp oil (EHO) crosslinked with an MNA and maleinized hemp oil (MHO) mixtures. They recorded a flexural modulus of 300 MPa and a flexural strength lower than 7 MPa for the samples crosslinked using lonely MNA. Furthermore, as the crosslinker MHO content increased in the mixture of MNA/MHO, the modulus decreased constantly up to the samples crosslinked with the MNA50/MHO50 mixture, in this case, the modulus being around 60 MPa and the flexural strength around 6 MPa. At

**Figure 6.** Influence of cured samples based on EBNO cross-linked with different MHHPA:MBNO mixtures in terms of flexural strength and flexural modulus.

higher contents, the flexural modulus remained constant at around 7 MPa.

As for the mechanical characterization of the bioresins developed, Table 4 shows the results obtained for the Impact-absorbed energy and Shore D hardness of the cured samples. Following the same trend observed previously in the flexural assay, the hardness decreases linearly as the MBNO content in the samples increases. In this case, the maximum hardness is obtained for the sample crosslinked with MHHPA100, with a value of 57 Shore D. This value is very similar to that achieved by Samper *et al.* [57] when crosslinking of ELO with phthalic anhydride (PA) and maleic anhydride (MA), obtaining a value of 66 Shore D. The lowest hardness value obtained, 21.2 in the sample MHHPA60:MBNO40, once again provides an idea of the elevated ductile properties achieved using MBNO as a crosslinker.

The results of impact-absorbed energy determined by the Charpy impact test demonstrate how the resin developed solely with the petrochemical hardener has a toughness of  $1.4 \text{ kJ}\cdot\text{m}^{-2}$ . This reduced value results from the stiffness provided by the petrochemical hardener due to its low viscosity, molecular weight, and high reactivity. In the case of sample MHHPA100, it is observed that the value obtained is  $1.4 \text{ kJ}\cdot\text{m}^{-2}$ . When the content of MBNO increases up to 30%, MHHPA70:MBNO30, its value increases, reaching  $6.5 \text{ kJ}\cdot\text{m}^{-2}$ . As a result of the increased ductility, the sample developed with a 40% content of

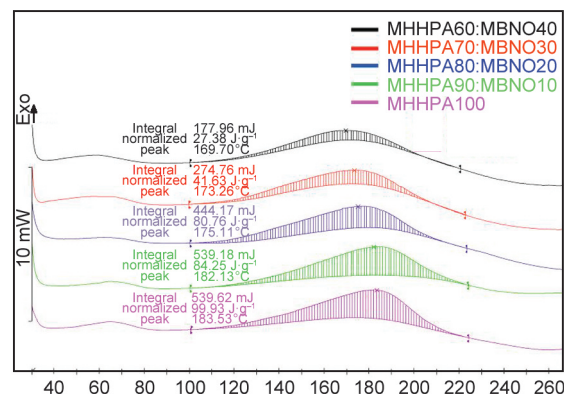
**Table 4.** Influence of cured samples based on EBNO cross-linked with different MHHPA:MBNO mixtures in terms of impact-absorbed energy and Shore D hardness.

Samples	Impact-absorbed energy [kJ·m <sup>-2</sup> ]	Shore D hardness
MHHPA100	1.4±0.2	56.9±5.0
MHHPA90:MBNO10	2.5±0.2	54.1±5.1
MHHPA80:MBNO20	4.7±0.6	35.9±3.2
MHHPA70:MBNO30	6.5±0.3	27.8±2.7
MHHPA60:MBNO40	Did not break	21.2±2.1

maleinized oil-based hardener did not break after being subjected to the impact of the pendulum in the test, demonstrating its ductility and flexibility. Therefore, this increase in flexibility and ductility can be beneficial in preventing impact fractures and rapid crack propagations typically associated with three-dimensional networks of high density, which are characteristic of thermoset resins [58]. Samper *et al.* [57] studied ELO and ESO mixtures cured with a crosslinker mixture based on PA and MA and obtained similar impact energy absorption values. Specifically, for the 100% ELO with PA/MA, the energy absorption was 4.2 kJ·m<sup>-2</sup>, lower than that of the present work.

### 3.4. Thermal properties

The exothermic character of the curing process of thermoset resins has been evaluated using DSC. As can be observed in Figure 7, the calorimetric curves are characterized by an exothermic peak, which provides information about the reaction between the EBNO-based epoxy resin and the MBNO and MHHPA hardeners. The main parameters obtained from each curve are summarized in Table 5. The onset and the end represent the start and end of the crosslinking reaction, while the peak of the exothermic curve represents the temperature at which the maximum crosslinking rate occurs. Furthermore, the area under each curve is representative of the normalized enthalpy of cure for the samples, measured in

**Figure 7.** Plot comparison of the dynamic DSC thermograms of the curing process of EBNO crosslinked with a mixture of MHHPA and MBNO.

J·g<sup>-1</sup>. As can be seen in Table 5, the crosslinking process starts at about 101–109 °C and ends between 203–224 °C, depending on the mixture of hardeners used. It is possible to observe in Figure 7 that as the ratio of MBNO increases, the curves tend to shift towards lower temperatures. This results in a lower peak temperature. It moves from 183.5 °C for the EBNO system crosslinked with MHHPA100 to values of 169.7 °C for the system crosslinked with a MHHPA60:MBNO40 mixture. This decrease in peak temperature can have a positive effect at an industrial level, as it requires lower temperatures and, therefore, lower energy costs for the crosslinking of the resins. The same trend is observed for the normalized enthalpy, which is maximum for the sample crosslinked with MHHPA100 with a value of 99.9 J·g<sup>-1</sup>. As the MBNO content in the crosslinker mixture increases, the maximum enthalpy decreases, indicating that MBNO leads to lower exothermicity. Hence, the EBNO resin cured with the MHHPA90:MBNO10 mixture shows a slight decrease in the enthalpy value (84.3 J·g<sup>-1</sup>), while the system crosslinked with the MHHPA60:MBNO40 mixture reaches minimum values of 27.4 J·g<sup>-1</sup>. The lower exothermicity provided by the presence of MBNO is directly related to the chemical structure

**Table 5.** Main parameters obtained by DSC of EBNO crosslinked with different MHHPA:MBNO mixtures.

Samples	Onset [°C]	Peak temperature [°C]	Endset [°C]	Enthalpy [J·g <sup>-1</sup> ]
MHHPA100	109.0	183.5	223.4	99.9
MHHPA90:MBNO10	106.8	182.1	223.6	84.3
MHHPA80:MBNO20	103.4	175.1	213.4	80.8
MHHPA70:MBNO30	102.7	173.3	207.2	41.6
MHHPA60:MBNO40	101.8	169.7	203.6	27.4

of MBNO, and can result in resins with higher ductile properties, as demonstrated in the previous section of mechanical characterisation.

Once the materials were cured, the  $T_g$  amount of MBNO in the MHHPA:MBNO mixtures increases. The sample with the highest  $T_g$  is MHHPA100 with a value of 55.1 °C. On the other hand, a significant decrease in  $T_g$  is observed with the addition of MBNO, with the lowest  $T_g$  value being obtained for the MHHPA60:MBNO40 sample with a value of 46.2 °C. This decrease in  $T_g$  after adding MBNO results in materials with higher ductility. If we compare these values with those obtained by Boonlert-uthai *et al.* [59] when curing a conventional resin from diglycidyl ether of bisphenol A (DGEBA), which is 140.2 °C (Table 6), it can then be observed that the thermoset materials fabricated in this work are significantly more ductile.

Furthermore, the thermal stability of the cured materials was measured. In general, it is observed that the maximum degradation rate ( $T_{max}$ ) appears at a higher temperature, which corroborates a greater degree of crosslinking. Specifically, the  $T_{max}$  values range between 334–360 °C, with the lowest thermal stability for materials cured with the 60MHHPA:40MBNO mixture and the highest stability for those cured with 100MHHPA (Table 6).

### 3.5. Morphological properties

The analysis using FESEM can complement the mechanical study conducted through flexural, hardness, and Charpy impact tests. The FESEM analysis of the fracture surface details the deformation patterns and helps identify whether the fracture is brittle or ductile. In this case, the FESEM analysis provides valuable insights into the microstructural characteristics and failure mechanisms of the materials, enhancing the understanding of their mechanical behavior and response. In our particular case, as it is possible to observe in Figure 8a the EBNO system crosslinked

with a MHHPA shows a smooth and homogeneous surface, typical of brittle polymers. Adding only 10% of MBNO does not influence the fracture surface, as its impact-absorbed energy is only 2.5 kJ·m<sup>-2</sup>, as shown in Figure 8b. The effects of MBNO incorporation on fractured surfaces are visible from the MHHPA/MBNO (80/20) mixture, as can be seen in Figure 8c where several crack fronts are observed, which are directly related to the increase in flexibility. As MBNO increases in the MHHPA/MBNO crosslinked mixtures, the number of crack fronts increases in both size and number, indicating increased ductility (Figure 8d). The sample made with 40% of MBNO is not analysed using FESEM as it does not break during the impact tests. These results are in agreement with the mechanical results indicating the role of MBNO in increasing ductility. Several studies where the maleinized oil content in the sample is increased show the same morphological aspects and, therefore, the same effect on mechanical properties, namely higher ductility [42, 55, 56].

### 4. Conclusions

For the first time, an EBNO has been used to develop a bio-based thermosetting epoxy resin. To minimise petrochemical components, MBNO has been developed as a curing agent, achieving over 75% bio-content. The modification of BNO to EBNO has been optimised, resulting in a reduction of the IV from 102 to 11.6 g I<sub>2</sub>·(100 g)<sup>-1</sup>, resulting in an Oo of 4.22%, similar to some commercially available EVOs. Analysis by FTIR has confirmed these two modifications made to BNO, with characteristic peaks of MBNO (1850 and 1250 cm<sup>-1</sup> corresponding to the C=O and C–O–C from maleic bonds primarily) and EBNO (824 cm<sup>-1</sup> corresponding to the epoxy group). FTIR analysis of the cured samples shows how these bonds tend to disappear because of the crosslinking of the resin's three-dimensional network. At the macroscopic level, the bio-based resin

**Table 6.** Main thermal parameters obtained by DSC and TGA of cured samples.

Samples	DSC results	TGA results		
	$T_g$ [°C]	$T_5$ [°C]	$T_{max}$ [°C]	$T_{90}$ [°C]
DGEBA	140.2	–	–	–
MHHPA100	55.1	227.3	360.0	440.1
MHHPA90:MBNO10	52.6	224.7	349.8	422.1
MHHPA80:MBNO20	51.3	227.1	345.1	439.6
MHHPA70:MBNO30	48.8	225.3	341.5	429.5
MHHPA60:MBNO40	46.2	220.9	334.0	433.3

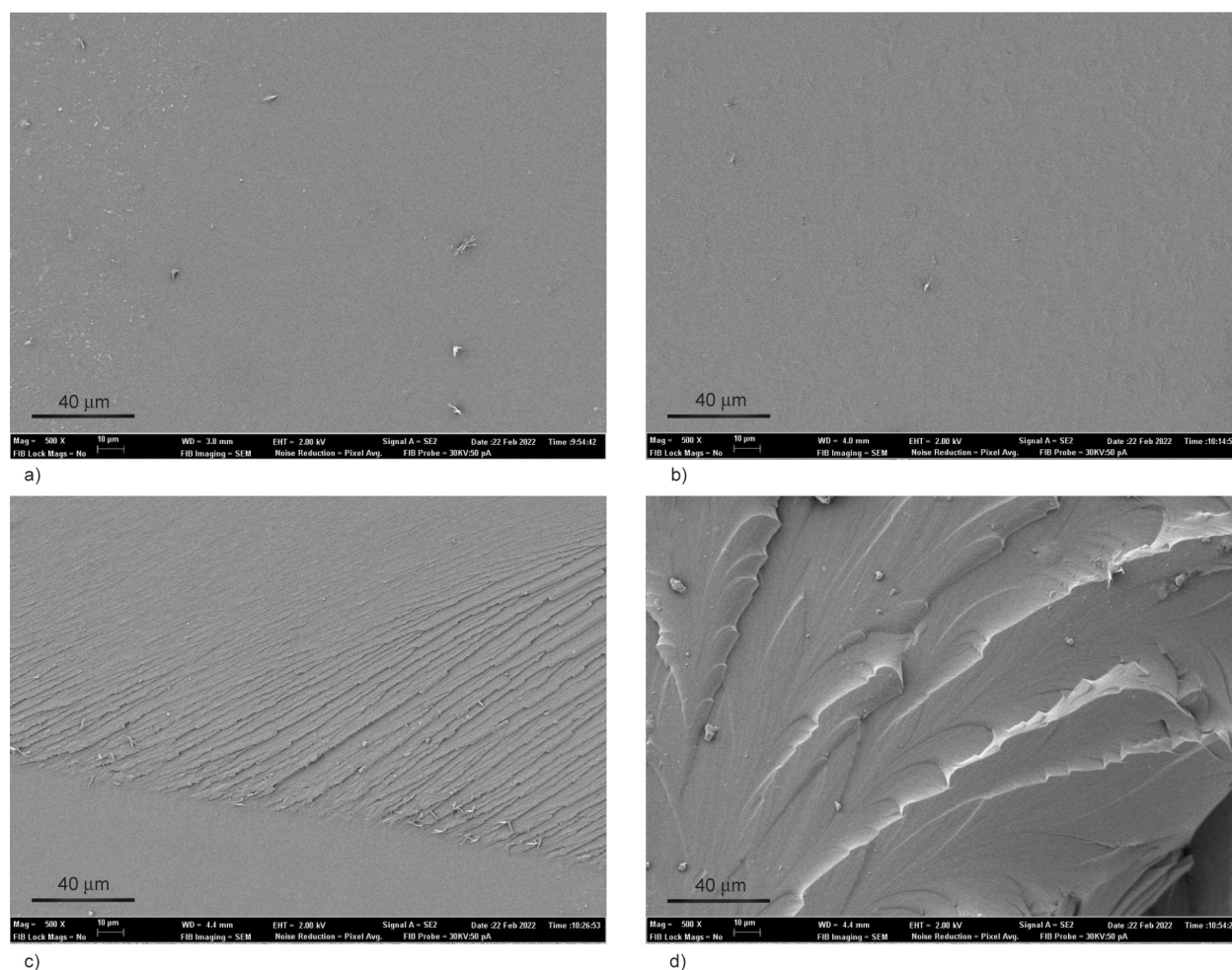


**Figure 8.** Field emission scanning electron microscopy (FESEM) images corresponding to fractured samples of crosslinked EBNO with a mixture of MHPA:MBNO, a) MHPA100, b) MHPA90:MBNO10, c) MHPA80:MBNO20 and d) MHPA70:MBNO30.

developed using MBNO as a crosslinker results in a ductile and flexible resin, as evidenced by a decrease in its flexural strength from 210 to 5.6 MPa and an increase in its toughness from 1.4 to 6.5 kJ·m<sup>-2</sup> for a sample with 30% MBNO. Additionally, at the thermal level, the addition of this new bio-based crosslinker leads to lower peak temperatures, with a reduction of 15 °C compared to the use of petrochemical hardeners, which can result in lower energy costs during the crosslinking process. FESEM images corroborate the ductile properties of the developed resins. Finally, based on the obtained results, it can be concluded that a bio-based thermosetting resin has been developed using EBNO as matrix and MBNO as crosslinker, achieving over 75% bio-based resin. This resin, with high ductile properties, minimises the risk of impact breakage and rapid crack propagation, making it a promising thermosetting material for applications where mechanical

stress is low or even for coatings. In future works, the intention is to study the incorporation of natural reinforcements (natural fibers) into the optimal resin-crosslinker formulation to achieve composite materials with higher stiffness and sustainability.

### Acknowledgements

This research work was funded by the Ministry of Science and Innovation – ‘Retos de la Sociedad’. Project references: PID2020-119142RA-I00.

### References

- [1] Quirino R. L., Monroe K., Fleischer III C. H., Biswas E., Kessler M. R.: Thermosetting polymers from renewable sources. *Polymer International*, **70**, 167–180 (2021). <https://doi.org/10.1002/pi.6132>
- [2] Mohan P.: A critical review: The modification, properties, and applications of epoxy resins. *Polymer-Plastics Technology and Engineering*, **52**, 107–125 (2013). <https://doi.org/10.1080/03602559.2012.727057>







- [3] Shieh P., Zhang W., Husted K. E., Kristufek S. L., Xiong B., Lundberg D. J., Lem J., Veyssat D., Sun Y., Nelson K. A., Plata D. L., Johnson J. A.: Cleavable comonomers enable degradable, recyclable thermoset plastics. *Nature*, **583**, 542–547 (2020).  
<https://doi.org/10.1038/s41586-020-2495-2>
- [4] Ma S., Webster D. C.: Degradable thermosets based on labile bonds or linkages: A review. *Progress in Polymer Science*, **76**, 65–110 (2018).  
<https://doi.org/10.1016/j.progpolymsci.2017.07.008>
- [5] Wang B., Wang Y., Du S., Zhu J., Ma S.: Upcycling of thermosetting polymers into high-value materials. *Materials Horizons*, **10**, 41–51 (2023).  
<https://doi.org/10.1039/D2MH01128J>
- [6] Flint S., Markle T., Thompson S., Wallace E.: Bisphenol A exposure, effects, and policy: A wildlife perspective. *Journal of Environmental Management*, **104**, 19–34 (2012).  
<https://doi.org/10.1016/j.jenvman.2012.03.021>
- [7] Chen J., Chu N., Zhao M., Jin F-L., Park S-J.: Synthesis and application of thermal latent initiators of epoxy resins: A review. *Journal of Applied Polymer Science*, **137**, 49592 (2020).  
<https://doi.org/10.1002/app.49592>
- [8] Yu Z., Ma S., Tang Z., Liu Y., Xu X., Li Q., Zhang K., Wang B., Wang S., Zhu J.: Amino acids as latent curing agents and their application in fully bio-based epoxy resins. *Green Chemistry*, **23**, 6566–6575 (2021).  
<https://doi.org/10.1039/D1GC02126E>
- [9] Gonçalves F. A., Santos M., Cernadas T., Ferreira P., Alves P.: Advances in the development of biobased epoxy resins: Insight into more sustainable materials and future applications. *International Materials Reviews*, **67**, 119–149 (2022).  
<https://doi.org/10.1080/09506608.2021.1915936>
- [10] Bobade S. K., Paluvai N. R., Mohanty S., Nayak S.: Bio-based thermosetting resins for future generation: A review. *Polymer-Plastics Technology and Engineering*, **55**, 1863–1896 (2016).  
<https://doi.org/10.1080/03602559.2016.1185624>
- [11] Galià M., de Espinosa L. M., Ronda J. C., Lligadas G., Cádiz V.: Vegetable oil-based thermosetting polymers. *European Journal of Lipid Science and Technology*, **112**, 87–96 (2010).  
<https://doi.org/10.1002/ejlt.200900096>
- [12] Wang X., Niu H., Guo W., Song L., Hu Y.: Cardanol as a versatile platform for fabrication of bio-based flame-retardant epoxy thermosets as DGEBA substitutes. *Chemical Engineering Journal*, **421**, 129738 (2021).  
<https://doi.org/10.1016/j.cej.2021.129738>
- [13] Feghali E., van de Pas D. J., Parrott A. J., Torr K. M.: Biobased epoxy thermoset polymers from depolymerized native hardwood lignin. *ACS Macro Letters*, **9**, 1155–1160 (2020).  
<https://doi.org/10.1021/acsmacrolett.0c00424>
- [14] Jawerth M. E., Brett C. J., Terrier C., Larsson P. T., Lawoko M., Roth S. V., Lundmark S., Johansson M.: Mechanical and morphological properties of lignin-based thermosets. *ACS Applied Polymer Materials*, **2**, 668–676 (2020).  
<https://doi.org/10.1021/acsapm.9b01007>
- [15] Ma S., Liu X., Jiang Y., Tang Z., Zhang C., Zhu J.: Bio-based epoxy resin from itaconic acid and its thermosets cured with anhydride and comonomers. *Green Chemistry*, **15**, 245–254 (2013).  
<https://doi.org/10.1039/C2GC36715G>
- [16] Liu C., Zhang Y., Li X., Luo J., Gao Q., Li J.: ‘Green’ bio-thermoset resins derived from soy protein isolate and condensed tannins. *Industrial Crops and Products*, **108**, 363–370 (2017).  
<https://doi.org/10.1016/j.indcrop.2017.06.057>
- [17] Aouf C., Benyahya S., Esnouf A., Caillol S., Boutevin B., Fulcrand H.: Tara tannins as phenolic precursors of thermosetting epoxy resins. *European Polymer Journal*, **55**, 186–198 (2014).  
<https://doi.org/10.1016/j.eurpolymj.2014.03.034>
- [18] de Espinosa L. M., Meier M. A.: Plant oils: The perfect renewable resource for polymer science?! *European Polymer Journal*, **47**, 837–852 (2011).  
<https://doi.org/10.1016/j.eurpolymj.2010.11.020>
- [19] Tschan M. J-L., Brulé E., Haquette P., Thomas C. M.: Synthesis of biodegradable polymers from renewable resources. *Polymer Chemistry*, **3**, 836–851 (2012).  
<https://doi.org/10.1039/C2PY00452F>
- [20] Alam M., Akram D., Sharmin E., Zafar F., Ahmad S.: Vegetable oil based eco-friendly coating materials: A review article. *Arabian Journal of Chemistry*, **7**, 469–479 (2014).  
<https://doi.org/10.1016/j.arabjc.2013.12.023>
- [21] Janković M. R., Govedarica O. M., Sinadinović-Fišer S. V.: The epoxidation of linseed oil with *in situ* formed peracetic acid: A model with included influence of the oil fatty acid composition. *Industrial Crops and Products*, **143**, 111881 (2020).  
<https://doi.org/10.1016/j.indcrop.2019.111881>
- [22] Carbonell-Verdu A., Garcia-Garcia D., Dominici F., Torre L., Sanchez-Nacher L., Balart R.: PLA films with improved flexibility properties by using maleinized cottonseed oil. *European Polymer Journal*, **91**, 248–259 (2017).  
<https://doi.org/10.1016/j.eurpolymj.2017.04.013>
- [23] Dominguez-Candela I., Gomez-Caturla J., Cardona S., Lora-Garcia J., Fombuena V.: Novel compatibilizers and plasticizers developed from epoxidized and maleinized chia oil in composites based on PLA and chia seed flour. *European Polymer Journal*, **173**, 111289 (2022).  
<https://doi.org/10.1016/j.eurpolymj.2022.111289>

- [24] Bueno-Ferrer C., Garrigós M., Jiménez A.: Characterization and thermal stability of poly(vinyl chloride) plasticized with epoxidized soybean oil for food packaging. *Polymer Degradation and Stability*, **95**, 2207–2212 (2010).  
<https://doi.org/10.1016/j.polymdegradstab.2010.01.027>
- [25] Sanders T.: Groundnut (peanut) oil. in ‘Vegetable oil in food technology: Composition, properties, and uses’ (ed Ginstone F. D.) Blakckwell Publishing, Oxford, 225–242 (2011).
- [26] Tiefenbacher K.: Technology of main ingredients – Sweeteners and lipids. in ‘Wafer and waffle’ (ed.: Tiefenbacher K. F.:) Elsevier, Amsterdam 123–225 (2017).  
<https://doi.org/10.1016/B978-0-12-809438-9.00003-X>
- [27] Bueno Ferrer C., Hablot E., Perrin-Sarazin F., Garrigos M.C., Jimenez A., Averous L.: Structure and morphology of new bio-based thermoplastic polyurethanes obtained from dimeric fatty acids. *Macromolecular Materials and Engineering*, **297**, 777–784 (2012).  
<https://doi.org/10.1002/mame.201100278>
- [28] Krist S.: Brazil nut oil. in ‘Vegetable fats and oils’ (ed.: Krist S.) Springer, Cham, 159–164 (2020).  
[https://doi.org/10.1007/978-3-030-30314-3\\_23](https://doi.org/10.1007/978-3-030-30314-3_23)
- [29] Kluczkowski A. M., Martins M., Mundim S. M., Simoes R. H., Nascimento K. S., Marinho H. A., Junior A. K.: Properties of brazil nuts: A review. *African Journal of Biotechnology*, **14**, 642–648 (2015).  
<https://doi.org/10.5897/AJB2014.14184>
- [30] Chunhieng T., Goli T., Piombo G., Pioch D., Brochier J., Montet D.: Recent analysis of the composition of brazil nut *bertholletia excelsa*. *Bois et Forêts des Tropiques*, **208**, 91–98 (2004).
- [31] Tan S., Chow W.: Biobased epoxidized vegetable oils and its greener epoxy blends: A review. *Polymer-Plastics Technology and Engineering*, **49**, 1581–1590 (2010).  
<https://doi.org/10.1080/03602559.2010.512338>
- [32] Gerbase A. E., Petzhold C. L., Costa A. P. O.: Dynamic mechanical and thermal behavior of epoxy resins based on soybean oil. *Journal of the American Oil Chemists’ Society*, **79**, 797–802 (2002).  
<https://doi.org/10.1007/s11746-002-0561-z>
- [33] Miyagawa H., Mohanty A. K., Misra M., Drzal L. T.: Thermo-physical and impact properties of epoxy containing epoxidized linseed oil, 1. *Macromolecular Materials and Engineering*, **289**, 629–635 (2004).  
<https://doi.org/10.1002/mame.200400004>
- [34] Ashcroft W.: Curing agents for epoxy resins. in ‘Chemistry and technology of epoxy resins’ (Ed.: Ellis B.) Springer, Cham, 37–71 (1993).  
[https://doi.org/10.1007/978-94-011-2932-9\\_2](https://doi.org/10.1007/978-94-011-2932-9_2)
- [35] Ding C., Matharu A. S.: Recent developments on biobased curing agents: A review of their preparation and use. *ACS Sustainable Chemistry and Engineering*, **2**, 2217–2236 (2014).  
<https://doi.org/10.1021/sc500478f>
- [36] Li Y., Xiao F., Wong C.: Novel, environmentally friendly crosslinking system of an epoxy using an amino acid: Tryptophan-cured diglycidyl ether of bisphenol A epoxy. *Journal of Polymer Science Part A: Polymer Chemistry*, **45**, 181–190 (2007).  
<https://doi.org/10.1002/pola.21742>
- [37] Fombuena V., Sánchez-Nácher L., Samper M. D., Juárez D., Balart R.: Study of the properties of thermoset materials derived from epoxidized soybean oil and protein fillers. *Journal of the American Oil Chemists’ Society*, **90**, 449–457 (2013).  
<https://doi.org/10.1007/s11746-012-2171-2>
- [38] Pin J-M., Sbirrazzuoli N., Mija A.: From epoxidized linseed oil to bioresin: An overall approach of epoxy/anhydride cross-linking. *ChemSusChem*, **8**, 1232–1243 (2015).  
<https://doi.org/10.1002/cssc.201403262>
- [39] Omonov T. S., Curtis J. M.: Biobased epoxy resin from canola oil. *Journal of Applied Polymer Science*, **131**, 40142 (2014).  
<https://doi.org/10.1002/app.40142>
- [40] Stemmelen M., Pessel F., Lapinte V., Caillol S., Habas J-P., Robin J-J.: A fully biobased epoxy resin from vegetable oils: From the synthesis of the precursors by thiol-ene reaction to the study of the final material. *Journal of Polymer Science Part A: Polymer Chemistry*, **49**, 2434–2444 (2011).  
<https://doi.org/10.1002/pola.24674>
- [41] Chen Y., Xi Z., Zhao L.: Curing kinetics of bio-based epoxy resin based on epoxidized soybean oil and green curing agent. *AIChE Journal*, **63**, 147–153 (2017).  
<https://doi.org/10.1002/aic.15486>
- [42] Samper M. D., Ferri J. M., Carbonell-Verdu A., Balart R., Fenollar O.: Properties of biobased epoxy resins from epoxidized linseed oil (ELO) crosslinked with a mixture of cyclic anhydride and maleinized linseed oil. *Express Polymer Letters*, **13**, 407–418 (2019).  
<https://doi.org/10.3144/expresspolymlett.2019.34>
- [43] Fombuena V., Petrucci R., Dominici F., Jorda-Vilaplana A., Montanes N., Torre L.: Maleinized linseed oil as epoxy resin hardener for composites with high bio content obtained from linen byproducts. *Polymers*, **11**, 18 (2019).  
<https://doi.org/10.3390/polym11020301>
- [44] Dominguez-Candela I., Lerma-Canto A., Cardona S. C., Lora J., Fombuena V.: Physicochemical characterization of novel epoxidized vegetable oil from chia seed oil. *Materials*, **15**, 3250 (2022).  
<https://doi.org/10.3390/ma15093250>
- [45] Perez-Nakai A., Lerma-Canto A., Dominguez-Candela I., Garcia-Garcia D., Ferri J. M., Fombuena V.: Comparative study of the properties of plasticized polylactic acid with maleinized hemp seed oil and a novel maleinized brazil nut seed oil. *Polymers*, **13**, 2376 (2021).  
<https://doi.org/10.3390/polym13142376>

- [46] Niedermann P., Szebényi G., Toldy A.: Effect of epoxidized soybean oil on curing, rheological, mechanical and thermal properties of aromatic and aliphatic epoxy resins. *Journal of Polymers and the Environment*, **22**, 525–536 (2014).  
<https://doi.org/10.1007/s10924-014-0673-8>
- [47] España J., Sánchez-Nacher L., Boronat T., Fombuena V., Balart R.: Properties of biobased epoxy resins from epoxidized soybean oil (ESBO) cured with maleic anhydride (MA). *Journal of the American Oil Chemists' Society*, **89**, 2067–2075 (2012).  
<https://doi.org/10.1007/s11746-012-2102-2>
- [48] De B., Gupta K., Mandal M., Karak N.: Biodegradable hyperbranched epoxy from castor oil-based hyperbranched polyester polyol. *ACS Sustainable Chemistry and Engineering*, **2**, 445–453 (2014).  
<https://doi.org/10.1021/sc400358b>
- [49] Kim J. R., Sharma S.: The development and comparison of bio-thermoset plastics from epoxidized plant oils. *Industrial Crops and Products*, **36**, 485–499 (2012).  
<https://doi.org/10.1016/j.indcrop.2011.10.036>
- [50] Ferri J. M., Garcia-Garcia D., Montanes N., Fenollar O., Balart R.: The effect of maleinized linseed oil as biobased plasticizer in poly(lactic acid)-based formulations. *Polymer International*, **66**, 882–891 (2017).  
<https://doi.org/10.1002/pi.5329>
- [51] Vlachos N., Skopelitis Y., Psaroudaki M., Konstantinidou V., Chatzilazarou A., Tegou E.: Applications of fourier transform-infrared spectroscopy to edible oils. *Analytica Chimica Acta*, **573**, 459–465 (2006).  
<https://doi.org/10.1016/j.aca.2006.05.034>
- [52] Maia D. L. H., Fernandes F. A. N.: Influence of carboxylic acid in the production of epoxidized soybean oil by conventional and ultrasound-assisted methods. *Biomass Conversion and Biorefinery*, **12**, 5861–5868 (2022).  
<https://doi.org/10.1007/s13399-020-01130-0>
- [53] Vianello C., Piccolo D., Lorenzetti A., Salzano E., Maschio G.: Study of soybean oil epoxidation: Effects of sulfuric acid and the mixing program. *Industrial and Engineering Chemistry Research*, **57**, 11517–11525 (2018).  
<https://doi.org/10.1021/acs.iecr.8b01109>
- [54] Mistri E., Routh S., Ray D., Sahoo S., Misra M.: Green composites from maleated castor oil and jute fibres. *Industrial Crops and Products*, **34**, 900–906 (2011).  
<https://doi.org/10.1016/j.indcrop.2011.02.008>
- [55] Dominguez-Candela I., Perez-Nakai A., Torres-Roca E., Lora-Garcia J., Fombuena V.: Development of a novel epoxy resin based on epoxidized chia oil as matrix and maleinized chia oil as bio-renewable crosslinker. *Journal of Applied Polymer Science*, **140**, 53574 (2023).  
<https://doi.org/10.1002/app.53574>
- [56] Lerma-Canto A., Samper M. D., Dominguez-Candela I., Garcia-Garcia D., Fombuena V.: Epoxidized and maleinized hemp oil to develop fully bio-based epoxy resin based on anhydride hardeners. *Polymers*, **15**, 1404 (2023).  
<https://doi.org/10.3390/polym15061404>
- [57] Samper M. D., Fombuena V., Boronat T., Garcia-Sanoguera D., Balart R.: Thermal and mechanical characterization of epoxy resins (ELO and ESO) cured with anhydrides. *Journal of the American Oil Chemists Society*, **89**, 1521–1528 (2012).  
<https://doi.org/10.1007/s11746-012-2041-y>
- [58] Rusmirović J. D., Radoman T., Džunuzović E. S., Džunuzović J. V., Markovski J., Spasojević P., Marinković A. D.: Effect of the modified silica nanofiller on the mechanical properties of unsaturated polyester resins based on recycled polyethylene terephthalate. *Polymer Composites*, **38**, 538–554 (2017).  
<https://doi.org/10.1002/pc.23613>
- [59] Boonlert-uthai T., Taki K., Somwangthanaroj A.: Curing behavior, rheological, and thermal properties of DGEBA modified with synthesized BPA/PEG hyperbranched epoxy after their photo-initiated cationic polymerization. *Polymers*, **12**, 2240 (2020).  
<https://doi.org/10.3390/polym12102240>

Research article

# Correlation between solution relative viscosity and the microstructural properties of the poly(3-hydroxybutyrate-co-3-hydroxyvalerate) – PHBV solution blow spun mats

Lucas Gomes Rabello<sup>1,2</sup>, Maira Rievers Nogueira Alvares<sup>1</sup>,  
Roberto Carlos da Conceição Ribeiro<sup>2</sup>, Paula Mendes Jardim<sup>1</sup>,  
Rossana Mara da Silva Moreira Thiré<sup>1\*</sup>

<sup>1</sup>Program of Metallurgical and Materials Engineering – PEMM/COPPE, Universidade Federal do Rio de Janeiro – UFRJ, 21941-598, Rio de Janeiro, Brazil

<sup>2</sup>Centre of Mineral Technology – CETEM, 21941-908, Rio de Janeiro, Brazil

Received 28 May 2023; accepted in revised form 12 September 2023

**Abstract.** In this study, we produced poly(3-hydroxybutyrate-co-3-hydroxyvalerate) (PHBV) fibrous mats via solution blow spinning (SBS) and evaluated their microstructural properties. We propose here the utilization of the theoretical estimative of relative viscosity ( $RV$ ) as an independent variable in a statistical design of experiments (DoE) to account for the polymer's molecular weight ( $M_w$ ) effect on the determination of the diameter and morphology of the fibers. The  $RV$  of the solution ( $42.3 \cdot 10^3$ – $287.4 \cdot 10^3$ ) and air pressure –  $AP$  (70–140 kPa) were varied. The analysis of variance (ANOVA) indicated that the increase in  $RV$  favored an increment in fiber size and resistance to alignment. Higher  $AP$  produced aligned and thinner fibers with higher crystallinity. The spinnability regions were determined based on the estimated  $RV$  of the PHBV solutions and the  $AP$  levels. Fibers were formed at 70 kPa from solutions with  $RV$  ranging from  $10 \cdot 10^3$  to  $10^6$ , while at 140 kPa, from  $42 \cdot 10^3$  to  $10^6$ . Nanofibers were produced from less viscous solutions ( $RV = 42.3 \cdot 10^3$ – $124.4 \cdot 10^3$ ), while microfibers were produced from solutions with  $RV = 287.4 \cdot 10^3$ . The developed ANOVA model predicted with good accuracy ( $R_{adj}^2 = 0.96$ ) the average diameter of the PHBV fibers produced from the SBS technique using polymers with distinct  $M_w$  values, including those available in the literature data.

**Keywords:** poly(hydroxy alkanoates), solution blow spinning (SBS), micro-and nanofibers, design of experiments, relative viscosity

## 1. Introduction

Polymeric micro- and nanostructured fibers capable of superior interfacial interaction within their working environment have been gaining prominence worldwide in applications such as sensing devices [1–3], air filtering [4–7], wastewater treatment [8–10], fiber-reinforced plastics [11, 12], protective clothing [13–15], and tissue engineering [16–27] due to their high surface area/volume ratio. In this sense, scientists

aware of this tendency must consider the critical need to reduce plastic waste production while selecting these materials by developing new sustainable polymers and aiming for manufacturing techniques that make them widely accessible. Under such a scenario, biodegradable biopolyesters are a creative and intelligent solution to tackle the human urge for sustainable polymeric materials and plastic waste environment pressure [28–30].

\*Corresponding author, e-mail: [rossana@metalmat.ufrj.br](mailto:rossana@metalmat.ufrj.br)

© BME-PT

Poly(3-hydroxybutyrate-*co*-3-hydroxyvalerate) – PHBV is one of the most promising biodegradable polyesters to replace petroleum-based plastics in terms of performance and reduction of plastic environmental impact. PHBV is considered environmentally friendly because of its microbiological origins, biodegradability, and null toxicity [31]. Additionally, it has a significant advantage over other polymers since it can be produced from waste materials and does not promote soil acidification and water eutrophication, like starch and corn-based biopolymers [32]. Consisting of a linear chain with randomly distributed methyl and ethyl side groups [30–40], PHBV has better processability than other hard-to-process poly(hydroxy alkanates) (PHA) and mechanical properties similar to those of high-density polyethylene (HDPE) and polypropylene (PP) [28–35, 40–42]. Besides, it has well-established applications in the manufacture of drug delivery systems [19, 34], bioabsorbable surgical sutures [19], biodegradable implants [19], biosensors [19], porous scaffolds [36–38], and food packaging [19, 41]. However, since its processability in the molten state is still inferior to those from fossil-based polymers, the referred PHA constitutes a small portion of the world's bioplastics production capacity [28, 29]. In this sense, wet-processing techniques involving polymeric solutions, such as electrospinning [16], bubble electrospinning [43], centrifugal spinning [44], and solution blow spinning (SBS) [16, 21], have garnered significant research interest for their potential to expand the polymer fiber's production capacity.

Electrospinning, for example, is a widely utilized method that employs a high electric field to draw a polymer solution into ultrafine fibers. While it offers the advantage of producing homogeneous nanometer-sized fibers, it suffers from low production rates and high energy costs, limiting its suitability for large-scale applications [16, 21]. Bubble electrospinning was developed as an alternative approach to address the production rate limitations by utilizing multiple bubbles as simultaneous fiber-drawing elements. However, despite its potential, bubble electrospinning still faces challenges in terms of high production costs associated with the demanded energy [43]. Centrifugal spinning, on the other hand, does not require high voltages since it utilizes centrifugal force to stretch and eject the polymer solution into fibers, offering higher efficiency compared to the previous methods. However, it does lack precise control over

fiber diameter [44]. In contrast, SBS has gained attention for its potential to achieve high productivity and energy efficiency. This method involves forcing a polymer solution through a nozzle while subjecting it to a high-speed gas stream as the driving force for the fiber formation. Moreover, its integration into continuous manufacturing processes makes it highly suitable for large-scale production. Consequently, SBS stands out as a promising alternative to other spinning techniques for the production of micro- and nanostructured mats [45–49].

Several biodegradable polymers, such as polylactic acid (PLA) [22, 50, 51], polycaprolactone (PCL) [20], polybutylene succinate (PBS) [52], and cellulose [21], have been used to produce micro- and nanofibrous non-woven mats. However, since SBS's advent in 2009 [53], only two papers have studied producing fibers from PHBV solutions, being of our group [54]. Souza *et al.* [55] presented a controlled release system of sodium diclofenac through drug encapsulation in PHBV nanofibers, while Carlos *et al.* [54] evaluated PLA and PHBV fiber mats via SBS encapsulating a bioactive agent system. However, these studies did not provide relevant statistical evidence to verify the influence of the processing variables on the PHBV fibers' morphology and diameter, nor did they account for the fact that distinct  $M_w$  values from the same polymer can result in drastic variations in the fibrous mats' characteristics, implying low reproducibility and application restrictions to the spun material. For example, Srinivasan *et al.* [56] produced beads on string fibers of PMMA using a weight average molecular weight  $M_w = 761 \cdot 10^3 \text{ g} \cdot \text{mol}^{-1}$  polymer. However, the same solution concentration was not spinnable at the same processing conditions when an  $M_w = 272 \cdot 10^3 \text{ g} \cdot \text{mol}^{-1}$  PMMA was utilized.

In brief, solutions are only spinnable in the semi-dilute regime with concentrations values above the overlap concentration ( $c^*$ ). The latter can be estimated by Equation (1), where  $M_w$  is the polymer molecular weight,  $R_g$  is the radius of gyration, and  $N_a$  is the Avogadro's number. Above this concentration, the polymer coils begin to entangle, increasing the solution viscosity and possibly allowing fiber formation [48, 49]. Notably, from Equation (1),  $c^*$  is not a unique value for a certain polymer/solvent system since it depends on the  $M_w$ . Thus, solutions of a high-molecular-weight polymer in general, have a lower  $c^*$  than a low-molecular-weight one,

as previously discussed by Srinivasan *et al.* [56] (Equation (1)):

$$c^* = \frac{3M_w}{4\pi R_g^3 N_a} \quad (1)$$

In contrast with the previous paragraph discussion, works have shown DoE studies for diameter and morphology prediction using the solution concentration as a processing variable of the SBS technique, not accounting for the polymer  $M_w$  effect [46, 47]. Even though these studies have found a good prediction capacity over the response variables, their results are restricted to a specific value of  $M_w$ , such as shown in the work of Srinivasan *et al.* [56], and do not solve the reproducibility problem of the spun biopolymers from natural sources.

According to Gupta *et al.* [57], the effect of the polymer concentration and  $M_w$  on the spinnability of semi-dilute solution of linear polymers are two faces of the same coin, called viscosity. These terms relate to the  $RV$  by the power law function shown in Equation (2), where  $\eta_s$  is the solvent zero-shear viscosity,  $\eta$  is the solution's zero-shear viscosity, and  $v$  is the Flory exponent (0.6 for good solvents). The authors also observed a strong correlation between the fiber's diameter and the relative viscosity ( $RV$ ) utilizing this power law dependence for the electrospinning technique. Hence, adopting the  $RV$  as a processing variable in a DoE instead of the solution concentration seems a promising approach to predict the SBS-fiber diameter and solve the low reproducibility problem that biopolymers have (Equation (2)):

$$RV = \frac{\eta}{\eta_s} = \left(\frac{c}{c^*}\right)^{\frac{3}{3v-1}} = \left(\frac{c}{c^*}\right)^{3.75} \quad (2)$$

In this sense, this study presents the generation of PHBV fibrous mats via SBS and its evaluation supported by a DoE to effectively contribute to a more efficient SBS process for producing reproducible micro- and nanofibers from PHBV. Here, we present a mathematical model developed by the experimental data collected in DoE using the  $RV$  and  $AP$  as processing variables to predict the fibers' diameter in semi-dilute solutions. In addition, the influence of these variables was also investigated on the fiber orientation and crystallinity. The same solvent (chloroform) within the same processing conditions as in the work of Carlos *et al.* [54] was used but with distinct polymer concentrations and  $M_w$  to evaluate the

model accuracy for the PHBV-spun material with the literature data.

## 2. Experimental section / methods

### 2.1. Materials

Samples were produced using PHBV with a 3-hydroxyvalerate (3HV) content of 2% [30], in powder form (ENMAT PHBV Resin Y1000P, TianAn Biologic Materials Co., Ningbo, China), gently supplied by Technische Universität Chemnitz, Germany. Chloroform stabilized with amylene (C2432), 99.5% purity, was purchased from Sigma-Aldrich, São Paulo, SP, Brazil.

### 2.2. Gel permeation chromatography (GPC)

The  $M_w$  were determined by gel permeation chromatography (GPC) with a Malvern Viscotek GPCmax chromatograph (Malvern, United Kingdom) equipped with three columns (Shodex GPC HFIP803, Shodex GPC HFIP-804 and Shodex GPC HFIP-805, Showa Denko, Tokyo, Japan). The analyses were performed in  $3 \text{ mg}\cdot\text{ml}^{-1}$  solutions using hexafluoroisopropanol (HFIP) as solvent at  $40^\circ\text{C}$  and with a constant solvent flow rate of  $1.0 \text{ ml}\cdot\text{min}^{-1}$ . A calibration curve was constructed with poly(methyl methacrylate) standards (American Polymer Standards, Mentor, USA).

### 2.3. Fiber production

The SBS system consisted of an air compressor supplied by Schulz (Joinville, Brazil), an analog manometer to adjust the air pressure, an injection pump (BSV 700 Flex Pump) provided by Biosensor (Americana, Brazil) coupled to a 12 ml syringe, an adapted injection device from core-shell fiber production containing co-axial needles [54], and a solid-static collector. Initially, the solutions of 3, 4, and 5%  $m/V$  were prepared by solubilizing the PHBV ( $M_w = 953 \cdot 10^3 \text{ g}\cdot\text{mol}^{-1}$ ) powder in chloroform under vigorous stirring at  $60^\circ\text{C}$ . Then, these were submitted to the spinning process using a distance from a static collector of 30 cm and with the same parameter used by Carlos *et al.* [54] but spun at 70 and 140 kPa.

### 2.4. Scanning electron microscopy (SEM)

The morphological analysis of PHBV fiber mats was performed by the SEM images obtained in a Hitachi TM3030Plus (Hitachi, Tokyo, Japan) equipment with a secondary electron detector (SED) at 15 kV. The fiber diameter was measured using the software

ImageJ, according to the procedure presented by Bortolassi *et al.* [58], with a minimum of 100 measurements for each SEM image. In addition, the fibers' orientation distribution was studied following Carlos *et al.* [54]. Finally, the alignment index ( $AI$  [%]) was calculated based on the method proposed by Sun *et al.* [59], utilizing, for each image analyzed, the vector field generated in the ImageJ plugin OrientationJ [60]. This method allows quantifying the fiber alignment through an index ( $AI$ ) that ranges from 0 (for totally random fibers) to 100 (for totally aligned fibers) [59].

Three SEM images ( $n = 3$ ) taken from different regions of a mat produced from a single experimental condition were evaluated to statistically represent the fibrous material's average fiber diameter and orientation [54, 58]. In the case of fiber diameter, more than 300 measurements were performed on a single fibrous mat. Additionally, ANOVA occurred utilizing the calculated average values of diameter and  $AI$  for each image (in triplicate) to increase the statistical accuracy of the estimated effects.

## 2.5. Schlieren's visualization method

The role of  $AP$  in fiber morphology was investigated using Schlieren's visualization method. This method allows for visualizing and evaluating the airflow profile as it leaves the injection device at different pressures and inferring how it affects the fiber morphology [61]. Figure 1 shows the test apparatus consisting of a point-light source, a biconvex lens of 10 cm in diameter, a thin razor positioned at twice the focal distance ( $f$ ), and a Sony Cyber-Shot DSC-HX100V (Sony, Tokyo, Japan) camera to capture the images. The emitted light gets refracted from its rectilinear path when the airflow passes between the lens and

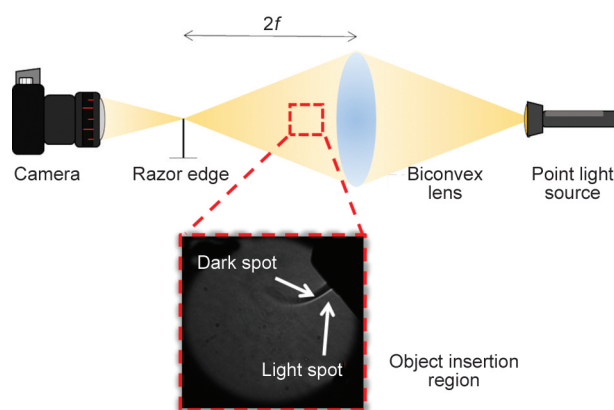


**Figure 1.** Schlieren's visualization apparatus for the airflow behavior acquisition.

the razor. If the deviation is large enough, as for the low-density regions in the airflow profile with a low refractive index, the razor blocks the light, forming dark zones in the image [61, 62]. The dashed red square in Figure 1 shows the test performed with an aerosol emitter, where light and dark zones can be seen, related to higher and lower air density regions in the aerosol flow, respectively.

## 2.6. X-ray diffraction (XRD)

The crystallographic analysis of PHBV mats was carried out in a SHIMADZU XRD-6000 diffractometer (Shimadzu, Kyoto, Japan), using  $\text{CuK}\alpha$  radiation (30 kV/ 30 mA/  $\lambda = 1,542 \text{ \AA}$ ), scanning from  $2^\circ$  to  $50^\circ$  ( $2\theta$ ), goniometer speed of  $2^\circ \cdot \text{min}^{-1}$  and step of  $0.02^\circ$ . The sample's crystallinity index ( $CI$  [%]) was determined by Equation (3), where  $A_c$  is the integrated area under the diffraction peaks and  $A_a$  is the integrated area under the amorphous region [37]. Furthermore, the interplanar distance and the crystallite size associated with the (020) and (110) planes were measured from the X-ray diffractograms employing the same experimental procedure as Souza *et al.* [55] using the software OriginPro 8.5 (Origin Lab, USA) (Equation (3)):

$$CI [\%] = \frac{A_c}{A_c + A_a} \cdot 100 \quad (3)$$

## 2.7. Solutions relative viscosity ( $RV$ ) estimation

Equation (2) was employed to estimate the solution's  $RV$ . To do so, the overlap concentration ( $c^*$ ) values for each solution were calculated via Equation (1). Additionally, the radius of gyration ( $R_g$ ) of the PHBV molecule solubilized in chloroform was inferred by converting the measured  $M_w$  values according to the function proposed by Zagar and Kržan [63].

## 2.8. Statistical evaluation

The experimental data was collected using a mixed 2-and 3-level design to assess the impact of 3, 4, and 5%  $m/V$  PHBV ( $M_w = 953 \cdot 10^3 \text{ g} \cdot \text{mol}^{-1}$ ) solutions'  $RV$  (values estimated through Equation (1) and Equation (2)) and  $AP$  on diameter and alignment. In addition, a 2-level and 2-factor design was employed to investigate crystallinity. The statistical significance of the results was determined using analysis of variance (ANOVA) with a significance level of 5% ( $p$ -value  $< 0.05$ ) [64]. Table 1 presents the variables

**Table 1.** List of the process variables and their levels based on a mixed 2-and 3-level design.

Experimental conditions	SC <sup>a</sup> [% m/V]	Independent variables	
		RV <sup>b</sup> ( $\cdot 10^3$ )	AP <sup>c</sup> [kPa]
1	3	(-1) 2.3	(-1) 70
2	3	(-1) 42.3	(1) 140
3	4	(0) 124.5	(-1) 70
4	4	(0) 124.5	(1) 140
5	5	(1) 287.5	(-1) 70
6	5	(1) 287.5	(1) 140

<sup>a</sup>SC – PHBV solution concentration;  
<sup>b</sup>RV – PHBV solution relative viscosity;  
<sup>c</sup>AP – air pressure.

and their levels, where -1, 0, and 1 denote the lowest, central, and highest levels, respectively. All the analyses were performed in triplicate ( $n = 3$ ). The developed mathematical model for the fibers' average diameter prediction has the form shown in Equation (4) and was based on the diameter experimental results collected through the mixed 2-level and 3-level design used in this work. Where  $Y$  is the response variable,  $\beta_i$  ( $i = 0, 1, 2, 3, 4,$  and  $5$ ) are the regression coefficients calculated by the ANOVA,  $X_1$  and  $X_2$  are the 3- and 2-level independent variables, respectively, and  $\epsilon$  is the random error component [46]. In addition, test fibrous mats were produced using the same experimental procedure presented in the 'Fiber's production' section and had

their morphology and average diameter measured to validate the developed model. For this purpose, solutions with concentrations ranging from 1.5 to 9%  $m/V$  were prepared employing a PHBV with distinct  $M_w$  (501, 672, and 933  $10^3 \text{ g}\cdot\text{mol}^{-1}$ ) (Equation (4)):

$$Y = \beta_0 + \beta_1 \cdot X_1 + \beta_2 \cdot X_2 + \beta_3 \cdot X_1 \cdot X_2 + \beta_4 \cdot X_1^2 + \beta_5 \cdot X_2 \cdot X_1^2 + \epsilon \quad (4)$$

### 3. Results and discussion

#### 3.1. Injection device configuration and airflow behavior in the SBS technique

Figure 2a shows the SBS apparatus used in this study, along with the fibrous mats that adhered on the collector during production. In the SBS technique, the polymeric solution is expelled from the device as a jet and directed toward the collector by accelerated airflow [45, 48, 49]. When the airflow hits the static collector, it spreads radially, assisting the formation of fibers. Figure 2b displays photographs of the injection device's nozzles during the spinning process of the same polymeric solution, spun at 70 and 140 kPa, respectively. At lower spinning pressures, the jet appears to have a laminar flow, while a dispersive one with turbulent behavior is evident at higher pressures. The latter may hinder the polymer jet's stability, induce fiber formation with varying morphologies, and create a return flow [65, 66]. Atif *et al.* [66] suggested that the convergence

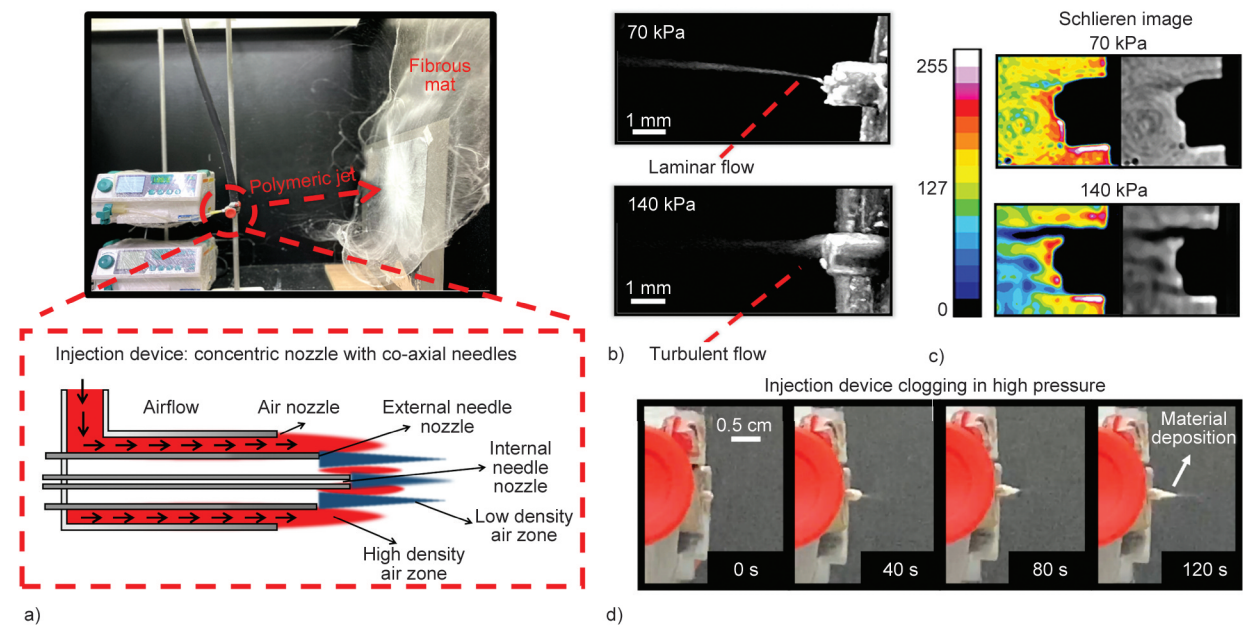


**Figure 2.** Airflow profile influence on the SBS technique: a) the SBS apparatus, the fibrous mats production, and injection device scheme; b) the polymeric jet near the nozzles photographed right after the spinning process started at 70 and 140 kPa; c) Schlieren's images of the nozzle tip at 70 and 140 kPa; d) material deposition and nozzle clogging.



of airflows in the low-pressure regions near the nozzles results in turbulence in the air motion, increasing in intensity with the released gas's velocity.

Figure 2c presents images obtained using Schlieren's method at the injection device's nozzle (right) without polymeric solution injection and with color filters (left) for enhanced visualization to support the previous discussion. It is possible to observe in Figure 2c lighter zones near the external and internal needle surfaces immediately after gas release, indicating denser air regions [61, 67]. Clearly,  $AP$  decreases significantly at the device's nozzles, creating dark, lower-density, triangular-shaped regions that cause airflow convergence to the nozzle, as predicted by Lou *et al.* [65]. This phenomenon allows the gas to increase its kinetic energy by conserving the energy lost by the drop in  $AP$ , generating the necessary driving force for solution ejection and polymer jet formation. However, contrary to what was reported by Lou *et al.* [65], up to three low-pressure zones were observed due to the injection device's configuration (adapted from a core-shell one) used in this work. The device has two concentric nozzles instead of one evaluated in the simulation presented by the authors. The low-density (dark) zones are more intense at pressures of 140 kPa than those of 70 kPa, which are difficult to observe with the adopted camera's resolution. For example, the injection device scheme shown in Figure 2a was created based on adapted literature simulations [65, 66], following the different density regions confirmed by the Schlieren images. This scheme clarifies the previous discussion by illustrating the opening for the air nozzle, the needles, and the airflow profile. Figure 2d evidences the return flow effect within the low-pressure zones at spinning pressures of 140 kPa. Notably, the needle's nozzle was entirely clogged in just 120 s due to the material deposition carried by the return flow, substantially reducing the SBS technique's productivity.

### 3.2. Processing parameters effect on the fiber morphology

Table 2 presents the estimated values of the radius of gyration ( $R_g$ ), overlap concentration ( $c^*$ ), and relative viscosity ( $RV$ ) for the solutions used in this work's DoE samples, the test samples, and the work by Carlos *et al.* [54]. The estimated  $RV$  values fall within the range of experimentally observed values for semi-dilute PHBV solutions in chloroform, as

**Table 2.** Estimate values of radius of gyration –  $R_g$  [nm], overlap concentration –  $c^*$  [%  $m/V$ ], and relative viscosity –  $RV$ .

$c^a$ [% $m/V$ ]	$R_g$ [nm]	$c^*$ [% $m/V$ ]	$c/c^*$	$RV$ ( $\cdot 10^3$ )
<b>This work design of experiment (DoE) samples (<math>M_w = 953 \cdot 10^3 \text{ g} \cdot \text{mol}^{-1}</math>)</b>				
3	60	0.17	17.13	42.3
4	60	0.17	22.84	124.4
5	60	0.17	28.55	287.4
<b>Test samples (<math>M_w = 953 \cdot 10^3 \text{ g} \cdot \text{mol}^{-1}</math>)</b>				
1.5	60	0.17	8.57	3.1
2	60	0.17	11.42	9.2
2.5	60	0.17	14.27	21.3
<b>Test samples (<math>M_w = 672 \cdot 10^3 \text{ g} \cdot \text{mol}^{-1}</math>)</b>				
3	46	0.27	10.94	7.8
4	46	0.27	14.59	23.1
5	46	0.27	18.24	53.5
6	46	0.27	21.88	106.0
7	46	0.27	25.53	189.0
8	46	0.27	29.18	311.8
9	46	0.27	40.27	1043.0
<b>Test samples (<math>M_w = 501 \cdot 10^3 \text{ g} \cdot \text{mol}^{-1}</math>)</b>				
4	43	0.25	15.98	3.2
6	43	0.25	23.98	149.3
8	43	0.25	31.97	439.3
<b>Carlos <i>et al.</i> [54] (<math>M_w = 170 \cdot 10^3 \text{ g} \cdot \text{mol}^{-1}</math>)</b>				
10	28	0.31	32.38	460.8

<sup>a</sup> $c$  – PHBV solution concentration.

reported by D'Haene *et al.* [68]. As expected, the results in Table 2 indicate that  $RV$  increases with the concentration of PHBV, which is associated with the number of entangled molecules in the solution [45]. Additionally, Table 2 shows that solutions with the same polymer content result in different  $RV$  values for varying  $M_w$ .

Equation (1) and Equation (2) demonstrate that the above-mentioned influence of polymer  $M_w$  on the estimated  $RV$  values derives from the radius of the entangled chain represented by  $R_g$  [56]. In summary, higher  $R_g$  values increase the likelihood of chain collisions and overlapping in solution, leading to the formation of molecular entanglements [45, 56]. Consequently, the increase in molecular interaction for polymers with higher  $M_w$  reduces the onset concentration for the polymeric chains to overlap ( $c^*$ ). Therefore, since  $RV$  grows exponentially with the  $c/c^*$  ratio, as seen in Equation (2), a larger  $c^*$  corresponds to a significantly lower  $RV$  [56]. For example, in 4%  $m/V$  solutions,  $c^*$  ranges from 0.25 to 0.17%  $m/V$  for PHBV  $M_w$  values of  $501 \cdot 10^3$  and  $953 \cdot 10^3 \text{ g} \cdot \text{mol}^{-1}$ ,

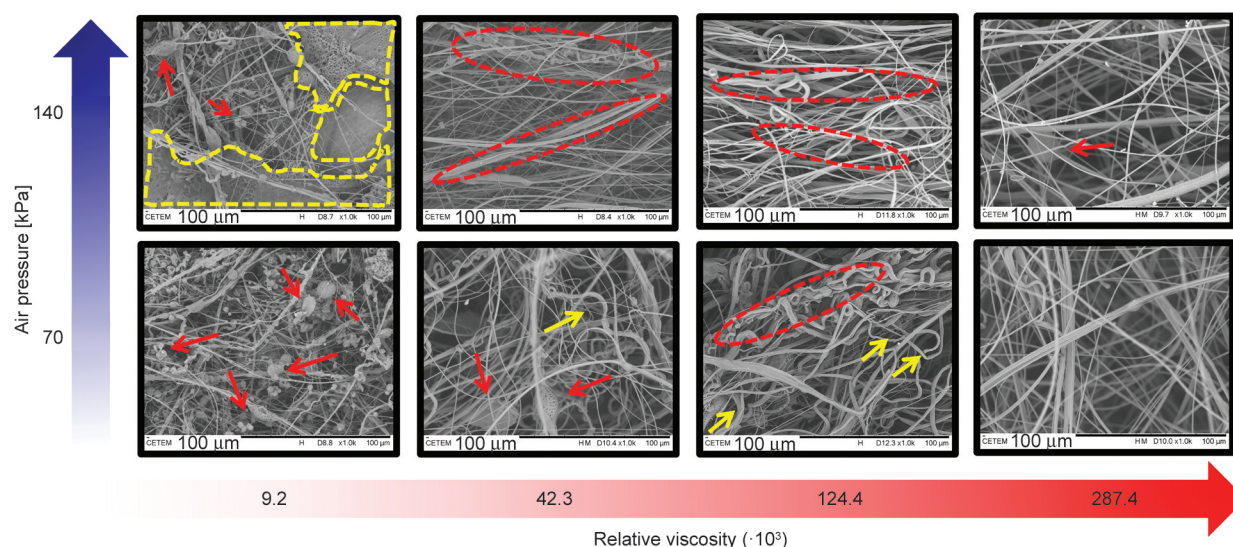
respectively, resulting in corresponding  $RV$  values of  $32.6 \cdot 10^3$  and  $124.5 \cdot 10^3$ . Thus, it is evident that changes in polymer  $M_w$  result in significant variations in solution rheology and should be taken into account in the DoE rather than solely considering the material concentration.

Figure 3 presents the SEM images of the produced PHBV mats spun from solutions with varying viscosities ( $9.2 \cdot 10^3$ ,  $42.3 \cdot 10^3$ ,  $124.4 \cdot 10^3$ , and  $287.4 \cdot 10^3$ ) and at different air pressure –  $AP$  (70 and 140 kPa) to demonstrate the effect of processing parameters on the mats' morphology. At  $RV = 9.2 \cdot 10^3$ , the solution forms fibers with many spherical structures known as beads when spun at 70 kPa. According to Dias *et al.* [49], this type of morphology is characteristic of low-viscous solutions, where the polymeric chain does not form enough entanglements to maintain fiber dimensional stability. As a result, there is sufficient mobility in the chains to form spherical structures with lower surface energy. However, at 140 kPa, cast films form along with the beaded fibers. In these circumstances, the air drag and turbulence of its flow provide instabilities in the still-liquid jet, breaking up the polymeric filament and forming a 'blown spray' deposited as a cast film [45]. For  $RV = 42.3 \cdot 10^3$  at 70 kPa, fibers were formed within a smaller amount of beads. In these conditions, the airflow turbulence effect generates a wave-like bending motion in the polymer jet, which provides filament thinning, aids in solvent evaporation, and deposits bent fibers in the collector [49, 69]. Besides the beads, fiber bundles tend to appear at

140 kPa recurrently from the simultaneous formation of different polymeric jets due to airflow turbulence near the nozzle. PHBV solutions with  $RV = 124.4 \cdot 10^3$  exhibit the same behavior, where a considerable amount of fiber bundles was reported, especially at higher pressures [45, 49].

At  $RV = 287.4 \cdot 10^3$ , the polymeric jet proved stable enough to form beaded-free fibers with controlled morphology when spun at 70 kPa. This finding supports the discussion presented by Dadol *et al.* [48], where increasing viscosity promotes bending-resistant polymeric jets, improving their stability and favoring the formation of non-bent stretched fibers without beads. However, the same solution presented a few beads when spun at 140 kPa concerning the airflow turbulence effect on the polymer jet.

Figure 4 displays a log-log plot of  $RV$  versus the  $c/c^*$  within the semi-dilute regime (where  $c$  represents the solution concentration) based on the results presented in Table 2. According to the estimated values of PHBV solutions  $RV$  and the  $AP$  levels, it is possible to determine the regions of spinnability and the fiber morphology. This determination was based on the morphological analysis discussed above (Figure 3) and the one performed over the fibers spun from the different solutions listed in Table 2 (including the analysis performed by Carlos *et al.* [54]). The results (Figure 4) suggest that a semi-dilute PHBV solution in chloroform can be classified into four different regions according to its spinnability regime. These regions are classified as follows: not spinnable – unentangled (I), spinnable – beaded fibers (II), spinnable



**Figure 3.** Fibers mat's morphology evaluation from PHBV solution with distinct  $RV$  and spun at 70 and 140 kPa. Yellow dotted region – cast film; yellow arrows – bent fibers; red dotted region – fiber bundles; red arrows – beads.

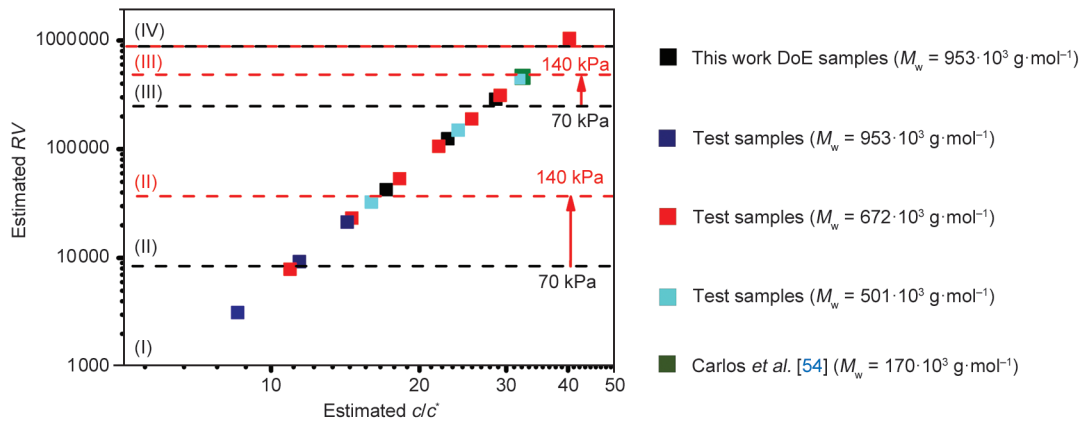


**Figure 4.** Viscometric analysis of the different PHBV solutions over its spinnability regions based on the estimated  $RV$  values as a function of the  $c/c^*$ .

– beads-free fibers (III), and not spinnable – concentrated (IV) [57].

The solution is not spinnable in Region (I), even above  $c^*$  (the onset concentration to the entanglements formation). In this case, the polymeric chains do not sufficiently entangle to sustain the liquid filament shape stability over the air drag stresses in the air/solution interface [48, 54, 57], considering the  $AP$  interval evaluated in this work. Increasing the solution  $RV$  and going to Region (II), the number of entanglements allows the fiber formation, but with spherical structures associated with it, as discussed above [49, 69]. In Region (III), beads-free fibers are formed since the number of entanglements in more viscous solutions restricts the relaxation movements in the polymeric chain that allow the bead's formation [48]. Finally, in Region (IV), the solution enters the concentrated regime, not being spinnable anymore, as the air drag does not overcome the solution's cohesive forces. In this case, the solution droplet ejected from the injection device does not form a polymeric jet. Instead, it evaporates while still in the needle, clogging the nozzle and impeding the spinning process [48, 56].

Besides the previous discussion ascertaining the  $RV$  effect on the spinnability interval, it was also observed in Figure 3 that the morphology of the mat is also affected by the  $AP$  level utilized. For instance, when the solution  $RV$  is around  $9 \cdot 10^3$ , the polymer jet breaks up, forming a spray in 140 kPa [69, 70]. On the other hand, reducing the  $AP$  allows for the formation of fibers with some beads. This occurs because the air drag exerts forces on the liquid polymeric filament, attempting to deform it by stretching the polymeric chains until it breaks. The viscosity of the solution provides resistance to these stretching

movements, affecting the behavior and stability of the jet [48, 54, 57]. In this regard, Figure 4 shows the different limits of the spinnability region for solutions spun at 70 kPa (indicated by black dashed lines) and 140 kPa (indicated by red dashed lines) based on the experimental data obtained.

Figure 4 illustrates that at 70 kPa, solutions are not spinnable for values of  $RV < 10,000$  (Region (I)). Notably, the Region (I) upper limit shifts from  $RV \sim 10,000$  to  $40,000$  for 140 kPa, increasing the minimum amount of entanglements to enable the spinning process. In Region (II), the solution starts being spinnable but with beads due to the chain mobility effect discussed previously. At  $RV \sim 290 \cdot 10^3$ , in the vicinity of Region (III) for solutions spun at 70 kPa fibers without beads were formed [45, 48, 49]. However, the airflow turbulence effect at 140 kPa shifts the upward limit of Region (II) to  $RV \sim 400 \cdot 10^3$ . Finally, for  $RV \sim 10^6$  (in Region (IV)), the resistance to solution deformation in a polymeric jet was too high, which hindered the fiber formation because the solution entered the concentrated regime [48, 49]. Note that the Region (IV) onset  $RV$  values for the solutions spun at 70 and 140 kPa are pretty much close to each other, possibly indicating that this spinnability limit is insensitive for  $AP$  variation (for the levels analyzed in this study), being governed by the viscosity increase in the transition between the semi-dilute to the concentrated regime.

Through the adopted approach for determining the morphology of the fibers, it was also possible to predict the morphology of the fibers produced in the work of Carlos et al. [54]. According to the estimated  $RV$  values based on the solution utilized in their work ( $RV = 460 \cdot 10^3$ ), the morphology should fall within the range of Region (III) for beaded-free

fibers. In fact, the authors found that using a 10% *m/V* solution of PHBV ( $M_w = 170 \cdot 10^3 \text{ g} \cdot \text{mol}^{-1}$ ) spun at  $AP = 165, 209, \text{ and } 295 \text{ kPa}$  ( $>140 \text{ kPa}$ ), PHBV fibers with a few defects could be produced, supporting the effect of  $RV$  and  $AP$  on the morphology determination.

### 3.3. Processing parameters effect on the fiber diameter

Figure 5 shows the diameter distribution histograms of each experimental condition evaluated in this work. The histograms embrace all the measurements made in a single fibrous mat, accounting for the different SEM images and totalizing more than 300 measurements. The average values in Figure 5 represent the average diameter of all the fibers analyzed in an experimental condition. The beads were discarded for fiber diameter measurements.

According to Figure 5, higher levels of solution viscosity lead to the formation of thicker fibers with greater diameter dispersion. This can be explained by the fact that a higher quantity of molecular entanglement in more viscous solutions makes it difficult for the polymeric chains to stretch and form thinner fibers [46, 47]. In addition, the formation of a more stable jet at higher viscosities with no bending movement, which would normally cause the polymeric filament to thin, results in larger diameters [66]. For example, nanometric fibers of 590 nm could be obtained at 70 kPa for a PHBV solution

with  $RV = 42.3 \cdot 10^3$ , while micrometric fibers of 1790 nm were obtained with  $RV = 287.4 \cdot 10^3$ . However, to overcome the polymer molecular interactions at higher concentrations, higher airflow shear forces are necessary, allowing the formation of fibers with smaller diameters and low deviation [66]. This effect was observed in fibers spun at 140 kPa, which had a reduced diameter compared to those spun at 70 kPa. For example, PHBV fibers from solutions of  $RV = 42.3 \cdot 10^3$  reduced their diameter by 27%, from 590 nm to 428 nm, when higher air pressure was used.

The results obtained from an ANOVA analysis through the mixed 2-and 3-level design support the earlier discussion. The linear effect of viscosity –  $RV(L)$  was found to be the most significant factor in increasing the average diameter ( $p\text{-value} = 8.5 \cdot 10^{-10}$ ). Additionally, the linear effect of pressure –  $AP(L)$  was statistically significant ( $p\text{-value} = 0.0065$ ), demonstrating the impact of airflow on fiber thinning. However, the linear interaction factor between  $AP$  and  $RV$  ( $I(L)by2(L)$ ) did not significantly affect the fiber diameter ( $p\text{-value} = 0.92$ ), indicating that changes in air pressure from 70 to 140 kPa do not depend on the viscosity levels examined in this study. Furthermore, the quadratic term of viscosity –  $RV(Q)$  ( $p\text{-value} = 0.72$ ) and its interaction factor did not have a significant influence –  $I(Q)by2(L)$  ( $p\text{-value} = 0.66$ ), indicating no quadratic relationship between solution viscosity and diameter.

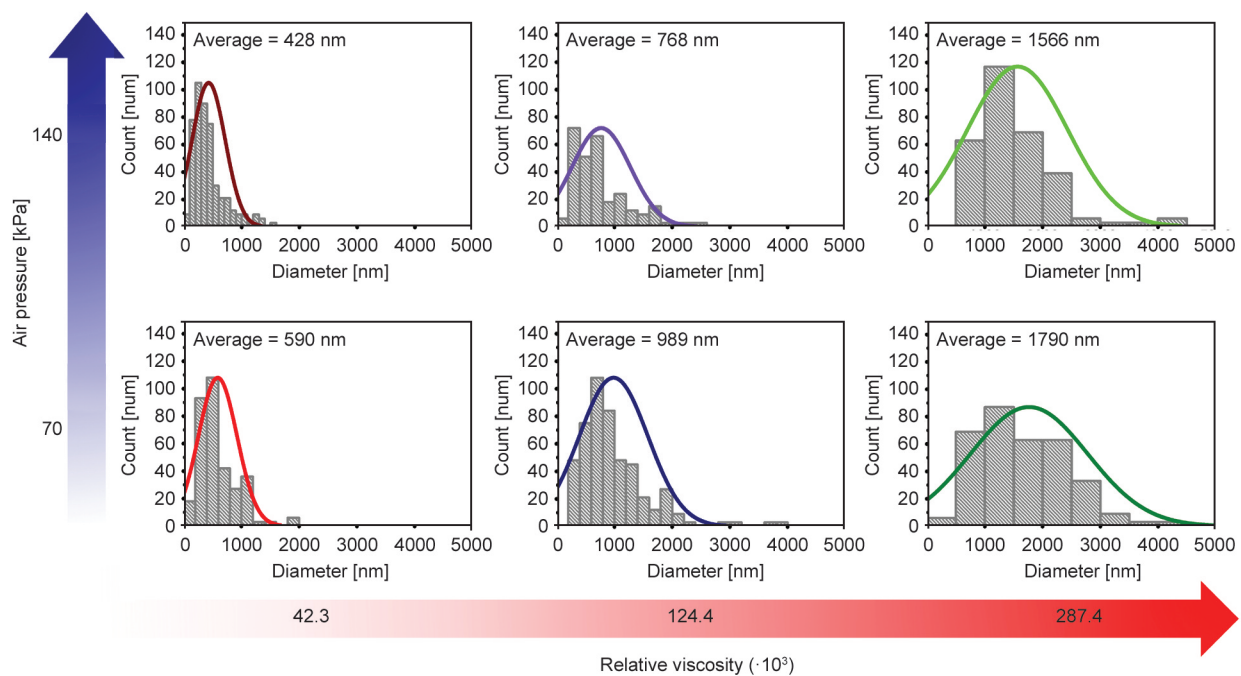


Figure 5. Measured fiber diameters and fiber diameter distribution histograms varying the PHBV solution  $RV$  and  $AP$ .

Based on the regression coefficients calculated through the ANOVA analysis, a strong correlation ( $R^2 = 0.9627 / R_{\text{adj}}^2 = 0.9574$ ) was observed between the experimental data for the average diameter and the values predicted by the mathematical model presented in Equation (5). Specifically,  $Y$  denotes the average diameter [nm],  $X_1$  represents the  $RV$ , and  $X_2$  stands for the  $AP$  [kPa]. The model, a reduced version of the one presented in Equation (4), excluded the non-influential factors, such as  $RV(Q)$ ,  $I(L)by2(L)$ , and  $I(Q)by2(L)$ . Therefore, the regression coefficients  $\beta_3$ ,  $\beta_4$ , and  $\beta_5$ , (shown in Equation (4)) correlated to each of those non-influential factors that were considered null. Additionally, the model indicates normality in the error term, and the variation

of the predicted values from the experimental consequences implies no systematic bias [46, 71]. As a result, Figure 6a displays the surface response plot generated based on the developed model for diameter prediction (Equation (5)):

$$Y = 575.11 - 2.59 \cdot X_2 + 0.004 \cdot X_1 \quad (5)$$

Figure 6b depicts the trend of predicted values versus experimental values, where the majority of experimental points overlap with the line of predicted values, affirming the accuracy of the model (Equation (5)). Therefore, to evaluate the model's predictive capability for the average diameter of PHBV fibers, Table 3 presents test samples produced from different

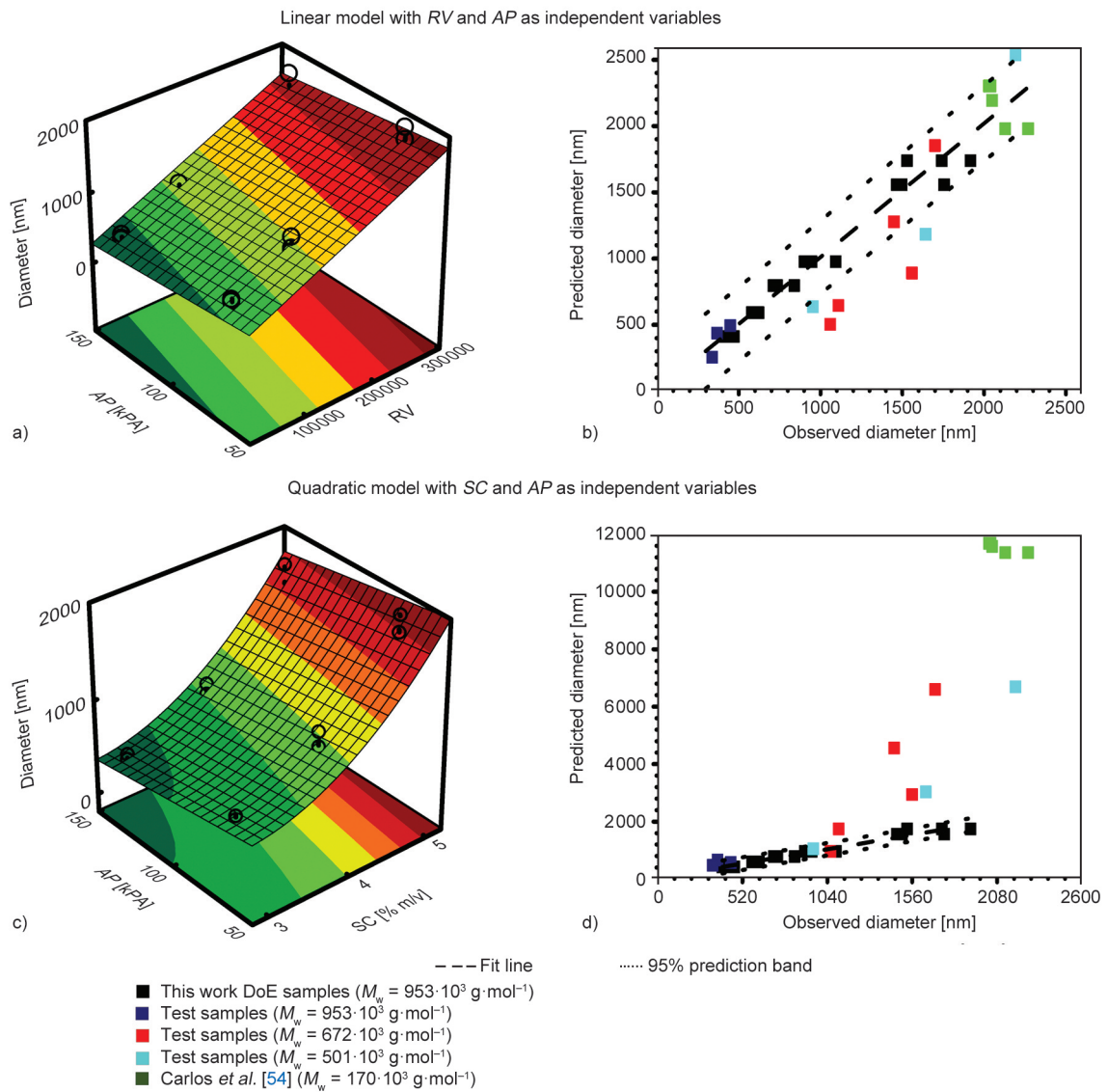


**Figure 6.** Comparison between the ANOVA models for PHBV fiber diameter prediction: a) response surface plot of diameter and b) predicted fiber diameters against experimental values from the DoE using  $RV$  and  $AP$  as independent variables; c) response surface plot of diameter and d) predicted fiber diameters against experimental values from the DoE using  $SC$  and  $AP$  as independent variables.

**Table 3.** Average diameter predicted values [nm].

<i>SC</i> [% <i>m/V</i> ]	<i>RV</i> [10 <sup>3</sup> ]	<i>AP</i> [kPa]	Predicted diameter values <sup>a</sup> [nm]	Predicted diameter values <sup>b</sup> [nm]
<b>This work DoE samples (<math>M_w = 953 \cdot 10^3 \text{ g} \cdot \text{mol}^{-1}</math>)</b>				
3	42.3	70	592	601
3	42.3	140	411	420
4	124.4	70	976	962
4	124.4	140	795	781
5	287.4	70	1737	1742
5	287.4	140	1556	1561
<b>Test samples (<math>M_w = 953 \cdot 10^3 \text{ g} \cdot \text{mol}^{-1}</math>)</b>				
2	9.2	70	437	659
2.5	21.3	70	494	578
<b>Test samples (<math>M_w = 672 \cdot 10^3 \text{ g} \cdot \text{mol}^{-1}</math>)</b>				
4	23.1	70	502	962
5	53.5	70	644	1742
6	106.0	70	890	2942
7	189.0	70	1277	4560
8	311.8	70	1851	6598
<b>Test samples (<math>M_w = 501 \cdot 10^3 \text{ g} \cdot \text{mol}^{-1}</math>)</b>				
4	32.6	35	637	1053
6	149.3	35	1183	3032
8	439.3	35	2537	6688
<b>Carlos <i>et al.</i> [54] (<math>M_w = 170 \cdot 10^3 \text{ g} \cdot \text{mol}^{-1}</math>)</b>				
10	460.8	165	2302	11 685
10	460.8	207	2193	11 576
10	460.8	290	1978	11 361

<sup>a</sup>Predicted values based on the ANOVA model using the *RV*;

<sup>b</sup>Predicted values based on the ANOVA model using *SC*.

$M_w$  with varying *RV* and *AP* values. Almost all experimental average diameters of the samples align with those predicted by the model within their respective predictive intervals (95% prediction band). Additionally, the model was also successful in predicting the fiber diameter from Carlos *et al.* [54] work.

A quadratic model was generated using PHBV solution concentration (*SC*) instead of *RV*, considering only the significant factor that provided the highest  $R_{\text{adj}}^2$  value (0.9548) based on the DoE to compare their effectiveness as independent variables in predicting the fibers' average diameter. The response surface plot in Figure 6c evidences the quadratic dependence of the average diameter with *SC* in the generated model. However, most of the test samples with varying  $M_w$ , including those from Carlos *et al.* [54] study, lie far outside the 95% prediction band, as shown in Figure 6d, which compares the predicted with the experimental values. These results suggest that concentration may not be the most suitable variable in a DoE for predicting SBS-fiber diameter, as it does not account for the impact of polymer  $M_w$  variations.

### 3.4. Processing parameters effect on the fiber orientation

In addition to changes in diameter, the *AP* and *RV* are responsible for the fiber's orientation. The air in contact with the solid and static collector spreads in the radial direction, promoting the fibers to align towards the direction of their scattering [10]. The degree or amount of this alignment depends on the resistance that the polymer jet promotes to deform in the airflow direction. In other words, the stability of the jet is also responsible for reducing the degree of the alignment of the fibers deposited in the collector [45, 66].

Having said that, in order to evaluate the influence of the processing variables on the fiber alignment, the SEM images were subjected to orientation distribution and alignment analysis using the OrientationJ plugin from ImageJ software [54, 59, 60]. The results shown in Figure 7a were obtained through orientation distribution curves, varying the fibers' orientation angles from  $-90^\circ$  to  $90^\circ$ , while Figure 7b presents the calculated alignment index (*AI*) values.

Color maps were produced to visualize the orientation distribution of the fibers in the mats [60]. In fibers produced from solution with  $RV = 42.3 \cdot 10^3$  and  $124.4 \cdot 10^3$ , the deposition angle was shown to be influenced by the effect of  $AP$ . At 70 kPa, such fibers did not show a preferential orientation, with a dispersed orientation distribution and average  $AI$  values of 60 and 63, respectively, indicating the formation of more random fibers. However, at 140 kPa, the mentioned fibers showed a preferential alignment, as can be seen in the orientation peaks close to  $0^\circ$  and new  $AI$  of 71 and 66%, respectively. On the other hand, for  $RV = 287.4 \cdot 10^3$  the effect of polymeric entanglements promoted resistance to alignment despite the air pressure value. When spun at 70 kPa, the fibers were deposited more randomly, while at 140 kPa, there was no formation of a single

orientation peak, but a more distributed curve with up to 3 peaks between  $-50^\circ$  and  $50^\circ$ . The ANOVA results based on the  $AI$  response values indicated that the drag force generated by the  $AP(L)$  is the most significant factor for the alignment of the fiber ( $p$ -value = 0.0003), followed by the  $RV(L)$  ( $p$ -value = 0.0027), corroborating with the previous discussion. In addition, the  $I(L)by2(L)$  was also influential ( $p$ -value = 0.0063), endorsing that the polymeric jet stability in more viscous solutions decreases the air drag alignment at higher  $AP$  levels. Finally, the  $RV(Q)$  also proved marginally influential ( $p$ -value = 0.0233). Thus, this work presents the possibility of obtaining PHBV fibers oriented in the radial direction using a solid and static collector, controlling the degree of this orientation through air pressure and PHBV concentration.

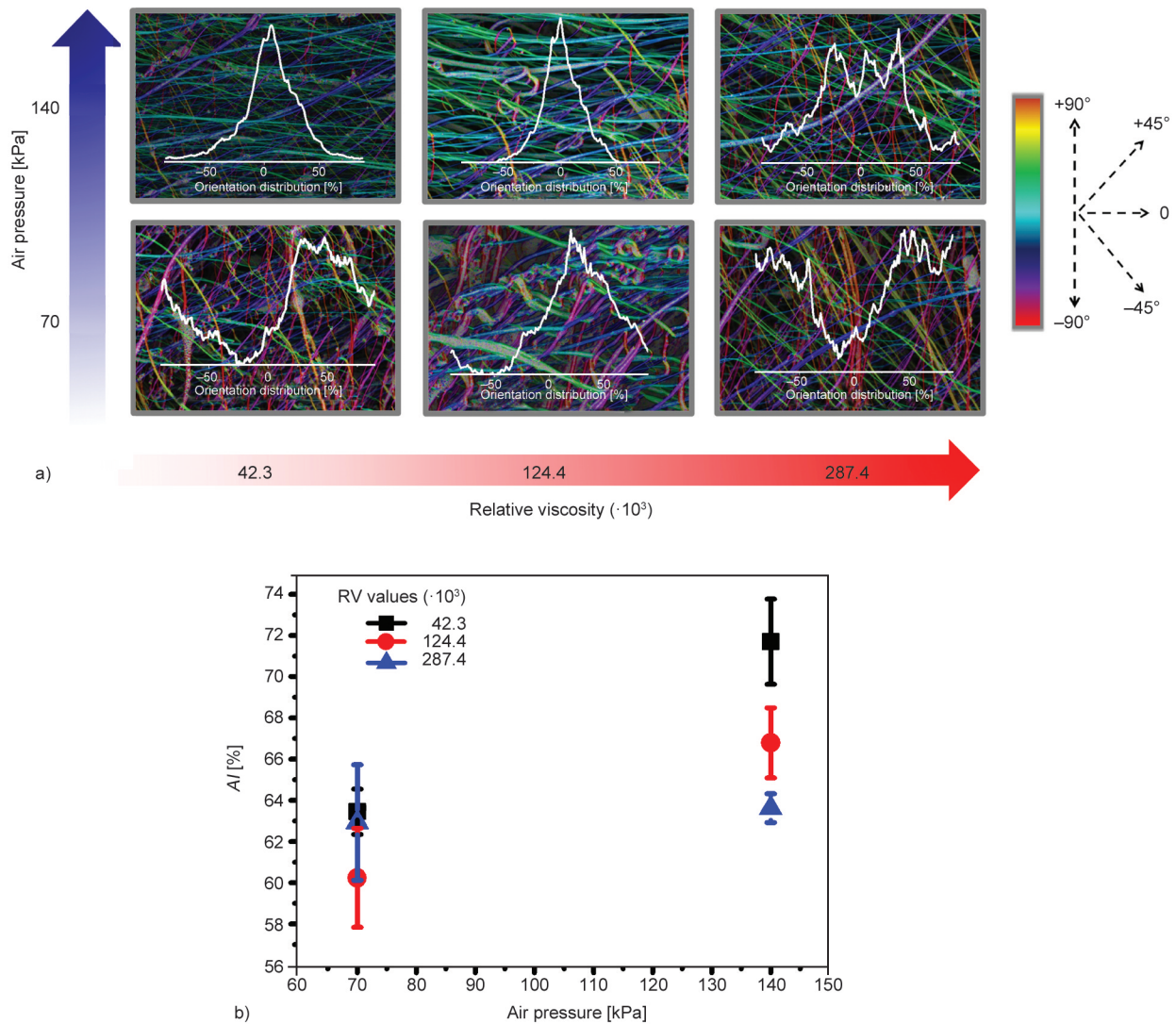
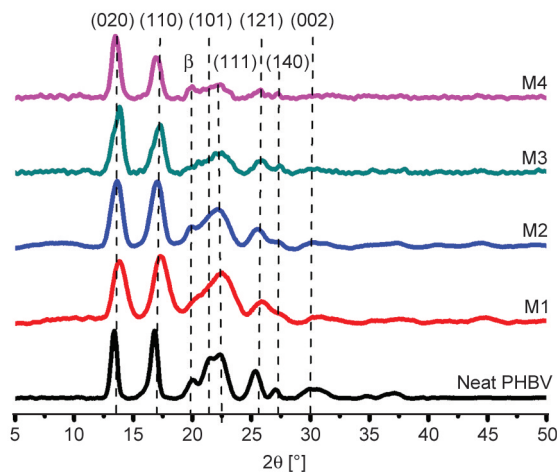


Figure 7. Fiber orientation analysis: a) mat's orientation distribution curves, and b) fibers  $AI$  response values.

### 3.5. Mats' crystalline analysis

Figure 8 presents the normalized X-ray diffractograms of the produced mats and the neat PHBV powder. Characteristic peaks of PHBV are observed for all samples at  $2\theta$  around  $14^\circ$ ,  $17^\circ$ ,  $22^\circ$ ,  $23^\circ$ ,  $26^\circ$ ,  $27^\circ$ , and  $30^\circ$ , which correspond to the planes (020), (110), (101), (111), (121), (040), and (002), respectively. These peaks refer to the helix conformation of the PHBV chains organized in an orthorhombic crystal lattice ( $\alpha$ -form) [72]. For the samples spun at 140 kPa and the neat PHBV, it was possible to observe a crystalline peak at  $20.5^\circ$ , referring to the  $\beta$ -form of the planar zig-zag conformation. According to Mottin *et al.* [73], the  $\beta$ -form depends on greater forces that induce the stretching and alignment of the polymeric chains to trap them in the planar zig-zag conformation. In addition, the  $\beta$ -form is correlated with the fibers' alignment [73], corroborating with the results observed for the AI (Figure 7). Therefore, the spinning pressure of 140 kPa favored the formation of the  $\beta$ -form in the PHBV mats crystalline lattice, which disappeared for the 70 kPa-spun samples compared to the neat material.

The effect of the spinning process parameter variations on the shape of the diffractograms' peaks that correspond to the (020) and (110) planes was evaluated using the interplanar spacing ( $d$ ) and crystallite size ( $D$ ). Figure 9a contains the measured values for  $d$  of the orthorhombic structures corresponding to the (020) and (110) planes. As can be seen, both  $d_{020}$



**Figure 8.** Mats' and neat PHBV's normalized X-ray diffractograms. M1 – mats spun at 70 kPa from solutions with  $RV = 42.3 \cdot 10^3$ ; M2 – mats spun at 140 kPa from solutions with  $RV = 42.3 \cdot 10^3$ ; M3 – mats spun at 70 kPa from solutions with  $RV = 287.4 \cdot 10^3$ ; and M4 – mats spun at 140 kPa from solutions with  $RV = 287.4 \cdot 10^3$ .

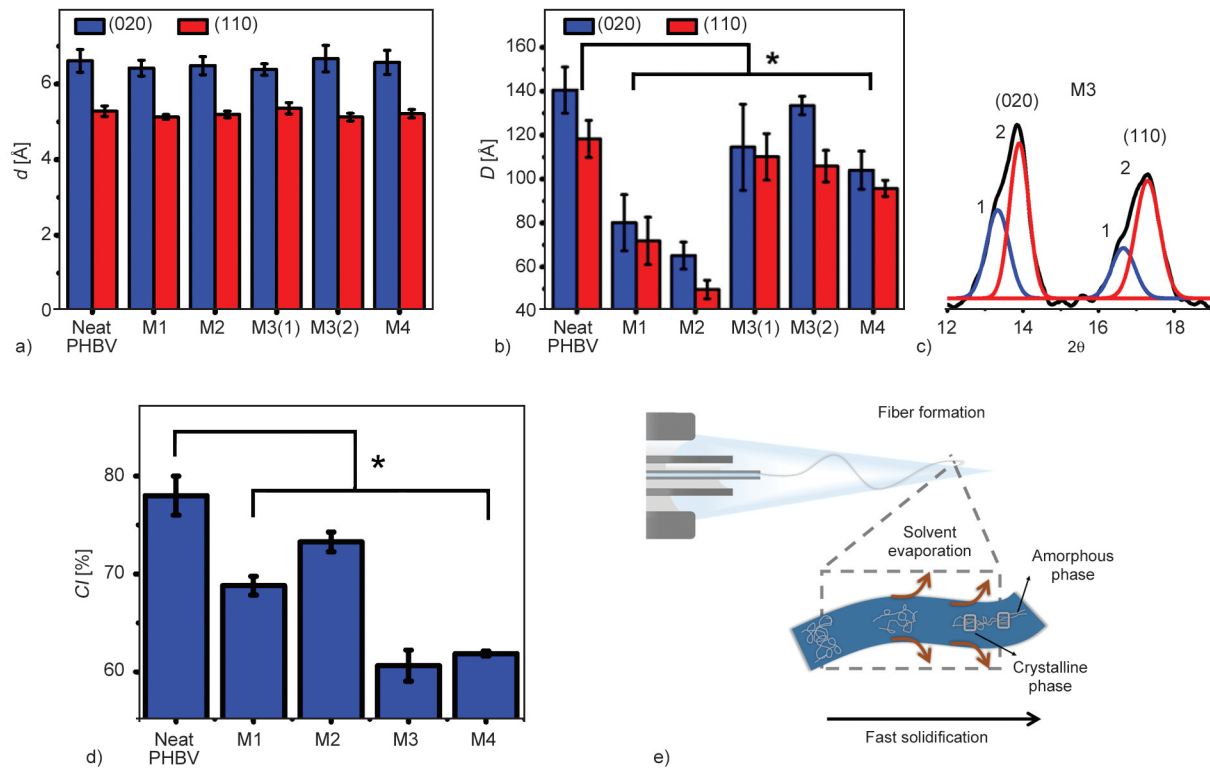
and  $d_{110}$  did not show significant variation after the spinning process compared to the neat material ( $p$ -value  $> 0.05$ ). They also remained insensitive to changes in processing parameters such as  $AP$  and  $RV$ , indicating a non-significant variation in the positioning of the crystalline peaks. Similar results were observed in the study by Souza *et al.* [55], where the type of processing undergone by PHBV did not alter the  $d$ -spacing for the same analyzed planes.

Figure 9b presents the values of  $D$  for the peaks corresponding to the (020) and (110) planes.  $D$  was significantly reduced after the spinning process compared to the neat material ( $p$ -value  $< 0.05$ ) associated with the rapid evaporation of the material during the solution blow spinning process and corroborated by the peaks broadening [55]. Similarly,  $D_{110}$  and  $D_{020}$  were affected by the levels of  $AP$  applied. Higher spinning pressures resulted in smaller crystalline structures for both (020) and (110) planes. However, an increase in viscosity led to the formation of larger crystals, narrowing the crystalline peaks. In the case of the mats produced under the M3 condition, a shoulder could be perceived in both analyzed planes (Figure 9c), indicating two different crystallite sizes. Therefore, two measurements were performed for this condition, as shown in Figures 9a and 9b as M3(1) and M3(2). The  $d$ -spacing and the crystal size followed the above-described trends for both cases.

Figure 9d shows the calculated values for the mats and neat PHBV crystallinity index [%] from the integrated area below the crystalline peaks. Notably, the SBS process is responsible for reducing the fibers' crystallinity since the neat polymer obtained a  $CI$  [%] equal to 77.4, higher than those from the produced mats ( $p$ -value  $< 0.05$ ). This effect is consistent with the literature since the fibers undergo rapid solidification during their trajectory to the collector in the SBS process, as exemplified in Figure 9e. Consequently, the degree of organization of the crystalline phase chains is reduced compared to the neat material [55].

ANOVA results for the  $CI$  [%] response indicate that the spinning conditions are significant for the spun material crystallinity.  $CI$  [%] is reduced with increasing  $RV(L)$  ( $p$ -value =  $2.4 \cdot 10^{-7}$ ) due to the restriction to chain movement into an organized crystalline lattice by the effect of the entanglements during solidification. Higher  $AP(L)$  levels were responsible for the increase in  $CI$  ( $p$ -value = 0.0017), probably related to the formation of  $\beta$ -form. The  $I(L)by2(L)$  factor





**Figure 9.** Mats' and neat PHBV's crystalline analysis: a) interplanar spacing [ $\text{\AA}$ ], b) crystallite size [ $\text{\AA}$ ], c) M3 mat's crystalline peaks deconvolution, d) crystallinity index values [%], and e) fibers solidification scheme. M1 – mats spun at 70 kPa from solutions with  $RV = 42.3 \cdot 10^3$ ; M2 – mats spun at 140 kPa from solutions with  $RV = 42.3 \cdot 10^3$ ; M3 – mats spun at 70 kPa from solutions with  $RV = 287.4 \cdot 10^3$ ; and M4 – mats spun at 140 kPa from solutions with  $RV = 287.4 \cdot 10^3$ . \* $p$ -value < 0.05.

proved marginally significant ( $p$ -value = 0.030), suggesting that the less-viscous ( $RV = 42.3 \cdot 10^3$ ) solutions are more susceptible to crystallization during the fiber formation at higher pressures than more viscous solutions ( $RV = 287.4 \cdot 10^3$ ). Finally, these results suggest that above some limit air velocity, which still must be studied, the PHBV amorphous phase tends to get re-oriented induced by air drag forces, increasing the  $CI$  [%], even though the fast solidification process significantly decreases the material crystallinity.

#### 4. Conclusion

PHBV fibrous mats were produced via SBS and had their diameter, morphology, orientation, and crystallinity evaluated through a systematic study of the processing variables. In this study, we proposed the utilization of the theoretical  $RV$  as an independent variable instead of the solution concentration to account for the polymer's  $M_w$  variation effect on the mat's properties. The ANOVA results showed that the increase in the  $RV$  favored the formation of thicker fibers ( $p$ -value =  $8.5 \cdot 10^{-10}$ ) with lower  $AI$

( $p$ -value = 0.002) and  $CI$  [%] ( $p$ -value =  $2.4 \cdot 10^{-7}$ ) values. Higher  $AP$  levels contributed to thinner ( $p$ -value = 0.0061) and more aligned fibers ( $p$ -value = 0.0001). The chain's stretching driven by air drag at 140 kPa increased the crystallinity ( $p$ -value = 0.0017) due to PHBV  $\beta$ -phase formation. Schlieren's visualization method was innovatively utilized for an SBS system with co-axial needles to visualize the airflow profile as it leaves the injection device at different pressures. It was possible to infer by the low- and high-density zones seen by Schlieren's method that the airflow at 70 kPa was more laminar when compared to 140 kPa, turbulent. The latter induced the formation of fiber bundles and beads. Based on the estimated  $RV$  and  $AP$  levels, it was also possible to identify the regions where spinning is feasible and determine the morphology of the fibers produced. Defect-free fibers could be obtained in  $RV = 290 \cdot 10^3$ – $10^6$  at 70 kPa, while for 140 kPa, between  $400 \cdot 10^3$  and  $10^6$ . The developed ANOVA model demonstrated good predictive capacity ( $R_{adj}^2 = 0.96$ ) over the average diameter of PHBV fibers produced by the SBS technique, even when

polymers with distinct  $M_w$  values were utilized. Overall, fibers with diameters varying from 428 to 989 nm were produced from PHBV solutions with  $RV = 42.3 \cdot 10^3$ – $124.4 \cdot 10^3$ , while microfibers (1.56–1.99  $\mu\text{m}$ ) from solutions  $RV = 287.4 \cdot 10^3$ . Finally, the morphology and diameter determination presented in this work via the theoretical  $RV$  estimate, aligned with a low-cost processing technique like SBS, make PHBV an attractive biodegradable material for several applications, especially those where the reproducibility in the microstructural properties directly affects its efficiency.

### Acknowledgements

The authors kindly acknowledge the Brazilian agencies Coordination of Superior Level Staff (CAPES), Fundação Carlos Chagas Filho de Amparo à Pesquisa do Estado do Rio de Janeiro (FAPERJ) and National Council for Scientific and Technological Development (CNPq) for the financial support, to the Multi-user Laboratory of Materials Characterization of the Program of Metallurgical and Materials Engineering (PEMM)/COPPE/UFRJ for XRD analysis, to the Thermal Analysis and Rheology Laboratory, located in the Center for Biofuels, Petroleum and its Derivatives (EQ/UFRJ) for the rheological experiment's assistance, and to CETEM for the SEM analysis.

### References

- [1] Li X., Zhuang Z., Qi D., Zhao C.: High sensitive and fast response humidity sensor based on polymer composite nanofibers for breath monitoring and non-contact sensing. *Sensors and Actuators B: Chemical*, **330**, 129239 (2021).  
<https://doi.org/10.1016/j.snb.2020.129239>
- [2] Wang S., Shi K., Chai B., Qiao S., Huang Z., Jiang P., Huang X.: Core-shell structured silk fibroin/PVDF piezoelectric nanofibers for energy harvesting and self-powered sensing. *Nano Materials Science*, **4**, 126–132 (2022).  
<https://doi.org/10.1016/j.nanoms.2021.07.008>
- [3] Abolhasani M. M., Azimi S., Mousavi M., Anwar S., Hassanpour Amiri M., Shirvanimoghaddam K., Naebe M., Michels J., Asadi K.: Porous graphene/poly(vinylidene fluoride) nanofibers for pressure sensing. *Journal of Applied Polymer Science*, **139**, 51907 (2022).  
<https://doi.org/10.1002/app.51907>
- [4] Souzandeh H., Wang Y., Netravali A. N., Zhong W-H.: Towards sustainable and multifunctional air-filters: A review on biopolymer-based filtration materials. *Polymer Reviews*, **59**, 651–686. (2019).  
<https://doi.org/10.1080/15583724.2019.1599391>
- [5] Xu J., Xiao X., Zhang W., Xu R., Kim S. C., Cui Y., Howard T. T., Wu E., Cui Y.: Air-filtering masks for respiratory protection from PM<sub>2.5</sub> and pandemic pathogens. *One Earth*, **3**, 574–589 (2020).  
<https://doi.org/10.1016/j.oneear.2020.10.014>
- [6] Lv D., Zhu M., Jiang Z., Jiang S., Zhang Q., Xiong R., Huang C.: Green electrospun nanofibers and their application in air filtration. *Macromolecular Materials and Engineering*, **303**, 1800336 (2018).  
<https://doi.org/10.1002/mame.201800336>
- [7] Tan N. P. B., Paclijan S. S., Ali H. N. M., Hallazgo C. M. J. S., Lopez C. J. F., Eborá Y. C.: Solution blow spinning (SBS) nanofibers for composite air filter masks. *ACS Applied Nano Materials*, **2**, 2475–2483 (2019).  
<https://doi.org/10.1021/acsanm.9b00207>
- [8] Makaremi M., De Silva R. T., Pasbakhsh P.: Electrospun nanofibrous membranes of polyacrylonitrile/halloysite with superior water filtration ability. *The Journal of Physical Chemistry C*, **119**, 7949–7958 (2015).  
<https://doi.org/10.1021/acs.jpcc.5b00662>
- [9] Park J. C., Kim J.-C., Park S., Kim D.-W.: Efficient waste polyvinyl(butylal) and cellulose composite enabled carbon nanofibers for oxygen reduction reaction and water remediation. *Applied Surface Science*, **510**, 145505 (2020).  
<https://doi.org/10.1016/j.apsusc.2020.145505>
- [10] Sow P. K., Ishita, Singhal R.: Sustainable approach to recycle waste polystyrene to high-value submicron fibers using solution blow spinning and application towards oil-water separation. *Journal of Environmental Chemical Engineering*, **8**, 102786 (2020).  
<https://doi.org/10.1016/j.jece.2018.11.031>
- [11] Hiremath N., Evora M. C., Naskar A. K., Mays J., Bhat G.: Polyacrylonitrile nanocomposite fibers from acrylonitrile-grafted carbon nanofibers. *Composites Part B: Engineering*, **130**, 64–69 (2017).  
<https://doi.org/10.1016/j.compositesb.2017.07.031>
- [12] Zheng N., Liu H.-Y., Gao J., Mai Y.-W.: Synergetic improvement of interlaminar fracture energy in carbon fiber/epoxy composites with nylon nanofiber/polycaprolactone blend interleaves. *Composites Part B: Engineering*, **171**, 320–328 (2019).  
<https://doi.org/10.1016/j.compositesb.2019.05.004>
- [13] Pham L. Q., Uspenskaya M. V., Olekhnovich R. O., Bernal R. A. O.: A review on electrospun PVC nanofibers: Fabrication, properties, and application. *Fibers*, **9**, 12 (2021).  
<https://doi.org/10.3390/fib9020012>
- [14] Karagoz S., Kiremitler N. B., Sarp G., Pekdemir S., Salem S., Goksu A. G., Onses M. S., Sozdutmaz I., Sahmetlioglu E., Ozkara E. S., Ceylan A., Yilmaz E.: Antibacterial, antiviral, and self-cleaning mats with sensing capabilities based on electrospun nanofibers decorated with ZnO nanorods and Ag nanoparticles for protective clothing applications. *ACS Applied Materials and Interfaces*, **13**, 5678–5690 (2021).  
<https://doi.org/10.1021/acsami.0c15606>

- [15] Chiu C-W., Huang C-Y., Li J-W., Li C-L.: Flexible hybrid electronics nanofiber electrodes with excellent stretchability and highly stable electrical conductivity for smart clothing. *ACS Applied Materials and Interfaces*, **14**, 42441–42453 (2022).  
<https://doi.org/10.1021/acsami.2c11724>
- [16] Kaniuk Ł., Stachewicz U.: Development and advantages of biodegradable PHA polymers based on electrospun PHBV fibers for tissue engineering and other biomedical applications. *ACS Biomaterials Science and Engineering*, **7**, 5339–5362 (2021).  
<https://doi.org/10.1021/acsbiomaterials.1c00757>
- [17] Dalgic A. D., Koman E., Karatas A., Tezcaner A., Keskin D.: Natural origin bilayer pullulan-PHBV scaffold for wound healing applications. *Biomaterials Advances*, **134**, 112554 (2022).  
<https://doi.org/10.1016/j.msec.2021.112554>
- [18] Paschoalin R. T., Traldi B., Aydin G., Oliveira J. E., Rütten S., Mattoso L. H., Zenke M., Sechi A.: Solution blow spinning fibres: New immunologically inert substrates for the analysis of cell adhesion and motility. *Acta Biomaterialia*, **51**, 161–174 (2017).  
<https://doi.org/10.1016/j.actbio.2017.01.020>
- [19] Rivera-Briso A. L., Serrano-Aroca A.: Poly(3-hydroxybutyrate-co-3-hydroxyvalerate): Enhancement strategies for advanced applications. *Polymers*, **10**, 732 (2018).  
<https://doi.org/10.3390/polym10070732>
- [20] Simbara M. M., Santos Jr A. R., Andrade A. J., Malmonge S. M.: Comparative study of aligned and non-aligned poly( $\epsilon$ -caprolactone) fibrous scaffolds prepared by solution blow spinning. *Journal of Biomedical Materials Research Part B: Applied Biomaterials*, **107**, 1462–1470 (2019).  
<https://doi.org/10.1002/jbm.b.34238>
- [21] Magaz A., Roberts A. D., Faraji S., Nascimento T. R., Medeiros E. S., Zhang W., Greenhalgh R. D., Mautner A., Li X., Blaker J. J.: Porous, aligned, and biomimetic fibers of regenerated silk fibroin produced by solution blow spinning. *Biomacromolecules*, **19**, 4542–4553 (2018).  
<https://doi.org/10.1021/acs.biomac.8b01233>
- [22] Tomecka E., Wojasinski M., Jastrzebska E., Chudy M., Ciach T., Brzozka Z.: Poly(L-lactic acid) and polyurethane nanofibers fabricated by solution blow spinning as potential substrates for cardiac cell culture. *Materials Science and Engineering: C*, **75**, 305–316 (2017).  
<https://doi.org/10.1016/j.msec.2017.02.055>
- [23] Kaniuk Ł., Ferraris S., Spriano S., Luxbacher T., Krysiak Z., Berniak K., Zaszczynska A., Marzec M. M., Bernasik A., Sajkiewicz P., Zaszczynska A., Marzec M. M., Bernasik A., Stachewicz U.: Time-dependent effects on physicochemical and surface properties of PHBV fibers and films in relation to their interactions with fibroblasts. *Applied Surface Science*, **545**, 148983 (2021).  
<https://doi.org/10.1016/j.apsusc.2021.148983>
- [24] dos Santos D. M., Correa D. S., Medeiros E. S., Oliveira J. E., Mattoso L. H.: Advances in functional polymer nanofibers: From spinning fabrication techniques to recent biomedical applications. *ACS Applied Materials and Interfaces*, **12**, 45673–45701 (2020).  
<https://doi.org/10.1021/acsami.0c12410>
- [25] Medeiros E. L. G., Braz A. L., Porto I. J., Menner A., Bismarck A., Boccaccini A. R., Lepry W. C., Nazhat S. N., Medeiros E. S., Blaker J. J.: Porous bioactive nanofibers *via* cryogenic solution blow spinning and their formation into 3D macroporous scaffolds. *ACS Biomaterials Science and Engineering*, **2**, 1442–1449 (2016).  
<https://doi.org/10.1021/acsbiomaterials.6b00072>
- [26] Kuppan P., Vasanthan K. S., Sundaramurthi D., Krishnan U. M., Sethuraman S.: Development of poly(3-hydroxybutyrate-co-3-hydroxyvalerate) fibers for skin tissue engineering: Effects of topography, mechanical, and chemical stimuli. *Biomacromolecules*, **12**, 3156–3165 (2011).  
<https://doi.org/10.1021/bm200618w>
- [27] Yilmaz S. S., Aytac A.: Fabrication and characterization as antibacterial effective wound dressing of hollow polylactic acid/polyurethane/silver nanoparticle nanofiber. *Journal of Polymer Research*, **29**, 473 (2022).  
<https://doi.org/10.1007/s10965-022-03309-7>
- [28] Singh S., Mohanty A. K., Sugie T., Takai Y., Hamada H.: Renewable resource based biocomposites from natural fiber and polyhydroxybutyrate-co-valerate (PHBV) bioplastic. *Composites Part A: Applied Science and Manufacturing*, **39**, 875–886 (2008).  
<https://doi.org/10.1016/j.compositesa.2008.01.004>
- [29] Pal A. K., Wu F., Misra M., Mohanty A. K.: Reactive extrusion of sustainable PHBV/PBAT-based nanocomposite films with organically modified nanoclay for packaging applications: Compression moulding vs. cast film extrusion. *Composites Part B: Engineering*, **198**, 108141 (2020).  
<https://doi.org/10.1016/j.compositesb.2020.108141>
- [30] Lajewski S., Mauch A., Geiger K., Bonten C.: Rheological characterization and modeling of thermally unstable poly(3-hydroxybutyrate-co-3-hydroxyvalerate) (PHBV). *Polymers*, **13**, 2294 (2021).  
<https://doi.org/10.3390/polym13142294>
- [31] Policastro G., Panico A., Fabbicino M.: Improving biological production of poly(3-hydroxybutyrate-co-3-hydroxyvalerate) (PHBV) *co*-polymer: A critical review. *Reviews in Environmental Science and Bio/Technology*, **20**, 479–513 (2021).  
<https://doi.org/10.1007/s11157-021-09575-z>
- [32] Gironi F., Piemonte V.: Bioplastics and petroleum-based plastics: Strengths and weaknesses. *Energy Sources Part A: Recovery, Utilization, and Environmental Effects*, **33**, 1949–1959 (2011).  
<https://doi.org/10.1080/15567030903436830>

- [33] Rabbani S., Jafari R., Momen G.: Superhydrophobic micro-nanofibers from PHBV-SiO<sub>2</sub> biopolymer composites produced by electrospinning. *Functional Composite Materials*, **3**, 1 (2022).  
<https://doi.org/10.1186/s42252-022-00029-5>
- [34] Liu Y., Chen X., Yu D-G., Liu H., Liu Y., Liu P.: Electrospun PVP-core/PHBV-shell fibers to eliminate tailing off for an improved sustained release of curcumin. *Molecular Pharmaceutics*, **18**, 4170–4178 (2021).  
<https://doi.org/10.1021/acsmolpharmaceut.1c00559>
- [35] Carli L. N., Bianchi O., Machado G., Crespo J. S., Mauler R. S.: Morphological and structural characterization of PHBV/organoclay nanocomposites by small angle X-ray scattering. *Materials Science and Engineering: C*, **33**, 932–937 (2013).  
<https://doi.org/10.1016/j.msec.2012.11.023>
- [36] Karbowniczek J. E., Kaniuk L., Berniak K., Gruszczynski A., Stachewicz U.: Enhanced cells anchoring to electrospun hybrid scaffolds with PHBV and HA particles for bone tissue regeneration. *Frontiers in Bioengineering and Biotechnology*, **9**, 632029 (2021).  
<https://doi.org/10.3389/fbioe.2021.632029>
- [37] de Carvalho Benini K. C. C., Ornaghi H. L., de Medeiros N. M., Pereira P. H. F., Cioffi M. O. H.: Thermal characterization and lifetime prediction of the PHBV/nanocellulose biocomposites using different kinetic approaches. *Cellulose*, **27**, 7503–7522 (2020).  
<https://doi.org/10.1007/s10570-020-03318-z>
- [38] Hammiche D., Boukerrou A., Grohens Y., Guermazi N., Arrakhiz F. E.: Mechanical properties and biodegradation of biocomposites based on poly(hydroxybutyrate-co-valerate) and alfa fibers. *Journal of Polymer Research*, **27**, 308 (2020).  
<https://doi.org/10.1007/s10965-020-02284-1>
- [39] Peshne H., Satapathy B. K.: Comparative studies of structural, thermal, mechanical, rheological and dynamic mechanical response of melt mixed PHB/bio-PBS and PHBV/bio-PBS blends. *Journal of Polymer Research*, **29**, 496 (2022).  
<https://doi.org/10.1007/s10965-022-03323-9>
- [40] Kanda G. S., Al-Qaradawi I., Luyt A. S.: Morphology and property changes in PLA/PHBV blends as function of blend composition. *Journal of Polymer Research*, **25**, 196 (2018).  
<https://doi.org/10.1007/s10965-018-1586-3>
- [41] Kaniuk L., Podborska A., Stachewicz U.: Enhanced mechanical performance and wettability of PHBV fiber blends with evening primrose oil for skin patches improving hydration and comfort. *Journal of Materials Chemistry B*, **10**, 1763–1774 (2022).  
<https://doi.org/10.1039/d1tb02805g>
- [42] Alane A., Zembouai I., Benhamida A., Zaidi L., Touati N., Kaci M.: Opuntia ficus indica fibers as reinforcement in PHBV biocomposites. *Materials Today: Proceedings*, **53**, 218–222 (2022).  
<https://doi.org/10.1016/j.matpr.2022.01.030>
- [43] Upson S. J., O’Haire T., Russell S. J., Dalgarno K., Ferreira A. M.: Centrifugally spun PHBV micro and nanofibres. *Material Science and Engineering C*, **76**, 190–195 (2017).  
<https://doi.org/10.1016/j.msec.2017.03.101>
- [44] Erben J., Kalous T., Chvojka J.: AC bubble electrospinning technology for preparation of nanofibrous mats. *ACS Omega*, **5**, 8268–8271 (2020).  
<https://doi.org/10.1021/acsomega.0c00575>
- [45] Daristotle J. L., Behrens A. M., Sandler A. D., Kofinas P.: A review of the fundamental principles and applications of solution blow spinning. *ACS Applied Materials and Interfaces*, **8**, 34951–34963 (2016).  
<https://doi.org/10.1021/acsmi.6b12994>
- [46] da Silva Parize D. D., Foschini M. M., de Oliveira J. E., Klamczynski A. P., Glenn G. M., Marconcini J. M., Mattoso L. H. C.: Solution blow spinning: Parameters optimization and effects on the properties of nanofibers from poly(lactic acid)/dimethyl carbonate solutions. *Journal of Materials Science*, **51**, 4627–4638 (2016).  
<https://doi.org/10.1007/s10853-016-9778-x>
- [47] Lou H., Li W., Li C., Wang X.: Systematic investigation on parameters of solution blown micro/nanofibers using response surface methodology based on box-behnken design. *Journal of Applied Polymer Science*, **130**, 1383–1391 (2013).  
<https://doi.org/10.1002/app.39317>
- [48] Dadol G. C., Kilic A., Tijjing L. D., Lim K. J. A., Cabatingan L. K., Tan N. P. B., Stojanovska E., Polat Y.: Solution blow spinning (SBS) and SBS-spun nanofibers: Materials, methods, and applications. *Materials Today Communications*, **25**, 101656 (2020).  
<https://doi.org/10.1016/j.mtcomm.2020.101656>
- [49] Dias F. T. G., Rempel S. P., Agnol L. D., Bianchi O.: The main blow spun polymer systems: Processing conditions and applications. *Journal of Polymer Research*, **27**, 205 (2020).  
<https://doi.org/10.1007/s10965-020-02173-7>
- [50] Ferreira K. N., Oliveira R. R., Castellano L. R., Bonan P. R., Carvalho O. V., Pena L., Souza J. R., Oliveira J. E., Medeiros E. S.: Controlled release and antiviral activity of acyclovir-loaded PLA/PEG nanofibers produced by solution blow spinning. *Biomaterials Advances*, **136**, 212785 (2022).  
<https://doi.org/10.1016/j.bioadv.2022.212785>
- [51] Oliveira J. E., Moraes E. A., Marconcini J. M., Mattoso L. H. C., Glenn G. M., Medeiros E. S.: Properties of poly(lactic acid) and poly(ethylene oxide) solvent polymer mixtures and nanofibers made by solution blow spinning. *Journal of Applied Polymer Science*, **129**, 3672–3681 (2013).  
<https://doi.org/10.1002/app.39061>
- [52] Bang J., Park S., Hwang S-W., Oh J-K., Yeo H., Jin H-J., Kwak H. W.: Biodegradable and hydrophobic nanofibrous membranes produced by solution blow spinning for efficient oil/water separation. *Chemosphere*, **312**, 137240 (2023).  
<https://doi.org/10.1016/j.chemosphere.2022.137240>

- [53] Medeiros E. S., Glenn G. M., Klamczynski A. P., Orts W. J., Mattoso L. H.: Solution blow spinning: A new method to produce micro- and nanofibers from polymer solutions. *Journal of Applied Polymer Science*, **113**, 2322–2330 (2009).  
<https://doi.org/10.1002/app.30275>
- [54] Carlos A. L. M., Mancipe J. M. A., Dias M. L., Thiré R. M. S. M.: Poly(3-hydroxybutyrate-co-3-hydroxyvalerate) core-shell spun fibers produced by solution blow spinning for bioactive agent's encapsulation. *Journal of Applied Polymer Science*, **139**, 52081 (2022).  
<https://doi.org/10.1002/app.52081>
- [55] Souza M. A., Sakamoto K. Y., Mattoso L. H. C.: Release of the diclofenac sodium by nanofibers of poly(3-hydroxybutyrate-co-3-hydroxyvalerate) obtained from electrospinning and solution blow spinning. *Journal of Nanomaterials*, **2014**, 129035 (2014).  
<https://doi.org/10.1155/2014/129035>
- [56] Srinivasan S., Chhatre S. S., Mabry J. M., Cohen R. E., McKinley G. H.: Solution spraying of poly(methyl methacrylate) blends to fabricate microtextured, superoleophobic surfaces. *Polymer*, **52**, 3209–3218 (2011).  
<https://doi.org/10.1016/j.polymer.2011.05.008>
- [57] Gupta P., Elkins C., Long T. E., Wilkes G. L.: Electrospinning of linear homopolymers of poly(methyl methacrylate): Exploring relationships between fiber formation, viscosity, molecular weight and concentration in a good solvent. *Polymer*, **46**, 4799–4810 (2005).  
<https://doi.org/10.1016/j.polymer.2005.04.021>
- [58] Bortolassi A., Guerra V., Aguiar M.: Characterization and evaluate the efficiency of different filter media in removing nanoparticles. *Separation and Purification Technology*, **175**, 79–86 (2017).  
<https://doi.org/10.1016/j.seppur.2016.11.010>
- [59] Sun M., Bloom A. B., Zaman M. H.: Rapid quantification of 3D collagen fiber alignment and fiber intersection correlations with high sensitivity. *PLOS One*, **11**, 157379 (2016).  
<https://doi.org/10.1371/journal.pone.0131814>
- [60] Rezakhaniha R., Agianniotis A., Schrauwen J. T. C., Griffa A., Sage D., Bouten C. V. C., van de Vosse F., Unser M., Stergiopoulos N.: Experimental investigation of collagen waviness and orientation in the arterial adventitia using confocal laser scanning microscopy. *Bio-mechanics and Modeling in Mechanobiology*, **11**, 461–473 (2012).  
<https://doi.org/10.1007/s10237-011-0325-z>
- [61] Tan D. H., Herman P. K., Janakiraman A., Bates F. S., Kumar S., Macosko C. W.: Influence of laval nozzles on the air flow field in melt blowing apparatus. *Chemical Engineering Science*, **80**, 342–348 (2012).  
<https://doi.org/10.1016/j.ces.2012.06.020>
- [62] Tanisali G., Sozak A., Bulut A. S., Sander T. Z., Dogan O., Dağ Ç., Gönen M., Can F., DeMirici H., Ergonul O.: Effectiveness of different types of mask in aerosol dispersion in SARS-CoV-2 infection. *International Journal of Infectious Diseases*, **109**, 310–314 (2021).  
<https://doi.org/10.1016/j.ijid.2021.06.029>
- [63] Žagar E., Kržan A.: SEC-MALS characterization of microbial polyhydroxyalkanoates. *Biomacromolecules*, **5**, 628–636 (2004).  
<https://doi.org/10.1021/bm0300731>
- [64] Rabello L. G., da Conceição Ribeiro R. C.: A novel vermiculite/ vegetable polyurethane resin-composite for thermal insulation eco-brick production. *Composites Part B: Engineering*, **221**, 109035 (2021).  
<https://doi.org/10.1016/j.compositesb.2021.109035>
- [65] Lou H., Han W., Wang X.: Numerical study on the solution blowing annular jet and its correlation with fiber morphology. *Industrial and Engineering Chemistry Research*, **53**, 2830–2838 (2014).  
<https://doi.org/10.1021/ie4037142>
- [66] Atif R., Combrinck M., Khaliq J., Hassanin A. H., Shehata N., Elnabawy E., Shyha I.: Solution blow spinning of high-performance submicron polyvinylidene fluoride fibres: Computational fluid mechanics modeling and experimental results. *Polymers*, **12**, 1140 (2020).  
<https://doi.org/10.3390/polym12051140>
- [67] Wieland M., Arne W., Marheineke N., Wegener R.: Melt-blowing of viscoelastic jets in turbulent airflows: Stochastic modeling and simulation. *Applied Mathematical Modelling*, **76**, 558–577 (2019).  
<https://doi.org/10.1016/j.apm.2019.06.023>
- [68] D'Haene P., Remsen E. E., Asrar J.: Preparation and characterization of a branched bacterial polyester. *Macromolecules*, **32**, 5229–5235 (1999).  
<https://doi.org/10.1021/ma981911k>
- [69] Benavides R. E., Jana S. C., Reneker D. H.: Nanofibers from scalable gas jet process. *ACS Macro Letters*, **1**, 1032–1036 (2012).  
<https://doi.org/10.1021/mz300297g>
- [70] Mossige E., Chandran Suja V., Islamov M., Wheeler S., Fuller G. G.: Evaporation-induced Rayleigh–Taylor instabilities in polymer solutions. *Philosophical Transactions of the Royal Society A*, **378**, 20190533 (2020).  
<https://doi.org/10.1098/rsta.2019.0533>
- [71] Shi L., Wang Y., Zhang Y., Zhuang X., Liu H., Hu Y.: Optimization of the preparation process of electrostatic-solution blow spinning nanofiber yarn using response surface methodology. *Textile Research Journal*, **92**, 4437–4449 (2022).  
<https://doi.org/10.1177/00405175221101179>
- [72] Xu Y., Zou L., Lu H., Chen Z.: Preparation and characterization of electrospun poly(3-hydroxybutyrate-co-3-hydroxyvalerate) fibrous mat. *IOP Conference Series: Materials Science and Engineering*, **87**, 012047 (2015).  
<https://doi.org/10.1088/1757-899X/87/1/012047>
- [73] Mottin A. C., Ayres E., Oréface R. L., Câmara J. J. D.: What changes in poly(3-hydroxybutyrate) (PHB) when processed as electrospun nanofibers or thermo-compression molded film? *Materials Research*, **19**, 57–66 (2016).  
<https://doi.org/10.1590/1980-5373-MR-2015-0280>

Research article

# Thermoplastic modification of polyvinyl alcohol for preparing water-splittable sea-island fiber

Bing Song<sup>1</sup>, Liang Wang<sup>1\*</sup>, Jiawei Zhao<sup>1</sup>, Yake Shen<sup>2</sup>, Xiaoming Qian<sup>1</sup>

<sup>1</sup>School of Textiles Science and Engineering, Tiangong University, 300387 Tianjin, P.R. China

<sup>2</sup>Mingxin Xuteng (Jiangsu) Innovation Research Institute Limited Company, Xinyi 221433, Jiangsu, P.R.China

Received 6 June 2023; accepted in revised form 14 September 2023

**Abstract.** Polyvinyl alcohol (PVA) is a type of water-soluble polymer that is a candidate for ‘sea’ polymer to prepare sea-island fibers in industry. In this study, two types of polyols (sorbitol ether and neopentyl glycol) were mixed in different proportions and used to prepare thermoplastic PVA (TPVA) as a compound plasticizer. When the plasticizer was introduced, a blue shift occurred on the characteristic band of hydroxyl in the Fourier transform infrared spectroscopy (FTIR) pattern. The melting temperature ( $T_m$ ) of the corresponding TPVA decreased, and their initial decomposition temperature ( $T_d$ ) increased to some degree. The addition of compound plasticizer made PVA show an improved  $T_d$  up to 273.1 °C. Moreover, it led to an increment of the melting flow index and improved the resistance to oxidation at a temperature higher than 200 °C. The increased spinnability enabled TPVA in PVA-PLA sea-island fiber making. PLA superfine fibers were obtained after splitting in water at 95 °C for just 3 min.

**Keywords:** fiber, textile processing, fiber spinning, melt-blowing, polyvinyl alcohol

## 1. Introduction

Polyvinyl alcohol (PVA) is a type of water-soluble and biodegradable polymer that is commonly used in fields such as textile, medicine, and architecture, to name a few [1–3]. PVA fibers are usually prepared through a wet-spinning technique, which generates a large amount of industrial wastewater [4, 5]. As a comparison, melting-spinning shows a higher spinning efficiency, and organic solvents are avoided during spinning. However, a large quantity of hydroxyls in PVA molecules forms strong intra/intermolecular hydrogen bonding. This makes PVA lose its thermoplastic processing window.

On the other side, thermoplastic PVA (TPVA) was desirable to be used as a ‘sea’ polymer to prepare sea-island fibers in industry. The involved sea-island fibers would be split into ultra-fine fibers through an energy-saving and efficient water-reduction process

[6, 7]. Nevertheless, there are rare reports on research or industrial practice to our best knowledge. Ultra-fine fiber is generally defined to have a diameter of less than 0.55 dtex. Owing to small fineness, the rigidity of fiber decreases exponentially, and the specific surface area of fiber increases [8, 9]. Corresponding textile products normally show a novel softness and excellent absorption or filtration properties [10–12].

The thermoplastic modification of PVA could be realized via a chemical copolymerization or physical blending. The former method introduces a second monomer to break the macromolecular tacticity of PVA. It will reduce the crystalline degree as well as the melting temperature of PVA [13, 14]. The latter strategy is more frequently reported owing to a facile operation and higher production. The addition of plasticizers with polar functional groups, such as

\*Corresponding author, e-mail: [liangwang@tiangong.edu.cn](mailto:liangwang@tiangong.edu.cn)

© BME-PT

polyols [15], is one of the most effective methods to improve the thermoplastic processing property of PVA. Generally, various plasticizers, such as glycerol or water, are blended with commercial PVA pellets in a screw extruder. This will reduce inter-molecular interaction between PVA molecules. The melting temperature of PVA usually decreases, generating a proper thermoplastic processing window [16]. Xu *et al.* [17] prepared a pseudo-ionic liquid as a plasticizer to modify the thermoplastic behavior of PVA. The cations, anions, and hydrogen bond acceptors in the plasticization system formed stronger hydrogen bonds with the hydroxyl groups of PVA. Melt-spun PVA fibers with smooth surfaces and uniform cross-sections were prepared. However, the content of plasticizer is usually higher than 30 wt%, which will significantly decrease the crystalline ability of PVA fiber. In addition, owing to the evaporation behavior, the plasticizer is easy to migrate during melt-spinning, affecting the rheological property of TPVA [18]. How to reduce the usage of plasticizers and meanwhile maintain their spinnability are urgent problems for TPVA.

Poly (lactic acid) (PLA), with good biodegradability, has become one of the most popular materials in some fields, such as tissue engineering, scaffolding, and packing [19–21]. PLA fiber and corresponding textiles raise great interest as a biodegradable candidate for realizing carbon neutralization. In this study, two types of polyols were mixed in different proportions to make a compound plasticizer that was used to prepare TPVA. The influence of plasticization on the thermal properties of PVA and hydrogen bonding interaction was studied. In addition, PVA-PLA sea-island fibers were prepared, and corresponding PLA superfine fibers were obtained after water splitting. It is of significant importance to promote the efficient and green splitting of sea-island fibers during the making superfine fibers.

## 2. Experimental

### 2.1. Materials

Polyvinyl alcohol (PVA, trademark 098-05) pellets were supplied by Anhui vinylon factory of Sinopec Co. Ltd. (Wuhu, China). Sorbitol ether (SE) and neopentyl glycol (NPG) were purchased from Aladdin Agent Co. (Shanghai, China). Polylactic acid (PLA) pellets were brought from Fengyuan Co. Ltd. (Bengbu, China).

**Table 1.** The components' ratio setting of each sample granule.

Sample ID	PVA [wt%]	SE [wt%]	NPG [wt%]
1:1	94	3	3
2:1	94	4	2
4:1	94	4.8	1.2
1:2	94	2	4
A	94	6	0
B	94	0	6

### 2.2. Thermoplastic modification of PVA

The raw PVA was plasticized using SE and NPG. The content of the plasticizer was 6 wt%, respectively. SE/NPG (A/B) proportion was 4:1, 2:1, 1:1 and 1:2, respectively. The details are included in Table 1. All components were homogeneously blended and then matured for 2 h at 80 °C. A twin-screw (RXT2, Ruiya, Nanjing, China) with a diameter of 25.4 mm, *L/D* ratio of 40, and a speed of 250 rpm was employed. The processing temperature was controlled at different zones of the extruder to obtain an ascending temperature profile from 110 to 190 °C. Those prepared granule were named thermoplastic PVA (TPVA). TPVA obtained by adding a single component of SE (A) or NPG (B) were set as blank samples.

### 2.3. Preparation of PVA and sea-island PVA/PLA pre-oriented yarn

The prepared TPVA granule and PLA pellets were dried at 90 °C in a vacuum oven for 24 h before melt-spinning, respectively. The spinning of TPVA was conducted in a single-screw spinner. After undergoing temperature ascending in the extruder in different zones (210, 215, 220, 225, 230 °C), the melt was extruded from the spinneret with 48 filaments. The spinning speed was set as 1000 m/min. The sea-island spinning was conducted on a conjugated bicomponent spinning machine (Fangchen, Zhibo, China). TPVA was used as a 'sea' ingredient in extruder A (210, 215, 220, 225, 230 °C). PLA ('island' polymer) was sequenced out by extruder B (205, 210, 220, 230, 235 °C). The temperature of the die was set as 235 °C. The sea/island component mass ratio was set as 3:7. The rolling speed was set as 1000, 1200, 1500, and 2000 m/min, respectively.

### 2.4. Characterization

Molecular dynamics simulation was carried out using the Gromacs-4.6.7 software package. The details

were described as follows. Two cubic boxes were built. One contained 100 chains of pure PVA. The other one was put in 100 PVA chains and 300 sorbitol ethers to get TPVA. The PVA was simulated at a temperature of 698 K and a pressure of 100 bar for 5 ns to enable the polymer chain to relax sufficiently. The equilibrium structure was then simulated at 298 K, 1 bar for 10 ns. All the all-atom MD simulations were based on a general AMBER force field with restrained electrostatic potential (RESP) charges [22]. The system was a relaxed liquid configuration at 298 K. We used the relaxed system as a starting configuration. As it is prior to system relaxation MD, energy minimization was carried out with a composite protocol of steepest descent using termination gradients of 100 J/(mol·nm). The particle Mesh-Ewald method [23] was used to compute long-range electrostatics within a relative tolerance of  $1 \cdot 10^{-6}$ . A cut-off distance of 1 nm was applied to real-space Ewald interactions. The same value was used for van der Waals interactions. The Library of Integrated Network-Based Cellular Signatures (LINCS) algorithm [24] was applied to constrain bond lengths of hydrogen atoms. A leap-frog algorithm was used with a time step of 2 fs.

The prepared TPVA granules have undergone a series of characterizations. Fourier Transform Infrared Spectroscopy (FTIR) spectra were recorded using a Nicolet iS50 spectrometer (Thermo Fisher Scientific, USA) with 30 scans in the 4000 to 400  $\text{cm}^{-1}$  range at room temperature. X-ray diffraction (XRD) analysis was conducted using a D8 Discover model X-ray diffractometer (Bruker, Germany) in the range of  $2\theta = 5\text{--}40^\circ$  at 40 kV and 30 mA of Cu  $K_\alpha$  radiation. Differential scanning calorimetry (DSC) patterns were recorded on an equipment Model 200F3 (Netzsch, Germany). A 10 mg specimen was heated from 30 to 250  $^\circ\text{C}$  at a ramp rate of 10  $^\circ\text{C}/\text{min}$ . Thermogravimetric analysis (TGA) is conducted on the STA449F3 thermal analyzer (Netzsch, Germany). The sample was heated at 10  $^\circ\text{C}/\text{min}$  from 30 to 800  $^\circ\text{C}$  under  $\text{N}_2$  atmosphere. The thermal oxidation property of prepared TPVA was evaluated by holding TPVA at 230 or 250  $^\circ\text{C}$  for 10 min in a TGA test in an air atmosphere (80%  $\text{N}_2$  and 20%  $\text{O}_2$ ). The rheological studies were carried out using an MCR302 (Anton Paar, Graz, Austria) rheometer having a disk geometry of 25 mm diameter. The rheometer instrument measure shear rate was up to 100  $\text{s}^{-1}$ . The melt flow index (MFI) was measured using a MFI-1221

instrument (Jinjian instrument, Chengde, China) under 240  $^\circ\text{C}$  at a constant load of 2.16 kg.

The morphology of the prepared sea-island fibers was observed by using a scanning electron microscope model S4800N (Hitachi, Japan) after spraying with a layer of gold. The tensile properties of the prepared fibers were investigated using a universal testing machine model 3369 (Instron, USA) according to the test standard of GB/T 14337-2008. The grip distance of the head was set as 20 mm, and the speed was 40 mm/min. Each fiber was repeated for 15 specimens.

### 3. Results and discussion

#### 3.1. Plasticization mechanism

The intermolecular and intramolecular H-bonding determine the thermal properties of PVA. It was studied by FTIR analysis, and the corresponding spectra are shown in Figure 1a. The peak located at 1250  $\text{cm}^{-1}$  is ascribed to the C–C stretching. The band at 1650  $\text{cm}^{-1}$  contributed to OH bending [25]. Raw PVA showed a characteristic band at 3326  $\text{cm}^{-1}$  that contributed to OH stretching [26]. As a comparison, this band shifted to a lower wavenumber upon adding polyols to varying degrees. When a compound plasticizer composed of polyol A and polyol B was used, a larger blue shifting occurred. Moreover, the position of this band varied with the blending ratio of polyol A/B. When the weight ratio of polyol A and B reached 2:1, the position of the characteristic peak was around 3288  $\text{cm}^{-1}$ . Such prominent blue shifts strongly indicated polyol addition decreased intermolecular H-bonding of PVA by breaking macromolecular interaction [27]. Polyol B has a smaller dimension and is more easily to penetrate PVA, generating a greater breaking effect to intra-molecular H-bonding of PVA, as illustrated in Figure 1b.

To further study the effect of plasticization on the interaction between PVA molecules, a molecular dynamic simulation was conducted on raw PVA and its modified counterpart. The corresponding conformation is shown in Figures 1c and 1d. Compared to the pure PVA system, the calculated root means square deviation (RMSD) of TPVA modified by SE was 24% higher (Figure 2a), the spin-back radius of the polymer increased from 5.5 to 6.1 nm (Figure 2b), and the number of hydrogen bonds between PVA decreased from about 7000 to 2000 (Figure 2c). The free volume fraction in the plasticizer system decreased by 0.9% relative to the pure



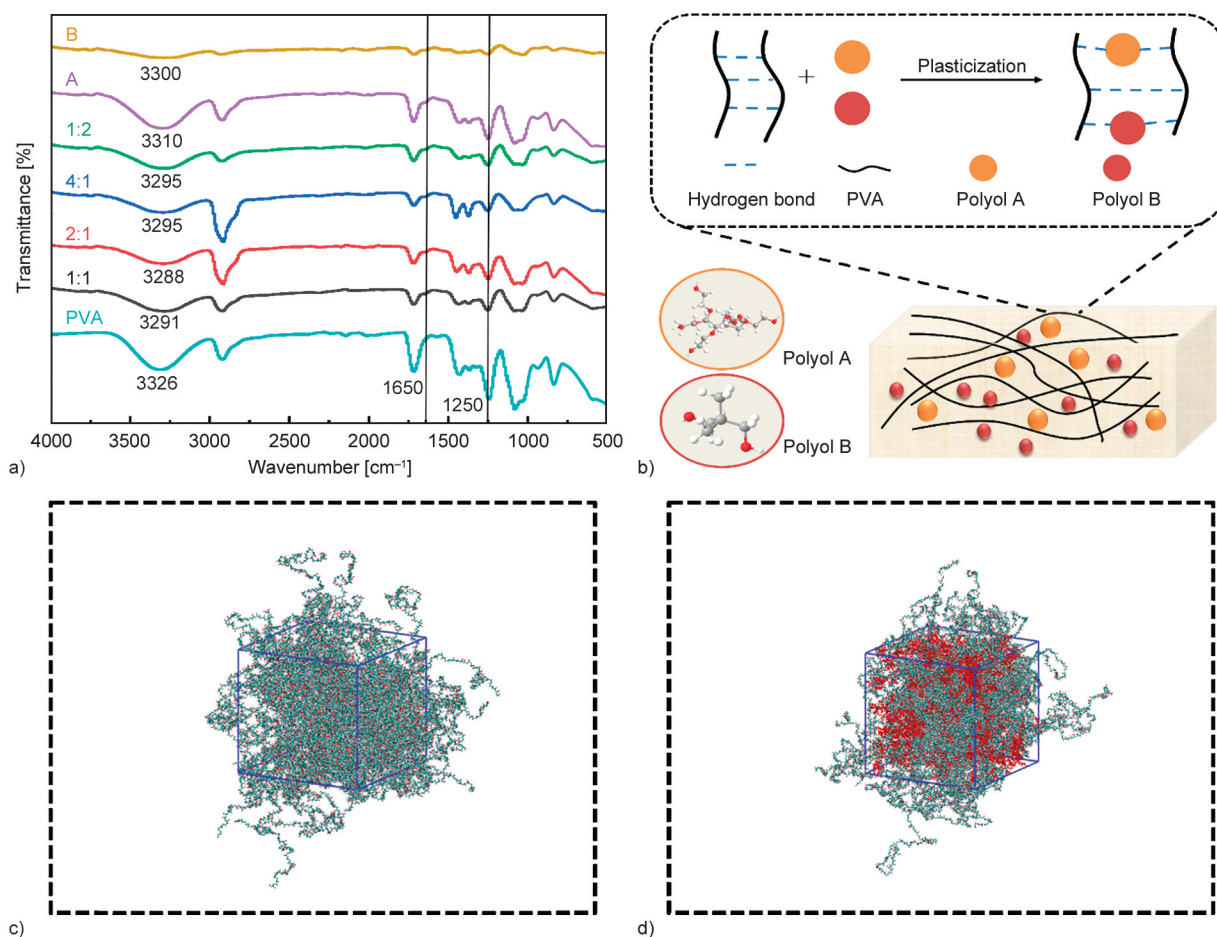


**Figure 1.** a) FTIR of PVA and TPVA modified with different ratios of polyols; b) mechanistic diagram of polyol-modified PVA; simulation conformation of PVA before (c) and after (d) polyol A addition.

**Table 2.** Free volume and internal potential energy of different polymer systems.

Samples	PVA	TPVA
Free volume fraction [%]	11.7	10.8
Internal potential energy [kJ/mol]	-1174.53	-1126.56

PVA polymer system, and the required internal potential energy decreased by 47.97 kJ/mol (Table 2). The simulation results effectively indicated that the plasticizer diffusion in PVA and the introduction of small molecules of plasticizer into PVA formed PVA-plasticizer hydrogen bonds so that intermolecular chain forces of PVA were disrupted to a large extent.

### 3.2. Thermal properties of TPVA

The effect of polyol A/B blending ratio on thermal properties was studied by DSC and TGA, as shown in Figures 3a–3c, respectively. The initial decomposition temperature ( $T_d$ ) and melting temperature ( $T_m$ ) are listed in Table 3. The raw PVA had a  $T_m$  of 199.8 °C. With the addition of plasticizers, the  $T_m$  of

all obtained TPVA decreased. The reason was that the plasticizer penetrated PVA chains, which weakened the H-bonding of PVA. Compared to the role of a single polyol plasticizer, a synergistic plasticizing effect was observed between the compound polyol, further lowering the  $T_m$  of TPVA. When the ratio of SE and NPG is 1:1, the  $T_m$  of TPVA decreases to 185.6 °C. Polyol A has more OH bands than polyol B. It could form more H-bonding with PVA. When polyol A and B were blended as a compound plasticizer, modified TPVA showed multiple melting phenomena. It indicated there were different crystalline states in modified TPVA.

In general, the PVA macromolecules began to cleave when the temperature was higher than 200 °C [28]. The effect of the ratio addition of compound plasticizers on the thermal stability of PVA was also investigated. The initial decomposition temperature ( $T_d$ ) of unmodified PVA was 214.7 °C. With the addition of plasticizer, the  $T_d$  of modified TPVA increased to 262.9 °C at least. This was because the hydroxyl of

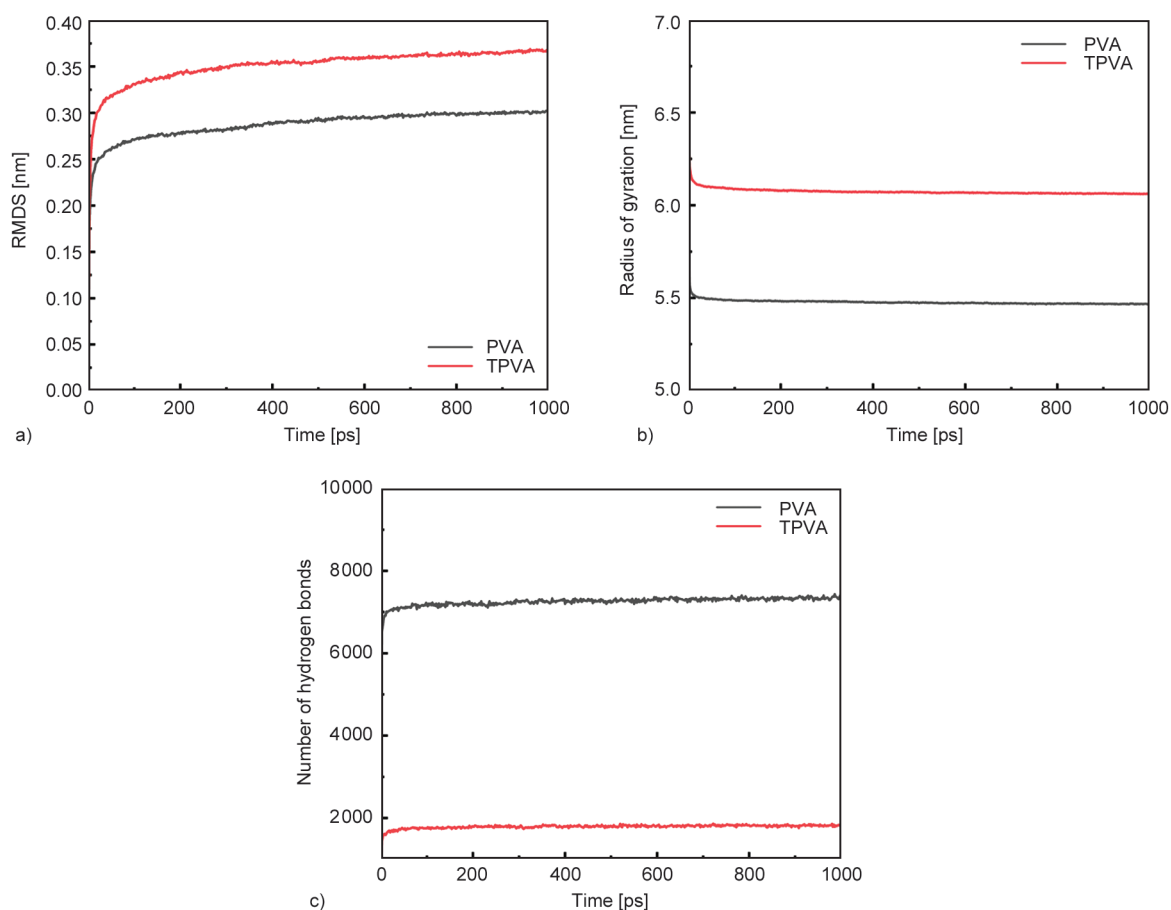


**Figure 2.** a) RMSD of different polymer systems; b) radius of gyration of different polymer systems; c) variation of the number of hydrogen bonds with time for different polymer systems.

polyol formed a new and stronger H-bonding with PVA [29]. The thermal processing window ( $\Delta T = T_d - T_m$ ) was elevated to 81.5 °C when the SE/NPG mixing ratio reached 2:1, as shown in Table 3. This indicates that polyol blending is beneficial in improving the thermal stability of PVA. Even at temperatures higher than 260 °C, the weight loss of prepared TPVA did not exceed 5%. Moreover, the maximum decomposition rate ( $dW/dT$ ) greatly decreased, and temperature at this rate increased by adding polyols.

PVA was rich in OH groups that were prone to be oxidized through a hydration reaction. This affected the processing, like rheological properties [30]. TGA test was conducted at a constant temperature under an air atmosphere to study the thermal oxidation behavior of TPVA. The one modified by SE/NPG = 2:1 was taken as a presentative example. The corresponding patterns are shown in Figure 3d. When PVA was kept at 230 °C for 10 min, a large weight loss of 5% was observed. At the same temperature, the thermal weight loss rate of TPVA was reduced by approximately 1%. This is because the addition of

polyols depresses the oxidation of PVA. When the temperature was raised to 250 °C, 3% weight loss occurred, indicating that the prepared TPVA should be processed under 250 °C.

### 3.3. Rheological properties of TPVA

The rheological properties of TPVA were studied. The modified PVA showed a typical shear thinning behavior, as shown in Figure 4. At a constant temperature, the shear viscosity decreased with the increase of shear rate. This was because the secondary bonds between the molecules were broken by a larger shear force. Levering the temperature from 210 to 240 °C, the viscosity of the corresponding TPVA decreased due to the reduction of inter-molecular bonding. As the temperature increased, fluctuation appeared in the rheological curves of TPVA modified with polyol B. This was because polyol B had a boiling temperature lower than 230 °C. When the temperature was higher than 220 °C, the polyol began to evaporate and caused the change of rheological behavior of TPVA. Moreover, it was observed that the rheological properties of TPVA with polyol A/B = 2:1 were more

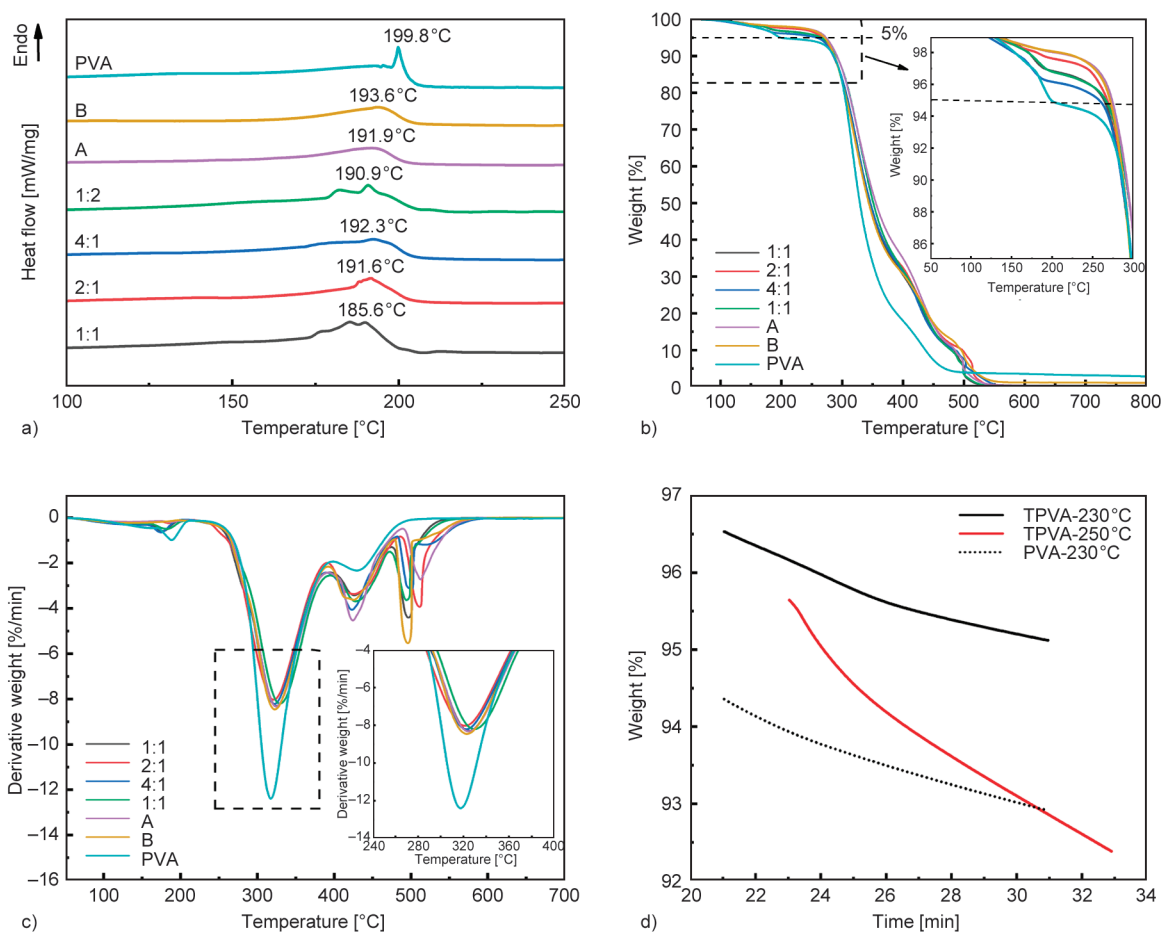


**Figure 3.** Thermal properties of PVA and TPVA modified with different ratios of polyols: a) DSC patterns; b) TGA curves and c) DTG patterns under  $N_2$  atmosphere; d) thermal oxidation behavior of TPVA modified by 2:1 of polyol A/B under air atmosphere.

**Table 3.** Thermal properties of PVA and TPVA modified with different ratios of polyols.

Sample	PVA	1:1	2:1	4:1	1:2	A	B
$T_m$ [°C]	199.8	185.6	191.6	192.3	190.9	191.9	193.6
$T_d$ [°C]	214.7	266.5	273.1	262.9	269.1	271.1	272.7
$\Delta T$ [°C]	14.9	80.9	81.5	70.6	78.2	79.2	79.1
$T_{d\max}$ [°C]	317.9	324.9	321.5	322.5	329.5	324.6	322.9
$dW/dT$ [%/min]	12.4	8.31	8.03	8.22	8.20	8.33	8.46

sensitive to the temperature. This indicated the corresponding TPVA had a high flow activation energy.

### 3.4. Spinnability of TPVA

The MFI and spinnability of TPVA pellets, as described above, were studied. The corresponding results are shown in Table 4. Raw PVA and the one modified with polyol A did not show a value of MFI under the testing. This indicated the H-bonding in PVA was still maintained, and the prepared TPVA showed no melt-flowing behavior. It kept consistent with the investigation of FTIR spectra. When polyol B was introduced, the MFI of TPVA increased, and

they were possibly processed in the melting state. The possible reason was listed previously. Polyol B was prone to penetrate the PVA amorphous region due to its small molecular size. However, it contained less  $-OH$  band than polyol A. Therefore, the interaction effect between polyol B and PVA was lower. The corresponding TPVA showed higher MFI. When a blended polyol was used, the TPVA showed a higher value of MFI. Especially when the polyol A/B ratio was higher than 1:2, the spinnability of prepared TPVA increases. A synergistic effect of plasticization was observed between polyols A and B. The tensile properties of TPVA fibers are also listed

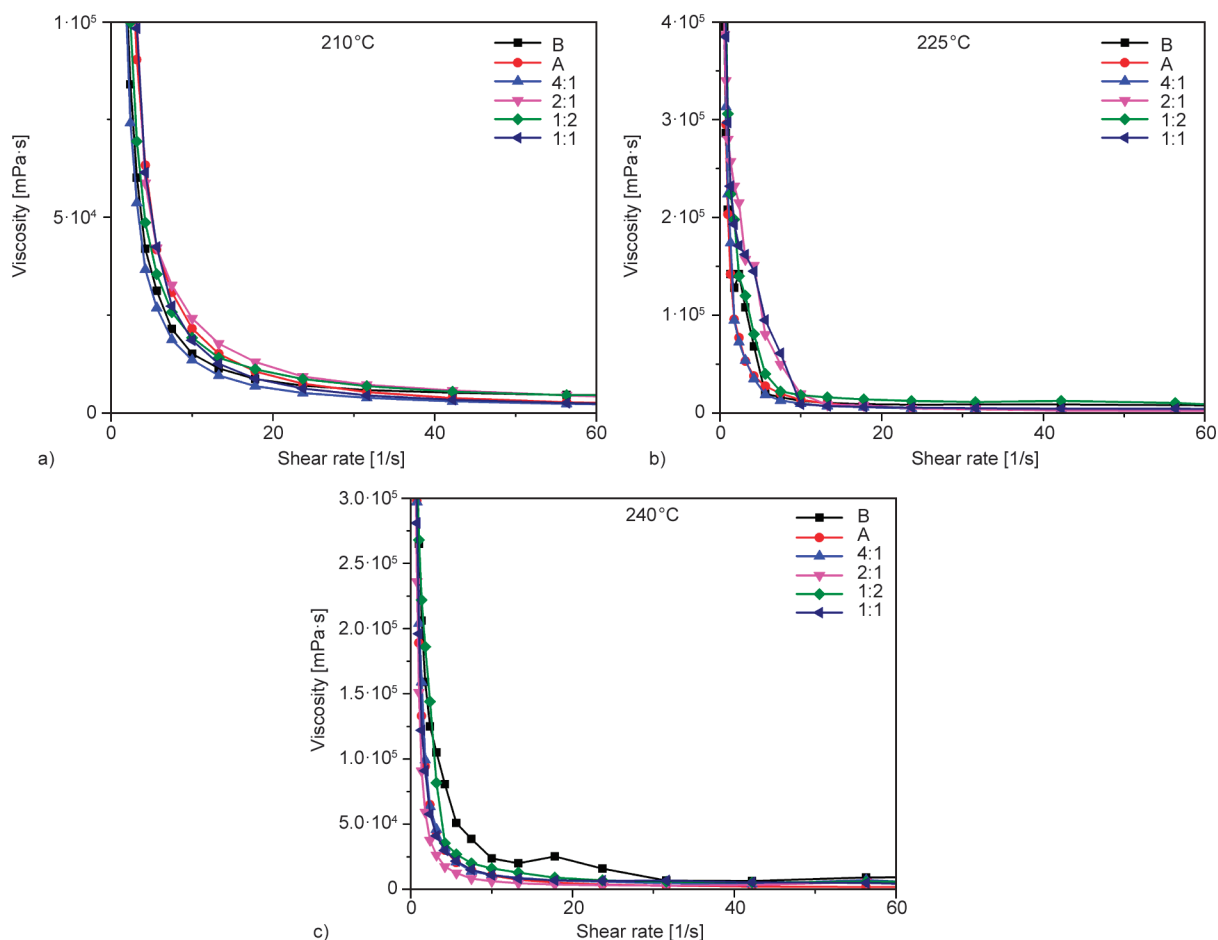


Figure 4. Shear viscosity change with shear rate at different temperatures a) 215 °C; b) 225 °C; c) 240 °C.

Table 4. Spinnability of TPVA pellets and tensile properties of prepared TPVA POY fibers.

Sample	Spinnability	MFI [g/10 min] (230 °C)	Elongation at break [%]	Breaking strength [cN/dtex]
PVA	×	/	/	/
1:1	√	30±3	65.3±6.1	0.73±0.07
2:1	√	35±2	76.7±6.6	0.85±0.08
4:1	√	32±2	72.1±5.6	0.81±0.09
1:2	×	29±2	/	/
A	×	20±3	/	/
B	×	27±3	/	/

in Table 4. When spinning at 230 °C with the polyol A and B ratio of 2:1, the melt flow index reached 35 g/10 min. The breaking strength and elongation at the break of corresponding TPVA fibers were also higher than those of PVA fibers modified by 1:1 or 4:1 polyol A/B.

### 3.5. TPVA-PLA sea-island fiber

The preparation of TPVA-PLA sea-island fibers is shown in Figure 5a. TPVA obtained from the polyol A

and B blending ratio of 2:1 was selected as the ‘sea’ phase due to the large thermal processing window and good mechanical properties of corresponding PVA fibers. The effect of spinning speed on the tensile properties of sea-island pre-oriented yarns (POY) was studied, and the corresponding results are shown in Figure 5b–5d. As the spinning speed increased, linear density and diameter naturally decreased. When the spinning speed increased from 1000 to 1500 m/min, there was no significant change on the tensile strength of POY fibers (around 0.94 cN/dtex). This was possible because the crystallization of fibers was not affected at such a low spinning speed [31]. However, when the speed reached 2000 m/min, the mechanical strength reduced to 0.82 cN/dtex owing to the breaking of some filament in POY bundles during stretching. Breaking elongation of POY sustained at a high value of over 100% due to a lack of thermo-fixing treatment. The value decreased with the increase in spinning speed. Usually, a higher orientation was obtained once undergoing a higher spinning speed, which reduced the elongation at break.

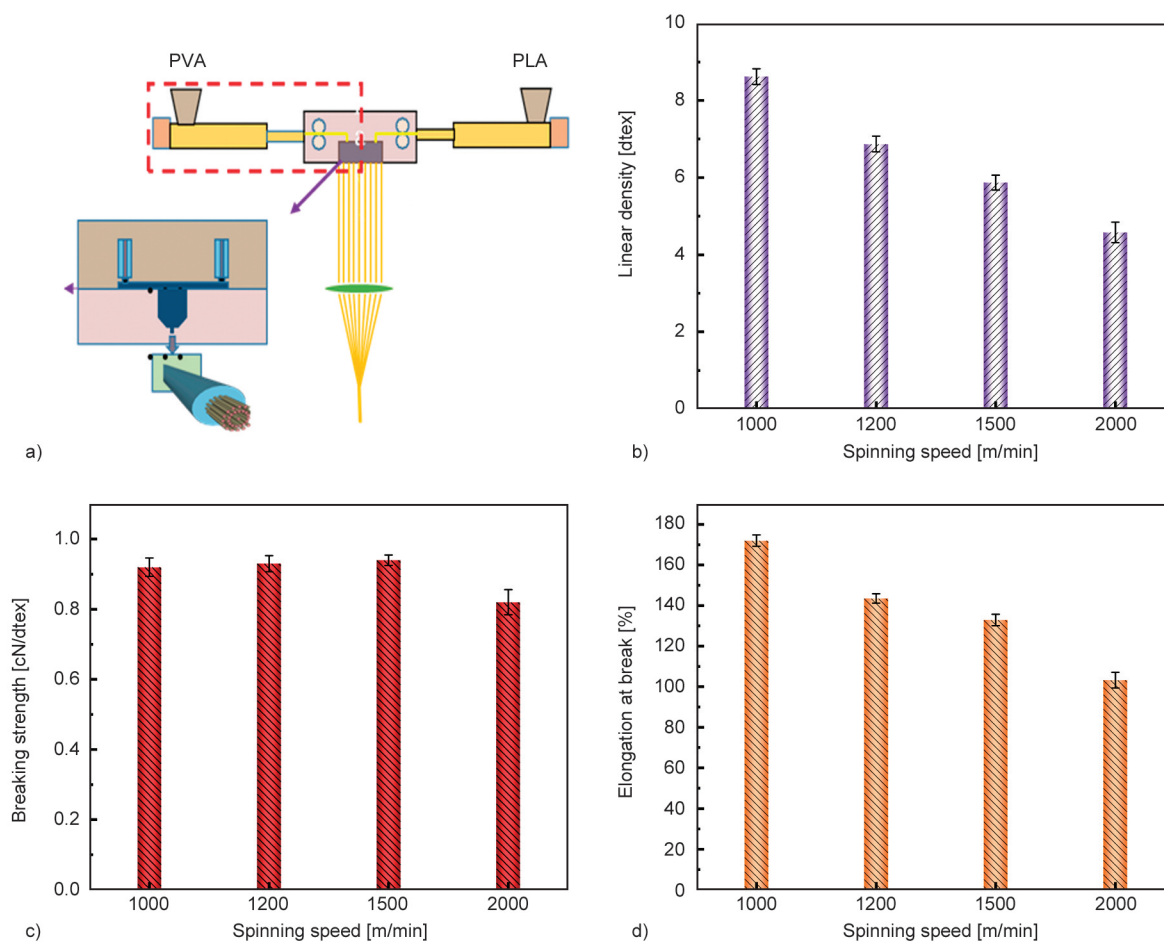


**Figure 5.** a) PVA-PLA sea island fiber processing diagram; PVA-PLA fibers: tensile properties b) linear density, c) breaking strength, d) breaking elongation vs. spinning speed, respectively.

The morphology of the prepared PVA-PLA island fiber, as well as the corresponding PLA superfine fibers, are shown in Figure 6. A distinct interfacial phase of PVA-PLA fibers was observed. This was due to the prominent difference in melt properties between PVA and PLA. Increasing the spinning speed the diameter of sea-island fiber reduced. However, SEM photos showed that the cross-section of fiber began to deform when the speed was higher than 1200 m/min. This is because the TPVA melt breaks under a high stretching speed. The superfine PLA microfiber was obtained after water splitting in hot water at 95 °C for 3 min. PLA microfibers with a uniform diameter of about 6.5  $\mu\text{m}$  (0.42 dtex) were obtained, as shown in Figure 6e. Compared to the traditional benzene or alkali reduction for the splitting of sea-island fiber, the use of water-soluble TPVA could effectively reduce splitting time during the preparation of superfine fibers.

#### 4. Conclusions

This work proposed a novel industrial method to prepare TPVA by physical blending. Two types of polyols were blended and used as a compound plasticizer. The plasticization effect changed with the mass ratio of polyol A and polyol B. Polyol A had a larger molecular volume and contained more hydroxyl, enabling the formation of a stronger H-bonding with PVA macromolecules. As a comparison, polyol B showed a smaller dimension and easily penetrated PVA, breaking the inter-molecular interaction of PVA more effectively. A synergistic effect was found between them. Even though the usage dose of polyols was just 6 wt%, the obtained TPVA showed an MFI as high as 35 g/10 min. This ensured the good spinnability of TPVA. The modified TPVA also had excellent thermal stability and showed an initial decomposition temperature of 273 °C. After plasticization, the window for thermoplastic processing

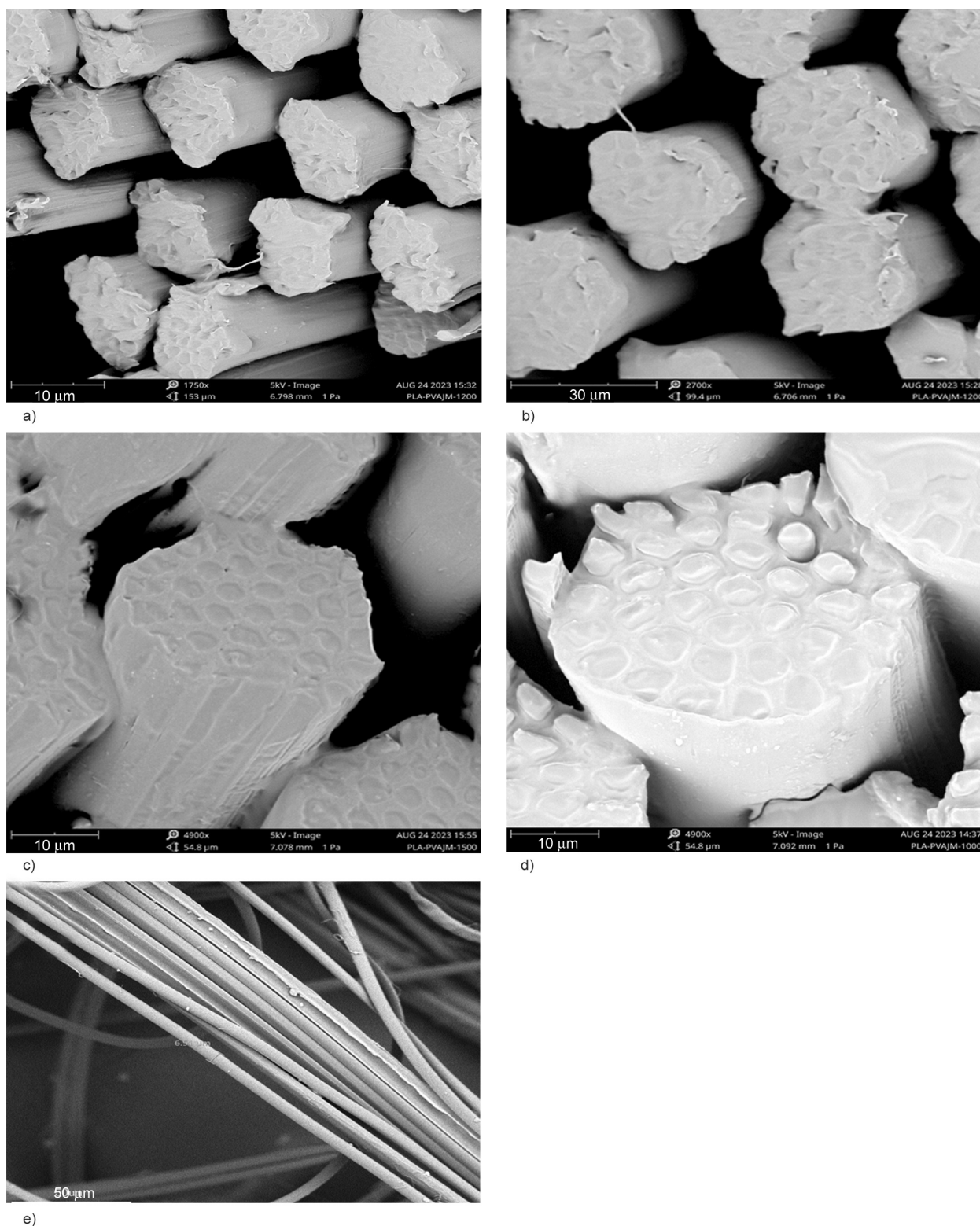


**Figure. 6** Cross-section of PVA-PLA sea-island fiber prepared by different rolling speeds a) 2000 m/min; b) 1500 m/min; c) 1200 m/min; d) 1000 m/min and the corresponding PLA superfine fiber e) after PVA removal.

enlarged, and the resistance to oxidation at high temperatures also enhanced greatly. This ensured a conjugated spinning of PVA/PLA blended melts. As-prepared sea-island POY showed a low mechanical strength. The highest tensile strength was 0.94 cN/dtex due to the lack of thermos-fixing

treatment. TPVA served as the sacrificial phase. The as-prepared sea-island fibers turned into superfine fibers with a diameter of 6.5  $\mu\text{m}$  in 3 min by water-splitting at 95  $^{\circ}\text{C}$ . This work provided a facile and economical approach to the high throughput fabrication of superfine fibers.

## Acknowledgements

This work was financially supported by National Key Research and Development Plan Project (No.2017YFB0309300) and by Tianjin Science and Technology Plan Project (No.17PTSYJC00150).

## References

- [1] Figueiredo K. C. S., Alves T. L. M., Borges C. P.: Poly(vinyl alcohol) films crosslinked by glutaraldehyde under mild conditions. *Journal of Applied Polymer Science*, **111**, 3074–3080 (2009).  
<https://doi.org/10.1002/app.29263>
- [2] Tian H., Yan J., Rajulu A. V., Xiang A., Luo X.: Fabrication and properties of polyvinyl alcohol/starch blend films: Effect of composition and humidity. *International Journal of Biological Macromolecules*, **96**, 518–523 (2017).  
<https://doi.org/10.1016/j.ijbiomac.2016.12.067>
- [3] Ahmed S. F. U., Mihashi H.: Strain hardening behavior of lightweight hybrid polyvinyl alcohol (PVA) fiber reinforced cement composites. *Materials and Structures*, **44**, 1179–1191 (2011).  
<https://doi.org/10.1617/s11527-010-9691-8>
- [4] Saari R. A., Maeno R., Marujiwat W., Nasri M. S., Matsumura K., Yamaguchi M.: Modification of poly(vinyl alcohol) fibers with lithium bromide. *Polymer*, **213**, 123193 (2020).  
<https://doi.org/10.1016/j.polymer.2020.123193>
- [5] Liu D., Zhu C., Peng K., Guo Y., Chang P., Cao X.: Facile preparation of soy protein/poly(vinyl alcohol) blend fibers with high mechanical performance by wet-spinning. *Industrial and Engineering Chemistry Research*, **52**, 6177–6181 (2013).  
<https://doi.org/10.1021/ie400521a>
- [6] Duo Y., Qian X., Zhao B., Qian Y., Xu P., Qi J.: Micro/nano microfiber synthetic leather base with different nanofiber diameters. *Journal of Industrial Textiles*, **50**, 1127–1142 (2021).  
<https://doi.org/10.1177/1528083719858763>
- [7] Kwon Y.-J., Koh J., Oh M. J., Kim S. D.: Alkaline weight reduction monitoring of sea-island type polyamide microfiber fabrics. *Fiber and Polymers*, **7**, 20–25 (2006).  
<https://doi.org/10.1007/BF02933597>
- [8] Huang W., Huang X., Wang P., Chen P.: Poly(glycolic acid) nanofibers *via* sea-island melt-spinning. *Macromolecular Materials and Engineering*, **303**, 1800425 (2018).  
<https://doi.org/10.1002/mame.201800425>
- [9] Nakata K., Fujii K., Ohkoshi Y., Gotoh Y., Nagura M., Numata M., Kamiyama M.: Poly(ethylene terephthalate) nanofibers made by sea-island-type conjugated melt spinning and laser-heated flow drawing. *Macromolecular Rapid Communication*, **28**, 792–795 (2007).  
<https://doi.org/10.1002/marc.200600624>
- [10] Zhang Z.-F., Tu W., Peijs T., Bastiaansen C. W. M.: Fabrication and properties of poly(tetrafluoroethylene) nanofibres *via* sea-island spinning. *Polymer*, **109**, 321–331 (2017).  
<https://doi.org/10.1016/j.polymer.2016.12.060>
- [11] Pan Z., Zhu M., Chen Y., Chen L., Wu W., Yu C., Xu Z., Cheng L.: The variation of fibrils' number in the sea-island fiber – low density polyethylene/polyamide 6. *Fiber and Polymers*, **11**, 494–499 (2010).  
<https://doi.org/10.1007/s12221-010-0494-x>
- [12] Zhang X., Jin G., Ma W., Meng L. Yin H., Zhu Z., Wang R.: Fabrication and properties of poly(L-lactide) nanofibers *via* blend sea-island melt spinning. *Journal of Applied Polymer Science*, **132**, 41228 (2015).  
<https://doi.org/10.1002/app.41228>
- [13] Zhang N., Wang S., Gibril M. E., Kong F.: The copolymer of polyvinyl acetate containing lignin-vinyl acetate monomer: Synthesis and characterization. *European Polymer Journal*, **123**, 109411 (2020).  
<https://doi.org/10.1016/j.eurpolymj.2019.109411>
- [14] Ding J., Chen S.-C., Wang X.-L., Wang Y.-Z.: Synthesis and properties of thermoplastic poly(vinyl alcohol)-graft-lactic acid copolymers. *Industrial and Engineering Chemistry Research*, **48**, 788–793 (2008).  
<https://doi.org/10.1021/ie8013428>
- [15] Mohsin M., Hossin A., Haik Y.: Thermomechanical properties of poly(vinyl alcohol) plasticized with varying ratios of sorbitol. *Materials Science and Engineering A: Structural Materials Properties Microstructure and Processing*, **528**, 925–930 (2011).  
<https://doi.org/10.1016/j.msea.2010.09.100>
- [16] Lv C., Liu D., Tian H., Xiang A.: Non-isothermal crystallization kinetics of polyvinyl alcohol plasticized with glycerol and pentaerythritol. *Journal of Polymer Research*, **27**, 66 (2020).  
<https://doi.org/10.1007/s10965-020-2038-4>
- [17] Xu Y., Xu Y., Sun C., Zou L., He J.: The preparation and characterization of plasticized PVA fibres by a novel glycerol/pseudo ionic liquids system with melt spinning method. *European Polymer Journal*, **133**, 109768 (2020).  
<https://doi.org/10.1016/j.eurpolymj.2020.109768>
- [18] Wang R., Wang Q., Li L.: Evaporation behaviour of water and its plasticizing effect in modified poly(vinyl alcohol) systems. *Polymer International*, **52**, 1820–1826 (2003).  
<https://doi.org/10.1002/pi.1385>
- [19] He W., Ye L., Coates P., Caton-Rose F., Zhao X.: Construction of fully biodegradable poly(L-lactic acid)/poly(D-lactic acid)-poly(lactide-co-caprolactone) block polymer films: Viscoelasticity, processability and flexibility. *International Journal of Biological Macromolecules*, **236**, 123980 (2023).  
<https://doi.org/10.1016/j.ijbiomac.2023.123980>
- [20] Karyappa R., Liu H., Zhu Q., Hashimoto M.: Printability of poly(lactic acid) ink by embedded 3D printing *via* immersion precipitation. *ACS Applied Materials and Interfaces*, **15**, 21575–21784 (2023).  
<https://doi.org/10.1021/acsami.3c00149>

- [21] Cheon S. Y., Kim J., Lee K-Y., Lee C-M.: Poly(L-lactic acid) membrane crosslinked with genipin for guided bone regeneration. *International Journal of Biological Macromolecules*, **30**, 1228–1239 (2021).  
<https://doi.org/10.1016/j.ijbiomac.2021.09.137>
- [22] Wang J., Wolf R. M., Caldwell J. W., Kollman P. A., Case D. A.: Development and testing of a general amber force field. *Journal of Computational Chemistry*, **25**, 1157–1174 (2004).  
<https://doi.org/10.1002/jcc.20035>
- [23] Hess B., Kutzner C., van der Spoel D., Lindahl E.: GROMACS 4: Algorithms for highly efficient, load-balanced, and scalable molecular simulation. *Journal of chemical theory and computation*, **4**, 435–447 (2008).  
<https://doi.org/10.1021/ct700301q>
- [24] Astrakas L. G., Gousias C., Tzaphlidou M.: Structural destabilization of chignolin under the influence of oscillating electric fields. *Journal of Applied Physics*, **111**, 074702 (2012).  
<https://doi.org/10.1063/1.3699389>
- [25] Wang C., Zou L., Wang H., Wang Y., Chen D.: Plasticizing effect of ionic liquid on poly(vinyl alcohol) with different degrees of polymerization. *Chemistryselect*, **7**, e202104035 (2022).  
<https://doi.org/10.1002/slct.202104035>
- [26] Shi B., Liang L., Yang H., Zhang L., He F.: Glycerol-plasticized spirulina-poly(vinyl alcohol) films with improved mechanical performance. *Journal of Applied Polymer Science*, **134**, 44842 (2017).  
<https://doi.org/10.1002/app.44842>
- [27] Tian H., Liu D., Yao Y., Ma S., Zhang X., Xiang A.: Effect of sorbitol plasticizer on the structure and properties of melt processed polyvinyl alcohol films. *Journal of Food Science*, **82**, 2926–2932 (2017).  
<https://doi.org/10.1111/1750-3841.13950>
- [28] Holland B. J., Hay J. N.: The thermal degradation of poly(vinyl alcohol). *Polymer*, **42**, 6775–6783 (2001).  
[https://doi.org/10.1016/S0032-3861\(01\)00166-5](https://doi.org/10.1016/S0032-3861(01)00166-5)
- [29] Wu Q., Chen N., Wang Q.: Crystallization behavior of melt-spun poly(vinyl alcohol) fibers during drawing process. *Journal of Polymer Research*, **17**, 903–909 (2010).  
<https://doi.org/10.1007/s10965-009-9382-8>
- [30] Yang F., Shi S., Nie M., Wang Q.: Freeze-drying-promoted effect of sorbitol plasticization for melt processing of poly(vinyl alcohol). *Industrial and Engineering Chemistry Research*, **61**, 16005–16012 (2022).  
<https://doi.org/10.1021/acs.iecr.2c02711>
- [31] Qin Q., Zhou T., Wang M., Li L., Chen N.: Structure evolution and performance of poly(vinyl alcohol) fibers with controllable cross-section fabricated using a combination of melt-spinning and stretching. *Polymer Testing*, **117**, 107867 (2023).  
<https://doi.org/10.1016/j.polymertesting.2022.107867>



Research article

# *In-situ* formation of ZnO anchored silica: Sustainable replacement of conventional ZnO in SBR/NR blends

Sreethu Thiyyanthiruthy Kumbalaparambil<sup>1</sup>, Ajay Haridas Chandaparambil<sup>1</sup>, Kinsuk Naskar<sup>\*1</sup>

Rubber Technology Centre, Indian Institute of Technology Kharagpur, 721302 West Bengal, India

Received 18 July 2023; accepted in revised form 19 September 2023

**Abstract.** The global concern over zinc leaching into aquatic ecosystems has led researchers to seek ways to reduce zinc oxide (ZnO) content in rubber products. Conventional micro-sized ZnO, commonly used in the rubber industry, poses dispersion challenges due to its hydrophilic nature and micron size within the hydrophobic rubber matrix. Therefore, higher amounts of ZnO are added, elevating the risk to aquatic life. A promising alternative involves using highly dispersible ZnO with active zinc (Zn) centers instead of conventional ZnO. Another approach includes incorporating ZnO-anchored silica particles into the rubber matrix, which requires additional ex-situ fabrication. This study presents an innovative method where ZnO-anchored silica is generated in situ during the blending of styrene-butadiene rubber/natural rubber (SBR/NR). The study also evaluates the effectiveness of active, nano-sized, and octylamine-modified ZnO as activators compared to conventional ZnO, by introducing silica filler, octylamine-modified and high surface area ZnO anchor onto the silica surface, forming Si–O–Zn covalent bonds. This protective layer reduces filler aggregation and the Payne effect. Even with 60% less usage, these activators in the SBR/NR blend significantly enhance tensile strength (31.27%) and elongation at break (49.13%) compared to conventional ZnO. These results point towards the possibility of a cost-effective and sustainable replacement for conventional ZnO.

**Keywords:** sustainability, ZnO anchored silica, activator, kinetics, payne effect

## 1. Introduction

Zinc oxide (ZnO) is regarded as the most efficient activator due to its faster cure kinetics; by interacting with sulfur and accelerators, ZnO forms zinc polysulfide complexes that bond to rubber chains to produce a three-dimensional crosslinked structure [1, 2]. The ability of Zn<sup>2+</sup> ions to form complexes is a crucial aspect of the activation mechanism [3]. It highly depends on its dispersion state in the rubber matrix, crystalline structure, surface area, and particle size [4, 5]. Traditionally, in rubber compounds, micron-sized conventional ZnO is being utilized. The inadequate dispersion of micro-sized conventional ZnO particles within the rubber matrix results in only a limited amount of ZnO being able to react effectively with other curing compounds. To compensate for this

limitation, a higher quantity of ZnO is typically added to rubber compounds, which raises significant environmental concerns due to its subsequent leaching during rubber products' production, application and disposal stages [6, 7]. It has shown detrimental effects on water quality and ecosystems, impacting various plants, invertebrates, and fish in freshwater/marine environments. Furthermore, excessive exposure to Zn poses a particular threat to aquatic organisms, disrupting their biochemistry [8]. In light of these environmental and ecological concerns, reducing the amount of ZnO in rubber compositions is imperative while maintaining desired performance levels [9, 10].

Various approaches have been proposed to address these concerns. Among them, the use of ZnO

\*Corresponding author, e-mail: [knaskar@rtc.iitkgp.ac.in](mailto:knaskar@rtc.iitkgp.ac.in)  
© BME-PT

nanoparticles was introduced first and gained significant interest because of the better dispersion in rubber matrix due to its small size, high surface area (7–10 m<sup>2</sup>/g.), and high surface-to-volume ratio, which lead to increased curing efficacy [11–17]. Yang and Xie [18] investigated the impact of particle size and surface area on the Zn<sup>2+</sup> release ratios from Zn particles. Nano ZnO releases more Zn<sup>2+</sup> than micro ZnO; the maximum ratios obtained were 85 and 60%, respectively. This is due to the nanoparticles' high surface-to-volume ratio, which provides an abundance of active zinc atoms on the surface. The same applies to active ZnO having a higher surface area with high Zn<sup>2+</sup> ions accessibility. Active ZnO, with a surface area of 35 m<sup>2</sup>/g, offers substantially more reaction sites on the particle surface than conventional ZnO, which possesses a surface area of 4.5 m<sup>2</sup>/g [19–21]. The high availability of Zn<sup>2+</sup> ions on its surface reduced the ZnO amount in rubber compounds. Recent studies explore the reduction of nano ZnO agglomeration tendency due to its smaller particle size with the surface modification of ZnO nanoparticles [22–26]. Qin *et al.* [27] modified nano ZnO with octylamine and the octylamine modifier prevented nanoparticle aggregation, resulting in a uniform dispersion of octylamine-modified ZnO nanoparticles in the rubber matrix. Since most studies were conducted on unfilled systems, the interaction between ZnO and the reinforcing filler remains unexamined.

Due to rising global concerns about emissions of greenhouse gases and climate change, silica-filled rubber compounds are gaining prominence [28]. The interaction between filler/filler and filler/polymer interaction primarily determines filler network structure. An essential criterion for developing highly reinforced rubber composites is the matrix's uniform distribution of filler particles. When mixed with non-polar elastomers, the polar surface chemistries of silica nanoparticles cause them to develop highly agglomerated structures. The utilization of silane coupling agents in silica/elastomer nanocomposites leads to a significant improvement in the dispersion of silica particles [29]. The cure activator ZnO also takes part in the dispersion of filler in the matrix. The surface silanol groups of silica are acidic and can, therefore, react with an alkali, such as ZnO. There are no extensive studies on the interaction of ZnO activators and fillers and how the type of ZnO affects the distribution of silica filler in rubber compounds. It has also proven to be a fascinating strategy to use

ZnO-anchored silica particles in rubber matrix, but this requires additional ex-situ fabrication of ZnO-anchored silica particles [1, 30].

The current study investigates the *in-situ* formation of ZnO-anchored silica particles during the processing. The study examined the effects of using different types of ZnO, including active, nano, and octylamine-modified ZnO, compared to conventional ZnO. With the inclusion of silica filler, the octylamine-modified ZnO and high surface area active ZnO were attached to the silica surface, forming covalent bonds as Si–O–Zn. This bonding process resulted in an extra protective layer on the surface of silica, which reduced the filler's aggregation and mitigated the Payne effect's occurrence. Fourier transform infrared (FTIR) spectroscopy and X-ray diffraction (XRD) analysis were performed to confirm the interaction between ZnO and silica particles.

These findings signify that the presence of highly reactive Zn<sup>2+</sup> on the surface of ZnO enables the anchoring of ZnO onto silica particles without additional steps or chemical agents. Furthermore, it has been observed that this process improves the efficiency of rubber curing and reduces the required amount of ZnO by 60%, thereby exploring the potential for a cost-effective and sustainable alternative to conventional ZnO. Additionally, the mechanical and thermal properties of the blends were influenced by the type of sulphide linkage formation. This insight was gained by analyzing the influence of various ZnO on sulphide linkage formation using temperature scanning stress relaxation (TSSR) and thermogravimetric analysis (TGA) techniques.

## 2. Experimental details

### 2.1. Materials

Natural Rubber SVR3L grade, sourced from JK Fener Pvt. Ltd. in Mysore, India. The styrene-butadiene rubber (SBR) grade 1502 was purchased from Reliance Industries Pvt Ltd. in Mumbai, India. The styrene-butadiene rubber/natural rubber (SBR/NR) blend system was activated with four distinct vulcanization activators, including commercial ZnO (POCL, Thiruvallur, India), active ZnO (Transpek Silox Industry, Gujarat, India), nano ZnO (Nano Research Lab, Jharkhand, India), and functionalized ZnO (Tata Chemicals Ltd, Pune, India). Highly dispersible silica (HDS)(Zeosil), the reinforcing filler used in this study, was obtained from Solvay silica (Aubervilliers, France).

**Table 1.** Composition of SBR/NR blends filled with silica filler incorporating various ZnO activators.

Ingredients [phr]	C5BS [phr]	A2BS [phr]	N2BS [phr]	F2BS [phr]
Styrene-butadiene rubber (SBR)	70	70	70	70
Natural rubber (NR)	30	30	30	30
Conventional ZnO	5	–	–	–
Active ZnO	–	2	–	–
Nano ZnO	–	–	2	–
Functionalized ZnO	–	–	–	2
Stearic acid (SA)	2	2	2	2
Highly dispersible silica (HDS)	60	60	60	60
Bis(triethoxysilylpropyl)tetrasulfide (TESPT)	5.6	5.6	5.6	5.6
Hydroquinone (HQ)	1.0	1.0	1.0	1.0
Sulfur (S)	1.5	1.5	1.5	1.5
Tetramethylthiuram disulfide (TMTD)	0.5	0.5	0.5	0.5
Cyclo benzyl sulfenamide (CBS)	1.2	1.2	1.2	1.2

phr: parts per hundred rubbers

## 2.2. SBR/NR blend mixing

The blend has been mixed in two steps. All the additives, except curatives termed as master batch, have been added to the Brabender internal mixer (Brabender GmbH, Duisburg, Germany). Throughout the mixing period, the temperature was kept at 140 °C. During the initial mixing stage, the rpm addition of rubber and activators was set at 30. After adding the remaining ingredients for compounding, the mixing speed was increased to 60 rpm, and the total mixing time was set to 4.5 min. The final batch containing the curatives mixed in the lab two-roll mill. The blend composition is shown in Table 1. Throughout the text, the blend contains 5 phr conventional ZnO called C5BS. The blend comprises active, nano, and functionalized ZnO called A2BS, N2BS, and F2BS. Here, 2 stands for 2 phr of ZnO addition, and S stands for the reinforcing filler, highly dispersible silica.

## 2.3. Instrumentation and characterizations

The curing characteristics of the SBR/NR blends were monitored by subjecting them to a moving die rheometer (Monsanto Rheometer (MDR 2000), Akron, USA) at 150 °C for 45 min under an oscillation angle of 3 arcs. To determine the cure kinetics, we cured the rubber mixtures at three different temperatures for 45 min: 140, 150, and 160 °C. The activation energy and rate constant were calculated using the Arrhenius equation for first-order kinetics and a nonlinear curve fitting according to the Kamal-Sourour model. The Flory-Rehner equation was employed to determine the crosslink density. A

comprehensive description of the procedure can be found in the supporting information section.

X-ray diffraction (XRD) and Fourier transform infrared spectrophotometry (FTIR) were employed to analyze the blend structures. XRD analysis was performed using a Bruker D8 Advance XRD instrument (Germany), utilizing Cu K $\alpha$  (wavelength = 1.54 Å) radiation. The XRD measurements covered an angular range of 20° to 90° with a step size of 0.04°. FTIR (Nicolet 6700, M/S thermo fisher scientific instruments, Madison, USA) in attenuated total reflectance (ATR) mode was used to detect the functional groups in the composites. The spectra were recorded between 400 and 4000 cm<sup>-1</sup> with a 16 scan and a force gauge setting 32. Using a thermogravimetric analyzer (Shimadzu TGA 50, Columbia, USA), mixtures were subjected to thermogravimetric analysis (TGA). Under a nitrogen atmosphere, samples of approximately 8 mg each in an alumina crucible were heated at 10 K/min.

To comprehend the blends thermomechanical characteristics, we carried out temperature scanning stress relaxation measurements using the TSSR-Tester (Brabender GmbH, Duisburg, Germany). The specimen shaped like a dumbbell (ISO 527, Type 5A) was cut from the molded sheet. The sample was placed in an electrically heated chamber and subjected to a 50% initial strain for 2 h at 23 °C. This was carried out so that short-term relaxation processes could dissipate. Then, a nonisothermal measurement up to 200 °C was carried out at a 2 K/min heating rate until the sample ruptured or stress relaxation was complete. Using stress-temperature curves derived from

TSSR testing was employed to assess crosslink density. This was achieved by calculating the initial slope of the curves using a modified Neo-Hookean equation.

The blend's tensile and tear properties were measured at room temperature using a Hiosk-Hounsfield universal testing machine (Surrey, England) (with a 10 kN load cell and 500 mm/min crosshead speed). Using ASTM D412 die C the specimens were cut from the moulded tensile sheet. To comply with ASTM D573 standards, accelerated aging was conducted using a forced air circulating oven (Blue M Electric, model N<sup>o</sup> F0 712, Blue Island, Illinois, USA). The aging process was performed at 70 °C for one week. After aging, the mechanical properties of the specimens were evaluated following a 40 h conditioning period at 23 °C and 50% relative humidity to ensure thermal equilibrium. The tensile strength, elongation at break, and modulus of aged samples were evaluated compared to those of unaged samples.

Temperature-sweep tests using an Eplexor 2000 instrument from Gabo Qualimeter (Netzsch, Geratebau GmbH, Selb, Germany) determined the rubbery nature of the samples. The sample of size 35×10×2 mm was cooled to –80 °C and then heated to 80 °C at a rate of 2 K/min and a constant frequency of 10 Hz.

The viscoelastic properties of the prepared rubber mixture were evaluated using a Rubber Process Analyzer (RPA) (RPA 2000, Alpha Technologies, UK). For the strain sweep study, the temperature was held constant at 100 °C. Adjusting the strain from 0.05 to 100% while maintaining a frequency of 0.33 Hz. By calculating the difference between the elastic moduli at low strain ( $G_0'$ ) and high strain ( $G_{\infty}'$ ), the Payne effect was determined from the RPA. This method was used to evaluate filler-filler interactions in compounds; the greater the Payne effect, the greater the filler-filler interaction.

The analysis of filler dispersion in the composites was conducted using transmission electron microscopy (TEM) with a JEM 2100F (Jeol, Japan) as well as scanning electron microscopy (SEM) using a Merlin microscope (Carl Zeiss SMT, Germany). The TEM instrument operates with a 120 kV electron beam at an accelerated voltage. Before the test, the rubber compounds were prepared with an ultramicrotome. After cryo fracturing in liquid nitrogen and overnight drying at 60 °C, SEM samples were prepared.

### 3. Results and discussion

#### 3.1. Effect of various activators on the cure characteristics

Table 2 summarises the cure parameters such as highest torque ( $M_H$ ), lowest torque ( $M_L$ ), delta torque ( $M_H - M_L$ ), optimum cure time ( $T_{c90}$ ), scorch time ( $T_{s2}$ ), and the cure rate index ( $CRI$ ), obtained from the rheocurve of silica-filled SBR-NR blends containing conventional, active, nano and functionalized ZnO. Figure 1 shows the acquired rheocurve and crosslink density of the SBR/NR blends. Octylamine-modified F2BS exhibited the lowest cure time among all blends. It is possible that octylamine, which raises basicity and speeds up the vulcanization process, is the cause of the F2BS low cure time and higher cure rate index [31, 32]. The highest torque ( $M_H$ ) of F2BS modified with octylamine was reduced, suggesting that blends of octylamine-modified ZnO with SBR/NR blend have a lower degree of rubber reticulation [27].

Blends N2BS and A2BS had a high  $T_{c90}$  and the low ( $CRI$ ) results from the extended duration needed for chelate formation at high Zn ions concentration, which was enabled by the smaller particle size and larger surface area of nano and active ZnO [5, 33].

However, the silanol or hydroxyl groups on the surfaces of silicas make them acidic and polar. Due to this, cure rates are slow and cure times are higher when compared to carbon black-filled blends inferred from our previous study. Notably, the silica-filled rubber vulcanizates exhibited a substantial delta torque ( $M_H - M_L$ ), reflected in the greater crosslink determined from swelling study densities (Table 2; Figure 1b). Since TESPT, a silane compound containing sulfur, was used as a coupling agent, the tetrasulfide groups in TESPT caused the silica particles to interact with the rubber chains. Consequently, additional monosulfidic crosslinks formed in addition to those produced by elemental sulfur [34]. In silica-filled blends, N2BS had the highest delta torque and a similar value to C5BS blend among all the batches and F2BS exhibited the lowest delta torque value with a

**Table 2.** Cure characteristics of SBR/NR blends filled with silica fillers cured at 150 °C.

Entry	$M_L$ [dN·m]	$M_H$ [dN·m]	$M_H - M_L$ [dN·m]	$T_{s2}$ [min]	$T_{c90}$ [min]	$CRI$ [min <sup>-1</sup> ]
C5BS	6.67	34.45	27.78	2.22	15.92	7.30
A2BS	7.19	33.95	26.76	2.05	17.50	6.47
N2BS	6.74	34.67	27.93	2.08	19.21	5.84
F2BS	3.67	22.98	19.31	1.32	7.71	15.65

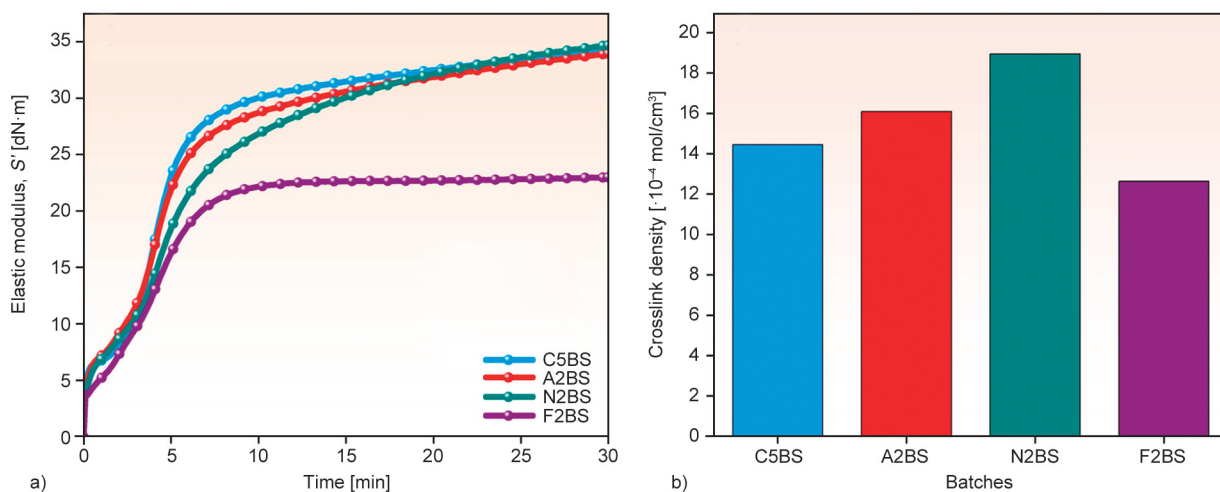


**Figure 1.** a) Time–elastic modulus curve, b) crosslink density measured from a swelling method using Flory Rehner equation.

30% reduction in the value. These results correlated with the crosslink density obtained in Figure 1b.

#### Activation energy

Cure kinetics tests were done on SBR/NR blends to see how different ZnO concentrations affected the activation of sulfur vulcanization. Analyzed the kinetic constant ( $k$ ) and activation energy ( $E_a$ ) of the SBR/NR blends using cure data obtained at 140, 150, and 160 °C. The Kamal-Sourour reaction model was used for kinetic analysis. The curing of rubber compounds has been explained using the Kamal-Sourour reaction model, which incorporates autocatalytic characteristics with an  $n^{\text{th}}$ -order reaction model [35, 36]. Equation (1) serves as the basis for the Kamal-Sourour reaction model, capturing the  $n^{\text{th}}$ -order reaction component with the first-rate constant ( $k_1$ ) and exponent ( $n$ ) and the autocatalytic contribution to the reaction with the second-rate constant ( $k_2$ ) and

exponent ( $m$ ). Every kinetic constant follows the Arrhenius equation (Equation (1)):

$$\frac{d\alpha}{dt} = (k_1 + k_2\alpha^m)(1 - \alpha^n) \quad (1)$$

By fitting above Equation (1) to the slope of the graph between  $d\alpha/dt$  and  $\alpha$ , the rate constant  $k$  can be determined. The activation energy was then determined by plotting  $\ln k$  vs.  $1/T$  (Figure 2a). It adheres to the Arrhenius equation (Equation (2)), which relates the rate constant ( $k$ ) to the pre-exponential factor ( $A$ ), activation energy ( $E_a$ ), universal gas constant ( $R$ ), and temperature ( $T$ ) in Kelvin. The obtained activation energy is shown in Figure 2b:

$$k = A e^{\frac{-E_a}{RT}} \quad (2)$$

The activation energy of the vulcanization reaction can serve to validate the efficiency of the activator

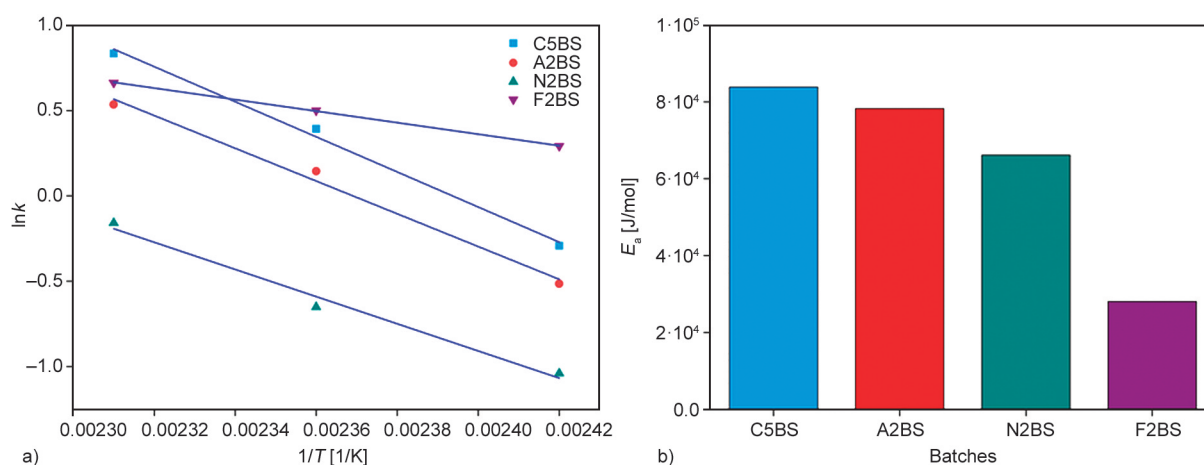


**Figure 2.** a)  $\ln k$  vs.  $1/T$  plot and b) obtained activation energy.

employed in the rubber formulation. The octylamine modified ZnO accelerates the vulcanization of rubbers by catalyzing the formation of a more active sulfurating agent due to the presence of amine on the surface. Consequently, the apparent activation energy of F2BS decreases. Figure 2b shows which F2BS had the lowest activation energy. This suggests that the F2BS vulcanizes more quickly in SBR/NR blends, consistent with the CRI in Table 2.

### 3.2. Characterizations-interfacial interaction of silica-filled SBR/NR blend with various ZnO

#### FTIR and XRD analysis

FTIR analysis was done on the four blends to investigate how ZnO interacted with the silica surface and stearic acid. C5BS, A2BS, N2BS, and F2BS, ATR-FTIR spectra were performed in the 400–4000  $\text{cm}^{-1}$  range. The zoomed region of the FTIR spectra from 750 to 1050  $\text{cm}^{-1}$  is displayed in Figure 3a. The peak at 954  $\text{cm}^{-1}$ , attributed to the Si–OH stretching

vibration, undergoes a distinct transformation within all blend compositions. Notably, the peak's position shifts to a higher frequency range of 963–965  $\text{cm}^{-1}$ , assuming a shoulder-like appearance, and concurrently, its intensity follows an ascending order of F2BS > A2BS > N2BS > C5BS (Figure 3a). Drawing parallels with previously documented spectra of ZnO–SiO<sub>2</sub> composites as found in the literature, this alteration is likely a consequence of the concurrent presence of Si–OH and symmetric Si–O–Zn stretching modes. This observation supports the proposition of covalent bonding between the surface silanol group filler and the activator ZnO particles [37–39]. This confirms the increased formation of Si–O–Zn bonds even during the ex-situ mixing of rubber compounds in the Brabender mixer.

Upon the interaction between ZnO and stearic acid, prominent peaks at 1538 and 1398  $\text{cm}^{-1}$  were detected (Figure 3b), signifying the asymmetric and symmetric stretching of COOH groups linked to zinc centers within the Zn stearate framework [40]. The

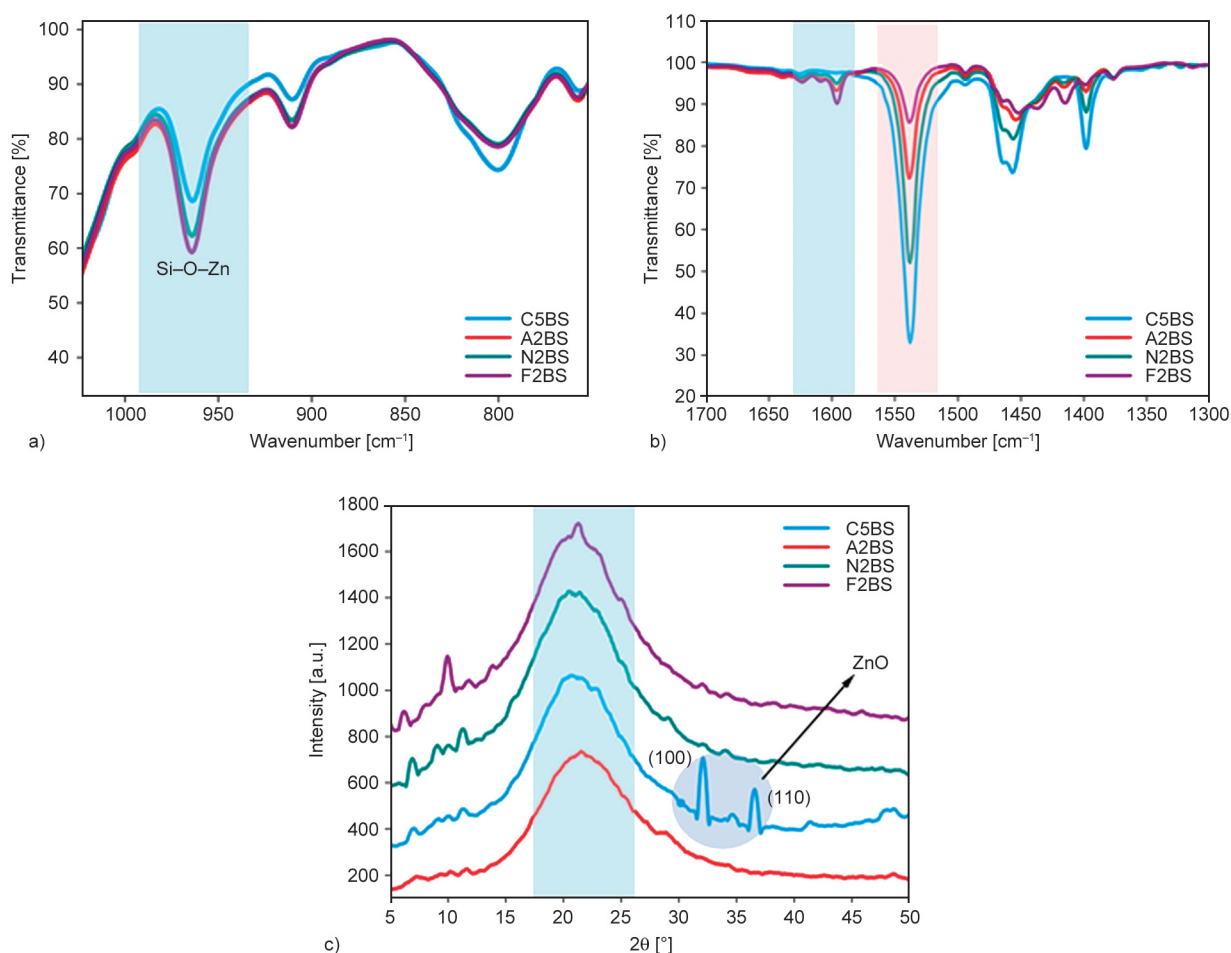


**Figure 3.** FTIR spectroscopy of C5BS, A2BS, N2BS and F2BS a) at zoomed wavelength of 1050–750  $\text{cm}^{-1}$ , b) at zoomed wavelength of 1700–1300  $\text{cm}^{-1}$ , c) XRD diffraction spectra of C5BS, A2BS, N2BS and F2BS.

interaction of ZnO-anchored silica particles with the stearic acid, especially within the F2BS and A2BS blends, showed a reduction in the intensity of the zinc stearate peaks. New peaks emerged at 1595, 1609, and 1624  $\text{cm}^{-1}$ , accompanied by vibrations at 1415  $\text{cm}^{-1}$ , with the order of intensity being F2BS > A2BS > N2BS > C5BS. These phenomena are believed to be associated with the formation of distinct surface zinc complexes due to the interaction of ZnO-anchored silica with stearic acid, as discussed by Ikeda *et al.* [41] and Mostoni *et al.* [40] that the spectral characteristics of ZnO/SiO<sub>2</sub> nanoparticles suggest the existence of bridging bidentate-coordinated zinc/stearate complexes in a dinuclear arrangement. Each stearic acid molecule links two zinc centers in this configuration, maintaining a Zn:SA molar ratio of 1:1. This arrangement results in two vacant positions on each Zn(II) site, potentially available for additional ligand binding.

Due to the silica's acidic surface silanol groups, an alkali like ZnO can react with them. Active ZnO, which had more readily available Zn<sup>2+</sup>, rapidly reacted with the silica surface to form the covalent bond Si–O–Zn, protect the silica particles with a layer, and reduce filler aggregation. Similarly, as demonstrated in Figure 9, octylamine-modified ZnO formed Si–O–Zn bonds and had a stronger affinity for the silica filler in F2BS due to its presence of an amine group in the surface of ZnO, making it more attracted to the silica surface and forming high-intensity Si–O–Zn bonds. Nano ZnO having a lower surface area (7–10  $\text{m}^2/\text{g}$ ) than the active ZnO (35  $\text{m}^2/\text{g}$ ) and a higher surface area than the conventional ZnO (4.5  $\text{m}^2/\text{g}$ ) make Zn<sup>2+</sup> ions availability less compared to active and more compared to conventional ZnO. Figure 3c represents the XRD pattern of C5BS, A2BS, N2BS and F2BS. In the case of C5BS, the intensity of the peaks  $2\theta$  at 31.6° and 36.11°, which represent the (100) and (101) diffractions of ZnO, respectively, is visible because the micron-sized ZnO particles it contains reduced dispersion, allowing for the visualization of unreacted ZnO particles. The non-crystalline silica is characterized by the diffraction peak  $2\theta$  at 22.5°.

### 3.3. Temperature scanning stress relaxation of highly dispersible silica filled SBR/NR blends with various ZnO activator systems

The thermal stability of the elastomer network is an essential attribute of rubber vulcanizates. As

temperature increases, the thermal degradation of the rubber network is often accompanied by a substantial reduction in stress. To better understand the impact of different ZnO activators on the thermal stability of SBR/NR blends, temperature scanning stress relaxation (TSSR) experiments were conducted by observing the non-isothermal relaxation behavior as a function of temperature. The temperature at which crosslink cleavage or scission of the main chains occurs is indicated by significant peaks appearing in the relaxation spectrum. Each peak simultaneously reflects a relaxation mechanism. Figure 4 depicts the stress as a function of the temperature and the relaxation spectra of SBR/NR blends with varying ZnO activators.

In silica-filled SBR/NR blends, nano ZnO-loaded N2BS showed the highest stress, followed by A2BS and C5BS (Figure 4b), justifying the cure parameters obtained as N2BS had the highest delta torque among all the blends. F2BS with functionalized ZnO had the lowest stress value at constant strain magnitude. The higher stress value of N2BS and lower stress of F2BS is due to the higher crosslink density of N2BS and lower crosslink density of F2BS [42]. N2BS had the highest crosslink density among all other blends, and F2BS had the lowest. The change of stress with the temperature of silica-filled blends is shown in Figure 4. The reduction in relaxation stress with an increase in temperature was linked to the molecular mobility process, which was more pronounced for N2BS the reduction in relaxation stress with an increase in temperature was more pronounced for N2BS; it had the highest stress than C5BS, A2BS, and F2BS. The C5BS and N2BS exhibited a comparable temperature-dependent stress relaxation response and the lowest was observed for F2BS. From Figure 4a, the thermal stability of the blends can be accessed from  $T_{10}$  and  $T_{50}$  temperatures at which the stress of the blend has reduced by 10 and 50% obtained values were listed in Table 3.

The initial stress decay with temperature was observed, and A2BS had the highest, around 104 °C. In the case of C5BS, the  $T_{10}$  was at a lower temperature of 79 °C. N2BS reported  $T_{10}$  at 89 and 87 °C for F2BS were shown. The higher thermal stability was observed for A2BS due to its high surface area and the presence of more reactive Zn sites; its  $T_{50}$  was reported at 172 °C whereas C5BS had a similar thermal stability and  $T_{50}$  value around 171 °C due to the presence of high ZnO content (5 phr) in the respective blend.

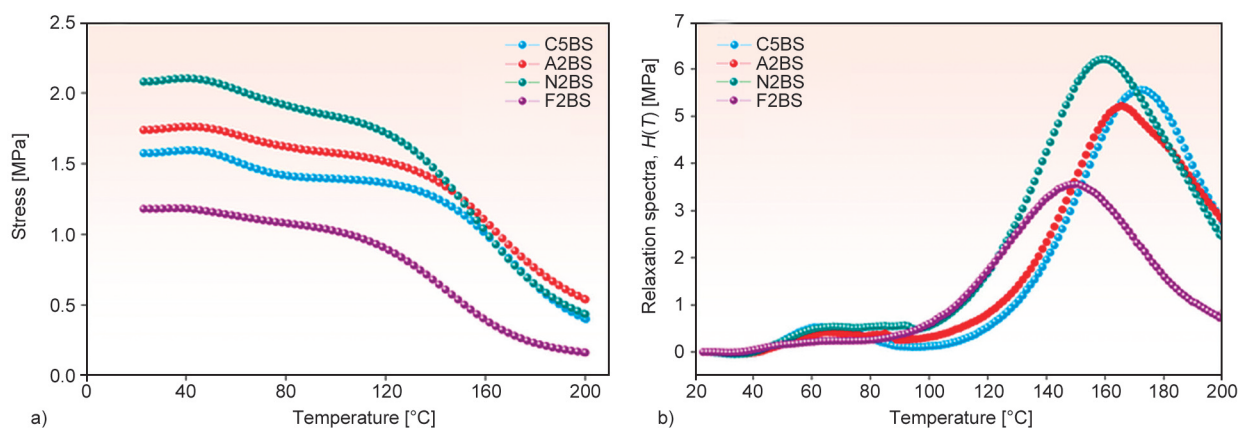


**Figure 4.** Non-isothermal stress relaxation test a) stress vs. temperature of HDS-filled SBR/NR blends with various ZnO as activators, b) relaxation spectra vs. temperature curve of HDS-filled SBR/NR blends containing various ZnO as activators.

**Table 3.** Degradation temperature obtained from the TSSR study.

Batch	$T_{10}$ [°C]	$T_{50}$ [°C]
C5BS	79.8	171.7
A2BS	104.6	172.7
N2BS	89.5	159.2
F2BS	87.2	145.3

N2BS shown  $T_{50}$  at 159 °C and F2BS at 145 °C shows the least thermal stability among all blends. The stress vs. temperature curve and the relaxation spectra vs. temperature are both shown in Figure 4. The relaxation spectrum  $H(T)$ , which is obtained from the stress vs. temperature curve, is obtained by differentiating the non isothermal relaxation modulus  $E(T)$  with respect to temperature ( $T$ ), as shown in Equation (3) [43]:

$$H(T) = -T \left( \frac{dE(T)}{dT} \right) \quad (3)$$

The peak around 110–150 °C indicates the decomposition of polysulfidic linkages, here F2BS exhibited a peak below 150 °C confirming that the presence of octylamine in the functionalized ZnO enables the faster curing and forming of the polysulfide linkages rather than di and monosulfidic. C5BS, A2BS and N2BS degradation peaks shifted to a higher temperature and showed a peak above 160 °C confirming the presence of mono and disulfide linkages [44]. In the case of conventional ZnO-filled C5BS showed a prominent peak at 174 °C. for A2BS 166, and 159 °C for N2BS, respectively; the F2BS peak was seen at a lower temperature of about 149 °C.

The stress of SBR/NR blends slightly increased in the 23–40 °C temperature range, as shown in Figure 4a. Entropy effects inherent to rubber vulcanizates are responsible for this. Furthermore, the crosslink density in rubber vulcanizates is represented by this area (23–40 °C) of the stress-temperature curve. Observing that stress-temperature graphs derived from the TSSR test were employed to assess crosslink density through the modified Neo-Hookean Equation (4) applied to the initial slope of the curves [44]:

$$\sigma = \nu RT \left( \left( \frac{\lambda}{1 + \alpha(T - T_0)} \right) - \left( \frac{\lambda}{1 + \alpha(T - T_0)} \right)^{-2} \right) \quad (4)$$

where  $\sigma$  represents stress,  $R$  stands for the universal gas constant, and  $\alpha$  represents the thermal expansion coefficient, corresponding to a value of  $2.4 \cdot 10^{-4} \text{ K}^{-1}$ . The extension ratio, denoted as  $\lambda$ , is the ratio of the final length  $l$  to the initial length  $l_0$ .  $T$  is the temperature in Kelvin.

The comparison of crosslink density obtained from TSSR and swelling study has been plotted in Figure 5, and it shows a positive correlation with the crosslink density obtained from the swelling study, as depicted in Figure 1b. The crosslink density of all the blends obtained from the TSSR experiment was lower than the one obtained from the swelling study. The resemblance in the crosslink density of blends derived from TSSR and swelling analysis demonstrates a consistent trend in the delta torque values. This suggests that the primary cause of torque development during vulcanization is the creation of crosslinks within the rubber matrix [45].



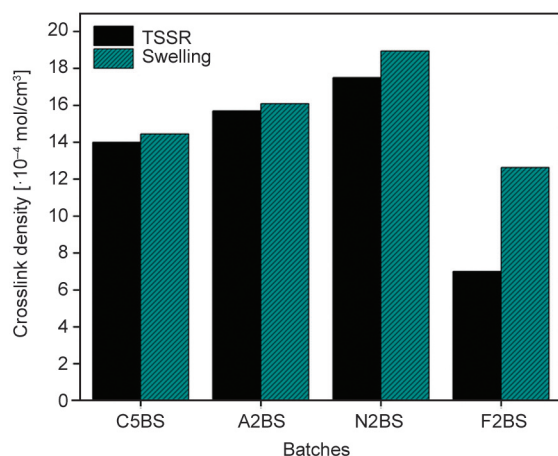


**Figure 5.** Crosslink density comparison between swelling and TSSR study of HDS-filled SBR/NR blends with various ZnO as activators.

### 3.4. Thermogravimetric Analysis (TGA)

The effect of the type of ZnO thermal stability on the silica-filled SBR/NR was investigated using the thermogravimetry (TG) technique and their derivative thermogravimetric (DTG) analysis. As seen in Figure 6a, the conventional ZnO-loaded C5BS had a little more residual weight after degradation than the other batches containing 2 phr of ZnO. This is due to the higher ZnO (5 phr) content of C5BS. The TG curves of all the samples under investigation primarily showed two degradation steps, as seen in the DTG curve (Figure 6). The rubber blend's plasticizer and volatile components degraded in the initial stage of degradation at around 370–400 °C. As can be seen, the degradation of SBR and NR caused most weight losses for all blends to occur between 420 and 480 °C. In Figure 6b, the degradation temperatures

of C5BS, A2BS, and N2BS are 461.67, 461.89, and 461.59 °C, respectively. It was nearly the same temperature range and demonstrates that the higher thermal stability of active ZnO and nano ZnO at 2 phr loading increases the thermal stability of the blend to the same level as conventional ZnO at 5 phr loading. The large dispersion of nanoparticles in the polymer matrix impeded the free radical's ability to diffuse, which delayed the degradation of rubber compounds. Additionally, ZnO nanoparticles' high heat capacity and thermal conductivity made them effective heat sinkers, absorbing more heat than the rubber matrix could hold onto, which increased the composites' thermal stability. Blends of A2BS and N2BS showed shifts to higher temperatures in their characterization temperatures due to their excellent dispersion in the matrix.

### 3.5. Dynamic mechanical analysis

The dynamic mechanical performance of the SBR/NR blends was analyzed over the temperature range of –80 to 80 °C. Figure 7 shows the comparative study of storage modulus and loss factor vs. temperature of silica-filled SBR/NR blends with various ZnO activators. The  $\tan \delta$  vs. temperature at 0 °C predicted wet skid, and the  $\tan \delta$  vs. temperature at 60 °C estimated rolling resistance and obtained values are listed in Table 4 [46]. A lower  $\tan \delta$  value indicated better fuel efficiency and lower rolling resistance at 60 °C. Better wet traction was suggested by a higher  $\tan \delta$  value at 0 °C. Change in traction was 0.6 and 1.1% lower for F2BS and A2BS than C5BS, which is negligible, and for N2BS, it was a 10% difference. The rolling resistance change was not in positive

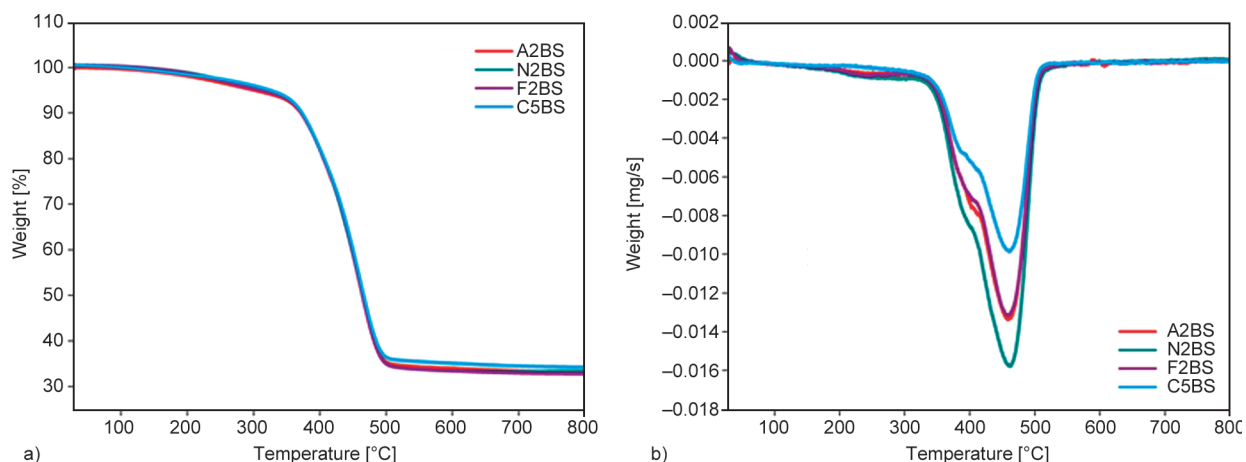


**Figure 6.** a) TGA curve of HDS-filled SBR/NR blends with various ZnO as activators, b) DTG plot of HDS-filled SBR/NR blends with various ZnO as activators.

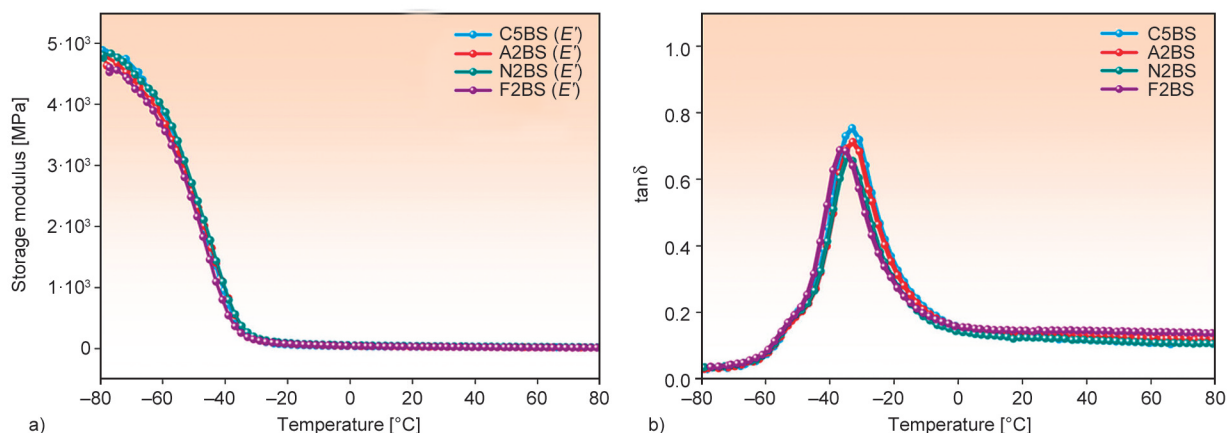


**Figure 7.** Dynamic mechanical analysis SBR/NR blends with various ZnO: a) storage modulus vs. temperature curve, b)  $\tan \delta$  vs. temperature curve.

**Table 4.** Traction and rolling resistance obtained from dynamic mechanical analysis.

SBR/NR Blend	Traction ( $\tan \delta$ at 0 °C)	Rolling resistance ( $\tan \delta$ at 60 °C)
C5BS	0.1597	0.1078
A2BS	0.1579	0.1218
N2BS	0.1433	0.1095
F2BS	0.1586	0.1412

association for F2BS and A2BS increase in 30 and 12% compared to C5BS; for N2BS, it was a 1.4% increase in the  $\tan \delta$  at 60 °C value.

The silica-filled blends showed no significant changes in the wet skid and rolling resistance in A2BS, N2BS, and F2BS compared to C5BS. Obtained rolling resistance and wet skid were in line with the value obtained for C5BS, thereby ensuring the reduction of ZnO is possible without affecting its main magic triangle properties of the tyre obtained from the dynamic mechanical analysis.

### 3.6. Payne effect interpretation of SBR/NR blends with various ZnO systems

Figure 8 depicts the RPA curve of storage modulus vs. strain and the resulting Payne effect obtained from the strain sweep analysis in the strain region of 0.5 to 100%. Here, we explore the Payne effect in silica-filled blends with various ZnO activators. The filler’s dispersion in the matrix significantly impacts the rubber blend mechanical performance. The Payne effect and SEM were used to analyze the dispersion state of blends. The storage modulus ( $G'$ ) of the rubber matrix reinforced with the silica filler increased as the strain increased, and the extent of this change under a final strain and initial strain was regarded as the Payne effect. The Payne effect can be resolved as  $\Delta G = (G_0' - G_\infty')$ .  $G_0'$  belongs to the storage modulus at the lowest strain, and  $G_\infty'$  is the storage modulus at the highest operating strain (at 100% strain) [47–49]. A lower Payne effect value indicates better

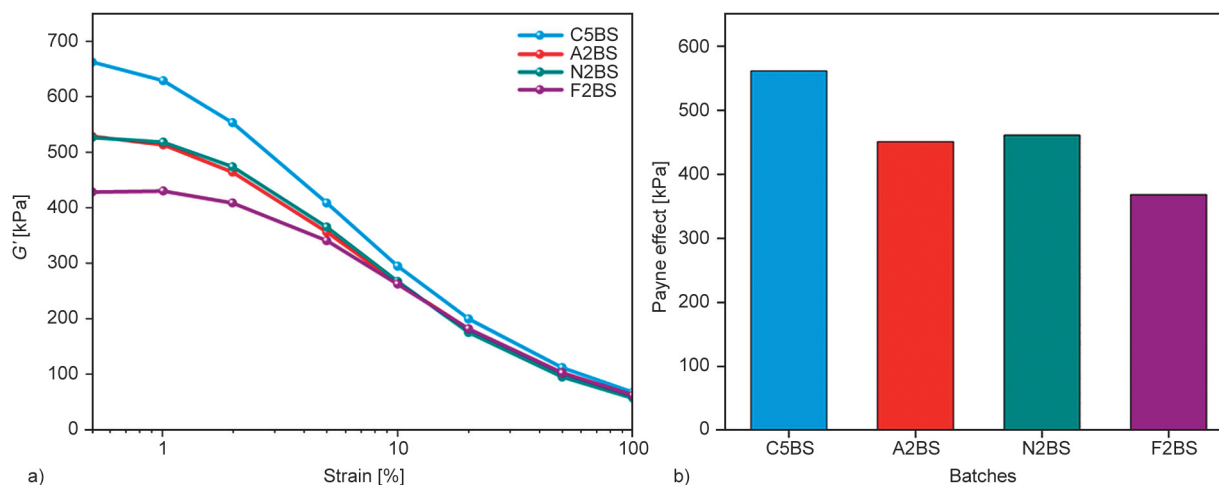


**Figure 8.** a) Strain sweep curve of ZnO in SBR/NR blends filled with highly dispersible silica, b) Payne effect in silica-filled blends.

filler dispersion, hence good polymer-filler interaction [50–52].

The F2BS blend containing octylamine-modified ZnO shows the lowest Payne effect. The octylamine-modified ZnO is known to improve the dispersion in thin film transistors [53]. Qin *et al.* [27] explored the octylamine-modified ZnO in NR and SBR matrix and found that the agglomeration has reduced and showed a better dispersion of Zn nanoparticles in the rubber matrix. Octylamine-modified ZnO exhibits uniform size distribution and a low tendency to form agglomerates [54, 55]. While active ZnO, which had more readily available  $Zn^{2+}$ , quickly reacted with the silica surface to form the covalent bond Si–O–Zn, protect the silica particles with a layer, and lessen the aggregation of filler in the matrix. Similarly, as shown in Figure 9, Octylamine modified ZnO formed the Si–O–Zn bonds and had a stronger affinity for the silica filler in F2BS. The filler-filler interaction was significantly reduced by an outer layer of octylamine and two layers covering the silica particles, resulting in a uniform distribution. This resulted in a lower filler-filler interaction and a low Payne effect. Compared to active ZnO, the available Zn sites were less in nano ZnO due to their lower surface area than active ZnO, resulting in a higher Payne effect than A2BS. C5BS had microsized conventional ZnO less available Zn sites reduced the dispersion in the matrix.

### 3.7. Mechanical characteristics of SBR/NR blends employing different ZnO

Table 5 lists the mechanical and physical properties obtained for the SBR/NR blends. The trend of the Payne effect was observed for the mechanical properties. As seen, the lower the Payne effect, the higher the polymer-filler interaction is, thereby improving the blends' mechanical properties; regarding the mechanical properties of silica-filled blends, functionalized ZnO as the activator exhibited the highest tensile strength and elongation at break compared to all other ZnO-filled blends. The higher reactivity of functionalized ZnO has been seen in the cure rate index analysis of the blends. A2BS had the second highest mechanical performance after F2BS; this could be due to the high reactivity of active ZnO to form an active-accelerator complex to react with sulfurating agents efficiently and increase the polymer-filler interaction. The lower particle size of nano ZnO increases the reactivity simultaneously, indicating a slight agglomeration at 2 phr loading, resulting in lower tensile strength and elongation at break than F2BS and A2BS. C5BS had lower tensile strength and elongation with a higher modulus due to its higher filler-filler interaction, lowering the mechanical performance of the blend as seen in the RPA analysis.

F2BS and A2BS silica-filled blends had the highest tensile strength and elongation at break, with increases

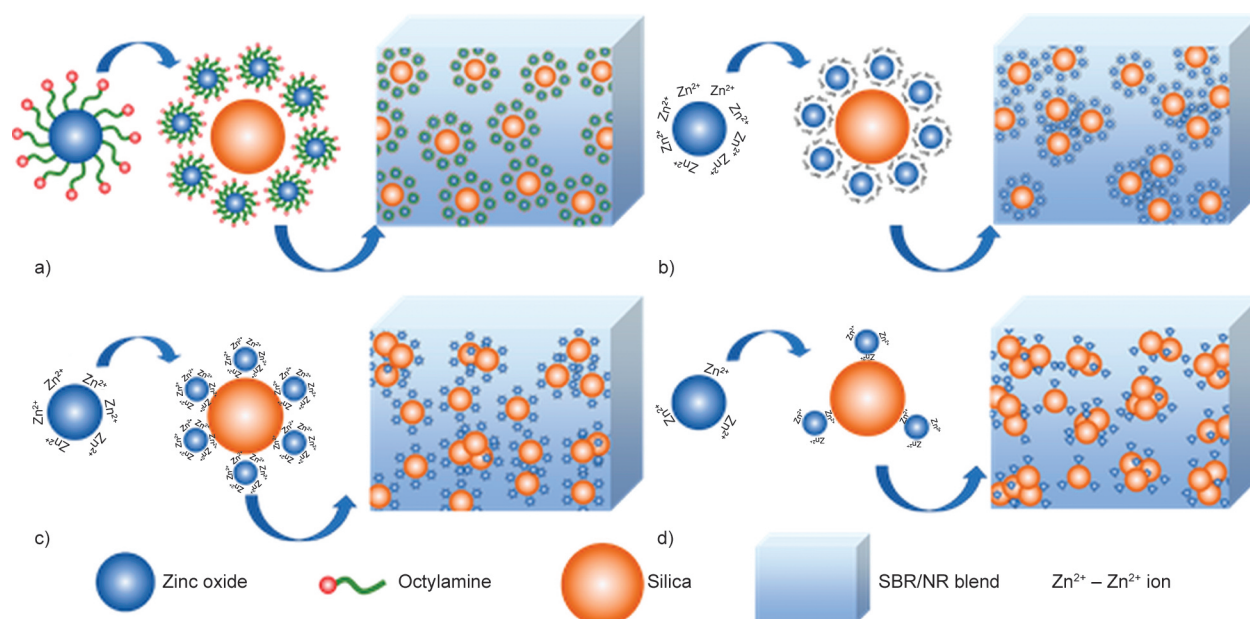


**Figure 9.** The proposed interaction of ZnO with silica particles in SBR/NR blends a) octylamine-modified ZnO in F2BS, b) active ZnO in A2BS, c) nano ZnO in N2BS, d) conventional ZnO in C5BS.

**Table 5.** Mechanical properties of SBR/NR blends.

Sample designation	Tensile strength [MPa]	Elongation at break [%]	Modulus at 300% [MPa]	Tear strength [N/mm]	Hardness [Shore A]
C5BS	15.1±2.4	362±61	12±1.2	85.0±3.4	68±1.3
A2BS	19.2±0.9	410±14	12.8±0.1	95.2±3.8	72±1.0
N2BS	15.5±2.4	351±49	12.7±0.4	74.1±2.1	68±1.8
F2BS	19.8±3.0	539±60	9.3±0.4	81.9±2.7	65±0.5

in tensile strength of 31% and elongation at break of 49% over C5BS. The highest tear strength was observed in A2BS among all the batches and had a 12% increase compared to C5BS. In terms of mechanical properties, active, nano, and functionalized ZnO at 2 phr were superior to conventional ZnO-loaded blends at 5 phr loading. The rubber compound's ZnO content is reduced by 60%, helping to lower the compound's cost and serving as a sustainable substitute additive to traditional ZnO.

### 3.8. Hot air accelerated aging study of SBR/NR blends with various ZnO

Figure 10 shows the crosslink density and mechanical property retention index of tensile strength, elongation at break and modulus values of silica-filled SBR/NR blends with various ZnO activators after accelerated aging study. The Equation (5) calculates the property retention index (*PRI*) [56]:

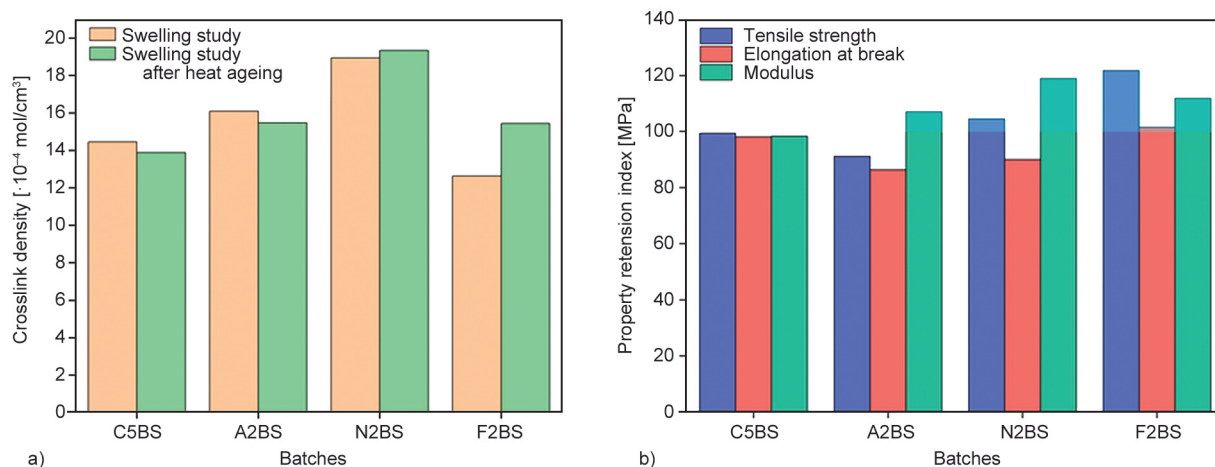
$$PRI [\%] = \frac{P}{P_0} \cdot 100 \quad (5)$$

where  $P_0$  is mechanical properties of the blends before ageing,  $P$  the mechanical properties of the blends after ageing.

An increase in tensile strength was seen for F2BS and N2BS blends compared to C5BS, where the rise

in tensile strength after aging was prominent in F2BS. The F2BS was uniformly dispersed in the rubber blend in accordance with the mechanical properties obtained before and after aging [5]. This characteristic may also result from the increased crosslink density accompanying aging. The study reveals notable alterations in the crosslink density of F2BS and N2BS, signifying an increase, while the blends C5BS and A2BS exhibit a reduction in crosslink density after heat aging. These crosslink density fluctuations are directly correlated with the corresponding changes in the mechanical properties observed following the aging study.

Through the process of aging, the crosslink density of elastomer chains is augmented as pendant groups on the chains undergo reactions with neighboring pendant groups. This leads to the formation of additional crosslinks, resulting in an enhancement of tensile strength. N2BS also increased the tensile strength and modulus after heat aging due to their more stable mono- and disulfide crosslinks and higher crosslink density increased the resistance to thermal aging because of their stable structure [5, 57]. A2BS, N2BS, and F2BS showed increased modulus and decreased elongation following the aging process due to the increased molecular rigidity. The elastomer chains experience an increase in average molecular weight at

**Figure 10.** a) Crosslink density and b) mechanical properties of C5BS, A2BS, N2BS, and F2BS after thermal aging.

high crosslinking densities, which restricts the mobility of individual chain segments. As a result, the elastomeric substance stiffens, which reduces the elongation at break values [58, 59].

### 3.9. Field emission scanning electron microscopy (FESEM) of SBR/NR blends with various ZnO

The sulfur vulcanization's activation state and the SBR/NR blends' mechanical performance are greatly influenced by the ZnO activator and silica filler's dispersion state in the blend. The vulcanization efficiency decreases because of the ZnO activator particle aggregation, which reduces their contact surface and interactions with other crosslinking system modules. SEM and TEM were used to assess the dispersion level of different ZnO and silica fillers in the SBR/NR blends to investigate the morphology of the composites.

The morphological analysis of the blends was carried out using scanning electron microscopy, as shown in Figure 11 below, to support the Payne effect results. C5BS, A2BS, N2BS, and F2BS were analyzed for their relative dispersion in the blend. The grey area depicts the SBR/NR blend, and the white spherical particles indicate the filler and ZnO present in the matrix. In SBR/NR blends, the incorporation of octylamine ligands effectively prevented nanoparticle aggregation, leading to the uniform dispersion of F2BS with octylamine-modified ZnO nanoparticles [60].

The rate of agglomeration was observed in C5BS, N2BS and A2BS, respectively. In C5BS, the micron-sized conventional ZnO was less dispersed in the hydrophobic matrix due to its hydrophilic nature. Although, compared to transmission electron microscopy, distinguishing ZnO and silica in the matrix in SEM analysis was quite tricky.

To get a clearer picture of the distribution of elements in the matrix, we performed an EDS analysis at 20  $\mu\text{m}$  scale. EDS spectrum and element mapping are given in Figure 12, and the atomic percentages of Si, O, and Zn have been provided. It has been observed that the atomic percentage of Si was 49% in F2BS, whereas in C5BS, it was 59%. It shows that the surface's layer formation of Si–O–Zn bonds has reduced the silica atomic % in the EDS spectrum.

### 3.10. Transmission electron microscopy of SBR/NR blends with various ZnO

The morphological changes in the bulk area of the SBR/NR blend system filled with highly dispersible silica at different ZnO activators can be determined from the TEM photomicrographs, as shown in Figure 13. In the C5BS blend, conventional ZnO with a cuboid structure was observed, along with silica particles in the SBR/NR blend, and it was discovered that the ZnO was not dispersed adequately within the matrix. To maintain consistency in the analysis, we used 100 nm-scale morphology images throughout the discussion section. The smaller particle size of nano ZnO leads to agglomeration in the blend, whereas active ZnO with more available  $\text{Zn}^{2+}$  readily reacted with the silica surface by forming the covalent bond Si–O–Zn and forming layer protection over the silica particles and reducing the aggregation of filler in the matrix. Similarly, using octylamine-modified ZnO had more affinity towards silica filler and formed the Si–O–Zn bonds, as shown in Figure 9. An outer layer of octylamine and two layers covering the silica particles drastically reduced the filler-filler interaction, resulting in uniform distribution [61]. Similar morphology was also observed in the SEM analysis. The SEM and TEM observations were in correlation with the obtained Payne effect.

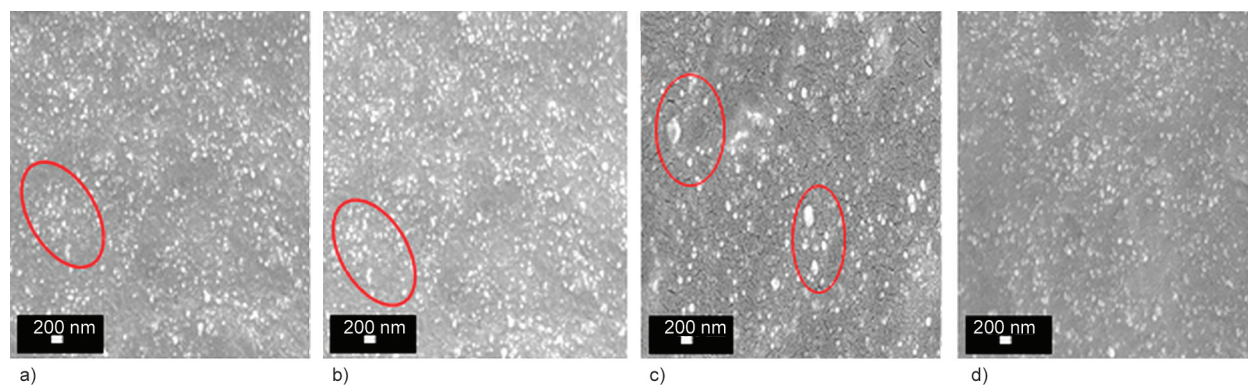
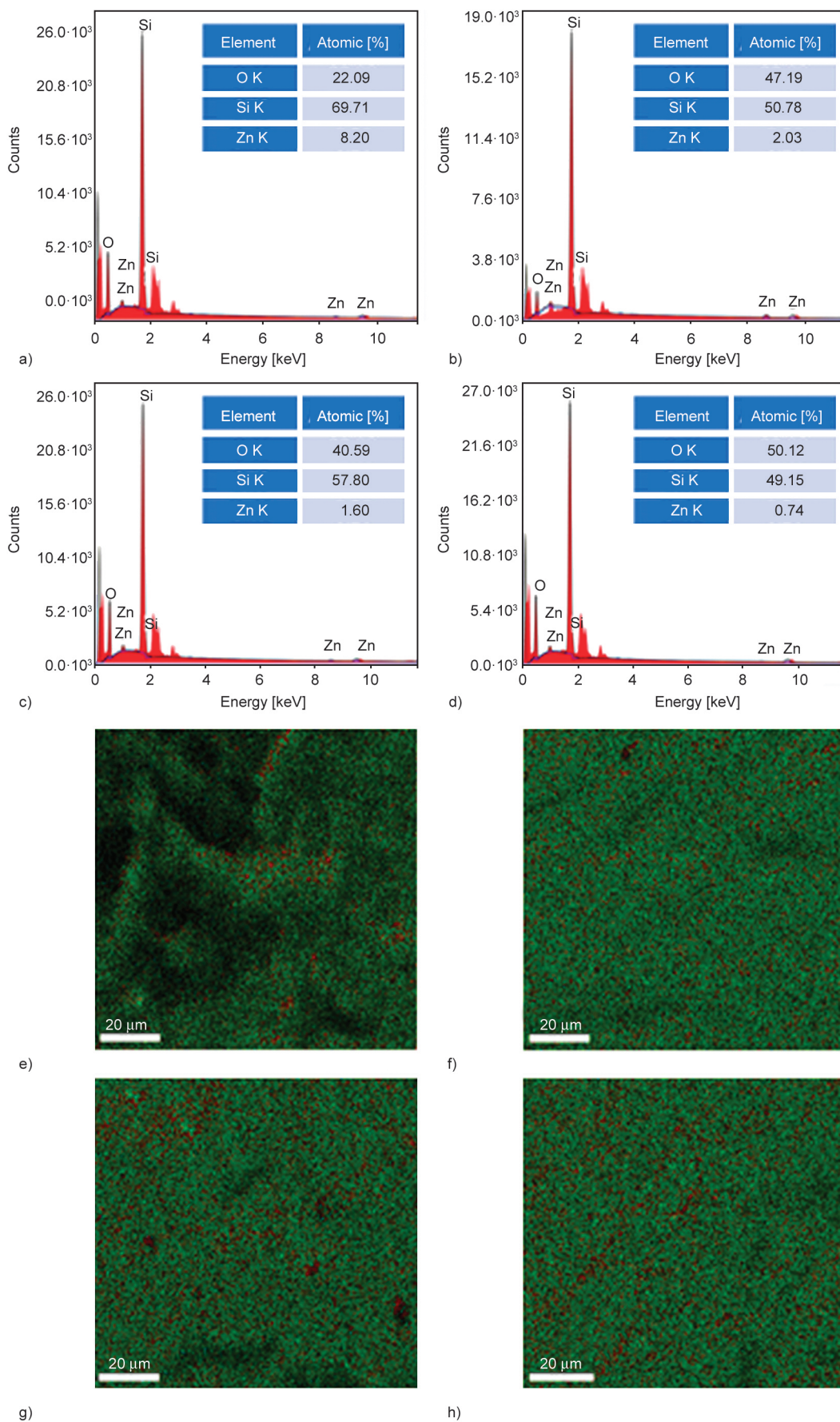
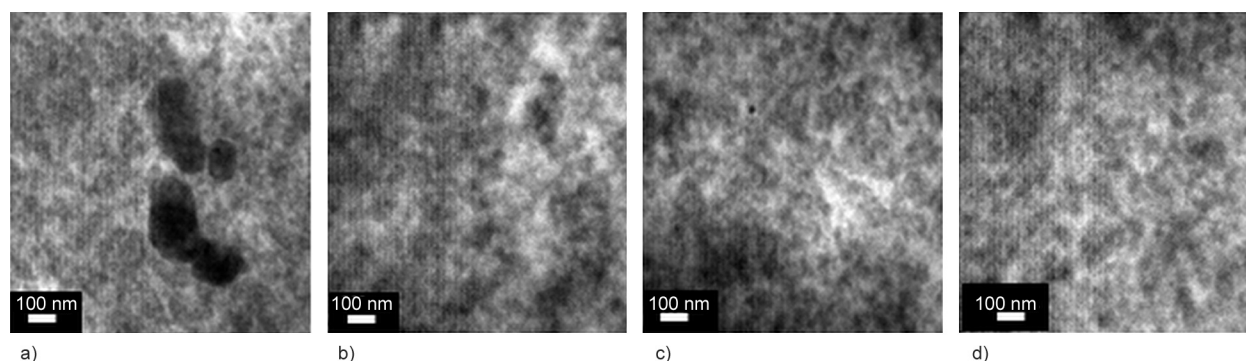


Figure 11. SEM images of a) C5BS, b) A2BS, c) N2BS, d) F2BS.



**Figure 12.** EDS spectrum of SBR/NR blends loaded with silica: a) C5BS, b) A2BS, c) N2BS, d) F2BS and EDX element mapping, e) C5BS, f) A2BS, g) N2BS, h) F2BS.



**Figure 13.** TEM images of SBR/NR blends loaded with silica: a) C5BS, b) A2BS, c) N2BS, d) F2BS.

#### 4. Conclusions

This study focuses on replacing conventional ZnO with more sustainable activators such as octylamine-modified, active, and nano ZnO. It investigates the effect of these alternatives on the cure characteristics, temperature scanning stress relaxation, mechanical properties, dynamic mechanical properties, Payne effect, and morphology of SBR/NR blends filled with silica. When octylamine-modified ZnO (F2BS) and active ZnO (A2BS) were used, they interacted with the silica filler and formed a protective layer around the silica particles, as indicated by the results. The reduced aggregation between the filler particles resulted in better dispersion and 31% tensile strength, and 49% improvement in elongation at break compared to C5BS. In addition, active ZnO exhibited exceptional thermal stability. The Zn–O–Si interface peak was most pronounced in F2BS and A2BS, followed by N2BS, whereas C5BS exhibited a weaker intensity. This was further supported by the fact that C5BS exhibited a more significant Payne effect. A small amount of agglomeration resulted from the addition of nano ZnO at a loading of 2 phr. Higher delta torque, crosslink density, and stress values seen in the isothermal measurements of TSSR analysis suggest that nano ZnO had a significant effect as an activator on cure characteristics. The better filler dispersion resulted in the highest tear strength of A2BS, which improved over C5BS by 12%. At a loading of 5 phr, traditional ZnO-loaded blends had inferior mechanical properties to active, nano, and functionalized ZnO. With the use of nano, active, and octylamine-modified ZnO, the rubber compound by 60%, a sustainable alternative to traditional ZnO is provided that not only helps to reduce costs.

#### Acknowledgements

The authors express their gratitude to IPF Dresden, Germany, for offering the testing facility for TSSR and DMA analysis. They also extend their appreciation to Prof. Sven Weissner, Dr. Amit Das, and Mr. Subradeep Mandal for their valuable suggestions and collaboration throughout this research.

#### References

- [1] Mostoni S., D'Arienzo M., Di Credico B., Armelao L., Rancan M., Dirè S., Callone E., Donetti R., Susanna A., Scotti R.: Design of a Zn single-site curing activator for a more sustainable sulfur cross-link formation in rubber. *Industrial and Engineering Chemistry Research*, **60**, 10180–10192 (2021).  
<https://doi.org/10.1021/acs.iecr.1c01580>
- [2] Alam M. N., Kumar V., Park S-S.: Advances in rubber compounds using ZnO and MgO as *co*-cure activators. *Polymers*, **14**, 5289 (2022).  
<https://doi.org/10.3390/polym14235289>
- [3] Yasuda Y., Minoda S., Ohashi T., Yokohama H., Ikeda Y.: Two-phase network formation in sulfur crosslinking reaction of isoprene rubber. *Macromolecular Chemistry and Physics*, **215**, 971–977 (2014).  
<https://doi.org/10.1002/macp.201400066>
- [4] Shaba E. Y., Jacob J. O., Tijani J. O., Suleiman M. A. T.: A critical review of synthesis parameters affecting the properties of zinc oxide nanoparticle and its application in wastewater treatment. *Applied Water Science*, **11**, 48 (2021).  
<https://doi.org/10.1007/s13201-021-01370-z>
- [5] Lee Y. H., Cho M., Nam J-D., Lee Y.: Effect of ZnO particle sizes on thermal aging behavior of natural rubber vulcanizates. *Polymer Degradation and Stability*, **148**, 50–55 (2018).  
<https://doi.org/10.1016/j.polymdegradstab.2018.01.004>
- [6] Rhodes E. P., Ren Z., Mays D. C.: Zinc leaching from tire crumb rubber. *Environmental Science and Technology*, **46**, 12856–12863 (2012).  
<https://doi.org/10.1021/es3024379>

- [7] Liu X., Wang J., Gheni A., ElGawady M. A.: Reduced zinc leaching from scrap tire during pavement applications. *Waste Management*, **81**, 53–60 (2018).  
<https://doi.org/10.1016/j.wasman.2018.09.045>
- [8] Salvaggio A., Marino F., Albano M., Pecoraro R., Camiolo G., Tibullo D., Bramanti V., Lombardo B. M., Saccone S., Mazzei V., Brundo M. V.: Toxic effects of zinc chloride on the bone development in *Danio rerio* (Hamilton, 1822). *Frontiers in Physiology*, **7**, 153 (2016).  
<https://doi.org/10.3389/fphys.2016.00153>
- [9] Raha S., Ahmaruzzaman M.: ZnO nanostructured materials and their potential applications: Progress, challenges and perspectives. *Nanoscale Advances*, **4**, 1868–1925 (2022).  
<https://doi.org/10.1039/d1na00880c>
- [10] Wang Z., Hou Z., Liu X., Gu Z., Li H., Chen Q.: Preparation of zinc oxide with core–shell structure and its application in rubber products. *Polymers*, **15**, 2353 (2023).  
<https://doi.org/10.3390/polym15102353>
- [11] Panampilly B., Thomas S.: Nano ZnO as cure activator and reinforcing filler in natural rubber. *Polymer Engineering and Science*, **53**, 1337–1346 (2013).  
<https://doi.org/10.1002/pen.23383>
- [12] Sahoo S., Maiti M., Ganguly A., George J. J., Bhowmick A. K.: Effect of zinc oxide nanoparticles as cure activator on the properties of natural rubber and nitrile rubber. *Journal of Applied Polymer Science*, **105**, 2407–2415 (2007).  
<https://doi.org/10.1002/app.26296>
- [13] Kim I.-J., Kim W.-S., Lee D.-H., Kim W., Bae J.-W.: Effect of nano zinc oxide on the cure characteristics and mechanical properties of the silica-filled natural rubber/butadiene rubber compounds. *Journal of Applied Polymer Science*, **117**, 1535–1543 (2010).  
<https://doi.org/10.1002/app.31996>
- [14] Begum P. M. S., Yusuff K. K. M., Joseph R.: Preparation and use of nano zinc oxide in neoprene rubber. *International Journal of Polymeric Materials and Polymeric Biomaterials*, **57**, 1083–1094 (2008).  
<https://doi.org/10.1080/00914030802341646>
- [15] Mottaghi M., Khorasani S. N., Esfahany M. N., Farzadfar A., Talakesh M. M.: Comparison of the effect of nano ZnO and conventional grade ZnO on the cross-linking densities of NR/BR and NR/SBR blends. *Journal of Elastomers and Plastics*, **44**, 443–451 (2012).  
<https://doi.org/10.1177/0095244312439446>
- [16] Maiti M., Basak G. C., Srivastava V. K., Jasra R. V.: Influence of synthesized nano-ZnO on cure and physico-mechanical properties of SBR/BR blends. *International Journal of Industrial Chemistry*, **8**, 273–283 (2017).  
<https://doi.org/10.1007/s40090-016-0107-7>
- [17] Sreethu T. K., Naskar K.: Zinc oxide with various surface characteristics and its role on mechanical properties, cure-characteristics, and morphological analysis of natural rubber/carbon black composites. *Journal of Polymer Research*, **28**, 183 (2021).  
<https://doi.org/10.1007/s10965-021-02536-8>
- [18] Yang Z., Xie C.: Zn<sup>2+</sup> release from zinc and zinc oxide particles in simulated uterine solution. *Colloids and Surfaces B: Biointerfaces*, **47**, 140–145 (2006).  
<https://doi.org/10.1016/j.colsurfb.2005.12.007>
- [19] Vatanserver N., Polat Ş.: Effect of zinc oxide type on ageing properties of styrene butadiene rubber compounds. *Materials and Design*, **31**, 1533–1539 (2010).  
<https://doi.org/10.1016/j.matdes.2009.09.015>
- [20] Sreethu T. K., Das M., Parathodika A. R., Bhattacharya A. B., Naskar K.: Understanding the role of ZnO as activator in SBR vulcanizates: Performance evaluation with active, nano, and functionalized ZnO. *Journal of Applied Polymer Science*, **140**, e53257 (2023).  
<https://doi.org/10.1002/app.53257>
- [21] Sreethu T. K., Jana S., Jana N. R., Naskar K.: Influence of active, nano, and functionalized zinc oxide particles on the mechanical, cytotoxicity, and thermal stability of carbon black filled SBR/NR blends. *Polymer Engineering and Science*, **63**, 2354–2370 (2023).  
<https://doi.org/10.1002/pen.26381>
- [22] Hong R., Pan T., Qian J., Li H.: Synthesis and surface modification of ZnO nanoparticles. *Chemical Engineering Journal*, **119**, 71–81 (2006).  
<https://doi.org/10.1016/j.cej.2006.03.003>
- [23] Khurana N., Arora P., Pente A. S., Pancholi K. C., Kumar V., Kaushik C. P., Rattan S.: Surface modification of zinc oxide nanoparticles by vinyltriethoxy silane (VTES). *Inorganic Chemistry Communications*, **124**, 108347 (2021).  
<https://doi.org/10.1016/j.inoche.2020.108347>
- [24] Rabin N. N., Morshed J., Akhter H., Islam M. S., Hossain M. A., Elias M., Alam M. M., Karim M. R., Hasnat M. A., Uddin M. N., Siddiquey I. A.: Surface modification of the ZnO nanoparticles with  $\gamma$ -aminopropyltriethoxysilane and study of their photocatalytic activity, optical properties and antibacterial activities. *International Journal of Chemical Reactor Engineering*, **14**, 785–794 (2016).  
<https://doi.org/10.1515/ijcre-2015-0141>
- [25] Luo M., Shen C., Feltis B. N., Martin L. L., Hughes A. E., Wright P. F. A., Turney T. W.: Reducing ZnO nanoparticle cytotoxicity by surface modification. *Nanoscale*, **6**, 5791–5798 (2014).  
<https://doi.org/10.1039/c4nr00458b>
- [26] Halbus A. F., Horozov T. S., Paunov V. N.: Surface-modified zinc oxide nanoparticles for antifungal and antiyeast applications. *ACS Applied Nano Materials*, **3**, 440–451 (2020).  
<https://doi.org/10.1021/acsnm.9b02045>
- [27] Qin X., Xu H., Zhang G., Wang J., Wang Z., Zhao Y., Wang Z., Tan T., Bockstaller M. R., Zhang L., Matyjaszewski K.: Enhancing the performance of rubber with nano ZnO as activators. *ACS Applied Materials and Interfaces*, **12**, 48007–48015 (2020).  
<https://doi.org/10.1021/acsmi.0c15114>



- [28] Presto D., Meyerhofer J., Kippenbrock G., Narayanan S., Ilavsky J., Moctezuma S., Sutton M., Foster M. D.: Influence of silane coupling agents on filler network structure and stress-induced particle rearrangement in elastomer nanocomposites. *ACS Applied Materials and Interfaces*, **12**, 47891–47901 (2020).  
<https://doi.org/10.1021/acsami.0c12106>
- [29] Kumar A., Basu D., Sahoo S., Khanra S., Kumar N., Gonzalez M., Chattopadhyay S.: Green approaches for functionalized silica-based natural rubber nanocomposites using eco-friendly sodium alginate biopolymers for superior static and dynamic behaviors. *ACS Sustainable Chemistry and Engineering*, **11**, 6866–6878 (2023).  
<https://doi.org/10.1021/acssuschemeng.2c06059>
- [30] Susanna A., Armelao L., Callone E., Dirè S., D’Arienzo M., Di Credico B., Giannini L., Hanel T., Morazzoni F., Scotti R.: ZnO nanoparticles anchored to silica filler. A curing accelerator for isoprene rubber composites. *Chemical Engineering Journal*, **275**, 245–252 (2015).  
<https://doi.org/10.1016/j.cej.2015.04.017>
- [31] El-Refaie E. S. M., Nasrat L. S., Mohamed M. K., Ibrahim I. A.: Investigation the dielectric strength and mechanical features of nitrile butadiene rubber enhanced by different nanoparticles. *Egyptian Journal of Petroleum*, **32**, 11–17 (2023).  
<https://doi.org/10.1016/j.ejpe.2023.03.001>
- [32] Pornprasit R., Pornprasit P., Boonma P., Natwichai J.: Determination of the mechanical properties of rubber by FT-NIR. *Journal of Spectroscopy*, **2016**, 4024783 (2016).  
<https://doi.org/10.1155/2016/4024783>
- [33] Wang R., Xie C., Zeng L., Xu H.: Thermal decomposition behavior and kinetics of nanocomposites at low-modified ZnO content. *RSC Advances*, **9**, 790–800 (2019).  
<https://doi.org/10.1039/c8ra09206k>
- [34] Movahed S. O., Ansarifar A., Mirzaie F.: Effect of various efficient vulcanization cure systems on the compression set of a nitrile rubber filled with different fillers. *Journal of Applied Polymer Science*, **132**, 41512 (2015).  
<https://doi.org/10.1002/app.41512>
- [35] Franieck E., Fleischmann M., Höleck O., Kutuzova L., Kandelbauer A.: Cure kinetics modeling of a high glass transition temperature epoxy molding compound (EMC) based on inline dielectric analysis. *Polymers*, **13**, 1743 (2021).  
<https://doi.org/10.3390/polym13111734>
- [36] Kamal M. R., Sourour S.: Kinetics and thermal characterization of thermoset cure. *Polymer Engineering and Science*, **13**, 59–64 (1973).  
<https://doi.org/10.1002/pen.760130110>
- [37] Collard X., El Hajj M., Su B-L., Aprile C.: Synthesis of novel mesoporous ZnO/SiO<sub>2</sub> composites for the photodegradation of organic dyes. *Microporous and Mesoporous Materials*, **184**, 90–96 (2014).  
<https://doi.org/10.1016/j.micromeso.2013.09.040>
- [38] Roy A., Polarz S., Rabe S., Rellinghaus B., Zähres H., Kruis F. E., Driess M.: First preparation of nanocrystalline zinc silicate by chemical vapor synthesis using an organometallic single-source precursor. *Chemistry – A European Journal*, **10**, 1565–1575 (2004).  
<https://doi.org/10.1002/chem.200305397>
- [39] Susanna A., D’Arienzo M., Di Credico B., Giannini L., Hanel T., Grandori R., Morazzoni F., Mostoni S., Santambrogio C., Scotti R.: Catalytic effect of ZnO anchored silica nanoparticles on rubber vulcanization and cross-link formation. *European Polymer Journal*, **93**, 63–74 (2017).  
<https://doi.org/10.1016/j.eurpolymj.2017.05.029>
- [40] Mostoni S., Milana P., D’Arienzo M., Dirè S., Callone E., Cepek C., Rubini S., Farooq A., Canevali C., Di Credico B., Scotti R.: Studying stearic acid interaction with ZnO/SiO<sub>2</sub> nanoparticles with tailored morphology and surface features: A benchmark for better designing efficient ZnO-based curing activators. *Ceramics International*, **49**, 24312–24321 (2023).  
<https://doi.org/10.1016/j.ceramint.2022.12.013>
- [41] Ikeda Y., Yasuda Y., Ohashi T., Yokohama H., Minoda S., Kobayashi H., Honma T.: Dinuclear bridging bidentate zinc/stearate complex in sulfur cross-linking of rubber. *Macromolecules*, **48**, 462–475 (2015).  
<https://doi.org/10.1021/ma502063m>
- [42] Yangthong H., Pichaiyut S., Wisunthorn S., Kummerlöwe C., Vennemann N., Nakason C.: Role of geopolymer as a cure activator in sulfur vulcanization of epoxidized natural rubber. *Journal of Applied Polymer Science*, **137**, 48624 (2020).  
<https://doi.org/10.1002/app.48624>
- [43] Vennemann N.: Characterization of thermoplastic elastomers by means of temperature scanning stress relaxation measurements. in ‘Thermoplastic elastomers’ (ed.: El-Sonbati A. Z.) Intech, London, 347–370 (2016).  
<https://doi.org/10.5772/35976>
- [44] Vennemann N., Schwarze C., Kummerlöwe C.: Determination of crosslink density and network structure of NR vulcanizates by means of TSSR. *Advanced Materials Research*, **844**, 482–485 (2014).  
<https://doi.org/10.4028/www.scientific.net/AMR.844.482>
- [45] Parathodika A. R., Sreethu T. K., Maji P., Susoff M., Naskar K.: Influence of molecular and crosslink network structure on vulcanizate properties of EPDM elastomers. *Express Polymer Letters*, **17**, 722–737 (2023).  
<https://doi.org/10.3144/expresspolymlett.2023.54>
- [46] Kim M. C., Adhikari J., Kim J. K., Saha P.: Preparation of novel bio-elastomers with enhanced interaction with silica filler for low rolling resistance and improved wet grip. *Journal of Cleaner Production*, **208**, 1622–1630 (2019).  
<https://doi.org/10.1016/j.jclepro.2018.10.217>
- [47] Yang R., Song Y., Zheng Q.: Payne effect of silica-filled styrene-butadiene rubber. *Polymer*, **116**, 304–313 (2017).  
<https://doi.org/10.1016/j.polymer.2017.04.003>

- [48] Khanra S., Sreenivasan P., Das S., Hore R.; Ganguly D., Chattopadhyay S.: Immobilization of a biobased process aid at the interface for binary silicone and fluoroelastomer based super specialty blends with silica for enhanced compatibility. *Journal of Materials Science*, **57**, 13974–13990 (2022).  
<https://doi.org/10.1007/s10853-022-07504-1>
- [49] Ramier J., Gauthier C., Chazeau L., Stelandre L., Guy L.: Payne effect in silica-filled styrene-butadiene rubber: Influence of surface treatment. *Journal of Polymer Science Part B: Polymer Physics*, **45**, 286–298 (2007).  
<https://doi.org/10.1002/polb.21033>
- [50] Bhattacharya M., Maiti M., Bhowmick A. K.: Influence of different nanofillers and their dispersion methods on the properties of natural rubber nanocomposites. *Rubber Chemistry and Technology*, **81**, 782–808 (2008).  
<https://doi.org/10.5254/1.3548232>
- [51] Payne A. R.: The dynamic properties of carbon black-loaded natural rubber vulcanizates. Part I. *Journal of Applied Polymer Science*, **11**, 57–63 (1962).  
<https://doi.org/10.1002/app.1962.070061906>
- [52] Li Y., Han B., Wen S., Lu Y., Yang H., Zhang L., Liu L.: Effect of the temperature on surface modification of silica and properties of modified silica filled rubber composites. *Composites Part A: Applied Science and Manufacturing*, **62**, 52–59 (2014).  
<https://doi.org/10.1016/j.compositesa.2014.03.007>
- [53] Weber D., Botnaraş S., Pham D. V., Steiger J., De Cola L.: Functionalized ZnO nanoparticles for thin-film transistors: Support of ligand removal by non-thermal methods. *Journal of Materials Chemistry C*, **1**, 3098–3101 (2013).  
<https://doi.org/10.1039/c3tc00576c>
- [54] Chang J., Waclawik E. R.: Experimental and theoretical investigation of ligand effects on the synthesis of ZnO nanoparticles. *Journal of Nanoparticle Research*, **14**, 1012 (2012).  
<https://doi.org/10.1007/s11051-012-1012-4>
- [55] Verbakel F., Meskers S. C. J., Janssen R. A. J.: Surface modification of zinc oxide nanoparticles influences the electronic memory effects in ZnO-polystyrene diodes. *Journal of Physical Chemistry C*, **111**, 10150–10153 (2007).  
<https://doi.org/10.1021/jp072999j>
- [56] Gujel A. A., Bandeira M., Giovanela M., Carli L. N., Brandalise R. N., Crespo J. S.: Development of bus body rubber profiles with additives from renewable sources: Part II – Chemical, physical-mechanical and aging characterization of elastomeric compositions. *Materials and Design*, **53**, 1119–1123 (2014).  
<https://doi.org/10.1016/j.matdes.2013.07.102>
- [57] Pimolsiriphol V., Saeoui P., Sirisinha C.: Relationship among thermal ageing degradation, dynamic properties, cure systems, and antioxidants in natural rubber vulcanisates. *Polymer – Plastics Technology and Engineering*, **46**, 113–121 (2007).  
<https://doi.org/10.1080/03602550601152861>
- [58] Takeoka Y., Liu S., Asai F.: Improvement of mechanical properties of elastic materials by chemical methods. *Science and Technology of Advanced Materials*, **21**, 817–833 (2020).  
<https://doi.org/10.1080/14686996.2020.1849931>
- [59] Gotoh H., Liu C., Bin Imran A., Hara M., Seki T., Mayumi K., Ito K., Takeoka Y.: Optically transparent, high-toughness elastomer using a polyrotaxane cross-linker as a molecular pulley. *Science Advances*, **4**, eaat7629 (2018).  
<https://doi.org/10.1126/sciadv.aat7629>
- [60] Mahmoodi N. M., Najafi F.: Preparation of surface modified zinc oxide nanoparticle with high capacity dye removal ability. *Materials Research Bulletin*, **47**, 1800–1809 (2012).  
<https://doi.org/10.1016/j.materresbull.2012.03.026>
- [61] Bomila R., Venkatesan A., Srinivasan S.: Structural, luminescence and photocatalytic properties of pure and octylamine capped ZnO nanoparticles. *Optik*, **158**, 565–573 (2018).  
<https://doi.org/10.1016/j.ijleo.2017.12.141>